BAM
Bundesanstalt für
Materialforschung
und -prüfung

Vijayendra K. Munikoti

On the propagation of elastic waves in acoustically anisotropic austenitic materials and at their boundaries during non-destructive inspection with ultrasound

Forschungsbericht
249

Die Aufgaben
der Bundesanstalt
stehen unter der Leitlinie:

Sicherheit und Zuverlässigkeit in Chemie- und Materialtechnik

Die Aufgaben

Die BAM ist im Aufgabenverbund „Material – Chemie –Umwelt – Sicherheit" zuständig für:

- Hoheitliche Funktionen zur öffentlichen technischen Sicherheit, insbesondere im Gefahrstoff- und Gefahrgutrechtsbereich;
- Mitarbeit bei der Entwicklung entsprechender gesetzlicher Regelungen, z.B. bei der Festlegung von Sicherheitsstandards und Grenzwerten;
- Beratung der Bundesregierung, der Wirtschaft sowie der nationalen und internationalen Organisationen im Bereich der Materialtechnik und Chemie;
- Entwicklung und Bereitstellung von Referenzmaterialien und -verfahren, insbesondere der analytischen Chemie und der Prüftechnik;
- Unterstützung der Normung und anderer technischer Regeln für die Beurteilung von Stoffen, Materialien, Konstruktionen und Verfahren im Hinblick auf die Schadensfrüherkennung bzw. -vermeidung, den Umweitschutz und den Erhalt volkswirtschaftlicher Werte.

Die Tätigkeitsbereiche

Das Tätigkeitsspektrum der BAM umfasst die sich ergänzenden und aufeinander bezogenen Tätigkeiten:

- Forschung und Entwicklung
- Prüfung, Analyse und Zulassung
- Beratung und Information.

Die nationale und internationale Zusammenarbeit

Die Aufgaben der BAM für Technik, Wissenschaft, Wirtschaft und Gesellschaft erfordern eine interdisziplinäre Zusammenarbeit. Insofern arbeitet die Bundesanstalt mit Technologieinstitutionen des In- und Auslandes, insbesondere den nationalen Schwesterinstituten eng zusammen. Sie berät Bundesministerien, Wirtschaftsverbände, Industrieunternehmen sowie Verbraucherorganisationen und unterstützt mit Fachgutachten Verwaltungsbehörden sowie Gerichte. Daneben ist sie in die internationale technische Zusammenarbeit eingebunden und im Bereich „Messwesen – Normung – Prüftechnik – Qualitätssicherung" (MNPQ) als nationale Institution für die Prüftechnik zuständig. Die Mitarbeiter der Bundesanstalt wirken in zahlreichen Fachgremien, gesetzlichen Körperschaften und normensetzenden Institutionen an der Aufstellung von technischen Regeln und Sicherheitsbestimmungen mit und vertreten die Bundesrepublik in nationalen und supranationalen Einrichtungen.

Der Status

Die BAM ist als technisch-wissenschaftliche Bundesoberbehörde im Geschäftsbereich des Bundesministeriums für Wirtschaft und Technologie Nachfolgeinstitution des 1871 gegründeten Staatlichen Materialprüfungsamtes sowie der 1920 gebildeten Chemisch-Technischen Reichsanstalt (CTR). Sie hat dementsprechend die Funktion einer materialtechnischen und chemisch-technischen Bundesanstalt. In ihr sind etwa 1600 Mitarbeiter, darunter mehr als 700 Wissenschaftler und Ingenieure, auf dem Stammgelände in Berlin-Lichterfelde sowie auf den Zweiggeländen in Berlin-Steglitz und Berlin-Adlershof tätig.

Dr.-Ing.
Vijayendra K. Munikoti (M. Tech.)

On the propagation of elastic waves in acoustically anisotropic austenitic materials and at their boundaries during non-destructive inspection with ultrasound

Forschungsbericht 249
Berlin, März 2001

Impressum

Forschungsbericht 249
März 2001
Herausgegeben von
Bundesanstalt für Materialforschung und -prüfung (BAM)
Unter den Eichen 87, 12205 Berlin
Telefon (030) 81 04-0
Telefax (030) 8 11 20 29

Herstellung und Verlag:
Wirtschaftsverlag NW
Verlag für neue Wissenschaft GmbH
Bürgermeister-Smidt-Str. 74-76, 27511 Bremerhaven
Postfach 10 11 10, 27611 Bremerhaven
Telefon (0471) 9 46 44-0
Telefax (0471) 9 45 44 77/88

Layout: Referat G.3

– D 83 –

ISSN 0938-5533
ISBN 3-89701-632-X

Sincerely dedicated to Dr.-Ing. E. Neumann

Zusammenfassung

In der vorliegenden Arbeit wird die Ultraschallausbreitung in akustisch anisotropen, homogenen Werkstoffen mit stengelkristalliner Textur wie austenitischen Plattierungen und Schweißverbindungen, austenitischem Guß oder geschweißten Komponenten aus austenitischem Guß modelliert.

Wie die in dieser Arbeit referierten metallurgischen Untersuchungen gezeigt haben, können austenitisches Schweißgut und stengelkristallin erstarrter austenitischer Guß makroskopisch als polykristallines Medium mit zylindersymmetrischer Textur behandelt werden, also als Medium mit transversal isotroper Symmetrie, obwohl mikroskopisch die einzelnen Stengelkristallite kubische Symmetrie aufweisen.

Die Schallausbreitung wird mit Hilfe des Ansatzes ebener Wellen modelliert. Obwohl bei der Ultraschallprüfung gepulste und begrenzte Schallbündel verwendet werden, liefert dieser Ansatz die bei der Ultraschallprüfung beobachteten Wellenarten mit Geschwindigkeiten und Polarisationen, Schallbündelablenkung und Reflexion und Brechung nach Richtung und Amplitude, so daß über das Modell der ebenen Welle hinausgehende Ansätze - auch für die Behandlung der Ultraschallstreuung an den Korngrenzen - nicht in Betracht gezogen werden mußten.

Die Auswerteprogramme zur numerischen Bestimmung von Reflexions- und Brechungskoeffizienten, Schallstrahlverläufen und Schwächungskoeffizienten wurden in FORTRAN 77 mit integrierter Graphikausgabe geschrieben.

Die Ergebnisse dieser Arbeit dienen als Vorgabe für Prüfanweisungen und Regelwerke, die besser als bisher an den Prüfgegenstand angepaßt sind.

Die Wellenmoden

In anisotropen Medien sind generell drei Wellenmoden möglich. Sie ergeben sich aus den Lösungen des mit Hilfe der Christoffel-Gleichung formulierten Eigenwertproblems mit richtungsabhängigen Phasen- und Gruppengeschwindigkeiten und richtungsabhängigen orthonormalen Polarisationen. In Medien mit transversal isotroper Symmetrie sind dies ein Wellenmode mit überwiegend longitudinalem Charakter, einer mit überwiegend transversalem Charakter und ein rein transversaler Wellenmode. Deren Phasen- und Gruppengeschwindigkeiten mit daraus abgeleiteter Schallbündelspreizung und deren Polarisationen als Funktion der Ausbreitungsrichtung für beliebige Ausbreitungsrichtungen in Medien mit transversal isotroper Symmetrie wurden dreidimensional berechnet. Der durch Eigenwert (Phasengeschwindigkeit) und Eigenvektor (Teilchenverschiebungsgeschwindigkeit, Polarisation) bestimmte Charakter der Ultraschallwelle wird im anisotropen Medium richtungsabhängig. Daher bleiben z. B. bei den Transversalwellen die Eigenschaften 'horizontal' und 'vertikal' polarisiert generell nicht erhalten und werden nur noch in kristallographisch ausgezeichneten Ausbreitungsrichtungen (z. B. bei Ausbreitung in der Meridianebene) beobachtet.

Reflexion und Brechung

Reflexions- und Brechungskoeffizienten werden als Energiekoeffizienten für die ungestörte Grenzfläche, für die gestörte (rißhaltige) Grenzfläche und für die Grenzfläche mit zähflüssiger Zwischenschicht (Prüfkopfankopplung) angegeben.

- Da die Polarisation der Ultraschallwelle richtungsabhängig ist, folgt unmittelbar, daß an Grenzflächen zwischen anisotropen Medien im allgemeinen Fall in Reflexion und Brechung immer alle drei Wellenmoden an einen einfallenden Wellenmode ankoppeln, anders als an Grenzflächen zwischen isotropen Medien. Die Modenwandlung zwischen longitudinalen und transversalen Wellen liegt dabei meist unterhalb von 10% der einfallenden Wellenenergie. Dies ist bei den beiden transversalen Wellen anders. Abhängig von den Orientierungen der Stengelkristallite (Textur) beidseits der Grenzfläche kann die Modenwandlung 100% der einfallenden Wellenenergie erreichen. Die Energieinhalte der beiden erzeugten Transversalwellen verhalten sich dabei wie die Komponenten der Polarisation der einfallenden Welle in Richtung der Polarisationen der beiden erzeugten Wellen.

- Wegen der konkaven Anteile der inversen Normalenfläche der quasi-Transversalwelle gibt es in einigen Positionen der Einschallebene mehrere Sektoren 'erlaubter' Wellenvektoren, so daß durch eine einfallende (quasi- oder reine) transversale Welle zwei quasi-Transversalwellen erzeugt werden können. Der Effekt kann in Reflexion und Brechung auftreten. Die Energiekoeffizienten der erzeugten zweiten quasi - Transversalwelle, die eine andere Phasengeschwindigkeit und eine andere Polarisation hat, werden angegeben.

- Die Transparenz einer rißhaltigen Grenzfläche nimmt selbst bei einem Rißflächenanteil von 75% nicht wesentlich ab. Entsprechend steigt der Anteil reflektierter und modengewandelter Energie der einfallenden Welle.

- Die Transparenz der viskoelastischen Flüssigkeitsschicht zwischen isotropem und transversal isotropem Medium (Prüfkopfankopplung) unterscheidet sich nicht wesentlich vom bekannten Fall der Flüssigkeitsankopplung von Prüfköpfen auf isotropem Material. Die Steigerung der Viskosität der Flüssigkeitsschicht liefert auch für Transversalwellen eine Durchlässigkeit von 50%, nicht viel weniger, als bei fester Kopplung erzielt werden würde.

Der Effekt des Bündelversatzes wird für die Grenzfläche zwischen flüssigem Medium und transversal isotropem Festkörper berechnet. Abgesehen davon, daß der Rayleigh-Winkel und die Phasengeschwindigkeit von Rayleigh-Wellen von der Stengelkristallitorientierung abhängen, ist der berechnete Bündelversatz und die Aufspaltung des reflektierten Bündels qualitativ ähnlich dem, was für den isotropen Fall gefunden wird.

Schallstrahlverfolgung

Es wurde ein numerisches Verfahren entwickelt, das die dreidimensionale Berechnung des Schallstrahlverlaufs (des Energieflusses) durch die Korngrenzen hindurch erlaubt. Wegen der Abweichung des Energieflusses von der Richtung des Wellenvektors tritt der Schallstrahl generell aus der Einschallebene heraus und muß deshalb dreidimensional dargestellt werden. Dabei wird ein Schallbündel durch sieben Strahlen, die vom Schalleintrittspunkt eines Prüfkopfs mit jeweils um ein Grad versetztem Einschallwinkel ausgehen, simuliert. Es ergibt sich, daß die quasi-Longitudinalwelle und die reine Transversalwelle weit weniger durch die Gefügetextur beeinflußt werden als die quasi-Transversalwelle. Der

Schallstrahlverlauf der wegen der konkaven Anteile der inversen Normalenfläche unter bestimmten Bedingungen entstehenden zweiten quasi-Transversalwelle wird ebenfalls angegeben.

Ultraschallstreuung

Wie die in dieser Arbeit referierten metallurgischen Untersuchungen gezeigt haben, wird die Ultraschallstreuung allein durch die Korngrenzen verursacht, die durch die aneinandergrenzenden Stengelkristallite unterschiedlicher elastischer Eigenschaften entstehen. Zur dreidimensionalen Berechnung der Ultraschallschwächung durch Streuung in einem beliebig zur Einschallebene orientierten Schweißgut mit stengelkristalliner Textur wurde von der vereinheitlichten Streutheorie nach Stanke und Kino in der Kellerschen Näherung ausgegangen; diese wurde auf das transversal isotrope Medium mit beliebiger Orientierung der Textur erweitert. Dabei wurde die im anisotropen Medium auftretende Polarisationsabweichung - anders als in früheren Arbeiten anderer Autoren - nicht vernachlässigt.

Die Streukoeffizienten werden für einen austenitischen CrNi-Stahl als Funktion der Ausbreitungsrichtung und der Frequenz angegeben. Während die Schwächung der quasi-Longitudinalwelle und der reinen Transversalwelle bei Ausbreitung in Stengelkristallitrichtung verschwindet und monoton anwächst, wenn die Ausbreitungsrichtung sich bis auf 90° zur Stengelkristallitrichtung verändert, hat die Schwächung der quasi-Transversalwelle bei etwa 45° einen Maximalwert und verschwindet bei 0° und 90°. Bezogen auf gleiche Wellenlänge ist die Schwächung der quasi-Transversalwelle geringer als die der beiden anderen Wellenarten. Es ist also nicht die hohe Schwächung der quasi-Transversalwelle, die sie für die Ultraschallprüfung austenitischer Schweißnähte ungeeignet macht, sondern die im Schweißgut entstehende hohe Bündelspreizung und Aufspaltung dieses Wellentyps. Die Schwächung aller drei Wellenarten nimmt mit zunehmendem Verhältnis von Wellenlänge zu Korngröße monoton zu und wird im Bereich der stochastischen Streuung frequenzunabhängig.

In Gegenwart von Ultraschallstreuung verändert sich die Phasengeschwindigkeit (bis zu $\approx$ 7% bei 2 MHz und 100 μm Korngröße). Ebenso wird Dispersion der Phasengeschwindigkeit gefunden (bis zu $\approx$ 6% im Bereich bis 5 MHz bei 100 μm Korngröße). Auch die Polarisationsabweichung verändert sich. Während die Polarisationsabweichung der reinen Transversalwelle jedoch unbeeinflußt immer senkrecht zum Wellenvektor bleibt, ergibt sich für quasi-Longitudinalwelle und quasi-Transversalwelle eine Veränderung der Polarisationsabweichung von bis zu 2°.

Contents

Chapter 1

Introduction: Status of research and technical development

1.1 Structure of austenitic weld metal

Austenitic welds though comprising a variety of weld processes and geometries with weld thicknesses ranging from 3 mm to over 100 mm, all exhibit a structural macroscopic texture, which makes the elastic properties to be direction dependent. This physical property of materials is referred to as 'anisotropy'.

The weld metal macro- and microstructure highly depends on the weld process with its specific conditions of solidification and on chemical composition which, moreover, determines metallurgical characteristics of different structural elements of the weld.

Due to recent advances in mathematical modeling of many metallurgical processes such as solidification phenomena, e. g. Kurz (1992 [20]), and weld phenomena, e. g. Cerjak et al. (1993-1997 [11]), modeling of the evolution of the grain structure with exact grain shape in austenitic stainless steel weld metal has been possible by statistical and computer simulation techniques based upon Monte-Carlo, FEM based cellular automaton and spline mathematics approaches. The results of simulation and actual micrographs agree fairly well, provided the welding input parameters and sufficient knowledge on mechanics of solidification in the weld pool are available.

Grain growth simulation software is available, e. g. Dilthey et al. (1996 [57], 1997 [58]), Pavlik et al. (1995 [149]), and Gandin et al. (1996 [69]), which works on a similar numerical method as the former, viz. CAFE (Cellular Automaton Finite Element) method. However, up to now there is no known interface available to integrate with the software dealing with ultrasound propagation in such simulated structures.

By 'Orientation Imaging Microscopy' with the Scanning Electron Microscope (Adams et al. 1993 [39], Field et al. 1996 [65]), the microstructure is mapped directly. For ultrasound propagation modeling purposes the grain orientation angles are stored in an array and are utilized to determine the local elastic constants in the weld metal.

On the other hand, anisotropy of polycrystalline materials needs only to be described in macroscopic terms which result from averaging the microscopic anisotropy of the single grains. This is the case especially for materials exhibiting a texture, induced during manufacturing processes such as rolling, or welding. To study ultrasound propagation in textured materials only the knowledge of the orientation distribution function of the grains is necessary. The orientation distribution function can be derived from

- texture measurements, e. g. by X-ray diffraction methods, as described e. g. by Bunge (1983 [10]), Roe (1964 [152, 153]), Yalda-Mooshabad (1995 [184])

- by observation of micrographs and developing a mathematical relation describing the orientation distribution. Ogilvy (1985 [139], 1986 [140], 1990 [146]) for her ultrasound ray-tracing model developed such an empirical relation to determine the local grain orientation in welds. Though this model does not consider any welding input parameters and weld pool data, the results using this model agree fairly well with experimental observations.

In order to model ultrasound propagation and scattering in austenitic textured weld metal informations on the following items are needed:

1. Overall weld metal texture acting on ultrasound propagation,
2. Structural properties of the weld metal, viz. of the columnar grains and their boundaries,
3. Metallurgical structural elements, e. g. segregations, poly-phases (e. g. delta ferrite), which also might affect propagational and scattering characteristics of ultrasound.

For this purpose, both, structural and metallurgical properties, of some most important weld metal grades: Cr-Ni steels - austenitic and fully austenitic steels -, nickel-based alloys, and ferritic-austenitic Duplex-steel are compiled. These weld metal grades mainly differ by their delta-ferrite content, which is the second phase besides the austenitic phase. The investigations to be reported here have been performed on these weld metal grades by metallography (Bauer 1999 [46]), by X-ray diffraction (Nolze 1999a [131]), by back-scattered electron diffraction patterns measured at the scanning electron microscope (Nolze 1999b [132]), and by scanning acoustic microscopy (Haubold 1999 [74]).

1.1.1 Metallography

1.1.1.1 Macrostructure

According to the number of beads per layer main directions of epitaxial grain growth are generated extending from weld root and weld fusion face up to the weld crown, figs. 1.1 - 1.3.
The higher the content of a second phase in the weld metal the lesser is the columnar grain texture: increase in the ferrite-content yields instead a Widmannstätten structure as shown in fig. 1.4 in the case of CrNi 19 9 weld metal. Due to reheating during welding of the bead above the dendritic columnar grain structure of the re-heat affected zone (HAZ) of a bead partially is transformed to equiaxed grain structure. Consequently columnar grains no longer grow epitaxially through the bead boundaries. Macroscopically this weld metal structure then appears to be isotropic, because the columnar grains do not extend out of a bead because of the interrupting HAZs of the beads.
The weld metal of a Duplex steel (figs. 1.5 and 1.6) is characterised by primary ferritic single-phase solidification. The austenitic phase is generated only after solidification of the weld metal during cooling down as a second phase within the ferritic matrix.
The precipitation of the austenite takes place at the grain boundaries in the form of crossing laths. The morphology of the austenitic phase is the acicular Widmannstätten micro-structure. The columnar structure extending over several beads observed in the austenitic weld metals is not present in this weld metal.

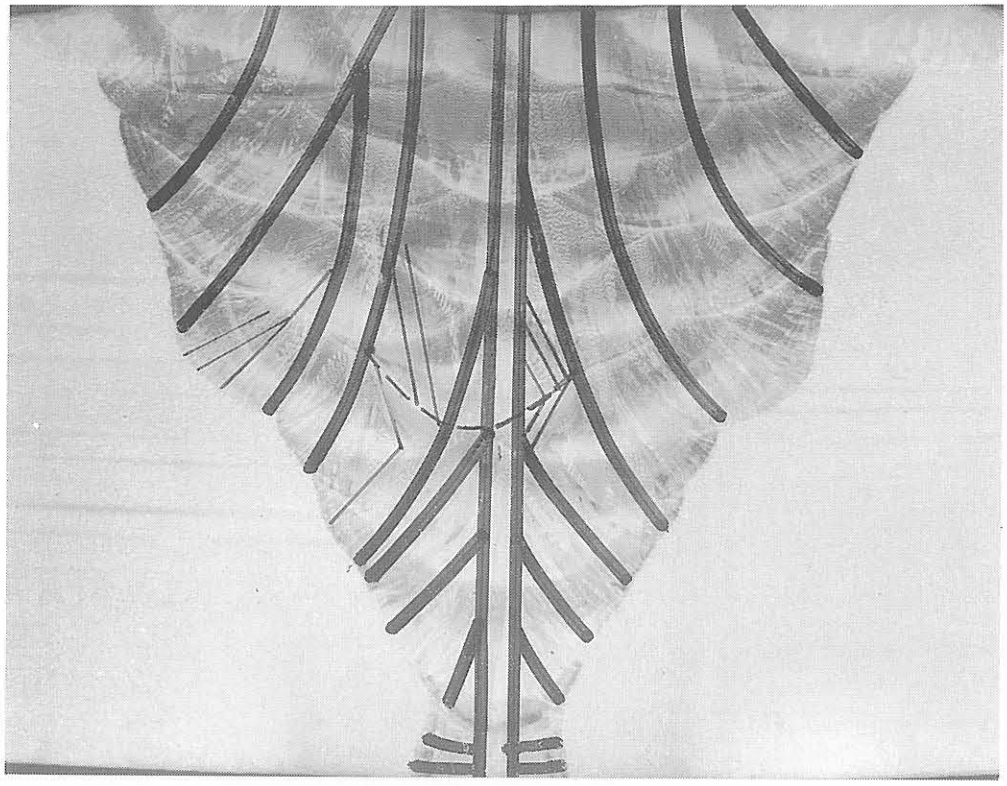

Figure 1.1: *Columnar grain configuration of Nickel-based weld metal Nicrofer 6025 HT, cross section, submerged arc welding (root: TIG) (Bauer 1999 [46])*

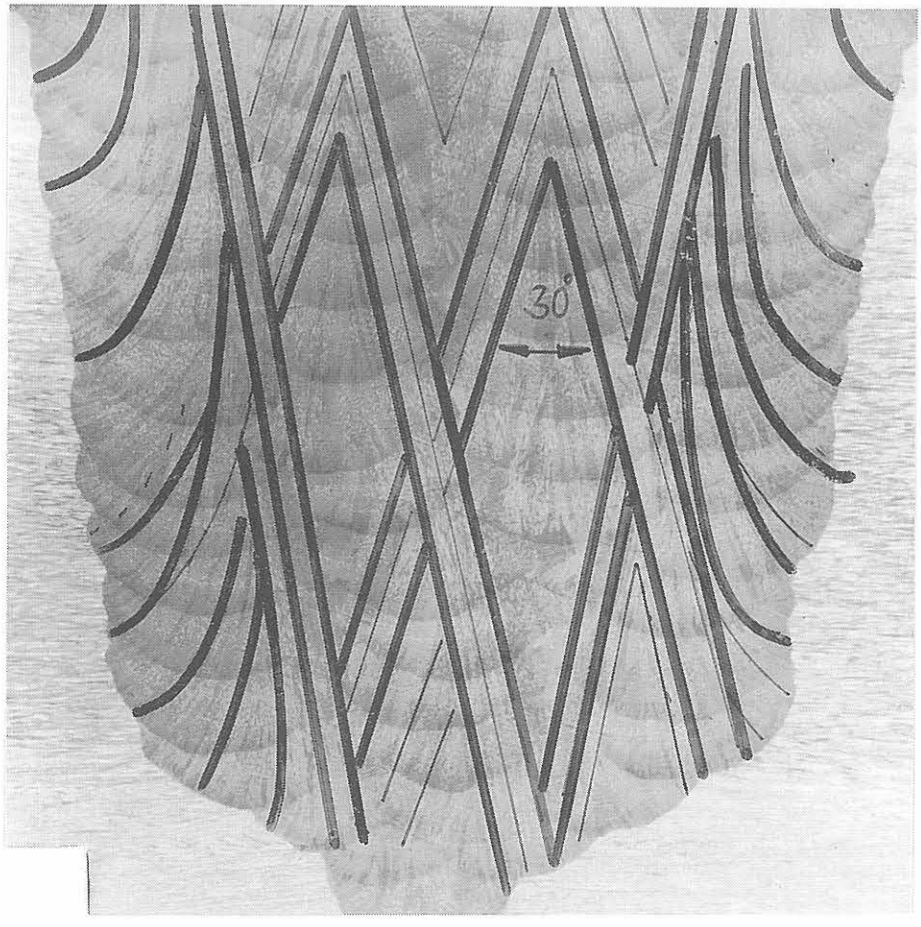

Figure 1.2: *Columnar grain configuration of austenitic weld metal X 6 CrNi 18 11 with delta ferrite (FN = 0), cross section; Weld data: submerged arc welding, wire diameter 3 mm, V-butt weld, thickness 45 mm, angle of bevel 10° (Bauer 1999 [46])*

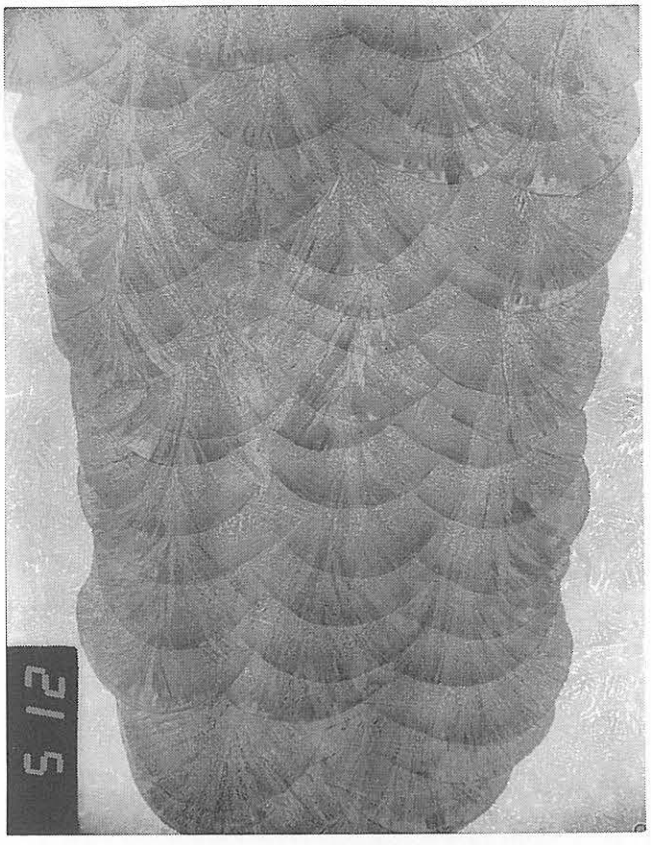

Figure 1.3:
X 2 CrNi 19 9; δ-ferrite 12 - 20%; cross section; Weld data: root tungsten inert gas welded (rod diameter 1,6 mm), filler layers submerged arc welded (wire diameter 4 mm), V-butt weld thickness 76 mm (Bauer 1999 [46])

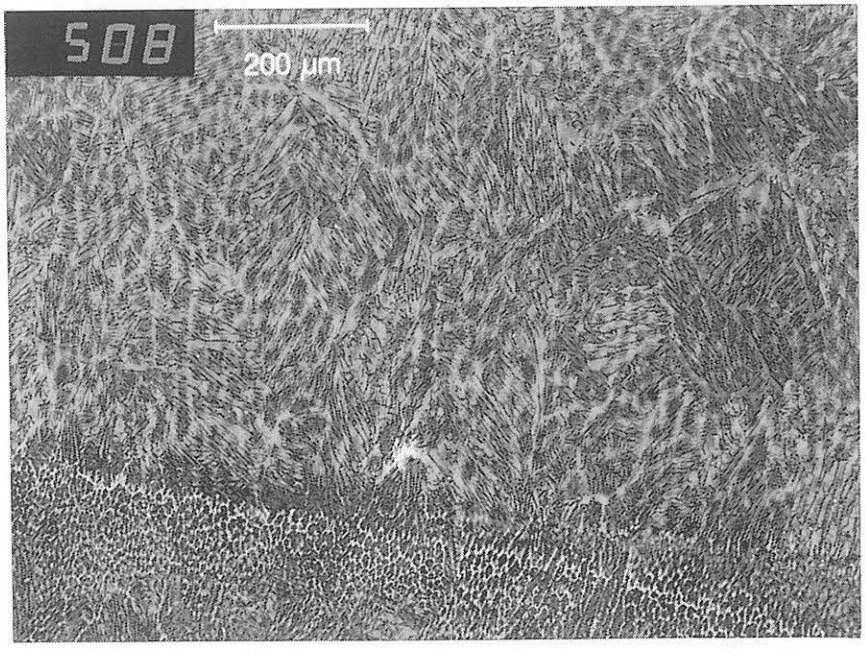

Figure 1.4:
X 2 CrNi 19 9; δ-ferrite 12 - 20%; longitudinal section in the welding direction; transition zone between the root and the following bead above; same weld as in fig. 1.3 (Bauer 1999 [46])

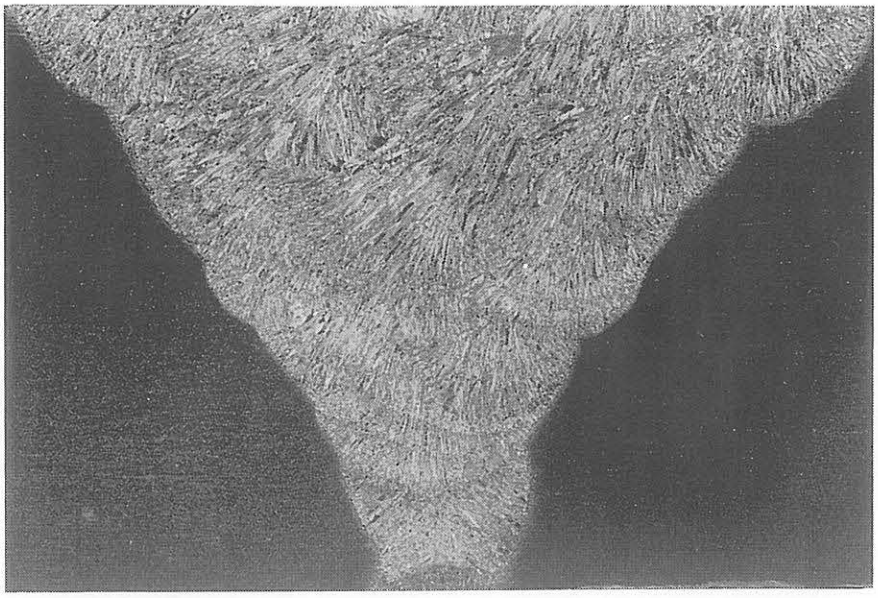

Figure 1.5:
High alloy Duplex weld; cross section; base metal: ferrite and austenite (α/γ)-solid solution; weld metal: Widmannstätten structure; Weld data: tungsten inert gas welded, circumferential V-butt weld thickness 35 mm, included angle 75° (Bauer 1999 [46])

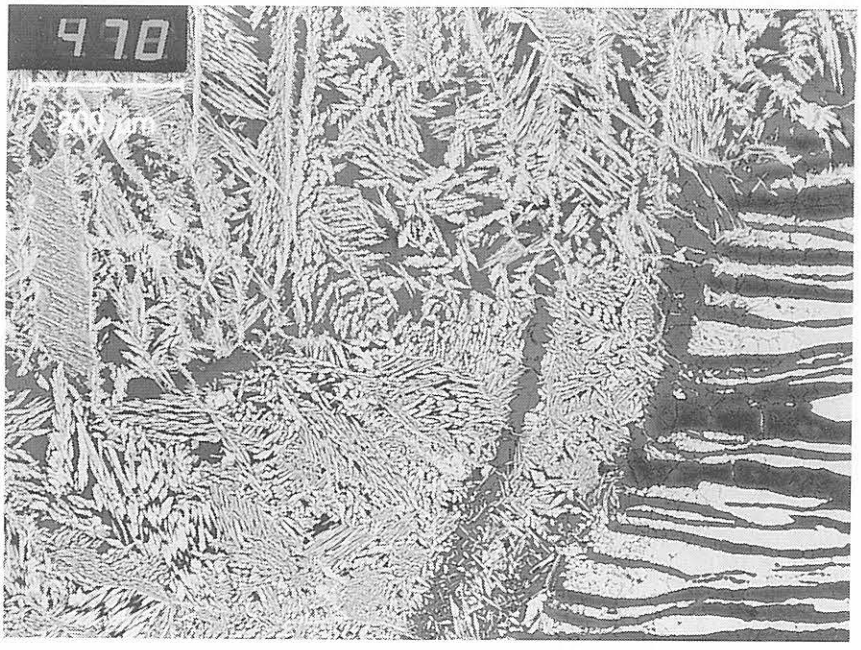

Figure 1.6:
Duplex weld metal; cross section; detail at the fusion face; base metal: ferrite and austenite (α/γ)-solid solution; weld metal: Widmannstätten structure; same weld as in fig. 1.5 (Bauer 1999 [46])

1.1.1.2 Structural elements

The fully austenitic nickel based weld metal NiCr 19 Nb (Alloy 182) exhibits dendritic and residual interdendritic melting areas, figs. 1.7 and 1.8.

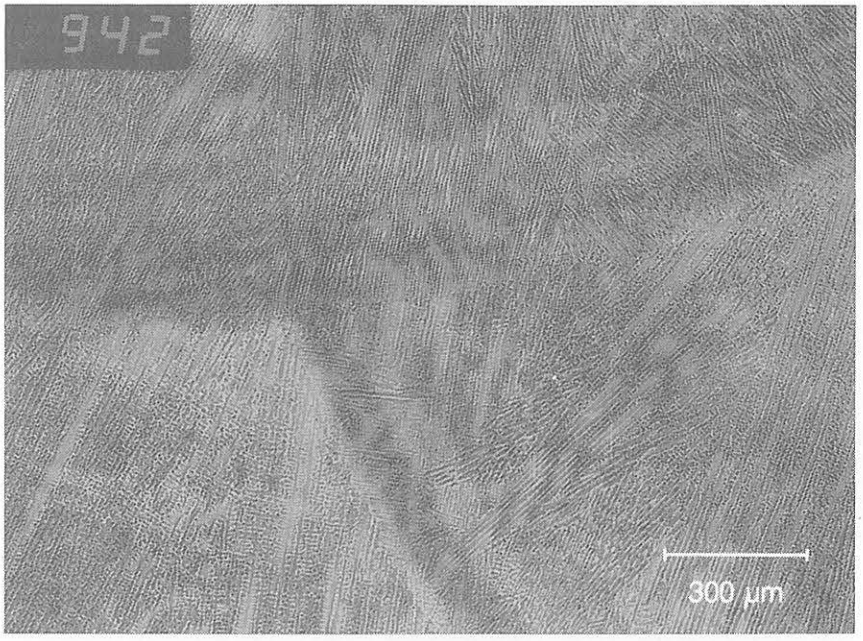

Figure 1.7: *Nickel based alloy weld metal NiCr 19 Nb (Alloy 182) (WSt.-Nr. 2.4648), cross section; dendritic microstructure also at the bead boundaries, interdendritic segregation without precipitations; Weld data: manual metal arc welded, V-butt weld thickness 30 mm, included angle 90°, parent material WSt.-Nr. 1.0488 (Bauer 1999 [46])*

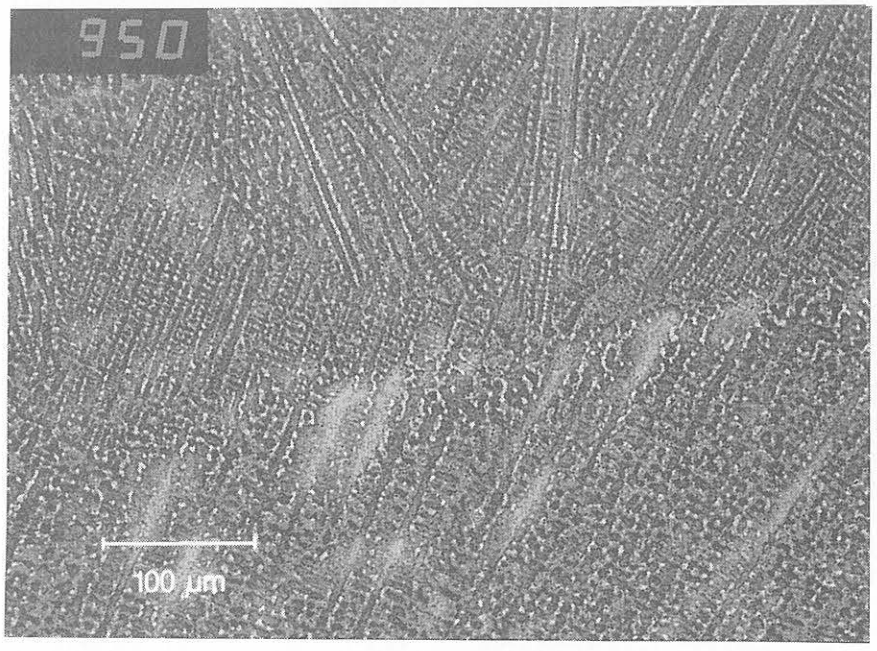

Figure 1.8: *Enlargement of fig. 1.7: Transition from coarse to fine dendritic structure at the bead boundary, obviously due to reheating during welding of the bead above (Bauer 1999 [46])*

No carbides or other types of precipitations or intermetallic phases are observed. Therefore, it has to be expected, that ultrasound scattering in this weld metal type is due to the columnar grains. Dendritic grains grow simply from the fusion line to the weld crown. According to the number of beads per layer main directions of epitaxial grain growth are also generated in this case. The structure is fan-like.

Micro-geometrical features such as distances of dendrites within a grain have been estimated to be maximum 25 μm. Lengths of dendritic grains are observed up to $\approx$ 15 mm.

However, cross-sections of the grains are irregular and their diameter varies in the range from 20 μm to 3 mm.

A nickel based alloy (Nicrofer) having a high carbon content consequently exhibits increased concentration of carbide precipitations in the fully austenitic weld metal matrix especially in the re-heat affected zones of the beads, figs. 1.9 - 1.11. The carbides

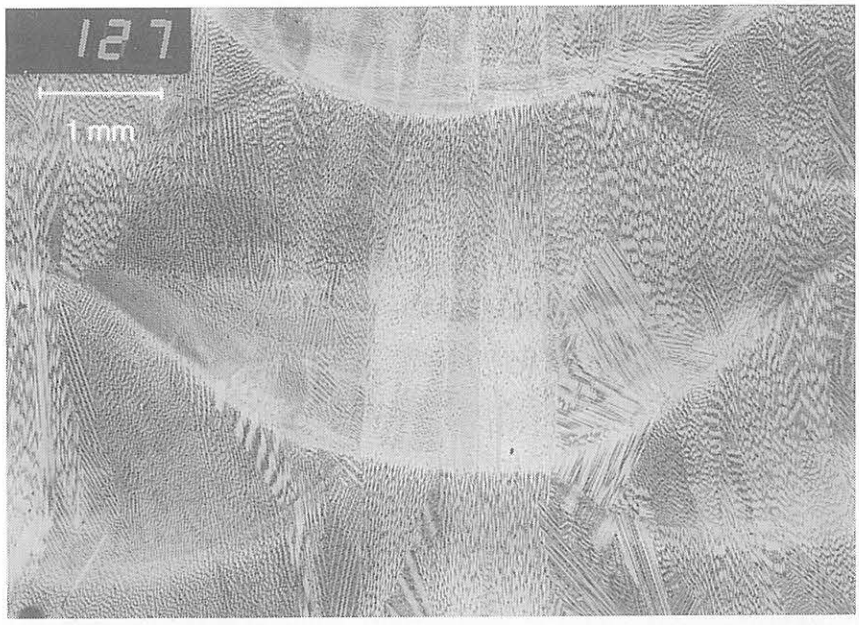

Figure 1.9:
Nickel based alloy weld metal 'Nicrofer' 6025 HT-alloy 602 CA (WSt.-Nr. 2.4633), cross section; Weld data: root and crown tungsten inert gas welded, filler layers submerged arc welded, V-butt weld thickness 20 mm, included angle 60° (Bauer 1999 [46])

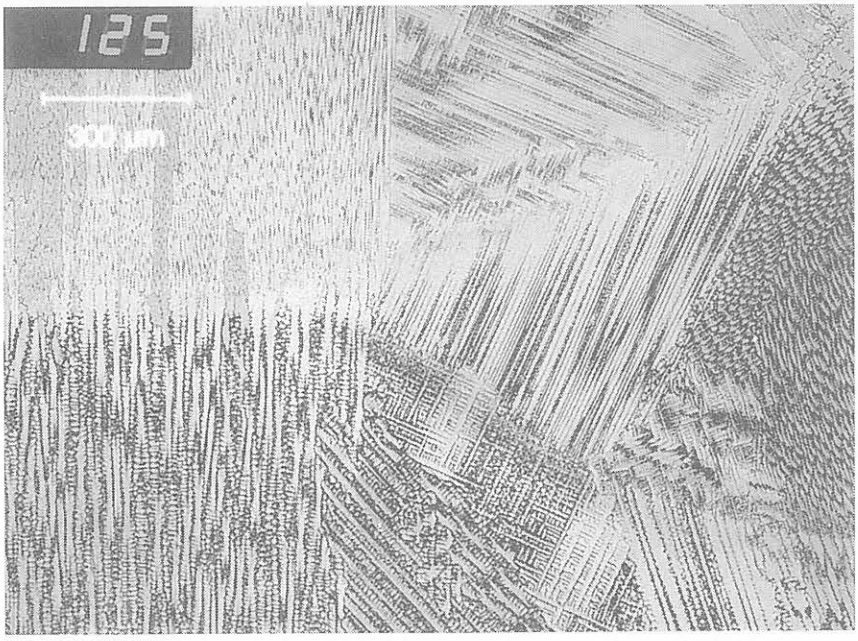

Figure 1.10:
Enlargement of fig. 1.9: carbide precipitations at the bead boundaries and change of growth direction at the bead boundary without change of crystallographic orientation (Bauer 1999 [46])

precipitate along the dendritic structure which can be better observed by this. Furthermore, reheating of beads during welding subsequent layers generate a re-heat affected zone (HAZ) at the bead boundary exhibiting an even more increased content of carbide precipitations.

Austenitic weld metal X 6 CrNi 18 11 with delta ferrite (FN = 0) typically consists of an austenitic matrix with the delta ferrite included. Delta ferrite is distributed irregularly with reduced concentration at weld root and fusion line, figs. 1.12 and 1.13.

Epitaxial grain growth is observed at the fusion line (fig. 1.13) where the grain structure of the base metal determines the columnar grain structure of the weld metal comprising

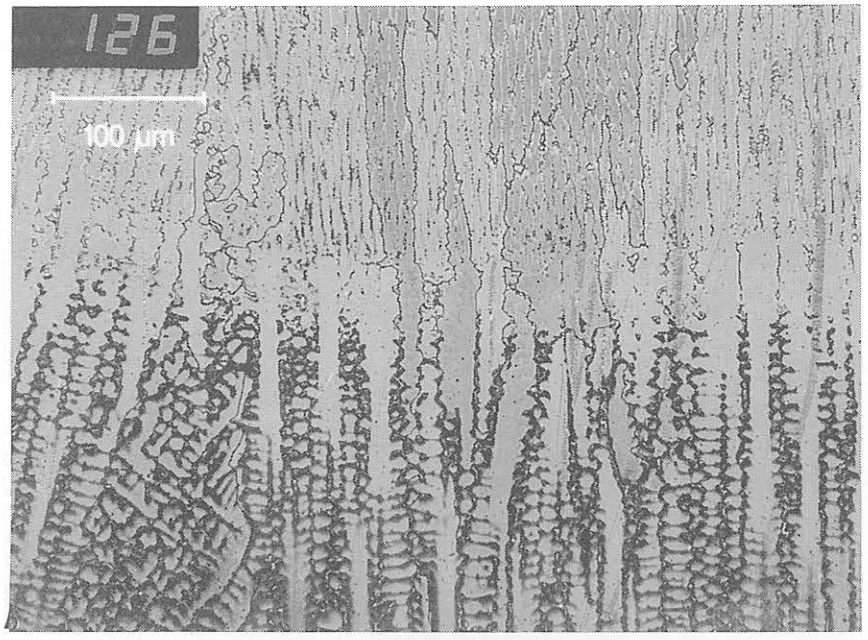

Figure 1.11:
Enlargement of fig. 1.9: bead boundary with carbide precipitations (black) in the lower bead (Bauer 1999 [46])

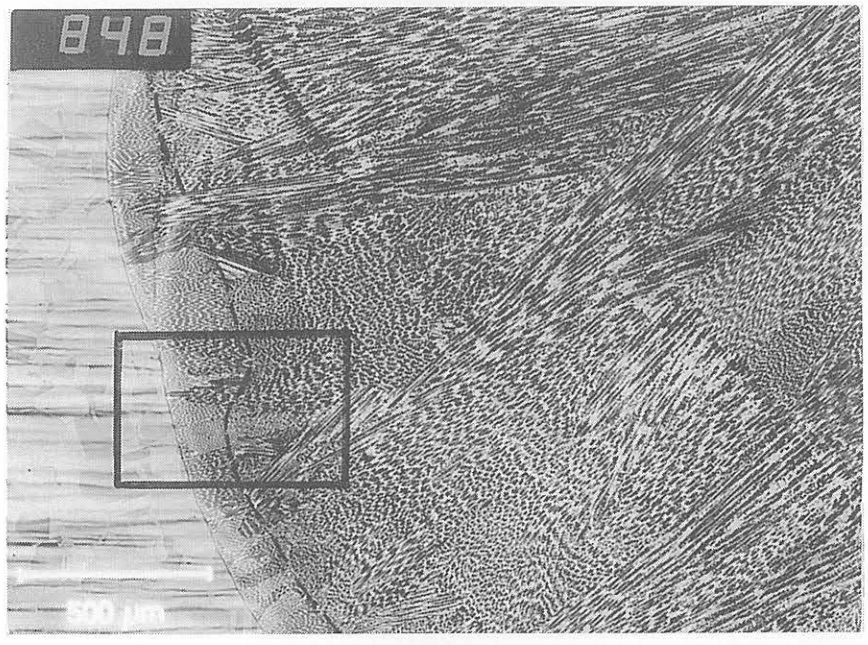

Figure 1.12:
Austenitic weld metal X 6 CrNi 18 11 with delta ferrite (FN = 0), cross section; small area of fully austenitic weld metal near the fusion line, austenitic-ferritic structure in the bulk; Weld data: submerged arc welding, wire diameter 3 mm, V-butt weld thickness 45 mm, angle of bevel 10° (Bauer 1999 [46])

statistically all orientations. However, during solidification only those grains are selected at the expense of all others, whose crystallographic axis has the direction perpendicular to the isotherms of solidification.

Columnar grain growth behaviour (direction and grain sizes) of austenitic weld metal is not uniform throughout the weld, figs. 1.14 and 1.15. Some grains start at the fusion line and grow separately up to the weld face, other grains finish their growth owing to selective grain growth or lead into main branches of grain growth. These main crystal growth directions vary periodically and may differ by 30° within a bead and sometimes even more. Preferred growth directions of columnar grains at boundaries of laterally adjacent beads may differ by 90°. Average values of columnar grain length up to 8 mm and columnar grain width up to 2 mm have been measured.

Grains of adjacent beads are intergrown in a defined manner in most cases. Hereby all three crystallographic directions are continued. However, dendritic configuration may be changed without changing the crystallographic orientation. Depending on the direction of

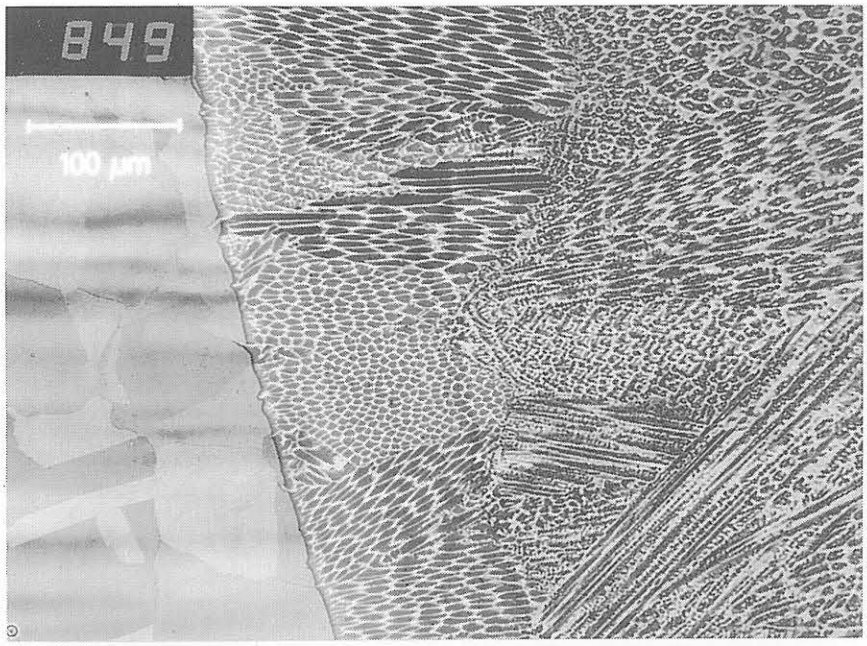

Figure 1.13: *Enlargement of fig. 1.12: primary austenitic solidification at the fusion line, primary ferritic solidification with delta ferrite in the bulk (Bauer 1999 [46])*

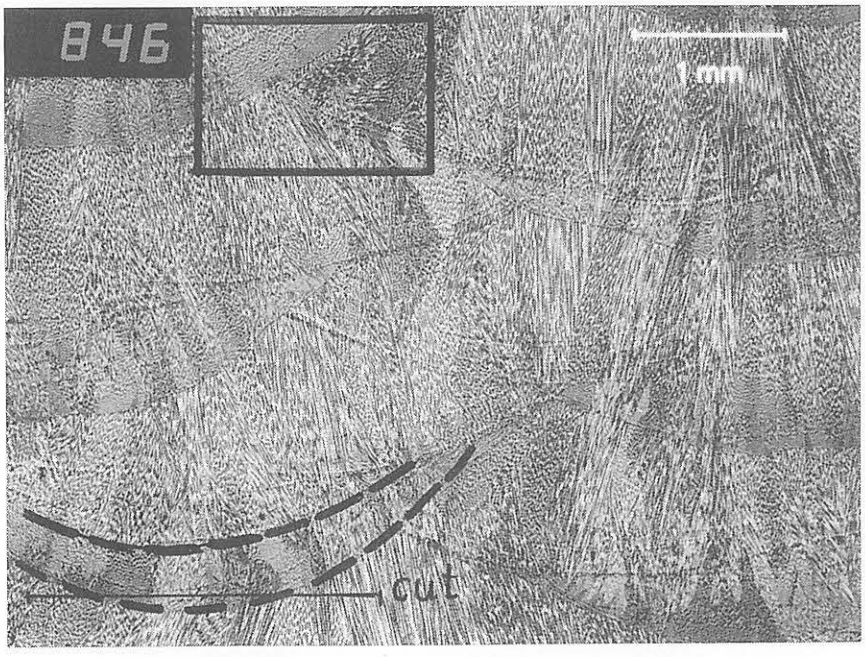

Figure 1.14: *Austenitic weld metal X 6 CrNi 18 11 with delta ferrite (FN = 0), cross section; same weld as in fig. 1.12 (Bauer 1999 [46])*

the maximum temperature gradient, the rate of crystallisation of the subsidiary branches may increase and one of these directions may become the main branch (preferred growth direction). This also can be observed in nickel based weld metal, fig. 1.10, at the bead boundary.

Ultrasound propagation does not get influenced by such changes of dendritic configuration at the bead boundaries, because the crystallographic directions $\vec{a}_1$, $\vec{a}_2$ and $\vec{a}_3$ remain unchanged. So, the bead boundaries are not detected by ultrasound, because they do not constitute an interface and it is only the weld texture, that determines the characteristics of ultrasound propagation.

Obviously due to higher cooling speed at the bottom of a bead small dendrite diameters are observed at the bottom of each bead going over to large dendrite diameters in the upper part of the bead. However, the diameter of the columnar grains is scarcely affected by this, and accordingly the epitaxial grain growth remains unaffected, figs. 1.15 and 1.16.

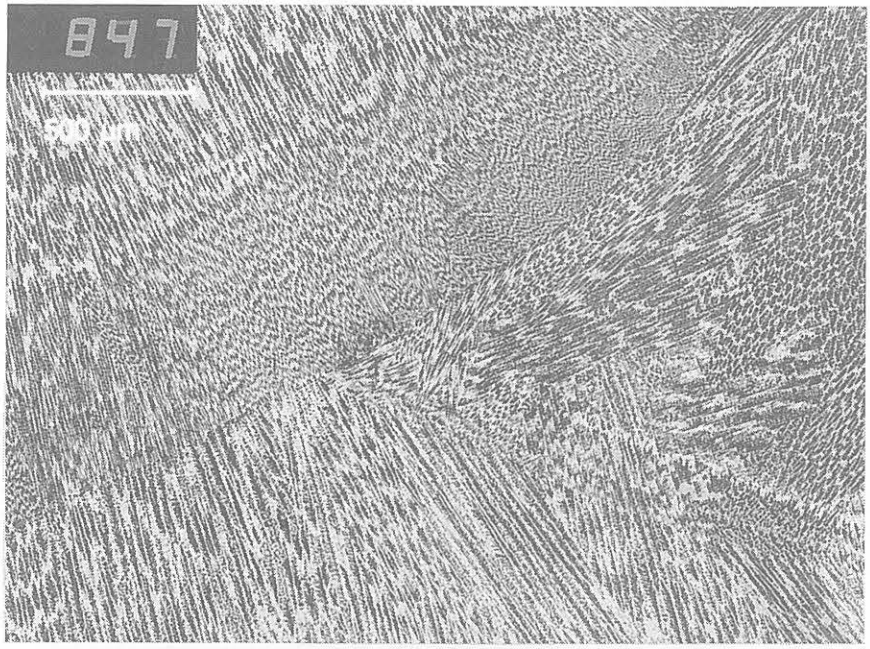

Figure 1.15:
Enlargement of fig. 1.14: growth directions of columnar grains at boundaries of laterally adjacent beads can differ by 90°; small dendrite diameters at the bottom of each bead and large dendrite diameters at the top of the bead (Bauer 1999 [46])

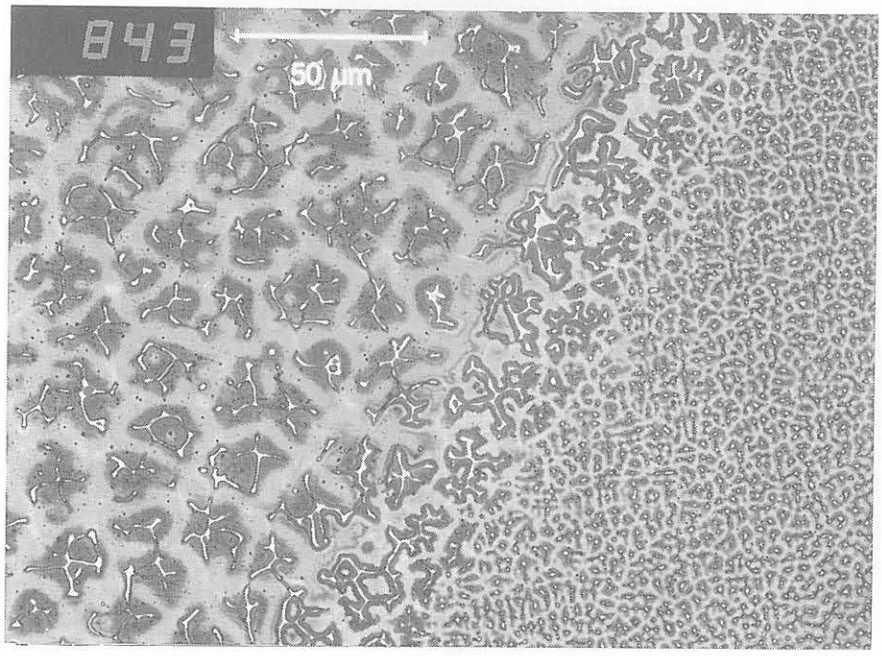

Figure 1.16:
Enlarged section perpendicular to the plane of fig. 1.14: Cross section through the dendrites: large diameter in the upper part of a bead (left hand) and small diameter in the bottom of the subsequent bead above (right hand) (Bauer 1999 [46])

The longitudinal section (fig. 1.17) through the upper part of a bead shows a grain boundary between adjacent columnar grains, which is generated by their different dendrite orientations in the section plane and at an angle to the section plane. As observed in figs. 1.16 and 1.17 the columnar grain is made up of dendrites and residual interdendritic melting areas exhibiting a distinct segregation structure.

Electron-probe microanalysis performed in line-scans ($100\mu m$ scan length, $2\mu m$ step size, $2\mu m$ diameter of the measuring points) at the metallographic specimen of fig. 1.16 revealed the following (Bauer 1999 [46]): Deltaferrit is contained in the core of the dendrites appearing as white in the figures. It is surrounded by Cr-enriched ($\approx +3,5\%$) and Ni-reduced ($\approx -3,5\%$) phase appearing blue, Cr supporting the delta-ferrite formation. The Cr-enriched phase is surrounded by Ni-enriched ($\approx +3,5\%$) phase appearing yellow, Ni supporting the austenite formation.

The residual interdendritic melting areas appearing yellow have reduced Cr-content ($\approx -1\%$) and enlarged ($\approx +1\%$) Ni-content, all figures being related to the average concen-

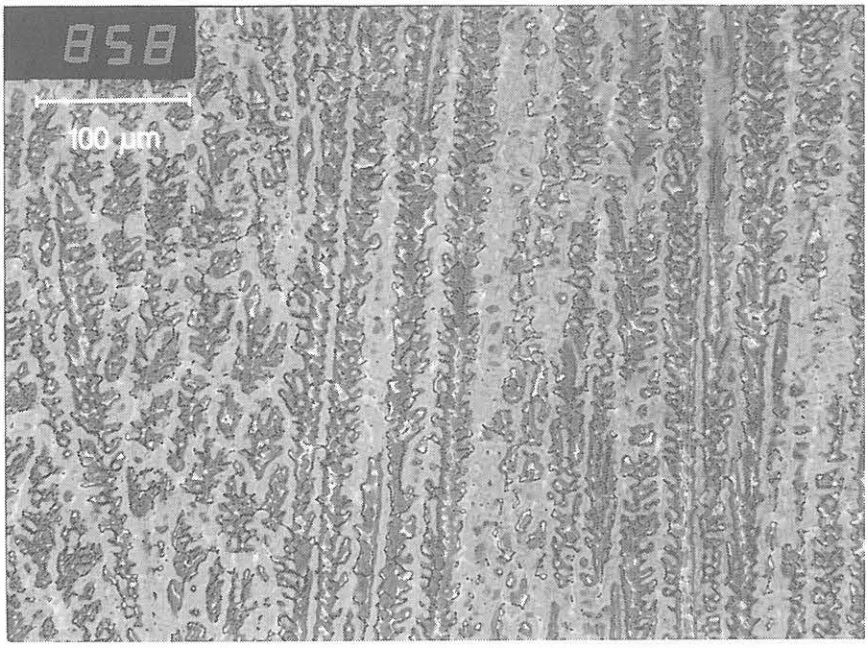

Figure 1.17:
Longitudinal section through the dendrites within two different columnar grains and grain boundary between adjacent columnar grains, which is generated by their different dendrite orientations; weld metal X 6 CrNi 18 11 as in fig. 1.12 (Bauer 1999 [46])

trations of these alloying elements.
The diameter of the dendrites (defined to be the blue area) is varying between $3 - 4\mu m$ at the bead bottom and $30 - 40\mu m$ in the upper part of the bead.

1.1.2 Crystallography

The crystallographic properties of the columnar grains in the weld metal, viz. the crystallographic directions of the dendrites and residual interdendritic melting areas within the grain and also the differences between orientations of adjacent grains have been investigated by X-ray diffraction at a 4-circle-diffractometer (Nolze 1999a [131]) and by backscatter electron diffraction (EBSD) at the scanning electron microscope (Nolze 1999b [132]). Results are reported for X 6 CrNi 18 11 weld metal.

1.1.2.1 X-ray diffraction

To assess the crystal orientation by X-ray diffraction a large grain has been chosen as displayed in fig. 1.17. This large grain consists of few sub-grains, which have slightly different orientations. This can be concluded from fig. 1.18, which shows the spatial intensity distribution of the 220 reflection. Each of the four intensity maxima splits into few separate peaks due to slightly different oriented diffracting planes. For the lattice plane {110} four peaks (one in each intensity maximum) correspond to a single grain. It is evident that the crystal orientation within the grain is uniform but the few adjacent sub-grains recorded by the X-ray beam have slightly different orientations.
The results are summarized as follows:

1. Within a grain bundles of dendrites are observed. Single dendrites of a such bundle are mutually skewed by maximum of 1°. These differences could be caused by segregations, or increased occurrence of crystal imperfections.

2. The bundles of dendrites observed within a grain can be mutually skewed by upto 4°. These differences in growth direction depend on the length of the bundles.

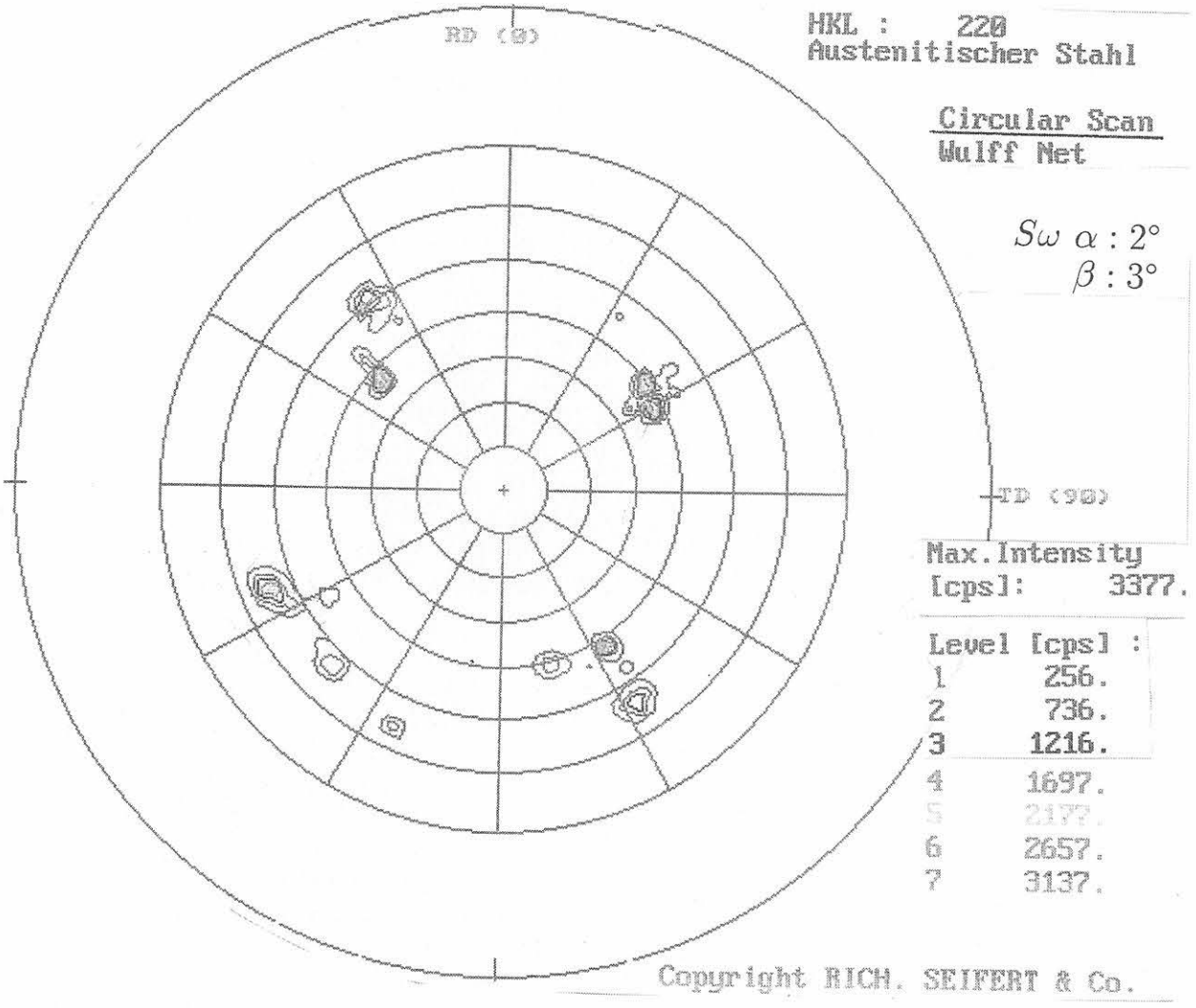

Figure 1.18: *Pole figure from the 220 reflection as a stereographic projection with 4 distinct intensity maxima gained at one measuring point of a grain extending through several beads. The pole figure shows increased intensity for well defined orientations of the sample. Distribution and arrangement of the intensity maxima allow to separate four single grains. Measurement was performed without masking with an aperturing lead foil. Therefore only one orientation can be attributed to the grain under investigation. The arrangement at the {011} lattice planes (using 220 reflections) demonstrate, that several nearly similar oriented single grains are existing (Nolze 1999a [131]).*

3. Within the grain both the dendrites and the residual interdendritic melting areas can be characterised by the same crystallographic basis vectors $\vec{a}_1$, $\vec{a}_2$ and $\vec{a}_3$. Especially the crystallographic orientations of the main elongation and the embranchments of a dendrite are identical. The observed small deviations of the growth direction (approximately 1° between neighbouring dendrites and 4° between neighbouring bundles) are supposed to play insignificant role during ultrasonic scattering, as different densities of dendrite and interdendritic material are supposed be insignificant.

4. Attempts have been made to determine the orientation distribution of the three basis vectors in adjacent grains within a bead. At 15 points the orientations have been measured and the basis vectors were estimated. However, it has not been possible to allocate the intensity maxima to certain orientations exactly. This uncertainty

of allocation increases with increase in number of grains in the measuring area. It must be interpreted therefore that only few grains within the bead are equally oriented. No uniform distribution of crystallographic axes within a bead could be found throughout.

In fact, there seems to be no mechanism which explains the orientation distribution of the crystallographic basis vectors $\vec{a}_1$ and $\vec{a}_2$ (the main dendritic growth direction being defined as $\vec{a}_3$) to become anisotropic. Rather it is more probable that during solidification $\vec{a}_1$ and $\vec{a}_2$ are distributed randomly.

1.1.2.2 Electron diffraction

To assess the crystal orientation at the X 6 CrNi 18 11 specimens in the range of the dendrite dimensions electron diffraction methods are suitable allowing in combination with a scanning electron microscope exact localisation of the measuring point. By using back-scatter electron diffraction (EBSD) crystallographic orientation deviations of approximately 0,5° may be determined.
Following facts have been determined and resp. confirmed:

1. Orientation of dendrites in grains of austenitic weld metal X 6 CrNi 18 11 has been determined. X-ray diffraction measurements have shown that within the grain both the dendrites and the residual interdendritic melting areas can be characterised by the same crystallographic basis vectors. It could be confirmed that the dendrites within a grain only exhibit insignificant variations (up to 4°) of dendrite orientation. Furthermore there have been no indications that the variation of the dendritic axis [001] is larger than that of both orthogonal basis vectors [100] and [010]. These properties can therefore be used to define a columnar grain as being an area of constant dendritic orientation.

2. The observation that at the boundary of adjacent beads a subsidiary branch of the dendrite may become the main branch without changing the crystallographic orientation and vice versa could be confirmed (fusion line epitaxy at bead boundaries). The effect depends on the temperature gradient. However, the crystal growth remains epitaxial.

3. Areas observed at the transition between beads have the same orientation as the bead volume underneath and transfer this orientation to the dendrites growing epitaxially above (fusion line epitaxy at bead boundaries).

1.1.3 Acoustic Microscopy

The same polished sections of the a. m. polycrystalline austenitic weld specimens have been used in metallography and in acoustic microscopy.
Acoustic microscopy reveals the grain structure in so far, as it is acoustically relevant. Since propagation of ultrasonic waves depend on elastic properties, and since the orientation of the crystal elastic tensor differs from one grain to the next, different grains give rise to different contrast. In acoustic microscopy surface waves at frequencies between 100 MHz and 1 GHz are used to investigate propagation on the grains and the effect of grain boundaries. Differences in acoustic impedances between different grains result in different SAW-velocities (transversal surface waves, sub-surface longitudinal wave).
By comparison of the findings of acoustic microscopy, with findings of metallography, X-ray diffraction and scanning electron microscopy ultrasonically relevant inhomogeneities, which give rise or contribute to ultrasonic scattering, can be identified.

Austenitic CrNi 18 11 and CrNi 19 9 steels and the Nickel based weld metal exhibit characteristic elongated grains under the acoustic microscope (discriminated by different grey tints according to different SAW-velocities[1]) which generate the texture, figs. 1.19 to 1.21.

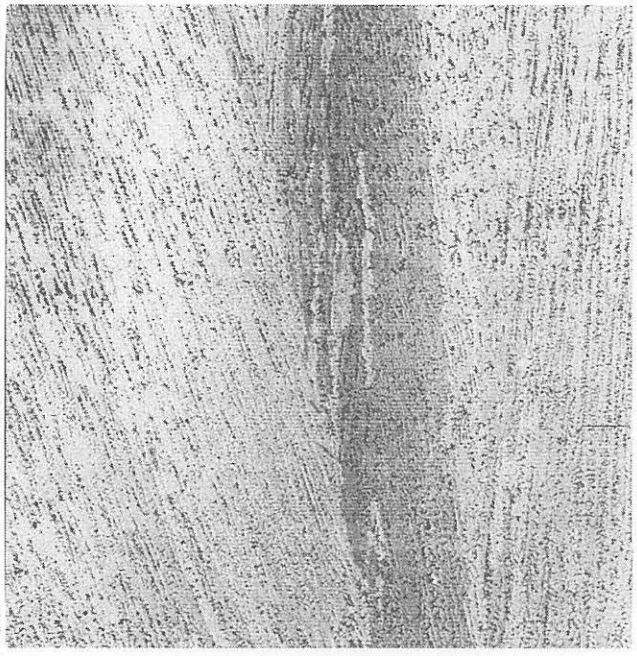

Figure 1.19:
Acoustic micrograph of a X 6 CrNi 18 11 weld metal cross section, 1mm × 1mm, 1 GHz (Haubold 1999 [74]

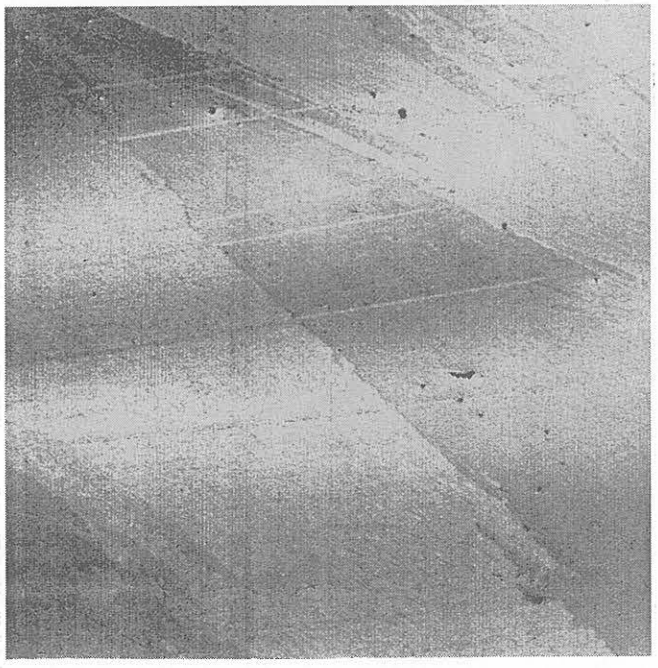

Figure 1.20:
Acoustic micrograph of a X 2 CrNi 19 9 weld metal cross section, 1mm × 1mm, 1 GHz (Haubold 1999 [74])

The details - presumably grain boundary precipitations, foreign phases and micro-inclusions - which can be observed at 1 GHz (figs. 1.19 to 1.21) and which are mainly arranged according to the general texture of the columnar grains fade away with decreasing frequency (100 MHz), (figs. 1.22 to 1.24). It is therefore concluded that the columnar grain

[1]One has to keep in mind, that brightness in an acoustic micrograph is not correlated with absolute values of sound velocity, only with sound velocity differences.

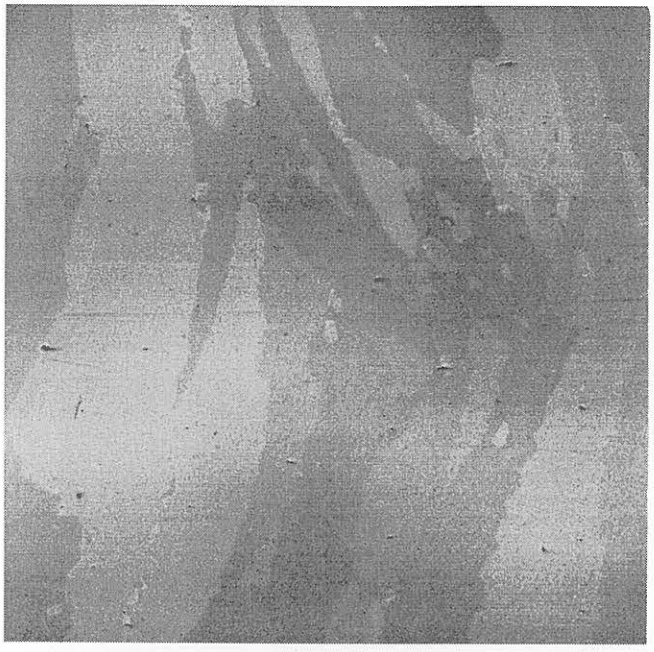

Figure 1.21:
Acoustic micrograph of Nickel based alloy NiCr 19 Nb weld metal, transverse weld section, $1mm \times 1mm$*, 1 GHz (Haubold 1999 [74])*

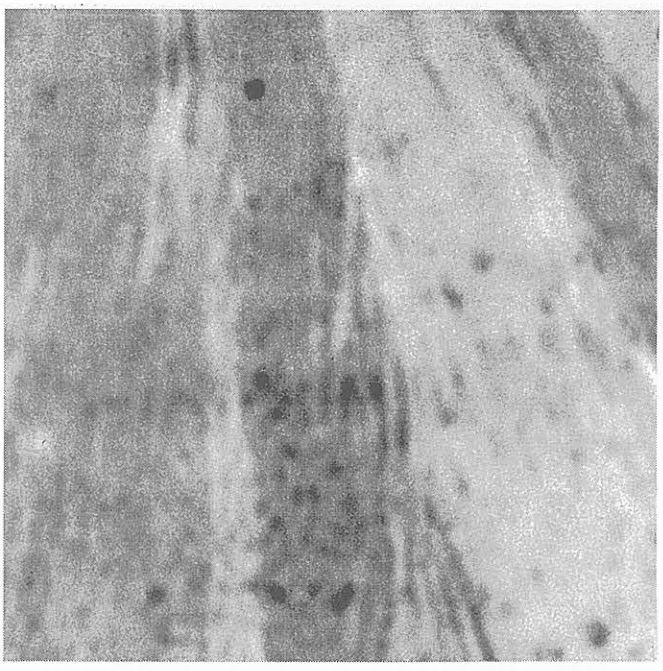

Figure 1.22:
Acoustic micrograph of a X 6 CrNi 18 11 weld metal cross section, $1mm \times 1mm$*, as in fig. 1.19 but* **100 MHz** *(Haubold 1999 [74])*

structure is the predominant feature of austenitic and Nickel-based weld metal, which determines sound propagation also at lower frequencies. There has been no evidence of the effect of other inhomogeneities of the weld structure, e. g. different degrees of segregations within grains and beads, on ultrasound propagation and scattering.

In contrast to this, the Duplex steel by acoustic microscopy does not reveal such a texture, although the grain structure is visible, similar to what is observed in metallography (figs. 1.5 and 1.6), fig. 1.25.

The velocities measured by the V(z)-curves in the weld as well as in the base metal are not very different. This suggests that the acoustic properties of base and weld metal are not very different. Therefore, there is no predominant feature, which determines sound propagation. Consequently, ultrasound attenuation due to macroscopic anisotropy and scattering is assumed to be low, which indeed has been measured at Duplex steel

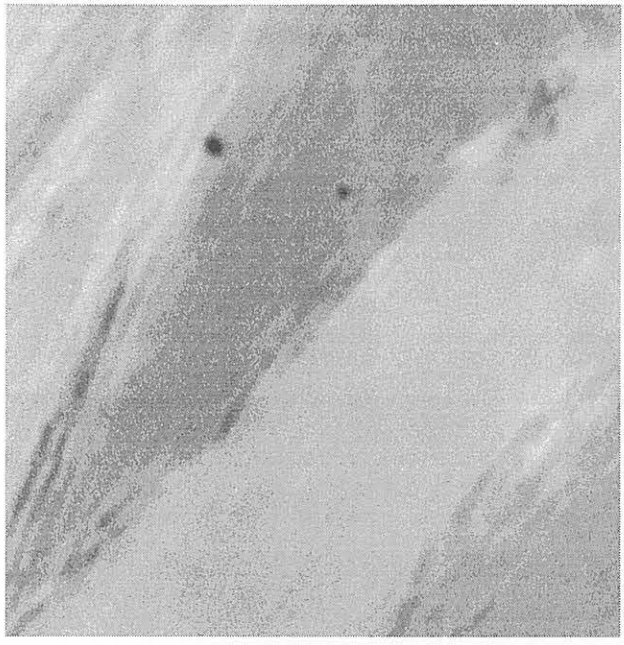

Figure 1.23:
Acoustic micrograph of a X 2 CrNi 19 9 weld metal cross section, with increased Ni-content, $1mm \times 1mm$*, as in fig. 1.20 but* **100 MHz** *(Haubold 1999 [74])*

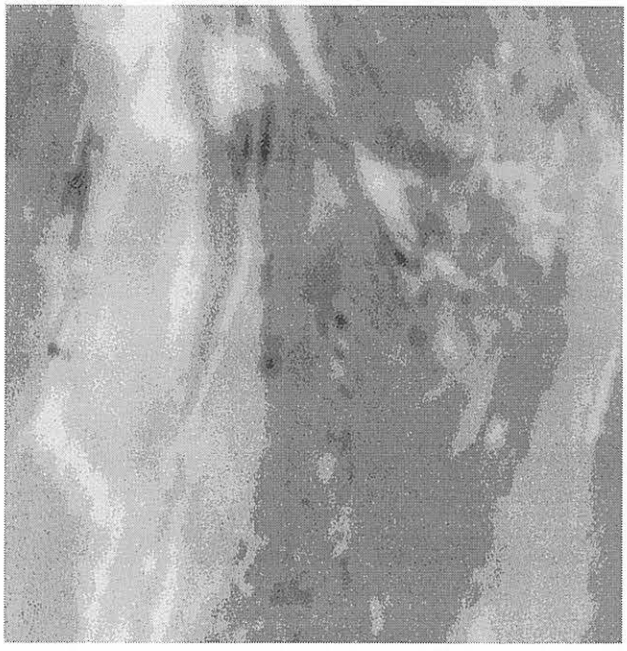

Figure 1.24:
Acoustic micrograph of Nickel based alloy NiCr 19 Nb weld metal, transverse weld section, $1mm \times 1mm$*, as in fig. 1.21 but* **100 MHz** *(Haubold 1999 [74])*

specimens. Furthermore, no directional dependence of ultrasonic attenuation could be measured (Ernst 1999 [60]-[62]).

Figure 1.25:
Acoustic micrograph of the ferritic-austenitic Duplex steel weld metal, transverse section with the fusion line, $1mm \times 1mm$*, 1 GHz, contrast increased by etching (Haubold 1999 [74])*

1.1.4 Conclusions

The results of the investigations on the structure of austenitic weld metal can be condensed as follows:

1. The columnar grain structure is the predominant feature of austenitic and Nickel-based weld metal determining both the macroscopic texture and the microstructure. Columnar grain growth epitaxially extends from weld root and weld fusion face up to the weld crown. Lengths of dendritic grains are observed up to $\approx$ 15 mm. Cross-sections of the grains are irregular and their diameter varies in the range from 20 μm to 3 mm.

2. Within the columnar grain both the dendrites and the residual interdendritic melting areas can be characterised by the same crystallographic basis vectors $\vec{a}_1$, $\vec{a}_2$ and $\vec{a}_3$. Whereas the main dendritic growth direction $\vec{a}_3$ of all columnar grains is anisotropic this is not the case for the other two orthogonal basis vectors of the columnar grains. Rather, during solidification the orientations of the basis vectors $\vec{a}_1$ and $\vec{a}_2$ of the columnar grains are distributed randomly.

3. All weld metal phases, foreign phases included, are aligned according to the general texture of the columnar grains. Therefore they seem to enhance the effect of texture on ultrasound propagation. However, their effect on ultrasound propagation evanesces at lower frequencies.

4. The weld metal of the ferritic-austenitic Duplex steel does not exhibit a predominant feature, which determines sound propagation. Accordingly ultrasound attenuation due to macroscopic anisotropy and scattering is observed to be low.

In order to model ultrasound propagation and scattering in austenitic weld metal also the weld metal microstructure needs to be modelled taking into account the following conclusions from the structural investigations:

- The weld metal is polycrystalline. The columnar grains consist of bundles of dendrites and residual interdendritic melting areas with uniform crystallographic orientation. Lengths of columnar grains are observed up to $\approx$ 15 mm. Cross-sections of the grains are irregular and their diameter varies in the range from 20 μm to 3 mm.

- The grain boundaries are generated by the change of the crystallographic orientations of adjacent columnar grains. Other metallurgical structural elements, e. g. segregations, poly-phases (e. g. delta ferrite), scarcely contribute to the propagational and scattering characteristics of ultrasound.

- Inspite of the fact, that the individual columnar grains have cubic symmetry, due to the random orientation distribution of the basis vectors $\vec{a}_1$ and $\vec{a}_2$ of the columnar grains the weld metal as a whole exhibits cylinder-symmetrical texture and therefore can be treated as a monocrystalline medium with transverse isotropic symmetry. This class of symmetry corresponds to four independent elastic constants. They can be obtained as follows:

$$C^t_{mnop} = \int_0^{2\pi} a_{mi}\, a_{nj}\, a_{ok}\, a_{pl}\, C^c_{ijkl} \tag{1.1}$$

  where the superscript t denotes transverse isotropy and c denotes cubic symmetry. $\mathbf{a}(\phi)$ is a direction cosine matrix and ϕ is the angle subtended between the new and old x axes after rotating the matrix around the z axis.

where the superscript t denotes transverse isotropy and c denotes cubic symmetry. $\mathbf{a}(\phi)$ is a direction cosine matrix and ϕ is the angle subtended between the new and old x axes after rotating the matrix around the z axis.

For determining physical properties such as phase and group velocities, and particle displacement polarization, the assumption of transverse isotropy is sufficient and agrees fairly well with the experimental values.

However, as a matter of fact, attenuation by grain boundary scattering is not comprised. This needs the extension of the model by the introduction of a spatial autocorrelation function to describe the geometry of the grains (Stanke 1984 [178]) (s. chapter 4).

- For ray tracing purposes the texture configuration throughout individual welds has to be fitted by empirical mathematical relations.

1.2 Modelling of ultrasound propagation in austenitic weld metal

Modelling elastic wave propagation in anisotropic materials different approaches are in use:

- numerical,
- approximate,
- analytical.

1.2.1 Numerical approaches

Finite element and elastodynamic finite integration techniques are the most frequently used methods to solve elastodynamic propagation problems.

The finite element method (FEM) is mainly applied to a wide variety of geometrical conditions in isotropic materials (Minachi a.o. 1993 [106]). Hereby the physical problem is not solved directly as differential equation but indirectly by variation of a perturbation integral using Newton's and Hooke's laws and the energy conservation principle. It involves breaking the complex geometry of the continuum into a mesh of "finite elements". Fineness of the mesh plays a decisive role on the precision of the results, especially in regions of large stress/strain gradients. Recently a variation of this technique, the so called P-version FEM, where the polynomial degree of the elements can be varied over a wide range, has been developed. The accuracy of the results are controlled not only by the mesh size but also by the degree of the polynomial. This technique uses fewer elements compared to the traditional FEM (Issa et al. 1992 [92]).

The elastodynamic finite integration technique (EFIT) addresses the problem of elastic wave propagation by discretizing the integral equations of linear elastodynamics in space and time (Fellinger 1991 & 95 [63, 64], Marklein 1995 & 97 [104, 105]). The propagation of an arbitrary elastic perturbation is traced by applying alternately the elastodynamic field equations to successive space and time steps. This method has been applied to the study of wave propagation in dissipative and homogeneous anisotropic media.

However, the following inherent limitations of these methods can not be overlooked:

- The methods are computationally intensive requiring often multiprocessor/parallel computers. In many applications limitation to the two dimensional case due to the requirement of large computer CPU time is necessary. Analysis of the fully three dimensional anisotropic solid presently is not possible.
- Errors may be introduced, which are associated with the artificial model boundaries necessary for solving a spatially infinite problem on a finite grid.
- Numerical dispersion may occur.

1.2.2 Approximate approaches

Elastodynamic propagation problems are solved on the basis of the Huygens' principle or by series development solution of plane waves owing an analytical solution.
The generalized point source synthesis (Spies 1992-96 [171]-[176]) using the concept of Gaussian wave packets and the synthesis of elastic wave fields by plane waves is based on the Huygens' principle. The method being partly analytical and partly numerical allows calculation of sound propagation in homogeneous anisotropic media much faster than would be possible with the elastodynamic ansatz [174].
The pulse-integration-method (PIM) also uses the Huygens principle taking into account the point directional effect of the Huygens point source (Wüstenberg 1974 [183]). The method applies to isotropic as well as to anisotropic media (Boehm 1992-94 [49]-[51], Hesselmann 1993 & 94 [77, 78]). Special algorithms have been developed for sound propagation in specimens with curved surfaces which have to be introduced into the modelling (Schumm 1997 [168]).
Forward ray tracing (Furukawa 1995 [67, 68]) by modeling the soundfield as a bundle of rays principally also is synthesizing the beam as a series development solution of plane waves.

1.2.3 Analytical approaches

To achieve an analytical solution of the elastodynamic wave equation the ansatz of a time harmonic plane wave must be chosen. The approach has been discussed thoroughly in the textbooks e. g. Federov 1968 [15], Musgrave 1970 [23], Payton 1983 [27], Rosenbaum 1988 [29], Auld 1990 [3], Kline 1992 [18], Neumann 1995 [25]. Experimental evidence proves that this assumption describes the following features of ultrasound propagation in anisotropic media correctly (e. g. Neumann et al. 1995 & 99 [25, 127], Gripp 1999 [70]):

- the wave modes propagating
  - their (phase- and group-) velocities and
  - polarisations
- the beam skewing

and, in case of boundaries, direction (Snells' law) and amplitude of

- reflected,
- refracted and
- mode converted

wave modes. Except for diffraction and aperture effects it turns out that the other approaches do not yield any progress beyond these results.
Some details on the status of research and development which will be starting points of the present work are reported as follows:

1.2.3.1 Reflection and refraction

Ultrasonic inspection purposes require to study the wave interaction at various types of interfaces, viz. at the

- perfect interface, e. g. with rigid contact at the smooth solid-solid interface,
- imperfect interface, e. g. the interface being rough, possibly containing a certain defect distribution,

1.2.3.1.1 Perfect interfaces: Reflection and transmission phenomena discussed in the a. m. textbooks mostly are restricted to the isotropic case.
The reflection and transmission phenomena at interfaces between two anisotropic materials are more complicated due to the quasi nature of waves and beam skewing, which means that - unlike in isotropic materials - the energy flow direction generally does not coincide with the direction of wave propagation. Further, all the three wave modes couple at the interface in the case of anisotropic materials. This topics have been treated by Rokhlin et al. 1986-91 [155]-[158], Munikoti et al. 1991-98 [107]-[117], Neumann et al. 1995-99 [25], [123]-[127].
The problem of ultrasound propagation in multilayered systems, which involves multiple scattering of waves at interfaces, is addressed by Brekhovskikh 1980-92, [7, 8, 9], Ewing 1957 [14], Nayfeh 1995 [24].

1.2.3.1.2 Imperfect interfaces: In practice not all interfaces are smooth and the contact is not always 100%, though this assumption is good enough when the wave length of the ultrasound is much greater compared to the RMS value of the surface roughness or the dimension of the defect. Nevertheless, the effects of surface roughness and defect distribution on the propagational characteristics of the sound wave influence reflection and transmission at interfaces, as at the austenitic weld fusion face, at the cladding interface, and at columnar grain boundaries, as well as between ultrasonic probe and cladding surface with a liquid coupling layer inbetween.
The theory of wave scattering from rough surfaces is treated thoroughly by Ogilvy 1991 [26].
For the isotropic case various aspects of an imperfect interface on ultrasound propagation are discussed in a special issue of the Journal of Nondestructive Evaluation [28], by Huang et al. 1992&95 [88, 89] and by Rokhlin et al. 1980-93 [154] - [164].
In the spring model based on the quasi static approximation suggested by Baik et al. 1984 [45] the interface is assumed to consist of springs, which are used to join the two semi spaces. When a traction force is applied to this system, the total displacement is defined as the sum of the displacement in the absence of a discontinuity (imperfection) and an extra local deformation in the vicinity of the interface. At sufficiently long wavelengths, the interface is assumed to be represented by the combination of distributed spring and mass to correctly reproduce the static deformation. The interfacial stiffness can be evaluated from the solutions for the extra local displacement which are reported in the literature for a variety of interfacial conditions (Tada 1973 [33]). The boundary conditions for a perfect interface are continuity of particle displacement velocity and traction force across

the interface. These conditions are modified by incorporating the spring model. The model is valid as long as the wavelength is much larger than the interfacial imperfection.

The interface with distribution of pores and inclusions has been considered by Margetan 1988 [101]. The effect of frequency on reflection and transmission coefficients is discussed and the results are compared with experimental values.

However, for other types of defects, which are of interest to NDE, suitable static deformation solutions are not available. An example for this is the case of transverse wave reflection from an interface containing a distribution of oblate spheroidal inclusions.

Ultrasonic reflection from imperfect interfaces is analyzed in the time domain in the presence of defects by Rose et al. 1992 [165]. The case of an anisotropic layer sandwiched between two anisotropic solids is analyzed by Huang et al. 1992 [88]. First and second order asymptotic boundary conditions are introduced to model this case.

1.2.3.2 The bounded beam

The ultrasound being emitted by a finite sized transducer a bounded beam is generated. The concept of the bounded beam can be easily understood as a summation of an infinite number of plane waves. This concept allows understanding of the Schoch effect (1952 [166]), which means that at an interface between water and solid the ultrasound beam gets displaced at incidence angles around the Rayleigh angle.

Expressions for the displacement of the ultrasound beam for the water/metal interface are found in [166]. The unified theory developed by Bertoni et al. 1973 [47] and Ngoc et al. 1980-82 [128]-[130] removed the limitations in the Schoch's theory so that it is valid for large beam widths in isotropic media.

The case of nonspecular reflection of beams from liquid-(isotropic) solid interfaces are analysed by Zeroug et al. 1992 [185]. Equations are developed not only for the case of the plane surface but also for cylindrically curved layered geometries, and simultaneous excitation of multiple leaky waves. The ultrasound beam is assumed to be quasi-Gaussian. By the use of the complex source point (CSP) method the reflection problems are solved rigorously by wavenumber spectral decomposition.

1.2.3.3 Ray tracing

Generally the texture of austenitic welds is not unidirectional. The ultrasound in such a structure does not normally travel in straight lines but due to local changes in elastic properties, the energy flow direction of the beam gets skewed. Therefore the total map of the beam path is curved. The path depends on the local anisotropy. The process of iteratively "tracing" the energy flow direction at very small distances of sound travel ϵ and mapping the path is known as ray tracing. This subject is not new in geophysical application. A thorough monograph on this subject is presented by Červený 1977 [12].

This method has also been applied to wave propagation in austenitic welds using both two-dimensionally (i. e. restricted to the incidence plane) geometric ray acoustics (Silk 1981 [170], Ogilvy 1985-92 [137]-[147], Stansfield 1987 [179], Champigny 1987 [55], Harker 1990-91 [72, 73], Nouailhas 1990-91 [134]-[136], Munikoti et al. 1994-95 [114, 25], Spies 1995-96 [173, 176]) and wave-mechanical acoustics (Klaholz et al. 1995 [94, 95], Marklein 1994-97 [103, 104, 105]).

By evaluating weld specimen micrographs it is possible to empirically simulate the microstructure by an empirical mathematical expression. Such an empirical relation to describe the local grain orientation as a function of weld specimen parameters is developed by Ogilvy 1985-92 [137]-[147]. The whole weld is approximated to be a polycrystalline medium with transverse isotropic symmetry.

Indeed, there are hints that the results of ray tracing by geometric ray acoustics using this microstructure model agree fairly well (qualitatively) with experimental results (see chapter 3) and results of ray tracing by wave-mechanical acoustics (Marklein 1997 [105]) inspite of the following restricting presumptions that have been made:

- The ultrasound in practice is a finite sized beam, whereas in ray tracing, a single ray is assumed.
- Weld parameters such as weld pool temperature and local thermal gradients which influences the grain growth direction, are not considered.
- Grain geometry is not incorporated in the model.
- Effect of frequency is not incorporated in the model.
- Multiple reflections at grain boundaries are neglected.

Therefore, the attenuation of the wave due to the total of scattering processes at grain boundaries cannot be accounted for.

1.2.3.4 Pulse propagation

The ultrasound beam has not only a finite size, but is also a time dependent pulse. Norris (1987 [133]) and Spies (1992 [171]) have developed the theory for pulse propagation in anisotropic materials. They define the pulse as a harmonically modulated Gaussian envelope. The spreading, pulse form changes, the reflection and transmission at planar and curved interfaces are discussed.

1.2.3.5 Scattering of ultrasound in polycrystalline materials

A stochastic model for ultrasound wave propagation has been published 50 years ago by Lifshits and Parkhomovski [99]. Based on this work a unified stochastic theory has been proposed by Stanke and Kino [177, 178]. They incorporated the second order Keller's approximation (1964 [93]), which has been the development of equations for wave propagation assuming the process to be stochastic. This unified theory is valid for all ranges of frequency viz., Rayleigh, stochastic and geometric regions. However, the theory was applied to evaluate the attenuation coefficients in the case of polycrystalline materials without any texture or other macroscopic anisotropy.

This theory was extended to textured materials. Most extensive work on this subject can be found in the publications of Ahmed and Thompson 1984-95 [40]-[43], and Hirsekorn 1982-88 [79]-[85]. However, the texture direction was assumed to be in the plane of incidence, whereas it is known that in the direction of welding a texture inclination of up to 20° is occurring.

Turner (1999 [181]) recently has discussed the ultrasonic scattering in heterogeneous anisotropic media (the heterogeneity being caused by and being proportional to the anisotropy of the grains) including Green's function for anisotropic media. His theory, however, is limited to the Rayleigh and stochastic regions and does not cover the geometric region of ultrasonic scattering.

1.3 The motivation for the present work

There is a strong incentive to perform reliable ultrasonic inspection of austenitic and nickel-based alloy welds both during manufacture and in-service similarly as it is usually

done for ferritic steel welds to detect and classify defects which could cause weld failure, e. g. [37]. This means that quality control and inservice inspection of welded austenitic stainless steel components and plant with ultrasound need

1. testing and defect assessment techniques adapted to the anisotropy problem,
2. codes and regulations specifying
   - the ultrasonic inspection procedure,
   - the rules for evaluating the ultrasonic indications, and
   - the defect acceptance/rejection criteria.

During more than two decades ultrasonic testing techniques for inspection of anisotropic materials have been developed based on experience and heuristic arguments enabling detection of defects with similar amount of reliability as during inspection of isotropic materials (e. g. Neumann 1995 [25]).
However, defect assessment by ultrasound has two purposes

- monitoring weld quality by detection of defects
- ensuring the absence of critical defects.

Since austenitic weld metal is anisotropic and polycrystalline, critical defects up to now had been difficult to discriminate by ultrasound. This is because the characteristics of the ultrasonic echoes not only depend on the properties of the reflecting flaw but also on the weld metal's elastic properties. The anisotropic elastic properties give rise to the following problems, which interfere with straightforward defect assessment:

- In anisotropic media the propagational characteristic of the beam is direction dependent, since the energy flow direction (group velocity) and the wave vector direction (phase velocity) generally do not coincide. Besides beam skewing this leads to beam spreading, which is quantified by the beam spreading factor defined as the second derivative of the circular frequency with respect to the wave vector, i. e. the ratio between a small change in group velocity for a corresponding change in phase velocity.

- When ultrasound is incident at an interface between two anisotropic media (adjacent columnar grains), generally three reflected and three transmitted waves couple, giving rise to reflected and transmitted ultrasonic signals which are measured as ultrasonic scattering amplitudes. In addition, excitation of inhomogeneous waves may occur.

  In contrast to that in the case of isotropic media, where the transverse waves are degenerated, from the usual waves used for non-destructive testing only the longitudinal and the vertically polarized transverse wave couple at interfaces, whereas the horizontally polarized transverse wave decouples. Consequently, less complication of coupling and mode conversion is associated with reflection and refraction in the isotropic medium.

The practical test situation described in the following example demonstrates a typical pitfall during ultrasound inspection of anisotropic austenitic steel welds [38]: As presented in fig. 1.26, the austenitic weld is interrogated from the parent metal side with a 45° SEL transducer[2]. The reflected signal can give misleading information, viz. that the ultrasound

[2]Longitudinal wave transmitter-receiver transducer

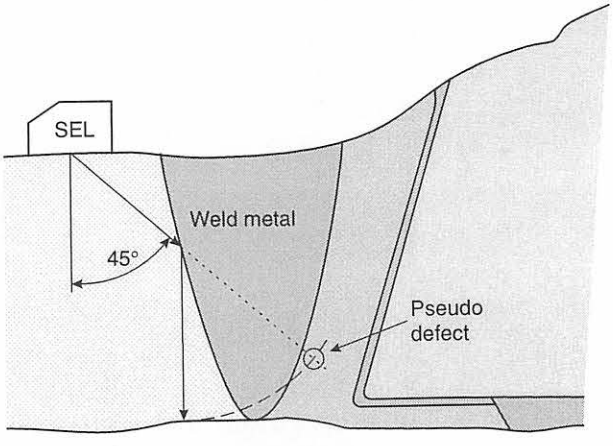

Figure 1.26: *Typical example of the pseudo defect signal during austenitic stainless steel weld inspection; SEL: longitudinal wave transmitter-receiver transducer; after [38]*

is reflected from a *pseudo (non-existing) defect* situated at point B, whereas in reality the ultrasound is totally reflected at the weld fusion face and reflected back from the bottom face of the parent metal. This is due to the fact that the weld fusion face is the interface between isotropic base (parent) metal and anisotropic weld metal and the ultrasound incident at such an interface as a matter of fact undergoes reflection and transmission.

The ultrasound transmitted into the anisotropic weld metal suffers beam splitting, beam skewing etc.. As described in section 1.1.1 grain orientations are not uniform throughout the weld. Therefore adjacent grains have different orientations and hence the wave in the weld metal at the interface between every pair of grains undergoes reflection and transmission, beam skewing etc., which would affect the sound path. The sound path turns out to be curved. The practical consequence of this is that the ultrasound beam might not intercept the defect which would lead to wrong interpretation of the result.

The problems to be addressed concerning the study of reflection and transmission phenomena at interfaces as a matter of fact are not restricted to the grain boundary scattering but also concern:

1. the efficiency with which ultrasound can be injected into (and received from) the anisotropic medium,

2. the efficiency with which ultrasound is reflected by the different types of defects within the anisotropic medium,

To develop reliable testing and defect assessment techniques for quality control and inservice inspection of welded austenitic stainless steel components and plant the knowledge of the energy flow directions in the poly-crystalline, anisotropic medium, of the energy reflection and refraction coefficients at interfaces, and of the energy scattering coefficients is needed.

Therefore the aim of the present work has been two fold:

- to understand the wave propagational characteristics in anisotropic materials

- to build the knowledge base, which would help in developing reliable methods for ultrasonic inspection of austenitic steel welds and in refining/improvising the present NDT codes and regulations.

Normally in NDT of structures, ultrasound examination is supplemented with several other NDT techniques to enable a more reliable report of the quality and reliability of the material. If the results of these different techniques contradict each other due to

the typical inspection problems discussed above, the decision making regarding quality, reliabiality and serviceability of the tested component would be very difficult.
Therefore in the inspection of anisotropic materials, lack of a-priori knowledge about the wave propagational behaviour in anisotropic materials might lead to unrealiable results and in inspection of structures used in nuclear, aero-space industries and other critical structures it might even lead to loss of human lives.

1.4 Objectives of the present work

In this work the characteristics of ultrasound propagation in the anisotropic medium shall be analyzed in order to develop ultrasonic defect assessment techniques and guidelines which are based on the physical insight into the sound propagation and scattering mechanisms.

1. As considered and justified in section 1.2.3 for wave propagation the plane wave ansatz is chosen. The eigenvalue problem which is represented by the Christoffel equation will be solved for the infinite space with transverse isotropic symmetry yielding phase and group velocities, and polarizations of the three wave modes: quasi-longitudinal, quasi-transversal, and pure transversal.

2. Reflection and transmission for the three wave modes at an interface between two general anisotropic media will be analyzed. The important features such as mode conversion of waves, and excitation of a secondary branch of the quasi transverse wave will be investigated.

   2.1 In the first step, a perfect (defect free) boundary will be considered. The boundary conditions in this case are that particle displacement velocity and traction forces are continuous.

   2.2 In the second step, the boundary conditions will be modified to incorporate the quasi static model, which allows to study imperfections contained in the interface. The imperfection considered will be the circular shaped crack.

   2.3 In the third step, the case of a viscous layer between an isotropic material and anisotropic weld and the effect of viscosity on reflection and transmission will be dealt with. This is important from the point of view of ultrasonic examination of welds, where the transducer is placed on the specimen with a couplant between the transducer and the anisotropic weld. In the literature this case has been analysed for isotropic materials but not for anisotropic materials.

   2.4 Lastly, the bounded beam reflection at an interface between water and anisotropic weld metal will be investigated. Though the plane wave assumption is sufficient for many applications, it is appropriate to consider the case of bounded beam incidence at an interface, since ultrasound is generated from a finite sized transducer and the plane wave does not exist in reality. The bounded beam is achieved simply by integrating an infinite number of plane waves over the transducer dimension. The so called Schoch displacement (1952 [166]) is observed when the ultrasound is incident around the Rayleigh angle at an interface between fluid and solid.

   Again, in the literature this case has been studied for isotropic material, where reflectance and transmission functions are quite simple compared to anisotropic material, where the texture direction plays an important role in the interaction of waves at an interface.

The reflection and transmission energy coefficients will be calculated as a function of incidence angle, frequency and texture direction in all cases.

3. Due to epitaxial grain growth extending from weld root and weld fusion face up to the weld crown austenitic welds show texture. The texture orientation determines the energy flow direction. The wave can be assumed to have crossed an 'interface', when the ultrasound travels from a region of one grain orientation to the other with a different grain orientation. Due to the local refraction at the assumed interface, the energy flow direction changes. Proceeding in the direction of energy flow in small steps finally the trace of the ultrasonic ray is achieved simply by mapping all the local changes of beam directions due to the local anisotropy. This iterative ray tracing procedure serves to analyze the sound path in anisotropic media.

   In isotropic materials, the ultrasound would travel in straight lines because the energy flow direction coincides with the wave vector direction.

   The ray tracing will be presented three-dimensionally for the three wave modes, viz. quasi longitudinal, quasi transverse and pure transverse waves as a function of:

   - incidence angle
   - transducer position
   - texture

   The theoretical predictions will be compared with two-dimensional calculations (Marklein 1997 [105]).

4. In the above models considered, the whole weld specimen has been assumed to be a monocrystalline medium with transverse isotropic symmetry. Attenuation due to multiple reflections at grain boundaries has been neglected. The stochastic model based on Keller's approximation which incorporates attenuation due to multiple reflections at grain boundaries will be introduced in the form of the unified theory proposed by Stanke and Kino (1984 [177, 178]). They, however, applied the theory to textureless materials. This was extended by Ahmed et al. (1984 [40]), and Hirsekorn (1986 [84]) to materials with texture but the texture direction was confined to the meridian plane.

   The theory now will be further extended to the more general case in welds, where the columnar grains are not only tilted in the plane of sound propagation but also out of it ('lay-back'), which is observed up to 20° in the welding direction. Moreover, the grain shape can be equiaxial or elongated, depending on the metallurgical conditions.

   The attenuation coefficients, phase velocities, and particle displacement polarizations will be calculated as a function of

   - incidence angle
   - lay-back angle
   - wave number

   The theoretical predictions will be compared with experimental studies (Neumann et al. 1999 [127]).

Chapter 2

Reflection and transmission at an interface between general anisotropic materials

2.1 Outline of the inspection problem

Fig. 2.1 shows a typical example of the ultrasound propagation during inspection of an austenitic stainless steel weld .

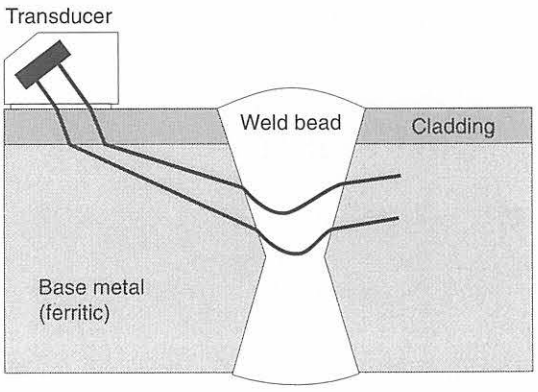

Figure 2.1: *Typical example of the ultrasound propagation during inspection of an austenitic stainless steel weld*

An ultrasonic pulse is emitted from a finite sized piezo-electric transducer. The finite size of the transducer moreover would result in a bounded ultrasonic beam. The cladding of the specimen under test being anisotropic, the ultrasound travels from the isotropic transducer wedge material (perspex) to the anisotropic austenitic cladding which are coupled by a thin layer of couplant material. Therefore the following two interfaces have to be considered:

- perspex - couplant material,
- couplant - cladding.

The ultrasound energy flow direction in the cladding generally does not coincide with the wave vector direction due to its anisotropy.
The next interface is

- cladding - isotropic ferritic base material.

In isotropic material the directions of energy flow and wave vector coincide.
Finally, the beam propagates through the interface

- isotropic base material - anisotropic weld metal.

Again due to anisotropy, the beam gets skewed and recurring beam skewing results in a curved beam path.
Moreover, the beam gets attenuated by scattering, as multiple reflections and mode conversions occur at grain boundaries.
Thus the effects of interfaces during wave propagation in anisotropic materials are treated in this chapter (Munikoti 1991-99 [107, 108, 110, 115, 118, 125]).
As considered and justified in section 1.2.3 the subject matter of this chapter is limited to time-harmonic plane wave propagation in the bulk of the medium and at different types of interfaces. Except for diffraction and aperture effects it has been discussed (see section 1.2.3) that in normal ultrasonic testing bounded beam and pulse propagation can be dealt with by the analytical time-harmonic plane wave approach and that the other approaches discussed in sections 1.2.1 and 1.2.2 principally do not offer any improvements in the results of plane wave modeling.

2.2 The Christoffel equation

2.2.1 Mathematical formalism and transformation properties

The particle displacement $\mathbf{u}$ of a plane wave is defined as follows:

$$\mathbf{u} = A\,\mathbf{p}\,\exp\left[\imath\,(k\,\mathbf{l}\cdot\mathbf{r} - \omega\,t)\right] \tag{2.1}$$

with
A = Particle displacement amplitude
$\mathbf{p}$ = particle displacement direction
$\mathbf{l}$ = unit wave vector;
$\mathbf{k} = k\,\mathbf{l}$; k is the wave number
$\mathbf{r}$ = Cartesian coordinates: x, y, z.

By considering Newton's law and Hooke's law, the Christoffel equation can be derived as [3]:

$$k^2\,\Gamma_{ij}\,v_j = \rho\,\omega^2\,v_i \tag{2.2}$$

$$\Gamma_{ij} = l_{iK}\,C_{KL}\,l_{Lj} \tag{2.3}$$

where
C_{KL}[1] is the stiffness constant matrix referred to the crystallographic system;
$K, L = 1 \cdots 6$;
$i, j = 1 \cdots 3$;

[1]The relation between stiffness constant matrix in full and abbreviated matrix notation is:

$$C_{IJ} = C_{ijkl}$$

$\mathbf{v}$ = particle displacement velocity ($\mathbf{v} = \dot{\mathbf{u}}$) and

$$-\imath\, k\, l_{iK} = -\imath\, k \begin{bmatrix} l_x & 0 & 0 & 0 & l_z & l_y \\ 0 & l_y & 0 & l_z & 0 & l_x \\ 0 & 0 & l_z & l_y & l_x & 0 \end{bmatrix}$$

$$-\imath\, k\, l_{Lj} = -\imath\, k \begin{bmatrix} l_x & 0 & 0 \\ 0 & l_y & 0 \\ 0 & 0 & l_z \\ 0 & l_z & l_y \\ l_z & 0 & l_x \\ l_y & l_x & 0 \end{bmatrix}$$

$l_x\ l_y\ l_z$ are the components of the wave vector direction along the x, y and z axes of the reference coordinate system.

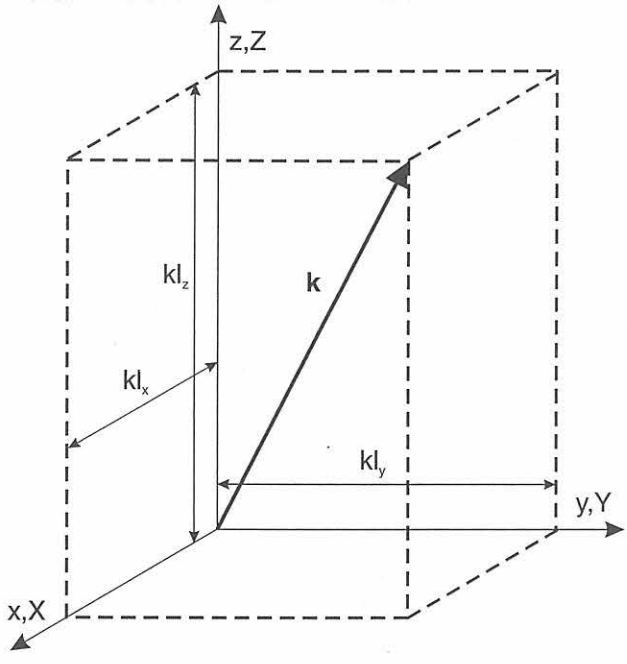

Figure 2.2: *Reference coordinate system showing the wave vector and its components*

The general Christoffel's equation (2.2) is not restricted to any particular coordinate system, but it is necessary that $\mathbf{l}$ and C_{IJ} be referred to the same coordinate system. Often, it is required to keep the laboratory (reference) coordinate system constant and rotate the crystallographic coordinate system, or the other way around. For example, in austenitic welds, the grains could be tilted both in the direction of welding and in the plane perpendicular to it due to local thermal gradients. This means that, the crystallographic Z axis which represents the columnar grain is located in 3 dimensional space with respect to the reference laboratory coordinate system. Then the elastic constants should be transformed to the reference coordinate system[2]. A general rotation of coordinates can be performed by applying successive rotations about different coordinate axes as shown in fig. 2.3.

The stiffness constants transformation law in abbreviated notation (see the footnote on the previous page) is given by Bond 1943, Auld 1990 [52, 3]:

[2]Elastic constants are always given with respect to the crystallographic system

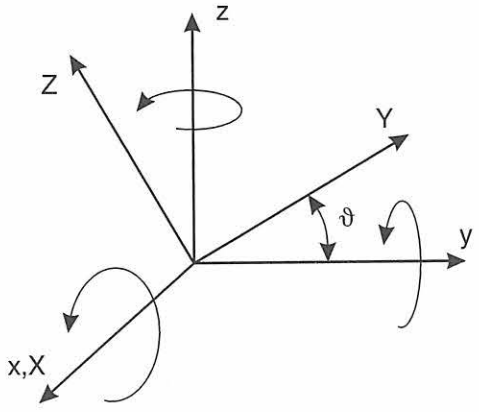

Figure 2.3: *General convention used in the rotation of coordinates around different axes*

$$C'_{HK} = M_{HI}\, M_{KJ}\, C_{IJ} \tag{2.4}$$

where the 6×6 matrix M is explicitly given in [52, 3]. The M matrix consists of elements of the unit rotation matrix. The new elastic constants C'_{HK} are then substituted in the equation (2.3).
Now, the Christoffel equation (2.2) can be recast as:

$$\left[k^2\, \Gamma_{ij} - \rho\, \omega^2\, \delta_{ij}\right]\, [v_j] = 0 \tag{2.5}$$

The elements of the Christoffel equation are functions *only* of the

- plane wave propagation direction,
- stiffness constants of the medium.

The angular dependence of phase velocity and the associated energy flow direction (group velocity direction) is due to the anisotropy of the material (which can be in turn attributed to the microstructure described in section 1.1) but *not* due to dispersion ($k(\omega)$). It may also be noted that, in many engineering materials, the phase velocity is constant for a given wave vector direction at long wave lengths but depends strongly on the frequency at short wavelengths, especially when the wavelength is of the order of the distance between molecules[3].
For nontrivial solutions of the Christoffel equation (2.5) the sufficient condition is

$$\left|k^2\, \Gamma_{ij} - \rho\, \omega^2\, \delta_{ij}\right| = 0 \tag{2.6}$$

[3]In ultrasound testing of austenitic steels, the ultrasonic frequencies of the transducers used lie in the range from 1 - 5 MHz, viz. the length of longitudinal waves is $\lambda \approx 6 - 1.2\ mm$ and of transverse waves $\approx 3 - 0.6\ mm$.
Further, it can be argued that the signal from the transducer travels with the signal velocity which could differ from the group velocity. However, in the materials of interest absorption and dispersion is negligible in the frequency ranges of NDT of austenitic steels. Therefore, signal and group velocities do not differ from each other (e. g. Brillouin 1960 [6]).

2.2.2 Slowness surface (Eigenvalues)

Unless explicitly stated, the following results are presented for materials with transverse isotropic symmetry.

Equation (2.5) represents an eigenvalue problem with three solutions. The three eigenvalues of (2.5) correspond to the phase velocities and the associated orthonormal eigenvectors to the particle displacement velocities (polarizations) of three wave types. One of the wave types has mainly longitudinal character (termed "quasi longitudinal" (qL)), one mainly transverse character (termed "quasi transverse" (qT1)) and one "pure transverse" (T2) character. The term "quasi" indicates that the polarization direction deviates from the **k**-vector direction in the case of the qL-wave and from the direction perpendicular to the **k**-vector direction in the case of the qT1-wave. For a given direction of the wave vector, the three polarization vectors are orthogonal to each other.

Considering the equation (2.6) the first term in the equation is proportional to k^2, whereas the second term is proportional to ω^2. This relation can be expressed in terms of the variable $\frac{k}{\omega}$, which is nothing else but the inverse of the phase velocity. It is called slowness. The introduction of this ratio reveals that the velocity (slowness) is only a function of the wave vector direction and is independent of frequency. Representing the slowness as a function of the wave vector direction a three sheeted surface in **k**-space is obtained. In contrast to the case of isotropic materials, the slowness surface shows non-spherical profiles, fig. 2.4.

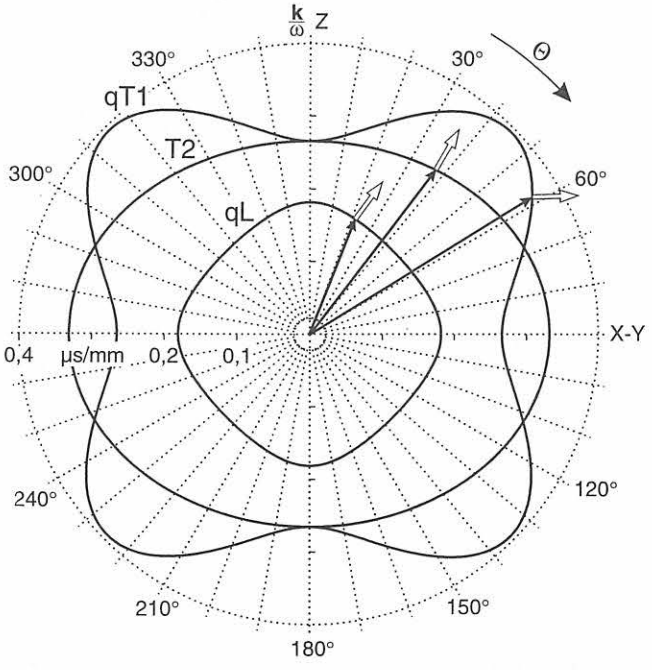

Figure 2.4: *Meridian section of the cylinder-symmetric three-sheeted slowness surface (Munikoti et al. 1996 [126]); stiffness constant matrix (2.64) of X 6 CrNi 18 11 austenitic weld metal; qL = quasi longitudinal wave, qT1 = quasi transverse wave, T2 = pure transverse wave; Θ = angle between wave vector and Z-axis; **k**-vectors (simple arrows) and group velocity directions (double lined arrows perpendicular to the slowness surfaces) of the qL, qT1, and T2 waves indicated for some angles Θ as examples*

2.2.3 Polarization (Eigenvectors)

For each phase velocity exists a corresponding eigenvector or particle displacement velocity (polarization) vector v_j.

Consider the equation (2.5) which could be expanded as:

$$\begin{bmatrix} \Omega_{11} & \Omega_{12} & \Omega_{13} \\ \Omega_{12} & \Omega_{22} & \Omega_{23} \\ \Omega_{13} & \Omega_{23} & \Omega_{33} \end{bmatrix} . \begin{bmatrix} v_x \\ v_y \\ v_z \end{bmatrix} = 0 \tag{2.7}$$

where

$$\Omega_{ij} = [C_{imjn} l_m l_n - \rho \left(\frac{\omega}{k}\right)^2_{qL} \delta_{ij}].[v_j] \tag{2.8}$$

$$\Omega_{ij} = [C_{imjn} l_m l_n - \rho \left(\frac{\omega}{k}\right)^2_{qT1} \delta_{ij}].[v_j] \tag{2.9}$$

$$\Omega_{ij} = [C_{imjn} l_m l_n - \rho \left(\frac{\omega}{k}\right)^2_{T2} \delta_{ij}].[v_j] \tag{2.10}$$

where $\frac{\omega}{k}$ is the phase velocity, and subscripts qL, $qT1$ and $T2$ represent the three wave types.
In the equations (2.8, 2.9 and 2.10) consider any two rows for each of the wave types qL, qT1 and T2:

$$\Omega_{11} v_x + \Omega_{12} v_y + \Omega_{13} v_z = 0 \tag{2.11}$$
$$\Omega_{12} v_x + \Omega_{22} v_y + \Omega_{23} v_z = 0 \tag{2.12}$$

The y and z components v_y and v_z are expressed as a function of v_x. This yields:

$$v_y = \frac{\Omega_{12}\Omega_{13} - \Omega_{23}\Omega_{11}}{\Omega_{12}\Omega_{23} - \Omega_{22}\Omega_{13}} \; v_x \tag{2.13}$$
$$v_z = \frac{\Omega_{11}\Omega_{22} - \Omega_{12}^2}{\Omega_{12}\Omega_{23} - \Omega_{13}\Omega_{22}} \; v_x \tag{2.14}$$

or

$$v_y = \frac{W_{23}}{W_{13}} \; v_x \tag{2.15}$$
$$v_z = \frac{W_{33}}{W_{13}} \; v_x \tag{2.16}$$

with

$$W_{ij} = \frac{1}{2} \epsilon_{ikl} \epsilon_{jmn} \Omega_{km} \Omega_{ln} \tag{2.17}$$

ϵ_{ikl} is the permutation tensor with the property:

$$\epsilon_{ikl} = \begin{cases} 1 & : \; i,k,l : 123, \; 231, \; 312 \\ 0 & : \; i,k,l : i = k, \quad k = l, \; l = i \\ -1 & : \; i,k,l : 132, \; 213, \; 321 \end{cases}$$

The eigenvectors then could be written as:

$$\mathbf{v} = [v_x,\ v_y(v_x),\ v_z(v_x)] \tag{2.18}$$

The eigenvectors are then normalized

$$\frac{\mathbf{v}}{|\mathbf{v}|}$$

The polarization directions vary as a function of the wave vector angle which is a feature of anisotropy, while in isotropic material polarizations are invariant.
The selection criteria for the eigenvectors for the transverse isotropic symmetry encountered in austenitic weld metal are as follows (fig. 2.5):

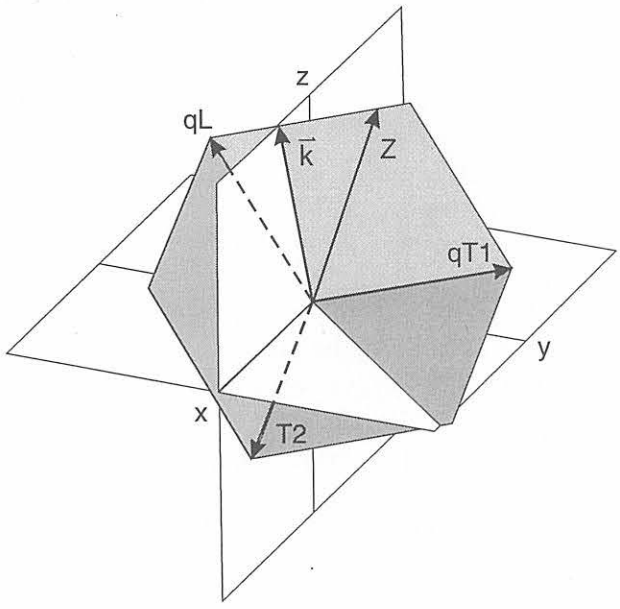

Figure 2.5: *Orientation of orthogonal particle displacement polarizations ('trihedral') quasi longitudinal (qL), quasi transverse (qT1), and pure transverse (T2) with respect to the* **k***-vector, plane of propagation xz, weld direction y, and texture Z (Munikoti et al. 1993 & 1996 [113, 126])*

1. In most of the engineering materials including the material considered here (X 6 CrNi 18 11), the longitudinal wave phase velocity has the highest magnitude. This means that the largest of the three eigenvalues corresponds to the longitudinal wave phase velocity. This eigenvalue is substituted in the equation (2.8) and the eigenvectors are determined. The relation between the eigenvector and the wave vector would be as follows:

$$\mathbf{l} \cdot \mathbf{v} \neq 0 \tag{2.19}$$

where $\mathbf{l}$ is the direction of the wave vector and $\mathbf{v}$ is the particle displacement velocity.

Equation (2.19) implies, that the eigenvector does not generally coincide with the wave vector direction except along the symmetry axes. Therefore, this wave type is termed as quasi longitudinal wave (qL).

2. The eigenvectors corresponding to the two transverse waves lie in a plane perpendicular to the eigenvector of the qL wave and correspondingly are associated with the smaller eigenvalues. Further distinction between the two transverse waves can be made as follows:

- In the general case the eigenvector of the qL wave does not coincide with the the crystallographic Z axis. If the eigenvector corresponding to one of the transverse waves is contained in the plane formed by the crystallographic axis Z and the eigenvector of the qL wave, then the eigenvalue corresponding to that eigenvector is termed as quasi transverse wave (qT1):

$$\mathbf{l} \times \mathbf{v} \neq 0 \tag{2.20}$$

  This again implies that the eigenvector is not perpendicular to the wave vector except along the symmetry axes.

- The other transverse wave is termed as pure transverse wave (T2), because for this wave type the following relation is valid:

$$\mathbf{l} \times \mathbf{v} = 0 \tag{2.21}$$

  This implies that the eigenvector is always perpendicular to the wave vector direction.

In the case of materials with other crystal symmetries, for example cubic symmetry, both the transverse waves generally are not perpendicular to the wave vector, i. e. all eigenvalues correspond to phase velocities of quasi waves. Then the quasi-transverse waves are sorted according to their magnitudes of phase velocity, viz. slow and fast quasi transverse waves and their corresponding polarizations qT1 and qT2, respectively, are defined. Only in certain specific planes with higher symmetry in-plane quasi-transverse and anti-plane pure transverse waves exist, so that the wave types can be sorted according to their polarizations as before.
Since polarization determines mode coupling at interfaces it is concluded that

- in the case of an interface between two *isotropic* materials, the horizontally polarized wave (T_H) does not couple with the other two waves, viz. with the vertically polarized shear wave (T_V) and the longitudinal wave (L) and vice versa,

- in the case of an interface between two *anisotropic* materials, always all three wave modes couple.

In the following examples polarization deviations (with respect to the wave vector direction) as a function of the incidence angle are shown. For this purpose a material with transverse isotropic symmetry is considered. The plane of wave incidence is assumed to be x, z. The crystallographic columnar grain axis Z is arbitrarily rotated around the X and Y axes by angles Ψ (layback) and Φ (columnar grain angle) respectively, so that the columnar grain is oriented in 3D space of the laboratory coordinate system x, y, z. The stiffness constants are transformed to the reference coordinate system using the relation described in section 2.4. Then the normalized eigenvectors for the three wave types which are evaluated using the equations (2.8), (2.9), (2.10) are plotted as a function of the **k**-vector direction in the case of layback angle $\Psi = -10°$ and grain tilt angle $\Phi = -20°$ as parameters.
If the columnar grain direction is not contained in the plane of wave propagation, the particle displacement polarizations are neither restricted to the plane of propagation nor perpendicular to it, fig. 2.6.

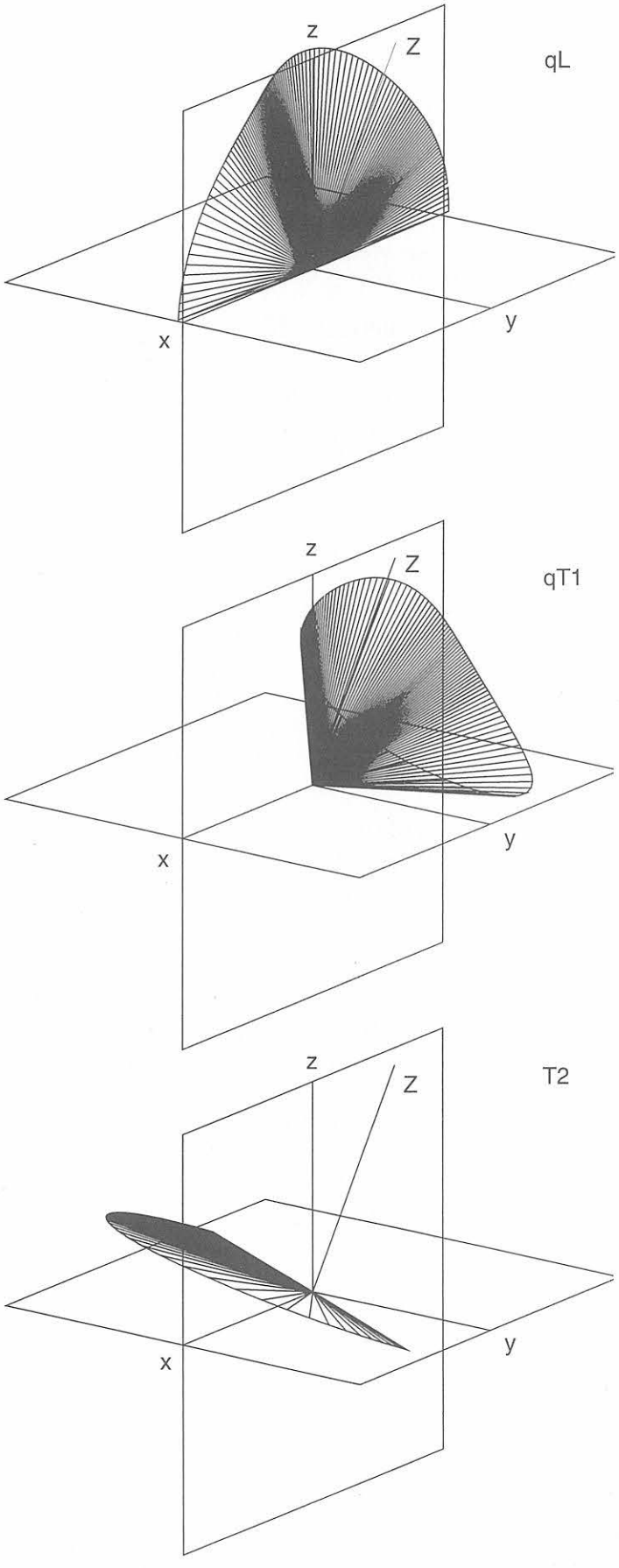

Figure 2.6: *Polarization directions of the three wave modes as a function of the wave vector direction in the range* $-90° \leq \Theta \leq 90°$*; plane of wave incidence* x, z*; crystallographic columnar grain axis* Z*; composite rotation of the crystallographic system:* $\Psi = -10°$ *around the* X *axis and* $\Phi = -20°$ *around the* Y *axis; the eigenvectors are evaluated using equations (2.8, 2.9 and 2.10); (Munikoti et al. 1992 & 1993 [109, 111, 112]).*

The directions of polarizations rather vary in the three dimensional space as a function of the **k** vector direction. Therefore the character of the waves which is described by the particle displacement polarizations is changed. In particular the character of the transverse waves, viz. vertically and horizontally polarized in the meridian plane generally is not maintained.
Following details can be gathered from fig. 2.6:

1. The properties of the T2 wave are as follows:
   - The polarization direction of the transverse wave T2 is invariant, i.e. always perpendicular to the columnar grain direction Z.
   - It is always perpendicular to the **k** vector. Therefore T2 has been defined as a pure wave.
   - The polarization of the T2 wave varies as a function of the **k** vector direction in the plane transverse to it. This means that it is not perpendicular to the plane of sound propagation and therefore T2 is generally not horizontally polarized.
2. The polarization direction of the transverse wave qT1 is not in the plane of sound propagation and therefore qT1 generally is no longer vertically polarized.
3. Increasing tilt of the columnar grain direction Z relative to the plane of wave propagation causes the transverse wave polarizations to change their 'roles':
   - 3.1 If the grain tilt reaches 90°, the polarization of the pure transverse wave T2 is contained in the plane of wave propagation, therefore being now vertically polarized, though as before perpendicular to **k** vector and columnar grain direction Z.
   - 3.2 If the grain tilt reaches 90°, the polarization of the now pure transverse wave T1 becomes independent of the wave vector direction, and will be perpendicular to the plane of wave propagation, i. e. horizontally polarized.

2.2.4 Group velocity

The velocity of energy transport in the lossless medium coincides with the group velocity[4]. Generally in anisotropic material the group velocity direction deviates from the direction of the wave vector. The practical consequence of this beam skewing is that in ultrasonic testing of anisotropic specimens the transducer has to be offset to effectively intercept the beam.
The group velocity which is defined as the velocity of modulation on a wave, is obtained by partially differentiating the circular frequency ω with respect to the wave vector:

$$\mathbf{V_g} = \frac{\partial \omega}{\partial \mathbf{k}} \tag{2.22}$$

Since the characteristic determinant of the Christoffel matrix is an implicit function of the circular frequency and the wave vector the equation (2.2) is implicitly differentiated:

$$|k^2\, \Gamma_{ij}(\mathbf{n}) - \rho\, \omega^2\, \delta_{ij}| = 0 \tag{2.23}$$

[4]Throughout this report the terminology group velocity direction and energy flow direction is used interchangeably. See appendix A for analytical proof of this.

A function f denotes equation (2.23) as:

(2.24)

$$f\left(\omega(k_x, k_y, k_z),\ k_x,\ k_y,\ k_z\right) = 0 \tag{2.25}$$

Differentiating with respect to k_x results in:

$$\frac{d\,f}{d\,k_x} = 0 = \frac{\partial f}{\partial k_x} + \frac{\partial \omega}{\partial k_x}\,\frac{\partial f}{\partial \omega} \tag{2.26}$$

Rearranging the above result yields:

(2.27)

$$\frac{\partial \omega}{\partial k_x} = -\frac{\frac{\partial f}{\partial k_x}}{\frac{\partial f}{\partial \omega}} \tag{2.28}$$

This is the expression for the x component of the group velocity.

Similarly the other components, viz. the $y-$ and $z-$ components of the group velocity $\frac{\partial \omega}{\partial k_y}$ and $\frac{\partial \omega}{\partial k_z}$, respectively, are obtained.

In the engineering materials considered here, the group velocity is greater than or equal to the phase velocities, and never smaller.

In the following examples, fig. 2.7, a similar presentation as in fig. 2.6 is shown to understand the beam skewing as a function of the incidence angle. Arbitrarily, the crystallographic system is rotated around the X axis by $\Psi = -10°$ and around the Y axis by $\Phi = -20°$. The resulting Z direction corresponds to the columnar grain direction. The stiffness constants are transformed to the reference coordinate system (section 2.4). The group velocity is then evaluated using implicit differentiation as described in equation (2.23).

It can be seen from fig. 2.7 that for all three wave modes the energy flow direction is not contained in the plane of wave incidence, but in 3D space, which is again dependent on the angle of incidence.

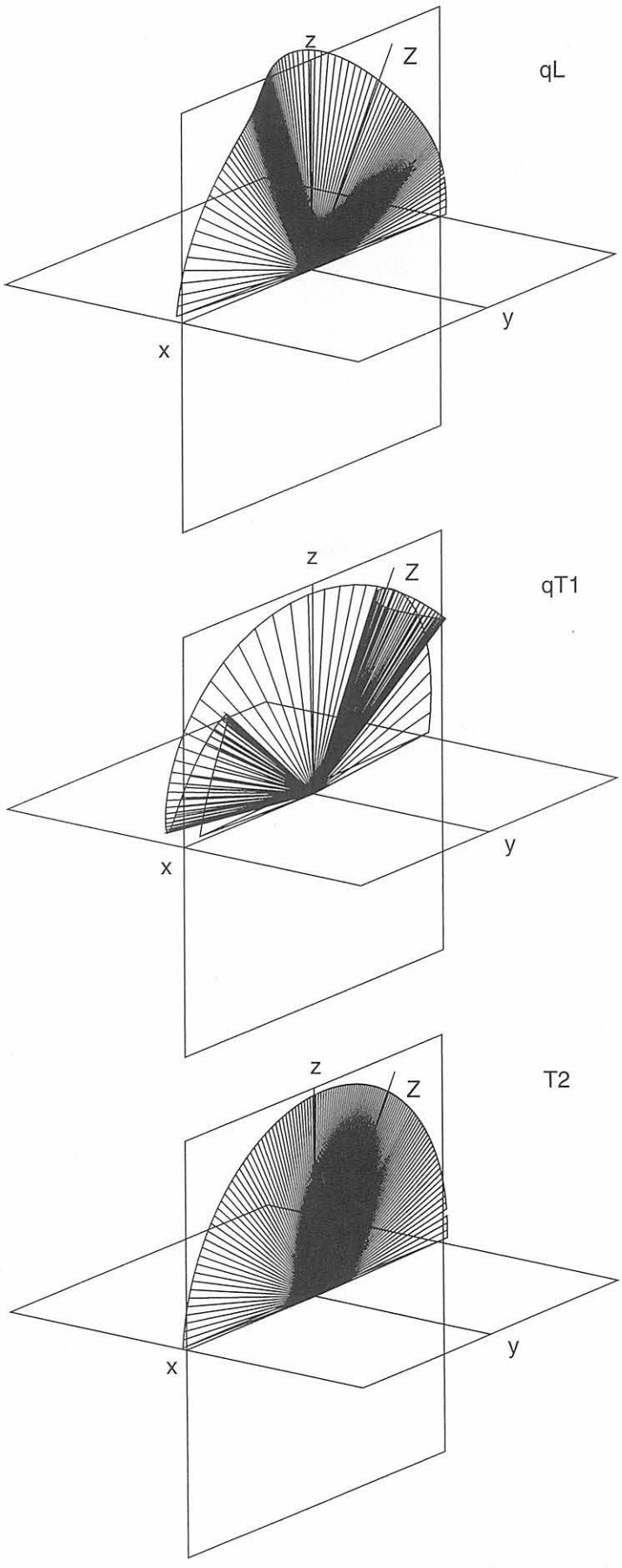

Figure 2.7: *Group velocity directions of the three wave modes as a function of the wave vector direction in the range* $-90° \leq \Theta \leq 90°$*; plane of wave incidence* x, z*; crystallographic columnar grain axis* Z*; composite rotation of the crystallographic system:* $\Psi = -10°$ *around the* X *axis and* $\Phi = -20°$ *around the* Y *axis (Munikoti 1994 [114]).*

2.2.5 Beam spreading

The second derivative of frequency with respect to the wave vector is defined as the beam spreading factor:

$$\frac{\partial^2 \omega}{\partial \mathbf{k}^2} \tag{2.29}$$

This factor gives the information about the spreading of the beam due to anisotropy. The higher the beam spreading, the higher is the energy scattered and the energy density of the main beam is reduced. These factors are calculated for austenitic stainless steel weld metal and compared with that of the beam spreading factor for isotropic material which is 1 as the direction of energy velocity and phase velocity coincide, fig. 2.8.
It can be inferred from fig. 2.8, that in the range of incidence angles relevant for ultrasonic weld testing

- the divergence of a quasi longitudinal beam is predominantly reduced,
- on the contrast the divergence of a quasi transverse beam is predominantly increased,
- the divergence of a pure transverse beam is least affected compared to the other wave types.

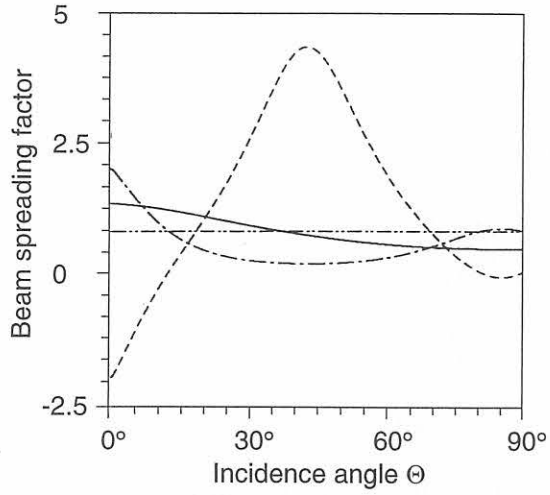

a) $\Psi, \Phi = 5°$

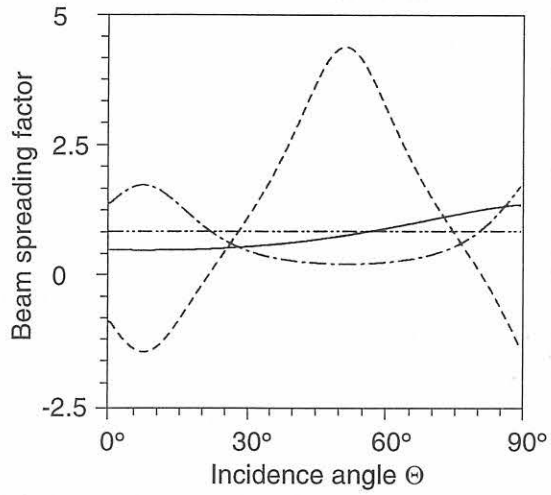

b) $\Psi, \Phi = 25°$

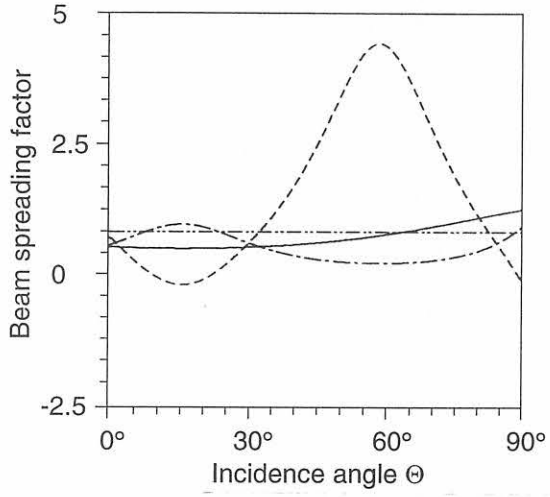

c) $\Psi, \Phi = 50°$

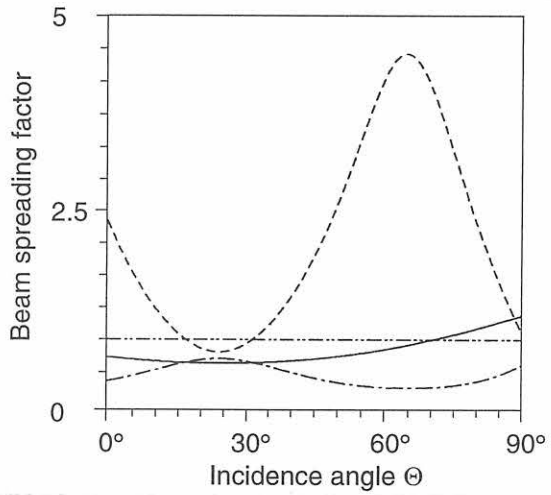

d) $\Psi, \Phi = 75°$

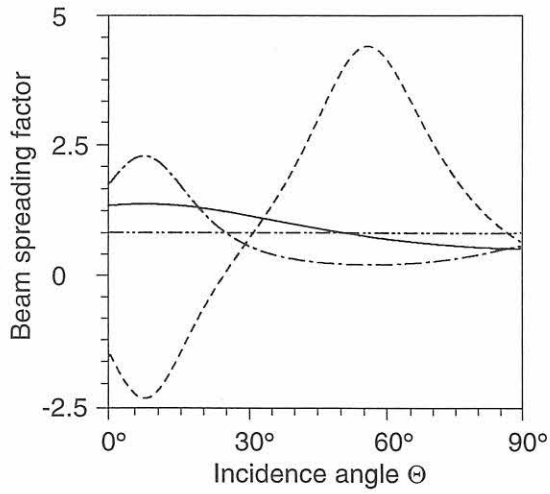

e) $\Psi, \Phi = 89°$

Figure 2.8: *Beam spreading factors for different columnar grain orientations:* $0° - 90°$*; the crystallographic system is rotated first around* Y *by the angle* Φ *and subsequently around* X *by the angle* Ψ *with the same magnitude (Munikoti 1995 cited in [25]).*
Isotropic: —··—; qL: ——; qT1: – – –; T2: —·—

2.3 Reflection and transmission coefficients at perfect interfaces

A schematic diagram describing the reflection and transmission phenomena at an interface between two anisotropic materials, which is the general case, is shown in Fig. 2.9.

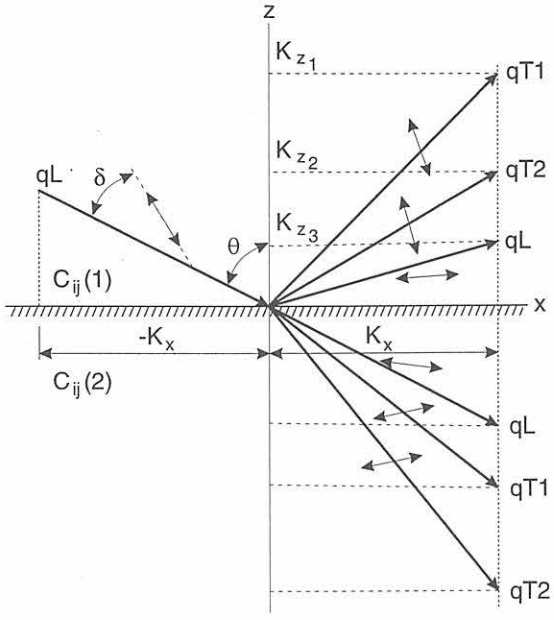

Figure 2.9: *Scheme of reflection and transmission between two anisotropic materials*

For the problem under consideration it is assumed that interfaces are

- in rigid contact,
- planar,
- smooth.

The boundary conditions are continuity of particle displacement velocity and traction forces across the interface[5]:

$$\mathbf{v} = \mathbf{v}' \tag{2.30}$$

$$\mathbf{T} \cdot \mathbf{n}^n = \mathbf{T}' \cdot \mathbf{n}^n \tag{2.31}$$

Using the equation (2.1), the boundary conditions (2.30) can be more explicitly written as follows:

[5]In geoscience literature these boundary conditions which are used for calculation of reflection and transmission coefficients are referred to as Knott's equations (Knott 1899 [96])

$$A_I\, v_{x_I}^{(0)} + A_{r1}\, v_{x1}^{(0)} + A_{r2}\, v_{x2}^{(0)} + A_{r3}\, v_{x3}^{(0)} = A_{t1}\, v'^{(0)}_{x1} + A_{t2}\, v'^{(0)}{}_{x2} + A_{t3}\, v'^{(0)}_{x3} \tag{2.32}$$

$$A_I\, v_{y_I}^{(0)} + A_{r1}\, v_{y1}^{(0)} + A_{r2}\, v_{y2}^{(0)} + A_{r3}\, v_{y3}^{(0)} = A_{t1}\, v'^{(0)}_{y1} + A_{t2}\, v'^{(0)}{}_{y2} + A_{t3}\, v'^{(0)}_{y3} \tag{2.33}$$

$$A_I\, v_{z_I}^{(0)} + A_{r1}\, v_{z1}^{(0)} + A_{r2}\, v_{z2}^{(0)} + A_{r3}\, v_{z3}^{(0)} = A_{t1}\, v'^{(0)}_{z1} + A_{t2}\, v'^{(0)}_{z2} + A_{t3}\, v'^{(0)}_{z3} \tag{2.34}$$

$$A_I\, T_{zz_I}^{(0)} + A_{r1}\, T_{zz1}^{(0)} + A_{r2}\, T_{zz2}^{(0)} + A_{r3}\, T_{zz3}^{(0)} = A_{t1}\, T'^{(0)}_{zz1} + A_{t2}\, T'^{(0)}_{zz2} + A_{t3}\, T'^{(0)}_{zz3} \tag{2.35}$$

$$A_I\, T_{xz_I}^{(0)} + A_{r1}\, T_{xz1}^{(0)} + A_{r2}\, T_{xz2}^{(0)} + A_{r3}\, T_{xz3}^{(0)} = A_{t1}\, T'^{(0)}_{xz1} + A_{t2}\, T'^{(0)}_{xz2} + A_{t3}\, T'^{(0)}_{xz3} \tag{2.36}$$

$$A_I\, T_{yz_I}^{(0)} + A_{r1}\, T_{yz1}^{(0)} + A_2\, T_{yz2}^{(0)} + A_{r3}\, T_{yz3}^{(0)} = A_{t1}\, T'^{(0)}_{yz1} + A_{t2}\, T'^{(0)}_{zz2} + A_{t3}\, T'^{(0)}_{yz3} \tag{2.37}$$

where $v_{x_I}^{(0)}, v_{x1}, v_{x2}, v_{x3}$ and $v'^{(0)}_{x1}, v'_{x2}, v'^{(0)}_{x3}$ are the components of the particle displacement velocities along the x direction for incident, reflected and transmitted waves, respectively, of the reference coordinate system at $z = 0$.

Similarly $v_{y_I}^{(0)}, v_{y1}, v_{y2}, v_{y3}$ and $v'^{(0)}_{y1}, v'^{(0)}_{y2}, v'^{(0)}_{y3}$ and $v_{z_I}^{(0)}, v_{z1}, v_{z2}, v_z 3$ and $v'^{(0)}_{z1}, v'^{(0)}_{z2}, v'^{(0)}_{z3}$ are the corresponding components along the y and z directions of the reference coordinate system.

The traction force components of incident, reflected, and transmitted waves are:

$$T_{zz_I}^{(0)},\ T_{zz1}^{(0)}, T_{zz2}^{(0)}, T_{zz3}^{(0)},\ T'^{(0)}_{zz1}, T'^{(0)}_{zz2}, T'^{(0)}_{zz3}$$

$$T_{xz_I}^{(0)},\ T_{xz1}^{(0)} T_{xz2}^{(0)}, T_{xz3}^{(0)},\ T'^{(0)}_{xz1}, T'^{(0)}_{xz2}, T'^{(0)}_{xz3}$$

$$T_{yz_I}^{(0)},\ T_{yz1}^{(0)}, T_{yz1}^{(0)}, T_{yz3}^{(0)},\ T'^{(0)}_{yz1}, T'^{(0)}_{yz2}, T'^{(0)}_{yz3}$$

$A_I, A_{r1}, A_{r2}, A_{r3}, A_{t1}, A_{t2}, A_{t3}$ are the amplitudes of incident, reflected and transmitted waves, respectively.

Referring to Auld 1990 [3] Hooke's law can be written

$$T_I = C_{IJ}\, S_J \tag{2.38}$$

with $I, J = 1 \cdots 6$ and the strain-displacement relation

$$S_J = \nabla_{Jk}\, u_k \tag{2.39}$$

The symmetric gradient operator has a matrix representation, e. g. Auld 1990 [3]:

$$\nabla_{Jk} = \begin{bmatrix} \frac{\partial}{\partial x} & 0 & 0 \\ 0 & \frac{\partial}{\partial y} & 0 \\ 0 & 0 & \frac{\partial}{\partial z} \\ 0 & \frac{\partial}{\partial z} & \frac{\partial}{\partial y} \\ \frac{\partial}{\partial z} & 0 & \frac{\partial}{\partial x} \\ \frac{\partial}{\partial y} & \frac{\partial}{\partial x} & 0 \end{bmatrix} \tag{2.40}$$

$$\begin{bmatrix} T_{xn^n} \\ T_{yn^n} \\ T_{zn^n} \end{bmatrix} = \begin{bmatrix} T_{xx} & T_{xy} & T_{xz} \\ T_{yx} & T_{yy} & T_{yz} \\ T_{zx} & T_{zy} & T_{zz} \end{bmatrix} \cdot \begin{bmatrix} n_x^n \\ n_y^n \\ n_z^n \end{bmatrix} \tag{2.41}$$

where $\mathbf{T}_{xn^n}$ is the traction force vector and $\mathbf{n}^n$ is the boundary normal vector.
The stress matrix in abbreviated subscript notation is

$$\mathbf{T} = \begin{bmatrix} T_{xx} & T_{xy} & T_{xz} \\ T_{xy} & T_{yy} & T_{yz} \\ T_{xz} & T_{yz} & T_{zz} \end{bmatrix} = \begin{bmatrix} T_1 & T_6 & T_5 \\ T_6 & T_2 & T_4 \\ T_5 & T_4 & T_3 \end{bmatrix} \tag{2.42}$$

The exponentials arising in the equations (2.32 - 2.37) must be true for all values of x at $z = 0$ and therefore must be equal. This means that the transverse components (components of the wave vector along the interface) of reflected and transmitted waves must be equal to that of the incidenct wave. This leads to the following relation:

$$k_x^I = k_x^r \quad \text{with } r = 1 \cdots 3 \tag{2.43}$$
$$k_x^I = k_x^t \quad \text{with } t = 1 \cdots 3 \tag{2.44}$$
$$k_y^I = k_y^r \quad \text{with } r = 1 \cdots 3 \tag{2.45}$$
$$k_y^I = k_y^t \quad \text{with } t = 1 \cdots 3 \tag{2.46}$$

where k_x and k_y are the components of the wave vector along the interface. The subscript I denotes the incident, r denotes the reflected, and t denotes the transmitted waves, respectively.
This is analogue to Snell's law in optics[6].

$$k_x = \frac{\omega}{V_{p_I}} \cdot \sin\theta_I \cos\phi_I \tag{2.47}$$

$$k_y = \frac{\omega}{V_{p_I}} \cdot \sin\theta_I \sin\phi_I \tag{2.48}$$

where V_{p_I} is the phase velocity of the incident wave. The wave vector is oriented in 3D space by rotating first around y axis by an angle θ_I and and next around x axis by an angle ϕ_I of the reference coordinate axes.
k_x and k_y are then the input parameters in the Christoffel's equation. Therefore, the unknown perpendicular components, viz. k_z of all reflected and transmitted waves can be determined by substituting (2.47) and (2.48) into the Christoffel equation, a sixth degree equation in k_z is obtained:

$$c_1\, k_z^6 + c_2\, k_z^5 + c_3\, k_z^4 + c_4\, k_z^3 + c_5\, k_z^2 + c_6\, k_z + c_7 = 0 \tag{2.49}$$

Here the $c_1 \cdots c_7$ are the coefficients described in Appendix B.
There is no analytical solution to the equation (2.49) except for special cases, when the wave propagation takes place in a meridian plane, i. e. when the plane of propagation is restricted to a particular plane e. g. XZ, YZ etc.. The procedure to determine the reflection and transmission coefficients is as follows:

- The polynomial (2.49) is solved numerically to determine the six roots as there is no analytical solution to it.

[6]This also is demonstrated by applying the Fermat's principle as shown in Appendix C

- An incident wave can excite three reflected and three transmitted wave modes. The polynomial (2.49) yields six roots for each medium. Each pair of roots corresponds to quasi longitudinal (pure longitudinal), quasi transverse (vertically polarized transverse), and pure transverse waves (horizontally polarized transverse).
- These roots are substituted in the Christoffel matrix and the corresponding Group velocity directions are determined as explained in section (2.2.4).
- Out of the six roots determined, only three solutions for each medium are sufficient to satisfy the boundary conditions (2.30, 2.31). The three valid roots are selected based on the group velocity direction (or energy flow direction):
  - For an incident wave, the group velocity vector should be directed towards the interface
  - for reflected and transmitted waves the energy flow direction should point away from the interface (Henneke 1972 [76]).
- The roots of the equation (2.49) whose group velocity directions meet the above requirement are chosen.

Since the group velocity direction (energy flow direction) decides the valid roots, the critical angle in the anisotropic case can then be redefined as that angle of incidence for which the energy flow direction for reflected or transmitted waves is 90°. The wave-vector $\mathbf{k}$ therefore can have an angle with the normal to the boundary greater than, less than, or equal to 90°.
The roots of the polynomial are generally complex. The following three cases arise:

1. Real roots (imaginary parts are zero) mean, the waves are propagating.
2. Purely imaginary roots correspond to evanescent waves, whose amplitude decays in the direction perpendicular to wave propagation.
3. Complex roots represent inhomogeneous waves, where a real part corresponds to a propagating wave and an imaginary part represents a wave with amplitude decay in the direction perpendicular to wave propagation.

2.3.1 Reflection and transmission coefficients as amplitude ratios

After selecting the valid roots, their corresponding group velocity directions, the polarization directions, the boundary conditions described in the equations (2.32 - 2.37) can be conveniently expressed as a 6×6 matrix. The six unknown amplitudes corresponding to the 6 waves (three reflected and three transmitted) can be determined as ratios of reflected to incident and transmitted to incident waves, respectively:

$$\begin{bmatrix} r_{1I} \\ r_{2I} \\ r_{3I} \\ t_{1I} \\ t_{2I} \\ t_{3I} \end{bmatrix} = \begin{bmatrix} v_{x1} & v_{x2} & v_{x3} & v'_{x1} & v'_{x2} & v'_{x3} \\ v_{y1} & v_{y2} & v_{y3} & v'_{y1} & v'_{y2} & v'_{y3} \\ v_{z1} & v_{z2} & v_{z3} & v'_{z1} & v'_{z2} & v'_{z3} \\ T_{zz1} & T_{zz2} & T_{zz3} & T'_{zz1} & T'_{zz2} & T'_{zz3} \\ T_{yz1} & T_{yz2} & T_{yz3} & T'_{yz1} & T'_{yz2} & T'_{yz3} \\ T_{xz1} & T_{xz2} & T_{xz3} & T'_{xz1} & T'_{xz2} & T'_{xz3} \end{bmatrix}^{-1} \cdot \begin{bmatrix} v_{xI} \\ v_{yI} \\ v_{zI} \\ T_{zzI} \\ T_{yzI} \\ T_{xzI} \end{bmatrix} \tag{2.50}$$

$r_{1I} = \frac{A_{r1}}{A_I} \cdots$ are the reflection coefficients (amplitude ratios of reflected waves to incident waves) and the $t_{1I} = \frac{A_{t1}}{A_I} \cdots$ are the transmission coefficients (amplitude ratios of transmitted waves to incident waves).

As stated above, generally at an interface three reflected and three transmitted waves can be excited when ultrasound is obliquely incident at an interface. Here $v_{x1}, v_{y1} \cdots$ are the particle displacement velocity components for the reflected wave 1 etc. and $v'_{x1}, v'_{y1} \cdots$ the particle displacement velocity components for the transmitted wave 1 etc. while $T_{zz1}, T_{yz1} \cdots$ are the corresponding traction force components.

The subscripts xI in the right most matrix correspond to the respective components for incident waves which are the input parameters.

2.3.2 Reflection and transmission coefficients as energy ratios

Since the energy flow direction generally does not coincide with the wave vector direction, energy coefficients would be more meaningful to characterize wave propagation in anisotropic media.

By calculating the balance of the time averaged energy flux density of all wave modes through the surface element of the boundary the energy conservation relation is obtained, s. fig. 2.10.

Consider the equation A.15 in Appendix A (time averaged energy flux density). The right hand side of the equation A.18 represents the energy velocity vector (group velocity) which can be substituted in the equation A.15:

$$\overline{E}_i = \frac{1}{2} A^2 \, \rho \, \omega^2 \, V_{g_i} \tag{2.51}$$

where $\mathbf{V}_g$ is nothing but the vector pointing the energy flow direction (group velocity vector), A is the amplitude and ρ is the density of the medium.

Now the reflection and transmission *energy* coefficients can be determined based on the equation 2.51, which is more meaningful in the case of anisotropic materials, as the directions of wave velocity vector and energy flow generally do not coincide.

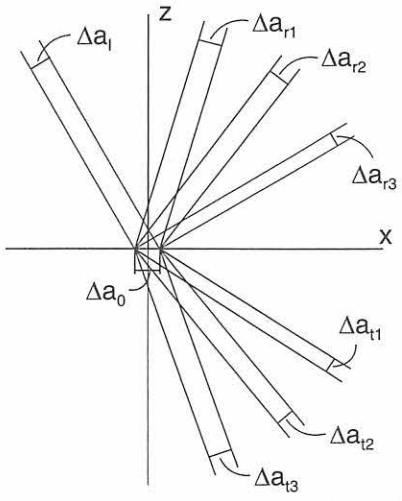

Figure 2.10: *Scheme of the energy balance of incident, reflected and transmitted ultrasound beams at an interface between two anisotropic materials;* $\Delta a_I, \Delta a_{r1} \cdots \Delta a_{r3}, \Delta a_{t1} \cdots \Delta a_{t3}$ *are the beam cross sectional areas of incident, reflected and transmitted waves, respectively.*

Consider the energy balance at an interface between two anisotropic materials where the energy reflected and transmitted per unit cross sectional area (fig. 2.10) can be formulated as:

$$\rho_1|V_{gI}|A^2{}_I\Delta a_I = \rho_1|V_{gr1}|A^2{}_{r1}\Delta a_{r1} + \rho_1|V_{gr2}|A^2{}_{r2} + \Delta a_{r2} + \rho_1|V_{gr3}|A^2{}_{r3}\Delta a_{r3}$$
$$+\rho_2|V_{gt1}|A^2{}_{t1}\Delta a_{t1} + \rho_2|V_{gt2}|A^2{}_{t2}\Delta a_{t2} + \rho_2|V_{gt3}|A^2{}_{t3}\Delta a_{t3} \quad (2.52)$$

where the $|V_{gsub}|$ are group velocities for incident wave (subscript I), reflected waves (subscript r1..r3) and transmitted waves (subscript t1..t3), respectively.
$\Delta a_I, \Delta a_{r1} \cdots \Delta a_{r3}, \Delta a_{t1} \cdots \Delta a_{t3}$ are the beam cross sectional areas of incident, reflected and transmitted waves, respectively.
ρ_1, ρ_2 are the densities of first and second medium, respectively.
Referring to the fig. 2.10 one obtains:

$$\Delta a_I = \Delta a \cos\theta_I \quad (2.53)$$
$$\Delta a_{r1} = \Delta a \ \cos\theta_{r1} \quad (2.54)$$
$$\Delta a_{r2} = \Delta a \ \cos\theta_{r2} \quad (2.55)$$
$$\Delta a_{r3} = \Delta a \ \cos\theta_{r3} \quad (2.56)$$
$$\Delta a_{t1} = \Delta a \ \cos\theta_{t1} \quad (2.57)$$
$$\Delta a_{t2} = \Delta a \ \cos\theta_{t2} \quad (2.58)$$
$$\Delta a_{t3} = \Delta a \ \cos\theta_{t3} \quad (2.59)$$

where the $\theta_I, \theta_{r1}, \theta_{r2}, \theta_{r3}, \theta_{t1}, \theta_{t2}, \theta_{t3}$ are the angles of the group velocities of incident, reflected and transmitted wave beams made with the z direction of the reference coordinate system. Substituting the equations (2.53 -2.59) in (2.52), Δa can be eliminated.
Dividing the equation 2.52 by $\rho_1 \ |V_{gI}| \ A^2{}_I \ \cos\theta_I$ and rearranging yields the energy conservation relation:

$$1 = \frac{|V_{gr1}| \ A^2{}_{r1} \ \cos\theta_{r1} + |V_{gr2}| \ A^2{}_{r2} \ \cos\theta_{r2} + |V_{gr3}| \ A^2{}_{r3} \ \cos\theta_{r1}}{|V_{gI}| \ A^2{}_I \ \cos\theta} +$$
$$\frac{\rho_2 \ |V_{gt1}| \ A^2{}_{t1} \ \cos\theta_{t1} + \rho_2 \ |V_{gt2}| \ A^2{}_{t2} \ \cos\theta_{t2} + \rho_2 \ |V_{gt3}| \ A^2{}_{t3} \ \cos\theta_{t3}}{\rho_1 \ |V_{gI}| \ A^2{}_I \ \cos\theta} \quad (2.60)$$

The $|V_{gI}| \cos\theta_I \cdots$ are the corresponding group velocity components in the direction perpendicular to the interface, viz. z and

$$\frac{A^2{}_{r1}}{A^2{}_I} \cdots \frac{A^2{}_{r3}}{A^2{}_I}$$

and

$$\frac{A^2{}_{t1}}{A^2{}_I} \cdots \frac{A^2{}_{t3}}{A^2{}_I}$$

are the squares of amplitude ratios determined by equation (2.50). The expression (2.60) can then be concisely written as:

$$\sum_{i=1}^{n} \frac{r_{iI}^2 \ V_{g,z}^{(i)}}{V_{g,z}^{(I)}} + \sum_{j=1}^{m} \frac{t_{jI}^2 \ V_{g,z}^{(j)} \ \rho_j}{V_{g,z}^{(I)} \ \rho_I} = 1 \quad (2.61)$$

where $V_{g,z}$ is the component of group velocity perpendicular to the interface. The symbols are:

i	=	Denoting of the reflected wave modes
j	=	Denoting of the transmitted wave modes
n	=	Number of reflected wave modes
m	=	Number of transmitted wave modes
ρ_I, ρ_i, ρ_j	=	Densities of the appertaining media

In equation (2.61) the energy reflection coefficients are

$$R_{iI} = \frac{r_{iI}^2 \, V_{g,z}^{(i)}}{V_{g,z}^{(I)}} \tag{2.62}$$

and the energy transmission coefficients are

$$T_{jI} = \frac{t_{jI}^2 \, V_{g,z}^{(j)} \, \rho_j}{V_{g,z}^{(I)} \, \rho_I} \tag{2.63}$$

2.3.3 Numerical results

The stiffness constant matrix for transverse isotropy[7] as measured on X 6 CrNi 18 11 austenitic weld metal (Neumann 1995 [25]) is as follows:

$$C_{IJ} = [10^{11} \frac{N}{m^2}] \begin{bmatrix} 2.4110 & 0.9692 & 1.3803 & 0 & 0 & 0 \\ & 2.6275 & 1.3803 & 0 & 0 & 0 \\ & & 2.4012 & 0 & 0 & 0 \\ SYM. & & & 1.1229 & 0 & 0 \\ & & & & 1.1229 & 0 \\ & & & & & 0.7209 \end{bmatrix} \tag{2.64}$$

By rotating the adjacent media separately first around the x, X-axis by the angle Ψ (corresponding to the columnar grain layback) and secondly around the crystallographic Y-axis by the angle Φ (corresponding to the columnar grain tilt against the crystallographic YZ-plane), fig 2.11, different crystallographic orientations in the adjacent media are generated. The incidence angle (between **k**-vector and z-axis of the laboratory coordinate system) is denominated by Θ.

The ultrasonic waves are incident from medium 1 to the interface. Each of three wave modes incident from medium 1 yields three reflected wave modes and three wave modes transmitted into medium 2. Inhomogeneous waves, which also can be excited, see section 2.3, page 46, are indicated in the figures.

[7] The reason for modeling the columnar grained structure as transverse isotropic has been substantiated in section 1.1.4.

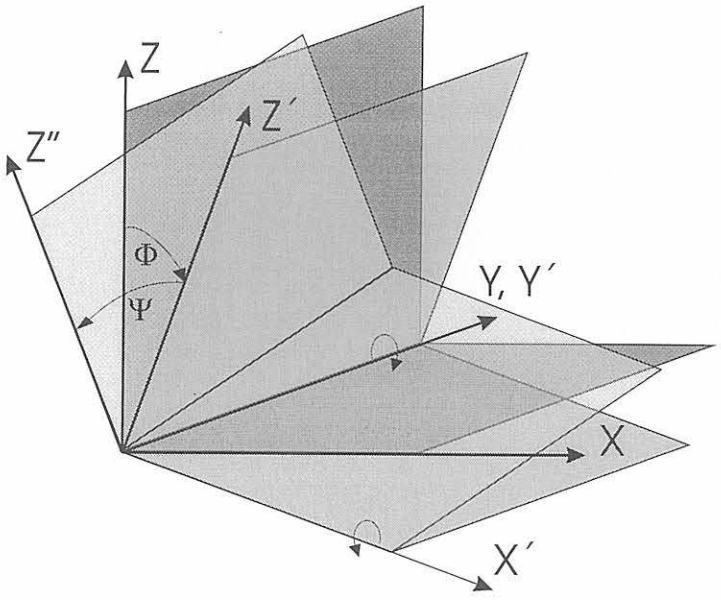

Figure 2.11: *Definition of columnar grain (Z) layback angle Ψ and columnar grain tilt Φ against the crystallographic YZ-plane*

Incident wave	Reflected wave	Transmitted wave
qL	r_{qT1qL}	t_{qT1qL}
	〃	t_{TvqL}
	r_{T2qL}	t_{T2qL}
	〃	t_{ThqL}
	r_{qLqL}	t_{qLqL}
	〃	t_{LqL}
qT1	r_{qT1qT1}	t_{qT1qT1}
	〃	t_{TvqT1}
	r_{T2qT1}	t_{T2qT1}
	〃	t_{ThqT1}
	r_{qLqT1}	t_{qLqT1}
	〃	t_{LqT1}
T2	r_{qT1T2}	t_{qT1T2}
	〃	t_{TvT2}
	r_{T2T2}	t_{T2T2}
	〃	t_{ThT2}
	r_{qLT2}	t_{qLT2}
	〃	r_{LT2}

Incident wave	Reflected wave	Transmitted wave
L	r_{TvL}	t_{qT1L}
	〃	t_{TvL}
	r_{ThL}	t_{T2L}
	〃	t_{ThL}
	r_{LL}	t_{qLL}
	〃	r_{LL}
Tv	r_{TvTv}	t_{qT1Tv}
	〃	t_{TvTv}
	r_{ThTv}	t_{T2Tv}
	〃	t_{ThTv}
	r_{LTv}	t_{qLTv}
	〃	r_{LTv}
Th	r_{TvTh}	t_{qT1Th}
	〃	t_{TvTh}
	r_{TvTh}	t_{qT1Th}
	〃	t_{ThTh}
	r_{LTh}	t_{qLTh}
	〃	r_{LTh}

In the above table and corresponding plots, the legend of type "r_{qLqL}" has the following meaning:

- the first letter r (or t) denotes the energy reflection (or transmission) coefficient.
- The first term qL (or L, Tv, Th, qT1, T2) of the subscript denotes the type of wave for which the energy coefficient is calculated.
  qL: quasi longitudinal wave,
  qT1: quasi transverse wave,
  T2: pure transverse wave,
  L: pure longitudinal wave,

Tv: vertically polarized transverse wave
Th: horizontally polarized transverse wave.

- The second term qL (or L, Tv, Th, qT1, T2) of the subscript denotes the type of the incident wave.

Many variations of crystallographic orientations of medium 1 and medium 2 to one another are possible, so that generally the incidence plane is not the meridian plane, neither in medium 1 nor in medium 2. Representative examples of interfaces have been selected.
Reflection and transmission energy coefficients are calculated[8] at the interfaces between:

1. Fine grained (isotropic) base material and columnar grained (transverse isotropic) austenitic weld metal, corresponding to the weld fusion face and the cladding interface (Munikoti et al. 1991-99 [107, 108, 110, 115, 118, 125, 126]).

2. Two transverse isotropic austenitic weld metal areas, corresponding e. g. to the interface between adjacent columnar grain bundles (Munikoti 1999 [118]).

2.3.3.1 Interface between isotropic and transverse isotropic media

Weld fusion face and cladding interface play an important role during ultrasonic testing of welded austenitic components (s. fig. 2.1) and, therefore, transparency of this type of interface is investigated comprehensively.
The columnar grains of the weld metal grow epitaxially at the fusion face (s. section 1.1.1.2). Therefore, the grain orientation of the base metal determines the columnar grain orientation of the weld metal at the fusion face. This comprises all orientations, viz. layback angle Ψ and tilt angle Φ in the range of $-90°$ and $90°$.
Figs. 2.12 - 2.14 display reflection and transmission at the interface between isotropic base metal and transverse isotropic weld metal with incidence from the base metal. In the figs. 2.12 - 2.14 Ψ is variable while Φ is parameter taking the value $\Phi = 0°$ in these three examples. The complete set of energy reflection and transmission coefficients is given in appendix D, figs. D.1 - D.31.

2.3.3.1.1 Longitudinal waves It can be observed that the transparency of the fusion face is fairly high and is approximately independent of the columnar grain orientation (grain angle and layback angle) (see fig .2.12, f).
Coupling of reflected and refracted wave modes to the incident wave principally is a matter of polarisation. Coupling only occurs, when the waves have co-planar particle displacement polarisation components. This can be estimated from fig. 2.6. Mode conversion of the incident longitudinal wave energy only marginally exceeds 10%, generally it is much lower (see figs. 2.12, a - d).

[8]The computer codes to evaluate equations (2.62) and (2.63) in the general case, where the meridian plane is not the incidence plane, are written in FORTRAN 77 with graphics integrated.

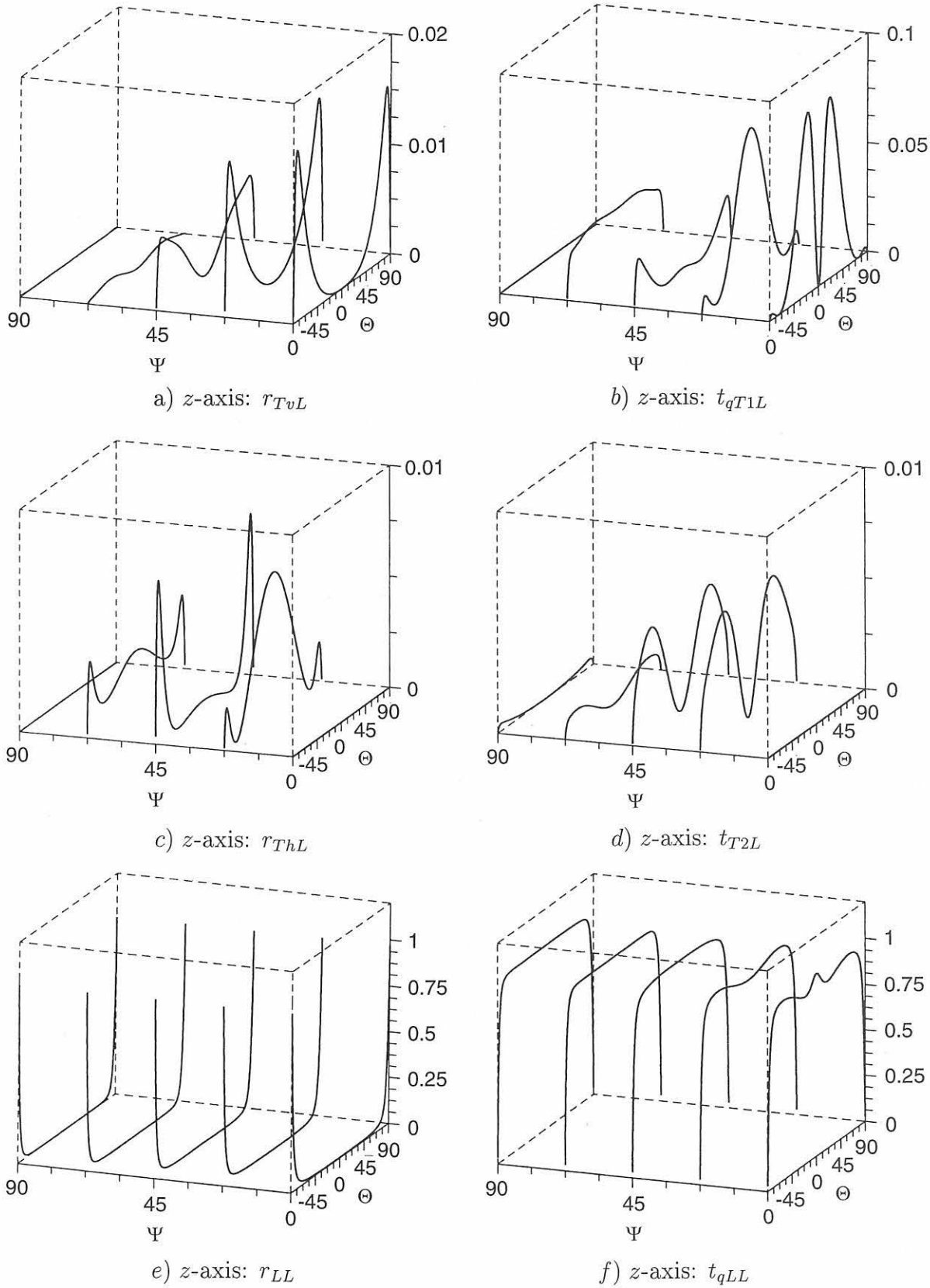

Figure 2.12: *Reflection and transmission energy coefficients of the three waves at the interface between isotropic and transverse isotropic media (fusion face) as a function of the incidence angle* Θ *and the layback angle* Ψ. **Longitudinal (L)** *wave incidence from the isotropic base metal. Columnar grain tilt angle* $\Phi = 0°$

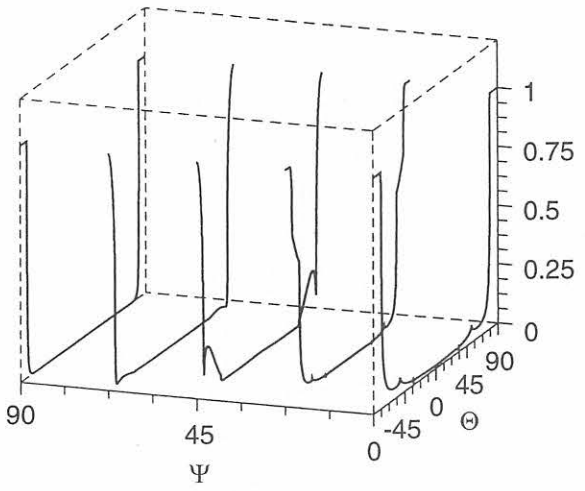

a) z-axis: r_{TvTv}

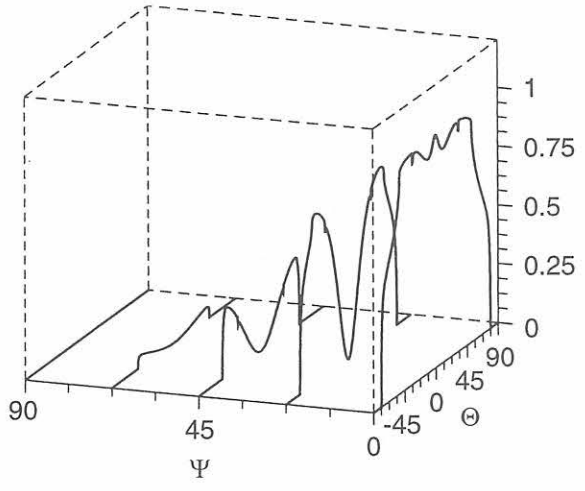

b) z-axis: t_{qT1Tv}

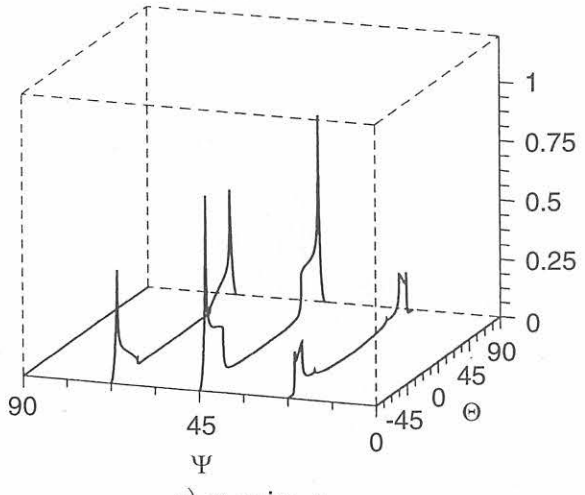

c) z-axis: r_{ThTv}

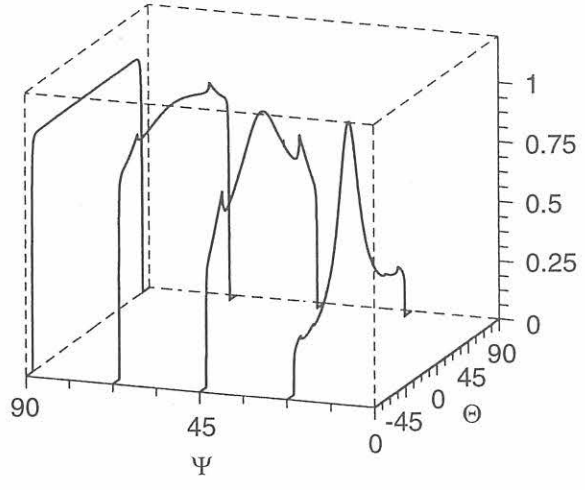

d) z-axis: t_{T2Tv}

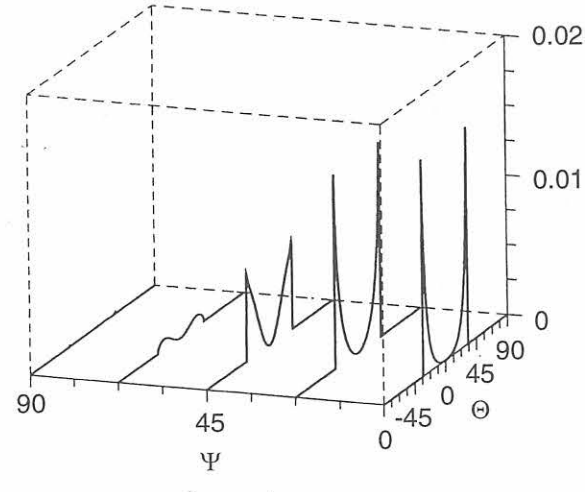

e) z-axis: r_{LTv}

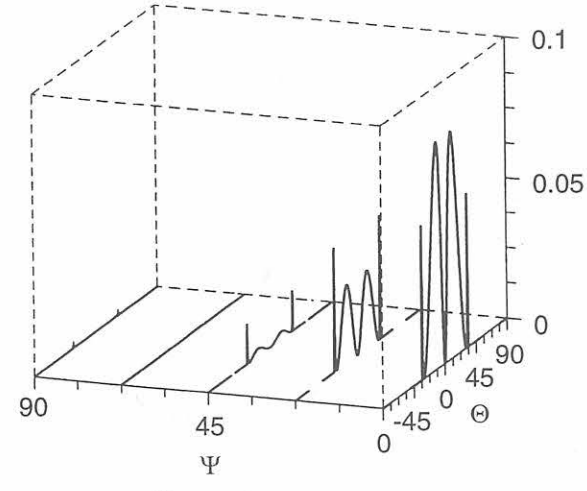

f) z-axis: t_{qLTv}

Figure 2.13: *Reflection and transmission energy coefficients of the three waves at the interface between isotropic and transverse isotropic media (fusion face) as a function of the incidence angle* Θ *and the layback angle* Ψ. **Transverse vertically polarized (Tv)** *wave incidence from the isotropic base metal. Columnar grain tilt angle* $\Phi = 0°$

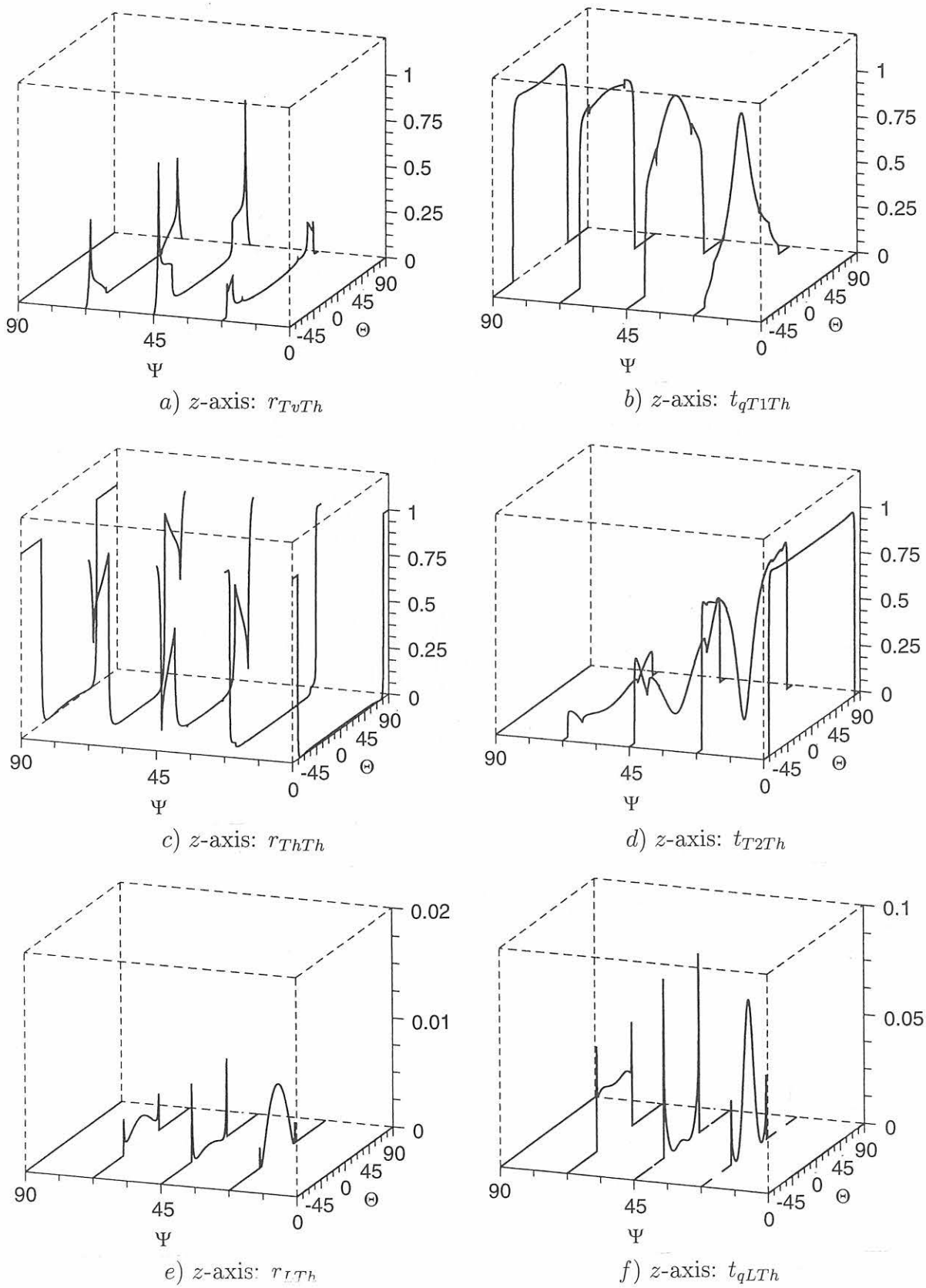

a) z-axis: r_{TvTh} *b*) z-axis: t_{qT1Th}

c) z-axis: r_{ThTh} *d*) z-axis: t_{T2Th}

e) z-axis: r_{rTh} *f*) z-axis: t_{qLTh}

Figure 2.14: *Reflection and transmission energy coefficients of the three waves at the interface between isotropic and transverse isotropic media (fusion face) as a function of the incidence angle* Θ *and the layback angle* Ψ. **Transverse horizontally polarized (Th)** *wave incidence from the isotropic base metal. Columnar grain tilt angle* $\Phi = 0°$

2.3.3.1.2 Transverse waves Mode conversion of transverse waves into longitudinal waves generally also does not exceed 10%.

The transparency of the fusion face also is not largely influenced by the columnar grain angle.

However, transverse waves exhibit mutual mode conversion at the fusion face, which depends on the columnar layback angle and can reach upto 100% (see Figs. 2.13 b, d and 2.14 b, d). The energy of the transmitted transverse waves depends on the polarization of the incident transverse wave, because only modes with (at least partially) identical polarizations couple to the incident wave.

The tables summarize transverse wave coupling at the weld fusion face and cladding interface as dependent on the columnar grain direction of the weld metal with respect to the incidence plane:

- Vertically (in-plane) and horizontally (anti-plane) polarised transverse waves are incident from the isotropic face.

Incident wave mode from isotropic base metal		Coupling wave modes in weld metal Columnar grains parallel | tilted | perpendicular to the incidence plane		
$\mathbf{T_H}$	anti-plane	T2	T2 + qT1	qT1
$\mathbf{T_V}$	in-plane	qT1	qT1 + T2	T2

Conventional ultrasonic probes generate either vertically polarised transverse waves or horizontally polarised transverse waves. These waves incident from the isotropic face are split at the fusion face. In the anisotropic medium only two orthogonally polarised transverse waves, qT1 and T2, exist. In the case the columnar grains are tilted relative to the plane of incidence, this decreases considerably the transverse waves' energy during examination of austenitic welds and cladded components. Both the transverse waves do not superpose due to different refraction angles.

In the symmetry planes parallel (meridian plane) resp. perpendicular to the columnar grain direction only one of the both transverse waves is excited.

- Both transverse waves are incident from the anisotropic face.

Incident wave mode from anisotropic weld metal				Coupling wave mode in isotropic base metal
	Columnar grains in the weld metal parallel | tilted | perpendicular to the incidence plane			
T2	anti-plane			T_H
		out-of-plane		$T_H + T_V = T$
			in-plane	T_V
qT1	in-plane			T_V
		out-of-plane		$T_V + T_H = T$
			anti-plane	T_H

In the isotropic base material, however, the both transmitted components, T_H and T_V, are degenerated and therefore form a resulting transverse wave T with polarization according to the intensities of both superposed components.

2.3.3.2 Interface between two transverse isotropic media

The interfaces chosen as examples from all possible variations are as follows:

- Special cases: The columnar grain direction Z of the transverse isotropic medium 1 is contained in the incidence plane (meridian plane). Under ideal conditions this situation is met during longitudinal flaw testing of welds. Orientations of the columnar grains in the meridian plane are chosen to be
  - perpendicular to the interface
  - parallel to the interface.

  The selected columnar grain directions Z of the transverse isotropic medium 2 may deviate from the meridian plane and are chosen as follows:
  $$\text{Layback angle } \Psi = 0°;\ 22.5°;\ 45°;\ 67.5°;\ 90°$$
  $$\text{Grain angle } \Phi = 67.5°$$
  The energy reflection and transmission coefficients are given in appendix D, section D.3, figs. D.32 - D.40.

- General case: The incidence plane is not the meridian plane, neither in medium 1 nor in medium 2. The selected columnar grain directions Z of the transverse isotropic medium 1 are
  $$\text{Layback angle } \Psi = -22.5°$$
  $$\text{Grain angle } \Phi = 0°;\ -67.5°;\ 90°$$
  The selected columnar grain directions Z of the transverse isotropic medium 2 are
  $$\text{Layback angle } \Psi = 0°;\ 22.5°;\ 45°;\ 67.5°;\ 90°$$
  $$\text{Grain angle } \Phi = 67.5°$$

The energy reflection and transmission coefficients are given in appendix D, section D.4, figs. D.41 - D.51.

2.3.3.2.1 Longitudinal waves The transparency of the interfaces made up by adjacent different crystallographic orientations is fairly high and is approximately independent of the columnar grain orientation (grain angle and layback angle). Mode conversion of the incident energy only at certain points exceeds 10%, generally it is much lower.

2.3.3.2.2 Transverse waves Mode conversion of transverse waves into longitudinal waves also is low.

However, direction dependent mutual mode conversion of transverse waves can reach 100% as before (s. paragraph 2.3.3.1.2).

At boundaries between two general transverse isotropic media with different grain orientations, when the propagation plane is not the meridian plane but an arbitrary plane, always both transverse wave modes couple simultaneously - with complementary energy distribution -, both with considerable energy, figs. D.41 - D.51, because the particle displacement polarization direction of the incident wave is not restricted by any crystallographic symmetry conditions.

Whereas the grain angle, which denotes the tilt of the columnar grains *in* the incidence plane, does not influence the transverse wave mode conversion at large scales, it is the layback angle denoting the tilt of the columnar grains *out of* the incidence plane, which governs the transverse wave mode conversion. In austenitic stainless steel weld testing with layback angles in the welding direction up to $\approx 20°$ and even more between adjacent dendritic bundles, large transverse wave mode conversion rates are to be predicted even in the low angle range, attenuating considerably the transverse wave actually used for testing.

In the special case where the columnar grains are contained in the meridian plane, i. e. no layback of the columnar grains in the incident plane, (medium 1) (figs. D.32 - D.40), mutual mode conversion of the transverse waves in medium 2 is similar to what is observed at the fusion face at wave incidence from the isotropic face. The table summarizes transverse wave coupling in this special case, where with increasing layback angle Ψ one transverse wave monotonously increases while the other one complementarily decreases to the same extent:

Incident wave mode from medium 1 Columnar grains, both perpendicular and parallel to the interface and contained in the meridian plane		Coupling wave modes in medium 2 Columnar grains parallel | oblique | perpendicular to the incidence plane		
$\mathbf{T2 = T_H}$	anti-plane	T2	T2 + qT1	qT1
$\mathbf{qT1 = qT_V}$	in-plane	qT1	qT1 + T2	T2

2.3.3.3 Splitting of the slowness surface domain of permissible wave vector angles of the quasi transverse wave

Due to the concave parts of the slowness surface of the quasi transverse wave in the transverse isotropic as well as in the cubic symmetry of austenite (see e. g. fig. 2.4) for certain incidence planes the slowness surface splits into disjoint sectors of "permissible" wavevectors.

This is because the existence criterion for reflected and transmitted ultrasonic waves is, that their energy flow direction (group velocity) vectors should be real and point away from the boundary, thus defining the sectors of the slowness surface containing the permissible wavevectors (Henneke 1972 [76]). The remaining sectors of the slowness surface contain "forbidden" wavevectors, because reflected and transmitted sound rays would be directed towards the interface: such rays do not exist.

This splitting phenomenon occurs both in transmission and reflection, when upon incidence of the quasi transverse wave qT1 and also of the pure transverse wave T2 the wave vector of the mode converted quasi-longitudinal wave qL reaches its critical angle. The incident energy then is redistributed and a qT1(2) wave is transmitted instead of the qL wave (see figs. D.9, D.14, D.25, D.31, D.35, D.39, D.37, D.45, D.48 of appendix D), the phase velocity having continuously decreased as a function of the incidence angle Θ from the value of the qL wave to the value of the quasi-transverse qT1(2) wave.

2.3.4 Energy balance of the waves at an interface and reciprocity relation

The reciprocity relations for the energy flow transformation coefficients (e. g. Tan 1977 [180], Rokhlin et al. 1986 [155])

$$r_{Wave_2Wave_1}(\Theta_1 \rightarrow \Theta_2) = r_{Wave_1Wave_2}(\Theta_2 \rightarrow \Theta_1) \quad (2.65)$$
$$t_{Wave_3Wave_1}(\Theta_1 \rightarrow \Theta_3) = t_{Wave_1Wave_3}(\Theta_3 \rightarrow \Theta_1) \quad (2.66)$$

(with notation according to the table on page 50) can be used to check the validity of the reflection and transmission energy coefficients given in section 2.3.3. These equations mean that the part of the energy flow from the incident wave to the mode converted reflected or transmitted wave is equal to the energy flow in the inverted case, viz. when the former mode converted wave now is incident, the same part of the energy flow is mode converted to the former incident wave, which is now reflected or transmitted.
As an example the following cases are considered:

- A quasi longitudinal wave (qL) is incident at an angle Θ_1 and a quasi transverse wave (qT1) is reflected at an angle Θ_2 fig. 2.15
- A quasi transverse wave (qT1) is incident at an angle Θ_2 and a quasi longitudinal wave (qL) is reflected at an angle Θ_1 fig. 2.16

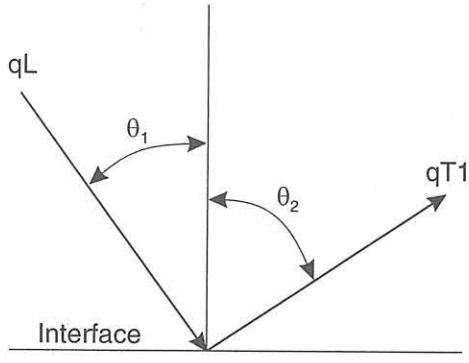

Figure 2.15: *Incident quasi longitudinal wave and reflected quasi transverse wave*

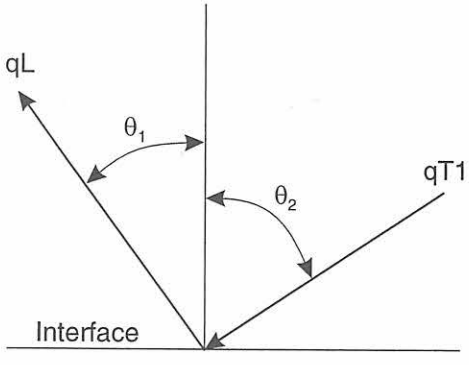

Figure 2.16: *Incident quasi transverse wave and reflected quasi longitudinal wave*

The columnar grains of the medium the wave is incident from are assumed to coincide with the z axis of the laboratory coordinate system. In the second medium, the columnar grains are rotated around the laboratory y axis by an angle of 20°.
In the first case, a quasi longitudinal is incident at an interface and the energy coefficient associated with the reflected quasi transverse (qT1) wave is plotted as a function of the incidence angle (fig. 2.17). The energy coefficient of qT1 is observed at the point where the incidence angle of qL is 80.7°. The energy amplitude of qT1 is 0.067 (A in fig. 2.17) and the corresponding reflection angle of qT1 is 29.9°.

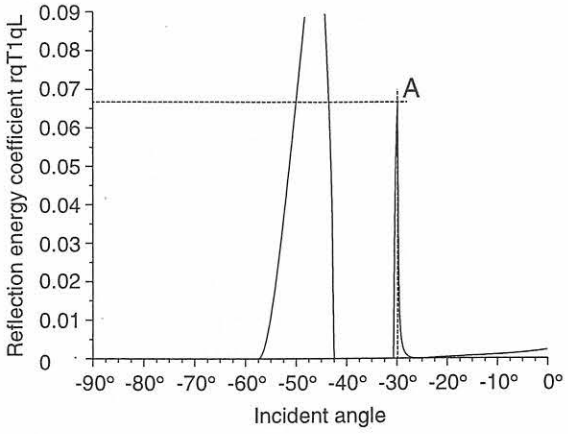

Figure 2.17: *Reflection energy coefficient of the quasi transverse wave (rqT1qL) upon incidence of a quasi longitudinal wave*

Now, in the second case (fig. 2.18), the quasi transverse is incident at an interface and the energy coefficient for the reflected quasi longitudinal wave (qL) is plotted as a function of the incidence angle. The energy coefficient of the reflected qL is observed at the point where the incidence angle of qT1 is 29.9°. The energy amplitude of qL has the same magnitude as in the first case, viz. 0.067 (B in fig. 2.18) and the corresponding reflected angle of qL is 80.7°.

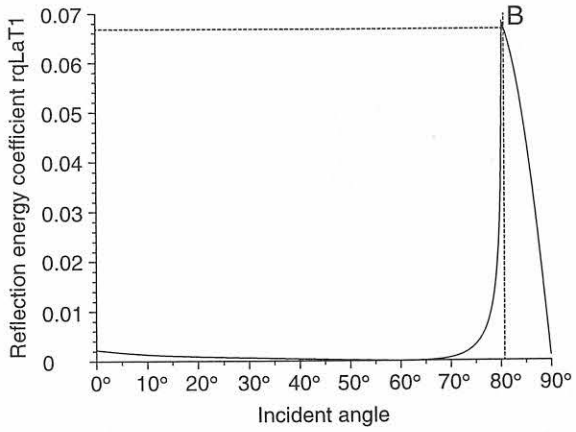

Figure 2.18: *Reflection energy coefficient of a quasi longitudinal wave (rqLqT1) upon incidence of a quasi transverse wave (qT1)*

This relation holds true for all the reflected and transmitted waves.

2.4 Reflection and transmission at imperfect interfaces

2.4.1 Theoretical procedure

As already discussed in section 1.2.3.1 surface roughness and defect distribution at interfaces influence reflection and transmission of the sound wave. Such interfaces can be the austenitic weld fusion face, the cladding interface, and columnar grain boundaries, as well as the layered system consisting of ultrasonic probe and cladding surface or weld metal (during transverse flaw testing) with a liquid coupling layer in between.

Consider a material with a perfect interface (free from disbonds, cracks, pores etc.). When

a static tensile force is applied to such a material, displacements on either of the interfaces would occur. Let the displacement at a far point on each side of the interface be $\frac{\Delta_{per}}{2}$. Now, for the same static tensile load, consider the material with *imperfect interface*, viz. interface with some types of defects. Because of the local deformations at the vicinity of the interface due to the defects, the displacement at the far point would be higher than if the interface were to be perfect.

Let this displacement be represented by $\frac{\Delta_{im}}{2}$. The total displacement on each side of the interface would be $\frac{\Delta_{per}+\Delta_{im}}{2}$. The displacement due to the presence of imperfections at the interface is dependent upon the type of defects, viz. volumetric defects, cracks etc., and it could be positive or negative depending on the geometry of the defects and the material's elastic constants (Baik et al. 1984 [45]). The imperfect interface can be replaced by an equivalent system, where it can be assumed, that the materials on either side of the interface have been connected with springs with stiffness per unit-area κ, fig. 2.19.

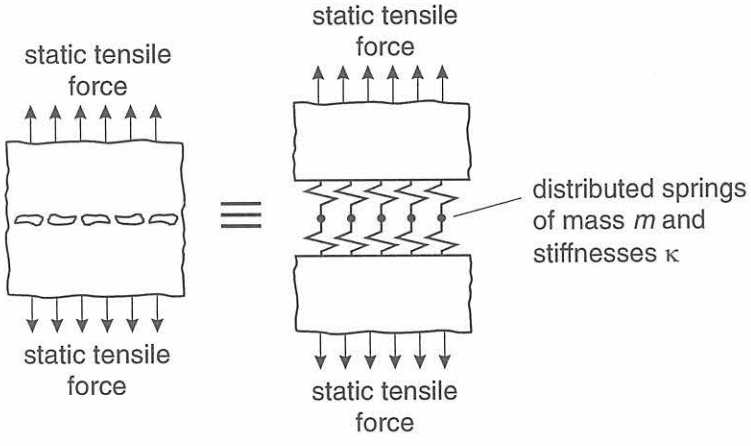

Figure 2.19: *Imperfect interface (containing flaws) replaced by an equivalent spring model, the quasi static model by Baik et al. 1984 [45]*

This stiffness κ of the spring is assumed to reproduce the increased displacement due to imperfections at the interface Δ_{im}. This spring model, which is based on heuristic argument, is the quasi static approximation (QSM) suggested by Baik et al. 1984 [45], Margetan et al. 1988 [101] and others [28].

A more rigorous approach has been given by Pecorari et. al., [150], where the QSM has been developed from the first principles and applied to an interface with a distribution of cracks. The authors Wang, Huang, Rokhlin, Schoenberg and others [28], [88], [89], [158], [159], [160], [161], [162], [163] and [164] adopt other approaches, where the elastic field vectors on either side of the interface are connected by the transfer matrix, which contains the properties of the interface. Under this so-called 'thin interface approximation' the matrix elements are asymptotically expanded. If the coupling terms arising in the expansion are neglected, the equations (2.67 - 2.72) are also obtained.

The validity of the QSM theory (equations (2.67 - 2.72)) is subject to following conditions:

- Ultrasonic wavelength $\lambda \gg$ *thickness* of the layer between two semi spaces, which usually is the case in non-destructive evaluation applications. Therefore, QSM is valid in low frequency applications.
- Mass and inertial parameters of the interface have to be assumed for volumetric defects (pores, inclusions) otherwise they could be neglected (e. g. cracks).

- The contact area does *not change* during the stress cycle due to only small stresses associated with the ultrasound wave. Otherwise, this would imply non-linearity.
- The frequency of the incident wave ω is small compared to the eigenfrequency of the *spring interface*, i. e. $\omega \ll \frac{4\,\kappa}{m}$

The *jumps* in the displacement due to imperfections at the interface can be modeled as linearly proportional to the magnitudes of the stress components across the interface. The boundary conditions (2.30) and (2.31) can then be modified as follows (Baik et al. 1984 [45]):

$$\kappa_1 \left(v_{x_I} + \sum_{r,t=1}^{3} \left(v_{x_r} - v_{x_t} \right) \right) = \frac{1}{2} \left(T_{zx_I} + \sum_{r,t=1}^{3} \left(T_{zx_r} + T_{zx_t} \right) \right) \tag{2.67}$$

$$\kappa_2 \left(v_{y_I} + \sum_{r,t=1}^{3} \left(v_{y_r} - v_{y_t} \right) \right) = \frac{1}{2} \left(T_{zy_I} + \sum_{r,t=1}^{3} \left(T_{zy_r} + T_{zy_t} \right) \right) \tag{2.68}$$

$$\kappa_3 \left(v_{z_I} + \sum_{r,t=1}^{3} \left(v_{z_r} - v_{z_t} \right) \right) = \frac{1}{2} \left(T_{zz_I} + \sum_{r,t=1}^{3} \left(T_{zz_r} + T_{zz_t} \right) \right) \tag{2.69}$$

$$T_{zx_I} + \sum_{r=1}^{3} \left(T_{zx_r} - T_{zx_t} \right) = \frac{-m\,\omega^2}{2} \left(v_{x_I} + \sum_{r,t=1}^{3} \left(v_{x_r} + v_{x_t} \right) \right) \tag{2.70}$$

$$T_{zy_I} + \sum_{r=1}^{3} \left(T_{zy_r} - T_{zy_t} \right) = \frac{-m\,\omega^2}{2} \left(v_{y_I} + \sum_{r,t=1}^{3} \left(v_{y_r} + v_{y_t} \right) \right) \tag{2.71}$$

$$T_{zz_I} + \sum_{r=1}^{3} \left(T_{zz_r} - T_{zz_t} \right) = \frac{-m\,\omega^2}{2} \left(v_{z_I} + \sum_{r,t=1}^{3} \left(v_{z_r} + v_{z_t} \right) \right) \tag{2.72}$$

where κ_1 and κ_2 are the transverse interfacial stiffnesses and κ_3[9] is the extensional (longitudinal) interfacial stiffness, ω is the frequency of the incident wave. In other words, interfacial spring forces are much greater than the inertial force, viz. the external force is transferred unaltered at the interface. The equations (2.70 - 2.72) which represent the equilibrium condition (Newton's law), relate the net force on a segment of the distributed spring interface to the acceleration of its center of mass (Margetan [102]). The center of mass of the spring is assumed to be located at the center of the two interfaces: $\frac{\mathbf{u}+\mathbf{u}'}{2}$, where $\mathbf{u}$ and $\mathbf{u}'$ are the particle displacements of the incident and transmitted waves, respectively.

$$\begin{aligned} F_1 &= m\,\frac{\partial^2 \left(\frac{\mathbf{u}+\mathbf{u}'}{2} \right)}{\partial t^2} \\ &= -m\,\omega^2\,\frac{\mathbf{u}+\mathbf{u}'}{2} \end{aligned} \tag{2.73}$$

where m is the mass of the spring; ω is the frequency of the incident wave and $\mathbf{u}$ and $\mathbf{u}'$ have the forms as described in the equation (2.1)

(2.74)

[9] κ is a diagonal matrix due to the assumed symmetry

The force F_1 has to balance the traction forces exerted on the opposite sides of the interface, viz. the vector sum of the traction forces:

$$\mathbf{T} - \mathbf{T}' = -m\,\omega^2\,\frac{\mathbf{u}+\mathbf{u}'}{2} \tag{2.75}$$

where $\mathbf{T}$ and $\mathbf{T}'$ are the traction forces on both sides of the boundary, viz. the wave is incident from and transmitted to, respectively. Nota bene the equation (2.75) is equivalent to the equations (2.70 - 2.72).

In this work a non-volumetric defect is considered and, therefore, the mass parameter is $m = 0$, which means continuity of traction forces at the interface.

These generalized boundary conditions (2.67)-(2.72) include the perfect interfaces as well as the imperfect interfaces. Whereas in the case of perfect interfaces the boundary conditions (2.67)-(2.72) are reduced to equations (2.30) and (2.31) by proper selection of the values for the κ_1, κ_2, κ_3 (see the following table), in the case of imperfect interfaces the interfacial stiffnesses representing disbond structures can take a large variety of values.

Furthermore, by equations (2.67) - (2.69) a frequency dependence of the reflection and transmission coefficients is introduced due to the partial differentials of the particle displacement velocities contained in the traction force components T_{ik}.

2.4.1.1 Imperfect interfacial topography

The imperfect interfacial topography considered as an example for disbond structures contains non-interacting circular material separations (Margetan et al. 1988 [101], Nagy 1991-97 [119] - [122]) (fig. 2.20) with diameter d such as microcracks (ultrasonic wavelength $\lambda \gg$ d) or a viscoelastic layer, which both are presumed to be thin ($\lambda \gg$ thickness).

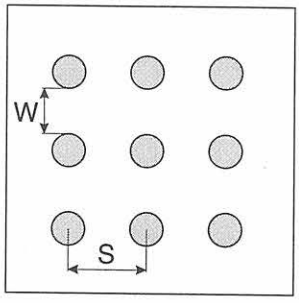

Figure 2.20: *Model of the disbond structure in the form of circular cracks in the interface. s = centre-to-centre distance of adjacent circular cracks, w = width of the perfect ligament (Margetan 1988 [101])*

The area fraction of the interface plane, which is composed of these discontinuities, is given by

$$A' = \frac{\pi(s-w)^2}{4s^2} \tag{2.76}$$

where s is the centre-to-centre distance of adjacent discontinuities and w is the width of the perfect ligament.

The interfacial stiffness constants in the table are calculated from the estimation of stiffnesses in the quasi-static spring model of solid state bonding given by Margetan 1988 [101].

2.4.1.2 Viscoelastic layers

Viscoelastic layers in the form of viscous couplants are used to bring about transmission of transverse ultrasonic wave energy into the specimen. In the case of ultrasonic testing welded austenitic components, the viscoelastic layer is between the isotropic wedge

material of the transducer, typically perspex, and the austenitic weld metal or austenitic cladding.
Due to damping losses in the viscoelastic layer there is some decaying of the ultrasonic waves in the layer, which is characterized by the penetration depth δ or the thickness of the 'hydrodynamic boundary layer' (Landau, Lifschitz 1981 [21], Rokhlin et al. 1986 & 1991 [157, 158])

$$\delta = \sqrt{\left(\frac{\nu}{\omega}\right)}$$

where ν is the kinematic viscosity of the viscous fluid and ω is the circular frequency. When the thickness of the hydrodynamic boundary layer δ is smaller than the thickness of the interface layer, shear stresses are not transmitted substantially. Therefore the transparency of the viscoelastic layer increases with kinematic viscosity ν and decreases with increase in frequency ω.
Transverse (κ_1, κ_2) and longitudinal (κ_3) interfacial stiffnesses are defined as (Nagy 1992 [121]):

$$\kappa_1, \kappa_2 = \frac{\mu'}{h} \tag{2.77}$$

$$\kappa_3 = \frac{G' + \frac{4}{3}\,\mu'}{h} \tag{2.78}$$

$$\tag{2.79}$$

where G' is the bulk modulus, μ' is the shear viscosity coefficient ($\mu' = \imath\,\omega\,\nu\,\rho'$), ρ' is the density, and h is the layer thickness. The complex structure of the interfacial stiffnesses of the viscoelastic couplants accounts for the losses in the couplant due to viscosity.
Two couplants have been introduced to the calculations

- Glycerine[10] with a shear viscosity coefficient at room temperature $\mu' = 1.2\ Ns/m^2$,

- High viscosity couplant Gel 3000 (Grade 60)[11] with a shear viscosity coefficient at room temperature $\mu' = 600\ Ns/m^2$,

which are assumed to be used between isotropic perspex (wedge material of the ultrasonic probe) and austenitic stainless steel weld metal[12].

[10] Phase velocity: 1.980 mm/μs; density: 1.260 g/cm^3

[11] Phase velocity: 1.3 .... 1.4 mm/μs; density: 0.931 g/cm^3, Sonotech, Inc., 774 Marine Drive, Bellingham, WA 98225, USA

[12] The elastic constants of perspex, as calculated from the data in Krautkrämer 1986 [19], are $c_{11} = 8.794422$, $c_{12} = 3.968458$, $c_{44} = 2.412982 \cdot 10^9\ N/m^2$ and the density is $\rho = 1.18\ 10^3 kg/m^3$. The elastic constants for the anisotropic (transverse isotropic) weld metal are given by the stiffness constant matrix on page 49.

Type of interface	Interfacial stiffness $[10^{15} N/m^3]$
Perfect interface (s. section 2.3):	
Rigid interface	$\kappa_1, \kappa_2, \kappa_3 = \infty$
Traction free surface	$\kappa_1, \kappa_2, \kappa_3 = 0$
Solid/fluid (slip) interface	$\kappa_1, \kappa_2 = 0, \kappa_3 = \infty$
Imperfect interface:	
Solid imperfect interface with circular microcracks (Margetan 1988 [101]) Crack area fraction A = 0.75, f = 5 MHz	$\kappa_1, \kappa_2 = 0.40$ $\kappa_3 = 0.47$
Thin viscoelastic layers at room temperature, h = 50μm, f = 2 MHz	
Glycerine	$\kappa_1, \kappa_2 = \imath\, 0.0003$ $\kappa_3 = 0.0988 + \imath\, 0.0004$
Gel 3000 (Grade 60)	$\kappa_1, \kappa_2 = 0.1508$ $\kappa_3 = 0.0339 + \imath\, 0.2011$

The solution to the equations (2.67)-(2.72) is described in section 2.3.

2.4.2 Numerical results and discussion

2.4.2.1 Solid imperfect interface between two anisotropic materials

Energy reflection and transmission coefficients at a solid imperfect interface with circular microcracks between two transverse isotropic materials as characterized in the table above are calculated, appendix E.1, figs. E.1 - E.6.

2.4.2.1.1 Longitudinal waves Comparing figs. D.42 and E.2 it can be observed that the transparency of the interfaces is still fairly high, though the crack area fraction comprises 75% of the interface. However, in contrast to the solid perfect interface a larger portion of the incident energy is reflected, mainly in the range below 45° incident angle Θ. This portion increases with frequency, and may be used to characterize the interface. Similarly it is observed that a larger portion of the incident longitudinal wave energy is mode converted to the quasi transverse wave qT1, which reaches 15% at incidence angles larger than 45°, both, in reflection and refraction, while mode conversion to the pure transverse wave T2 generally does not exceed 1%.

2.4.2.1.2 Transverse waves Comparing figs. D.46 and E.4 the same observation is made as with longitudinal waves: a larger portion of the incident energy is reflected, mainly in the range below 45° incident angle Θ. This portion also is increasing with frequency.

Also mode conversion during reflection is increasing and, furthermore, increases with frequency.

2.4.2.2 Thin viscoelastic layers between isotropic and anisotropic materials

Figs. E.7 - E.24 in appendix E.2 show the transparency of the coupling layer between ultrasonic probe and austenitic material in the case of a columnar grain tilts $\Phi = 0°$ and $67.5°$ and varying layback angle (Munikoti 1992 [108]). Basically the echo transparencies are similar to those obtained during coupling on isotropic material. The columnar grain direction in the weld metal relative to the coupling surface only has little influence on the echo transparency.
Generally, as a matter of fact, transverse waves do not pass a fluid coupling layer due to its vanishing viscosity. However, the viscosity of glycerine and even fresh water, though very small, is not zero. Therefore transverse waves are transmitted at a corresponding low level into the weld metal, e. g. figs. E.11 and E.18. The high viscosity couplant Gel 3000 provides transparency up to 50% for transverse waves, whereas solid coupling between perspex and weld metal only yields slightly increased transparency, e. g. fig. E.16.

2.5 Bounded beam displacement during reflection at the liquid-anisotropic solid interface

When an ultrasound beam is incident onto a liquid-isotropic solid interface at an angle around the Rayleigh angle the following effects occur (Schoch 1952 [166], Bertoni et al. 1973 [47], Ngoc et al. 1980-82 [128, 129, 130]):

1. lateral displacement of the reflected beam relative to its position predicted by geometrical acoustics,

2. splitting of the reflected beam, both partial beams being anti-phase,

3. a weak leaky wave field on one side of the reflected beam, opposite to the incident beam in the plane of incidence.

What happens, when such a beam is incident at an interface between fluid and *anisotropic* solid, is investigated here.
The amplitude field of a sound beam with finite lateral dimensions can be expressed as a sum of infinite plane waves using the Fourier integral transform pair (Bertoni et al. 1973 [47]).
A beam with Gaussian amplitude profile $f(x)$ is described as

$$f(x) = f_0 \ \exp(-\frac{x^2}{w^2}) \tag{2.80}$$

where w is the half beam waist at the amplitude $\frac{f_0}{e}$.
The area under the curve of such a gaussian function is:

$$Area = \int_{-\infty}^{\infty} f_0 \ \exp(-\frac{x^2}{w^2}) \ dx \tag{2.81}$$

This can be reduced to a standard Dawson's integral:

$$Area = f_0 \ w \int_{-\infty}^{\infty} \exp\left(-y^2\right) \ dy = f_0 \ w \sqrt{\pi} \tag{2.82}$$

Now, f_0 can be so chosen, that the area under the curve would be unity, viz.

$$f_0 = \frac{1}{w\sqrt{\pi}}$$

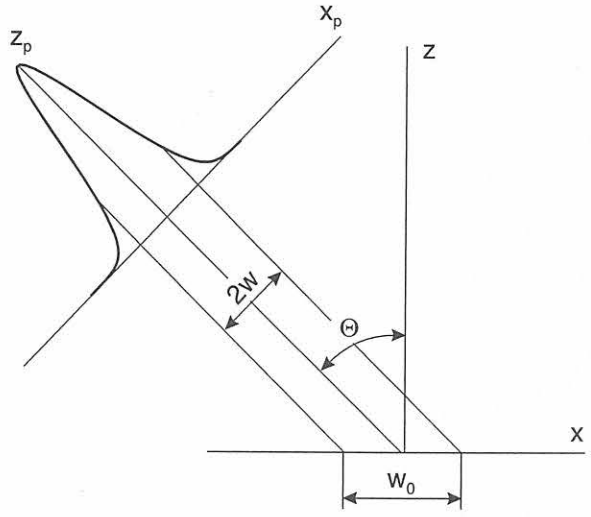

Figure 2.21: *Reference coordinate systems: x_p and z_p are the coordinates referred to the pulse and x and z is the main coordinate system*

Therefore, the equation 2.80 can be re-defined as:

$$f(x_p) = \frac{1}{w\sqrt{\pi}} \exp\left(-\frac{{x_p}^2}{w^2}\right) \tag{2.83}$$

Referring to the fig. 2.21, the following transformations are used:

$$x_p = x\ \cos\theta \tag{2.84}$$
$$z_p = x\ \sin\theta \tag{2.85}$$
$$w = w_0 \cos\theta \tag{2.86}$$

The beam is assumed to be well collimated, viz. $\frac{w}{\lambda} \gg 1$. Further, in the vicinity of the waist, the field can be well approximated by appending the plane wave variation $\exp(\imath\ k\ z_p)$ to the equation 2.83 [48]. The equations (2.84) can be substituted in the equation (2.83), which yields the particle displacement velocity v_{inc} having a profile described by the equation 2.83 characterized along the coordinate x transverse to the beam axis at $z = 0$ by

$$v_{inc}(x,0) = \frac{1}{\sqrt{\pi}\ w} \exp\left(-\frac{x^2}{{w_0}^2} + \imath\ k_i\ x\right) \tag{2.87}$$

where $k_i = k\ \sin\theta_i$ is the wave number along the interface and the component of the beam.
The Fourier transform of equation (2.87) is:

$$F(k_x) = \frac{1}{\cos\theta_i} \exp\left(-\frac{(k_x - k_i)^2\ w_0^2}{4}\right) \tag{2.88}$$

Assuming the incident wave to be contained in the x, z plane, where z is the boundary normal to the interface x, y, one obtains the Fourier integral transform pair

$$v_{inc}(x,z) = \frac{1}{2\pi}\int_{-\infty}^{\infty} F(k_x)\ \exp\left(\imath\,(\mathbf{k}\cdot\mathbf{r})\right)\ dk_x$$
$$F(k_x) = \int_{-\infty}^{\infty} v_{inc}(x,0)\ \exp(-\imath\ k_x\ x)\ dx \tag{2.89}$$

where $v_{inc}(x,z)$ is the particle displacement velocity of the field of the incident beam and $F(k_x)$ is the Fourier integral of the incident field at $z = 0$.
The Fourier integral (2.89) denotes the superposition of an infinite number of plane waves incident from water onto an austenitic weld with different amplitudes $F(k_x)$ but all having the same wavelength. However, their incidence angles are perturbed around the main beam incidence angle θ_{inc}. Reflected and transmitted beam profiles can be obtained by integrating over individual reflected or transmitted plane waves, respectively, which are dependent on the corresponding coefficients.
Rewriting equation (2.89) at an interface (z = 0) one obtains

$$v_{inc}(x,0) = \frac{1}{2\pi}\int_{-\infty}^{\infty} r(k_x)\ F(k_x)\ \exp(\imath\ k_x\ x)\ dk_x \tag{2.90}$$

Unlike in isotropic materials, in anisotropic austenitic weld metal three wave modes are excited, one quasi longitudinal, one quasi transverse, and one pure transverse wave. The reflectance or transmittance function, $r(k_x)$ or $t(k_x)$ is nothing but the reflection coefficient (or transmission coefficient) expressed as amplitude ratio between reflected (or transmitted) amplitude to that of the incident wave, with the transverse wave component (k_x) as a variable. This function can be derived from the equation 2.50. This function, however, for anisotropic material is lot more complicated than for isotropic material because of particle displacement deviation and consequently energy flow skewing as discussed in section 2.2.4 "Group velocity".
The integral (2.90) is solved numerically using the Gauss-quadrature relation for 64 points (Stroud et al. 1966 [32]).
At the boundary between solid and liquid half-spaces Rayleigh waves always exist (e. g. Viktorov 1967 [35]). But in anisotropic materials, the excitation of Rayleigh wave depends on the columnar grain orientation of the weld metal at the interface. Under certain conditions, the Rayleigh wave may not exist at all. Further, in anisotropic media the structure and properties of Rayleigh waves are more complicated than in isotropic media, there is no analytical expression for the phase velocity of Rayleigh waves and for the Rayleigh angle. Generally it is difficult to utilize Rayleigh waves for detecting surface or sub-surface defects in anisotropic materials due to the fact that the Rayleigh angle which is a function of grain orientation is difficult to determine. Nevertheless, the Rayleigh angle can be determined by varying the incidence angle around the supposed angle as demonstrated in fig. 2.22, which shows the particle displacement velocity (amplitude) $v_{inc}(x,0)$, equation (2.90), at incidence angles varying around the Rayleigh angle.

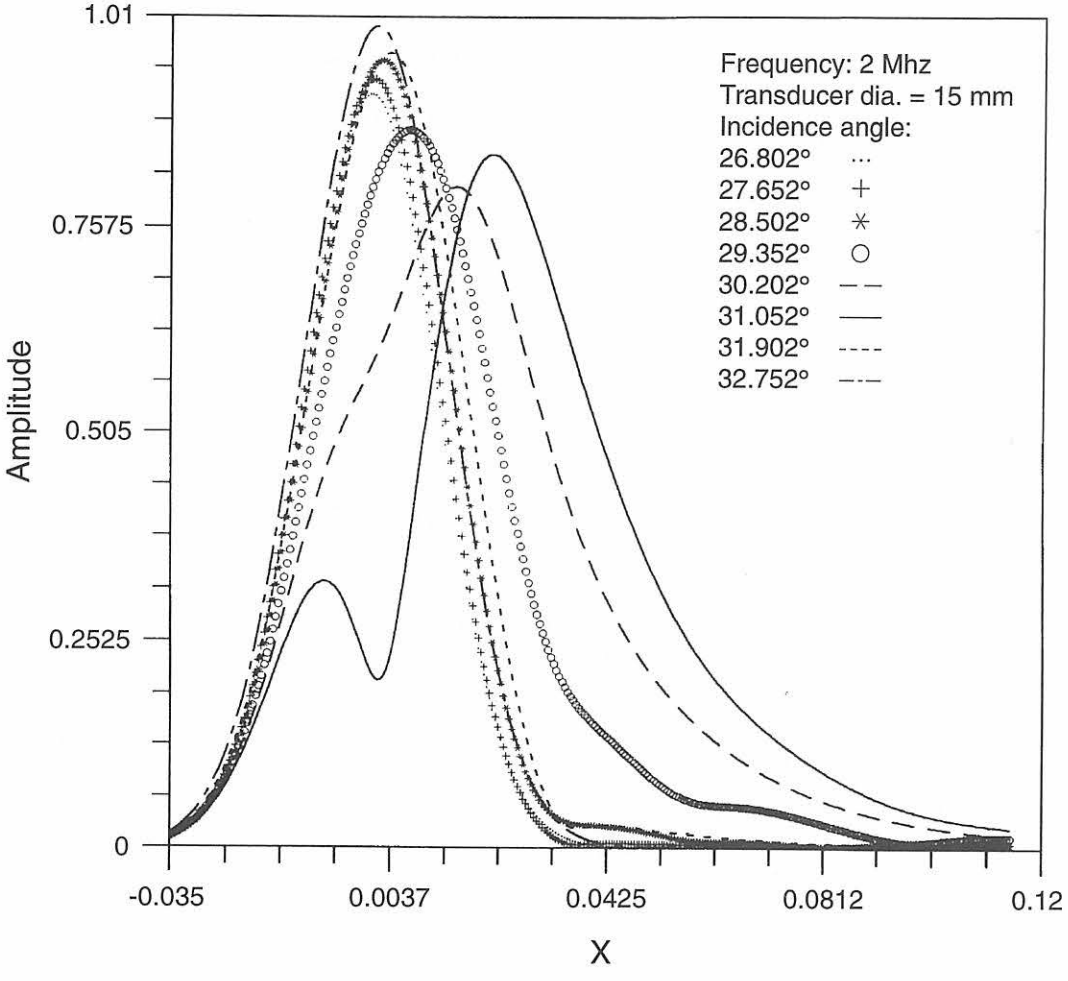

Figure 2.22: *Beam displacement: Profiles of the reflected longitudinal wave field due to a Gaussian beam incident at the water - austenitic weld metal interface. Incidence angle varying around the Rayleigh angle; grain tilt angle* $\Phi = 20°$ *and layback angle* $\Psi = 10°$*; ultrasonic frequency = 2 MHz; transducer diameter = 15 mm*

Chapter 3

Ray Tracing

3.1 Scheme of ray tracing

According to the results of the investigations on the structure of austenitic weld metal (section 1.1.4) for ultrasonic ray tracing in austenitic weld metal it is assumed that the weld metal can be modeled to be transverse isotropic. However, one has to take into account that the texture of the weld metal is not unidirectional.

The characteristic feature of the texture of different types of weld microstructure is modeled by the empirical relation given by Ogilvy 1985-90 [139]-[146]

$$\phi' = \arctan\left(\pm\frac{T'\,(D + z\,\tan\alpha')}{|x|^{\eta}}\right) \tag{3.1}$$

with (s. fig. 3.1)

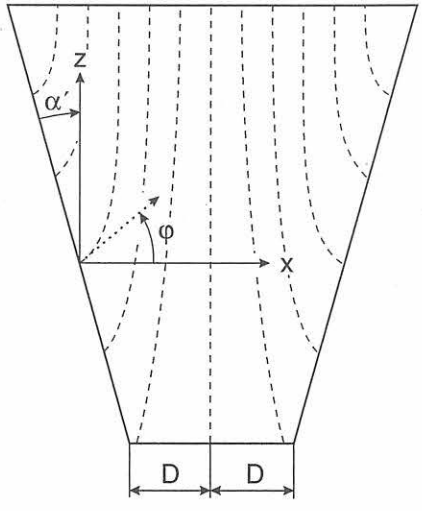

Figure 3.1: *Reference coordinate system and definition of parameters used to describe the texture of the weld*

ϕ' = Columnar grain angle measured with respect to the reference x-axis
D = Half width of the gap between root faces
T' = Measure of the slope of the columnar grain axis at the fusion faces
α' = Angle of bevel
η = Measure of the change of the grain orientation as a function of the distance x from the weld centre line, $0 \leq \eta \leq 1$

The ultrasound travels through the columnar grains each oriented differently than its adjacent neighbours. A fictitious grain boundary is assumed between every pair of grains for a given ray position. This is represented by the local coordinate system. The elastic

constants on both sides of the medium are transformed to this local coordinate system as described in the section 2.4. The boundary conditions (2.30, 2.31) are solved yielding the amplitude coefficients. The directions of energy flow (the group velocity directions) of the different wave types are calculated for each medium using the equation (2.22). The group velocity direction of the refracted ray of the wave type, for which the ray is traced, is stored in an array. This process is iteratively repeated for the wave type under consideration till the ray leaves the weld metal. The stored energy flow direction paths (group velocity direction) are mapped. Whereas this model satisfactorily predicts the sound path, the reflection and transmission coefficients calculated are of less significance, since the number of grain boundaries involved in the iterative process is fictitious.
Referring to fig. 3.2 the scheme of the ray-tracing procedure is as follows:

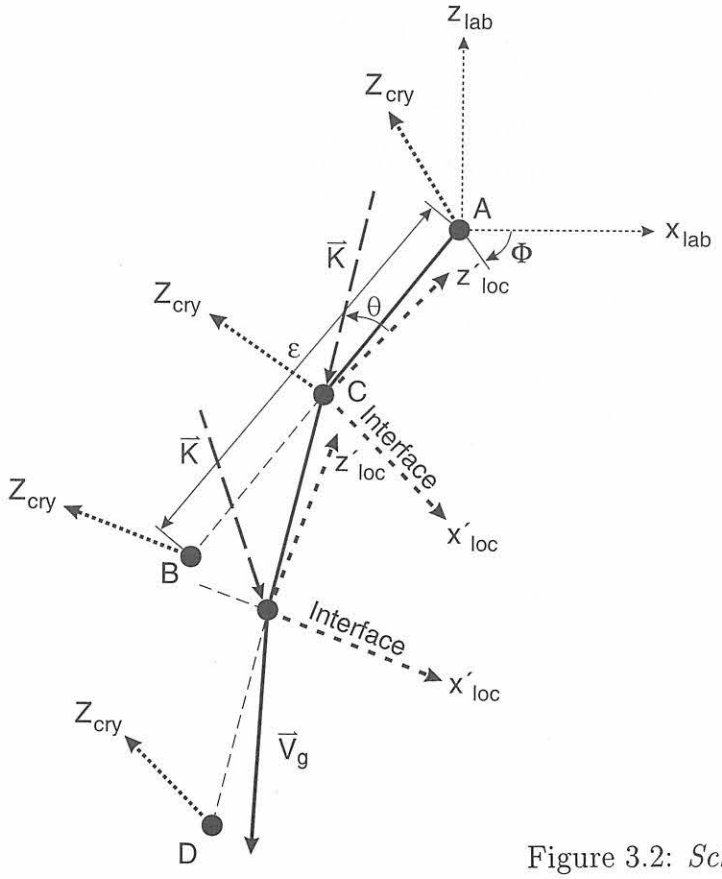

Figure 3.2: *Scheme of the ray tracing procedure*

- **A** is the position of the grain with Z_{cry} as the columnar grain direction determined by the empirical relation (3.1).
- **B** is the position of the grain at the end of the step with size ϵ in the group velocity direction[1] with the corresponding grain orientation Z_{cry}. It is assumed that the step crosses a grain boundary at $\frac{\epsilon}{2}$ denoted by **C**.
- After calculating the columnar grain orientations at positions **A** and **B** by equation (3.1) and determining the fictitious grain boundary crossed, the elastic constants are transformed (at point C between points A and B) to the local boundary

[1] ϵ is chosen to be small enough, so that smaller values do not influence the beam path

coordinate system $(x'_{loc}, y'_{loc}, z'_{loc})$ from the adjacent columnar grain crystallographic coordinate systems $(X_{cry}, Y_{cry}, Z_{cry})$ using the Bond matrix method (1943 [52]) as described by Auld 1990 [3]. x'_{loc}, y'_{loc} is the interface. y'_{loc} lies in the plane $\perp$ to the paper plane and is not shown.

- The components of the wave vectors tangential to the boundary in both media have to be equal and contained in the plane of incidence, see equation (2.43). Consequently, the components of all wave vectors perpendicular to the boundary generally differ.
- Since the x- and y-components of the wave vectors $\mathbf{K}$ are the input parameters, the Christoffel equation can be written as a polynomial of sixth degree with the z-component as the variable. This is solved numerically which yields six solutions for each medium, see section 2.3.
- The valid roots are determined by the group velocity directions as described in section 2.3.
- The group velocity direction of the refracted wave of interest is selected. Another step with size ϵ is taken in this direction from the position **C**.
- **D** is the position at the end of the step with size ϵ in the group velocity direction in the adjacent grain with local texture orientation Z_{cry}. Again it is assumed that the step crosses a grain boundary at $\frac{\epsilon}{2}$.
- The iteration is continued as shown in fig. 3.2 till the wave leaves the weld specimen and the stored group velocity directions are plotted[2].

3.2 Results and Discussion

Results for quasi longitudinal, quasi transverse and pure transverse waves (Munikoti et al. 1994-99 [114, 116, 118, 126]) are presented for different

- incidence angles
- transducer positions
- microstructures (textures).

To simulate a beam, seven rays are assumed to be generated at the probe index point. The divergence of the rays increases (decreases) by one degree steps with respect to the central ray direction.

Since the energy flow direction (direction of group velocity) is skewed with respect to the wave vector direction, ray paths in the figures are three dimensional in nature. For the sake of simplicity, two dimensional projections (side view and top view) are shown.

Beam paths of quasi longitudinal and pure transverse waves (fig. 3.3 and figs. F.1 - F.3 in Appendix F) are generally more straightforward than the paths of quasi transverse waves. However, it can be observed that beam paths are generally highly sensitive to the weld texture.

[2]The ray tracing code is written in FORTRAN 77 with graphics integrated. Efforts are underway to implement this software to a robotic inspection system, UltraSIM [66], of FORCE Institute, Denmark. This is a P-Scan based 3D robotic system for automated ultrasonic inspection of complex objects.

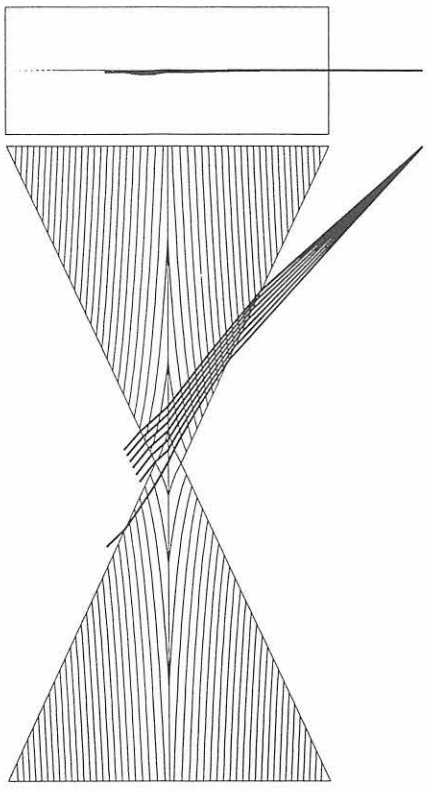

qL 45°

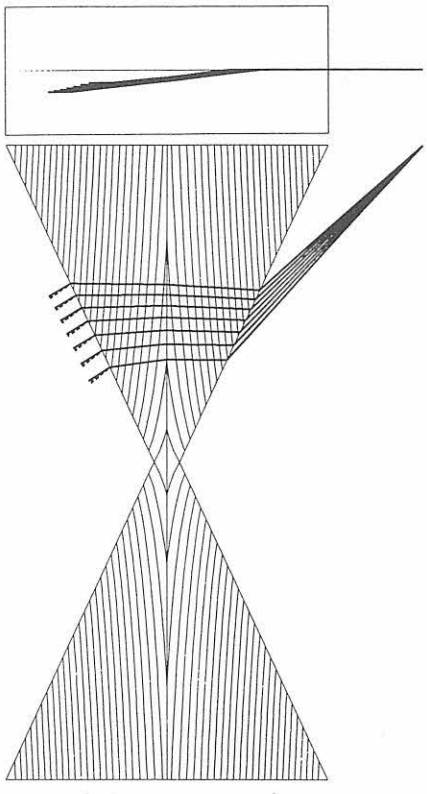

qT1 45°

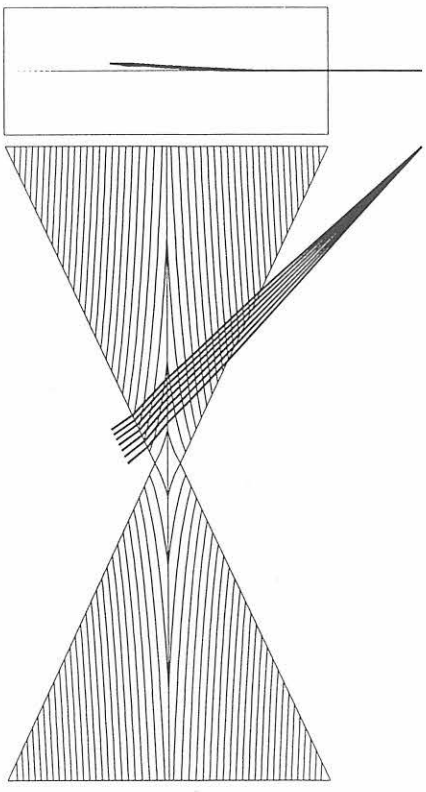

T2 45°

Figure 3.3: *Beam path (group velocity direction) of quasi longitudinal (qL), quasi transverse (qT1), and pure transverse (T2) waves calculated three-dimensionally (side-view and top-view). Stiffness constant matrix of the austenitic weld metal s. page 49. Incidence angle = 45°. Weld thickness = 25 mm. Angle of bevel $\alpha' = 25°$. Gap between root faces $D = 1$ mm. $T' = 4.0$, $\eta = 0$, s. equation 3.1 (Munikoti et al. 1994-99 [114, 116, 118, 126]*

This is due to the form of the slowness surfaces. The slowness surface of the quasi transverse wave exhibits concave and convex areas with cusps which results in largely varying group velocity (energy flow) directions and ray splitting.

When the quasi transverse wave is incident obliquely at the parent-weld metal interface, for a particular angle of incidence, the transmitted quasi longitudinal wave may not be propagating (evanescent). Then, due to the energy balance criterion discussed in the chapter 2 (section 2.3.2) the incident energy would be redistributed to the other propagating waves. Under these conditions there are two quasi transverse waves and one pure transverse wave propagating. The two quasi transverse waves, however, have different phase velocities, polarization directions and energy contents, fig. 3.4.

At every iterative step, there could be two quasi transverse waves branches, one with higher energy than the other. In this work both the possible rays have been traced. If the ray paths of both the quasi transverse waves are not significantly apart, then at the receiving end of the transducer, both the waves could *interfere* making it experimentally difficult to identify the waves, see fig. 3.3 and figs. F.1 - F.3.

Although the ray tracing model neglects some of the more complex conditions of sound propagation in anisotropic weld metal, such as

- in practice ultrasound is emitted from an emitter of finite dimension as a pulse, whereas the model considered assumes a plane wave consisting of a single ray,
- the grain boundaries are considered to be planar and smooth,
- the individual grain geometry is not considered, instead the whole weld metal is assumed to be a polycrystalline material with transverse isotropic symmetry[3],

the prediction of the precise ray path in the weld metal depends very much on the weld model itself. Since an empirical formula is used to determine the texture orientation which does not consider the actual weld parameters and solidification mechanics, it might not exactly represent the actual micrograph. Therefore only the ray path *trend* can be predicted which is only a qualitative information. Nevertheless this qualitative information is in good agreement with the corresponding theoretical predictions of sound propagation direction by the elastodynamic finite integration technique (EFIT) (Marklein et al. 1995 & 1997 [104, 105]).

[3]The reason for modeling the columnar grained structure of the weld metal as transverse isotropic has been substantiated in section 1.1.4

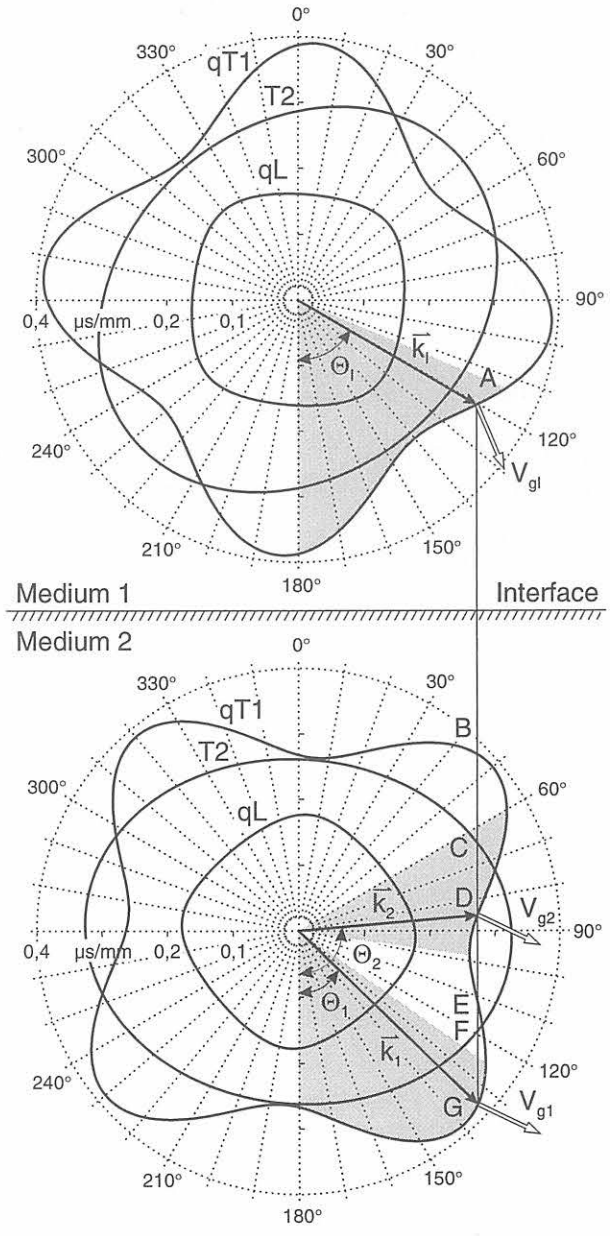

Figure 3.4: *Graphical construction to demonstrate the excitation of two refracted quasi transverse waves at the boundary between adjacent austenite grains with different crystallographic orientations (grain tilt in the plane of incidence and grain layback is assumed), e. g. Auld 1990, Neumann 1995 [3, 25]. Continuity of the components of the coplanar slowness vectors* $\frac{k_{tan}}{\omega}$ *of incident (from medium 1), reflected (not shown here), and refracted waves (into medium 2) tangential to the boundary directly yields the intersections (B - G) with the slowness surfaces of both adjacent media determining slowness vectors* $\frac{\mathbf{k}}{\omega}$ *and group velocity* $\mathbf{V}_g$ *directions of reflected and refracted waves. Due to* $\mathbf{V}_g = \frac{\partial \omega}{\partial \mathbf{k}}$ *the group velocity is perpendicular to the slowness surface. However, reflected and refracted waves only propagate, if their group velocities are bent away from the boundary, Henneke 1972 [76] (D and G in the case of the quasi transverse wave). In the present case there is no intersection with the qL-slowness surface in medium 2, the qL-wave is evanescent. Besides the two refracted qT1-waves (with permissible sectors of the slowness surface shaded) the T2-wave (intersection F, however, wave vector and group velocity direction not shown here) also is excited by the qT1-wave, see section D.4.*

Chapter 4

Scattering of ultrasound

4.1 Theoretical background

As pointed out in chapter 3 the ray tracing model satisfactorily predicts the sound path (energy flow direction), whereas the scattering coefficients calculated are of no significance, since the numerous (fictitious) grain boundaries involved in the iterative process do not represent a realistic weld. Additionally to predict attenuation of the sound beam due to multiple scattering at grain boundaries other models are needed. Sound attenuation by scattering as a function of texture direction and frequency is treated in this chapter.

As described in section 1.1, the weld metal consists of grains having discrete shape and crystalline structure, macroscopically exhibiting transverse isotropic property. Since in anisotropic materials the elastic properties are functions of the direction within the medium, the wave propagation in such materials shows "anisotropic" character viz., quasi nature of waves, associated polarization, and beam skewing as described in chapter 2. Furthermore, an ultrasonic wave traveling in such an inhomogeneous medium undergoes multiple reflection, transmission, and mode conversion (subsumed as scattering) at grain boundaries and, therefore, the ultrasound beam gets attenuated. Grain scattering depends on:

1. elastic anisotropy of the grains,
2. geometric features of the grains,
3. grain boundaries.

Therefore these properties have to be incorporated in the theoretical modeling.

In materials without texture the crystallographic axes of the grains are randomly oriented, so that statistically all directions are equally probable. Modeling of such material can be achieved, e. g., by assuming spherically shaped grains. But the case, which will be discussed here, is the material with texture, where not all crystallographic axes are randomly oriented. Texture can be induced by columnar grain growth in austenitic weld metal, see section 1.1, or during rolling and other similar manufacturing processes.

The unified model on elastic wave propagation in polycrystalline materials as proposed by Stanke and Kino 1984 [177, 178] will be used and extended to austenitic weld metal, an anisotropic, polycrystalline material with cylinder-symmetric texture.

4.2 Theory

4.2.1 The stochastic wave equation

The particle displacement of the field $u_k = p_k \exp\left(-\imath\, \vec{\beta}.\mathbf{r}\right)$ associated with the propagation of an plane elastic wave through a polycrystalline medium is governed by the stochastic wave equation given by Stanke and Kino:

$$\left[\Gamma_{ik} - \rho\, \frac{\omega^2}{\beta_t^2}\, \delta_{ik}\right] [v_k] \;=\; 0 \tag{4.1}$$

where

$$\Gamma_{ik} = \left[C^v_{ijkl} + \epsilon \left\langle \Delta^\xi_{ijkl} \right\rangle - \epsilon^2 \left\{ \left\langle \Delta^\xi_{ijmn} \Delta^\xi_{opkl} \right\rangle - \left\langle \Delta^\xi_{ijmn} \right\rangle \left\langle \Delta^\xi_{opkl} \right\rangle \right\} \times \int_v G_{mo}(\mathbf{r}) \left\{ W(\mathbf{r})\; e^{-\imath\, \mathbf{r}\cdot\vec{\beta}} \right\}_{,np} \right] n_j n_l$$

$$\vec{\beta} = \beta_t\, \mathbf{l}$$
$$\beta_t = k - \imath\alpha$$

The wave propagation is assumed to be along the z direction of the reference coordinate axis. Then the indices $j, l = 3$, viz. the components of the unit wave vector $= \{0, 0, 1\}$. Therefore the equation 4.1 can be written as:

$$\Gamma_{ik} = C^v_{i3k3} + \epsilon \left\langle \Delta^\xi_{i3k3} \right\rangle - \epsilon^2 \left\{ \left\langle \Delta^\xi_{i3mn} \Delta^\xi_{opk3} \right\rangle - \left\langle \Delta^\xi_{i3mn} \right\rangle \left\langle \Delta^\xi_{opk3} \right\rangle \right\} \times I_{monp} \tag{4.2}$$

$$I_{monp} = \int_0^\infty \int_0^\pi \int_0^{2\pi} G_{mo}(\mathbf{r}) \left\{ W(\mathbf{r})\; e^{-\imath\, \mathbf{r}\cdot\vec{\beta}} \right\}_{,np} r^2 \sin\theta\; d\,\phi\; d\,\theta\; d\,r \tag{4.3}$$

where $r^2 \sin\theta$ is the volume element of the spherically shaped grain.

The definitions of the terms in the stochastic wave equation (4.1) are given explicitly in appendix G.

The task is to determine k (wavenumber) and α (attenuation coefficient).

The solution to the Christoffel equation (2.2) has been treated in section 2.2. The eigenvalues of the matrix correspond to the phase velocities and the eigenvectors to the particle displacement velocities. For a given crystal system, there are three real eigenvalues and corresponding eigenvectors. In the case of the modified Christoffel equation (4.1) the eigenvalues are complex, the real part of which corresponds to the phase velocities and the imaginary part to the attenuation of the waves. Also, the eigenvectors are complex describing elliptical polarization (Fedorov 1968 [15]).

The first term of Γ_{ik} in equation (4.1) represents the Voigt's average elastic constants describing the elastic isotropy condition.

The second term which is a first order term in ε represents the one-point averages. At this stage, the solutions to equation (4.1) do not yet predict attenuation, but treat the material as a mono-crystal with transverse isotropic symmetry.

The second order term in ε includes the effects of frequency and grain shape (equiaxial or elongated) which yields attenuation by scattering.
The volume integral involving steady state Green's function (equation 4.3) contains the inverse autocorrelation function $W(\mathbf{r})$, which describes the grain shape. If the grains are equiaxed, e. g. are spherically shaped grains, having all the same average grain diameter to height ratio: $\frac{\overline{d}}{h} \to 1$, then $W(\mathbf{r})$ is replaced by $W(r)$[1].
On the other hand, when the grains are elongated in the growth direction, forming columnar grains as discussed in section 1.1, so that $\frac{\overline{d}}{h} \neq 1$, a "shape function" has been developed empirically by Ahmed et al. 1984 [40] and Hirsekorn 1988 [86]:

$$W(\mathbf{r}) = e^{-\frac{r}{l}\sqrt{1+\left[\left(\frac{\overline{d}}{h}\right)^2-1\right]\cos^2\theta}} \tag{4.4}$$

It can be easily seen that as $\frac{\overline{d}}{h} \to 1$ the correlation function for equiaxed grains is got back.

4.2.2 Method of solution to the stochastic wave equation

To solve the equation (4.1) the following assumptions are made:

- The grains have cubic symmetry, which can be expressed as:

$$C_{ijkl} = C_{12}\left(\delta_{ij}\delta_{kl}\right) + C_{44}\left(\delta_{ik}\delta_{jl} + \delta_{il}\delta_{jk}\right) + A\, a_{ni}\, a_{nj}\, a_{nk}\, a_{nl}$$

  $A = C_{11} - C_{12} - 2\,C_{44}$ is the anisotropy factor.

  The transformation matrix (or rotation matrix) $\mathbf{a} = a_{ik}$ is given in appendix G.

  The medium is single phased and polycrystalline. The polycrystalline medium however, exhibits a texture behaving macroscopically transversely isotropic. Therefore, the weld metal in the calculations is treated to have transverse isotropic symmetry.

- The anisotropy of the weld metal is treated as perturbation of the isotropic material status in the second order approximation. The perturbation parameter ε, which specifies the level of the microscopic inhomogeneities in elastic constants, is small, viz. $\varepsilon \ll 1$. This is the fundamental assumption for Keller's approximation. It is in principle arbitrary since only the product $\varepsilon\, \Delta_{ijkl}$ appears in the stochastic equation. It has been defined as root mean square variation in the propagation constant of the dominant mode, Stanke 1983 [177]:

$$\varepsilon^2 = \frac{\left\langle \left[\Re(\beta_t(\mathbf{r})) - k_0\right]^2 \right\rangle}{{k_0}^2} \tag{4.5}$$

  (subscript t can be qL, qT1 or T2) or in terms of effective elastic constants

$$\varepsilon^2 \approx \frac{1}{4}\frac{\left\langle \left[C_{IJ}(\mathbf{r}) - C^0_{IJ}\right]^2 \right\rangle}{{C^0_{IJ}}^2} \tag{4.6}$$

[1] $\overline{d}$ corresponds to the average cord or segment length $\overline{L}_s$ measured by the interrupted segment method according to DIN 50601

where $\Re(\beta_t)$ are the wave numbers of the type of wave under consideration in the presence of scattering and k_0 is the wave number of the corresponding wave in the absence of scattering, i. e. in isotropic material.

ε is considered for the indices $I, J = 3$, which means that wave propagation is in the z-direction, and for the layback angle $\Psi = 0°$, which means that wave propagation is in the meridian plane.

Using equation (G.3) together with equation (G.11), equation (4.6) yields:

$$\epsilon^2 = \frac{1}{4} \frac{A^2 \ (4449 + 2840 \ \cos 2\,\Phi + \cos 4\,\Phi + 2600 \ \cos 6\,\Phi + 2475 \ \cos 8\,\Phi)}{102400 \ C_{33}^{0\ 2}} \tag{4.7}$$

where Φ is the columnar grain tilt angle in the meridian plane. The function (4.7) is evaluated for the grain tilt angle range $0° \leq \Phi \leq 90°$, fig. 4.1.

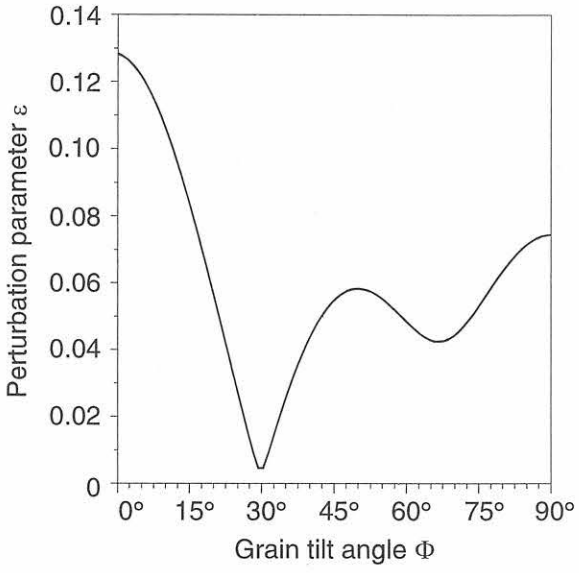

Figure 4.1: Perturbation parameter ε as a function of the columnar grain tilt angle in the meridian plane, corresponding to the direction of wave propagation in the meridian plane

It can be concluded that the condition $\varepsilon \ll 1$ is fulfilled.

- The Green's function for isotropic media, as given by Lifshits and Parkhomovski [99], Gubernatis 1977 [71], Mura 1987 [22], has beeen used.

The texture of the weld metal may exhibit layback (by the angle Ψ with respect to the z-axis of the laboratory system x, y, z) in the direction of welding and bending (by the angle Φ) in the direction perpendicular to it. Therefore the grain axis Z is generally not contained in the plane of ultrasound incidence.

Since the weld metal texture has transverse isotropic symmetry the associated (complex) eigenvalues of equation (4.1), which includes attenuation by scattering, are also rotational symmetric, it therefore would have been principally sufficient to calculate the (complex) eigenvalues and (complex) eigenvectors in the meridian plane. However, to determine attenuation for an arbitrarily oriented columnar grain texture (described by the angles Ψ and Φ) it is more convenient to solve equation (4.1) three-dimensionally.

Only normal incidence of sound is assumed. However, varying Φ and Ψ, this is no loss of generality since all directions of propagation are covered by this.
It has to be emphasized moreover, that no restrictive assumptions are made with respect to the polarization direction of waves, viz. polarization deviation is taken into account stringently.

4.2.2.1 Symbolic evaluation

In the stochastic wave equation (4.1) the indices $j, l = 3$, which mean the direction of propagation, are assumed to be in the direction of the z axis of the laboratory coordinate system.
The one-point averages and the two-point averages along with the integral containing Green's function are evaluated symbolically[2].

4.2.2.1.1 One point averages: The term $\left\langle \Delta^{\xi}_{ijkl} \right\rangle$ in equation (4.1) is evaluated with indices $j,\ l = 3,\ i,\ k \rightarrow 1 \cdots 3$.

4.2.2.1.2 Two point averages: The term

$$\left(\left\langle \Delta^{\xi}_{ijmn} \Delta^{\xi}_{opkl} \right\rangle - \left\langle \Delta^{\xi}_{ijmn} \right\rangle \left\langle \Delta^{\xi}_{opkl} \right\rangle \right) I_{monp}$$

in equation 4.1, where I_{monp} is the Green's integral (4.3), is evaluated with the indices $j,\ l = 3,\ i \rightarrow 1 \cdots 3$ and $m, n, o, p \rightarrow 1 \cdots 3$.
From the total of the two point averages the indices m, n, o, p of the 21 non-zero terms are:

Indices for m,n,o,p					
1	1,1,1,1	8	1,2,2,1	15	3,1,1,3
2	2,2,2,2	9	2,1,1,2	16	3,3,1,1
3	1,2,1,2	10	2,2,1,1	17	3,2,2,3
4	2,1,2,1	11	1,1,3,3	18	3,3,2,2
5	1,3,1,3	12	1,3,3,1	19	3,1,3,1
6	2,3,2,3	13	2,2,3,3	20	3,2,3,2
7	1,1,2,2	14	2,3,3,2	21	3,3,3,3

4.2.2.1.3 Green's integral: The procedure to evaluate Green's integral (4.3) in the equation (4.1) is shown in the flow chart fig. 4.2.
Green's integral I_{monp} is evaluated for the following indices:

$$I_{1111} = I_{2222} \tag{4.8}$$
$$I_{1122} = I_{2211} \tag{4.9}$$
$$I_{1133} = I_{2233} \tag{4.10}$$
$$I_{1212} = I_{1221} = I_{2112} = I_{2121} \tag{4.11}$$
$$I_{1313} = I_{1331} = I_{2323} = I_{2332} = \quad I_{3113} = I_{3131} = I_{3223} = I_{3232} \tag{4.12}$$
$$I_{3311} = I_{3322} \tag{4.13}$$
$$I_{3333} \tag{4.14}$$

[2]The commercially available software *Mathematica 3.0* [36] is used.

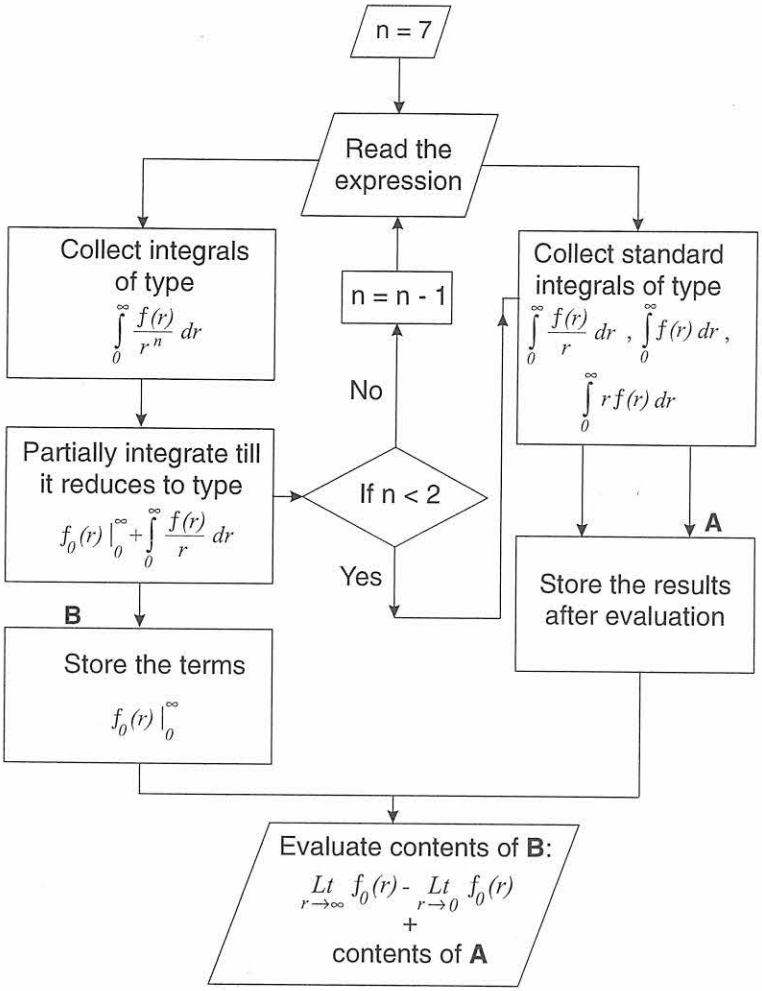

Figure 4.2: Flow chart for evaluating Green's integral

Due to the symmetry of the Green's function this task gets reduced to evaluation of seven integrals.
The symbolic computation of the Green's integral is as follows:

1. First it is integrated with respect to the polar angles θ and ϕ and then the r-integral is evaluated.

   The types of terms found after the angle integration are as follows, fig. 4.2:

   - Type 1: Terms free of the term r in the denominator. This type has the form

     $$\int_0^\infty f(r), \int_0^\infty r\, f(r)$$

     where $f(r)$ is of type $\exp(-a\,r)\ \sin b\,r$, $\int_0^\infty \exp(-a\,r)\ \cos b\,r$
   - Type 2: Terms of the type

     $$\int_0^\infty \frac{f(r)}{r}$$

   - Type 3: Terms containing $\int_0^\infty \frac{f(r)}{r^n}$, where the order of singularity $n = 7$.

4. The remaining terms of Green's integral are evaluated by taking the limits:

$$\lim(f(r))|_0^\infty$$

The sum of the results of type 1, 2 and 3 yields the required complex transcendental equation in symbolic form.

The standard integrals arising in the evaluation of Green's integral are given in appendix G (Gradshteyn 1965 [16] [3]).
However, the symbolic computation has been possible only for the case of equiaxed grains. In the case of elongated grains, where the inverse autocorrelation function (4.4) has to be used, the evaluation process has to be reversed, viz. 'r'-integration is carried out in the first step. The resulting expression must be evaluated numerically. All the standard integrals arising in evaluating this case are given in appendix G.

4.2.2.2 Numerical evaluation

From symbolic computation of the stochastic wave equation a $[3 \times 3]$-matrix is obtained as a function of the complex propagation constant β_t. The resulting characteristic equation, a univariant complex transcendental equation, is solved numerically[4]. To find the zeros of the equation Müller's method in addition to a method based on inverse quadratic interpolation is applied (Engeln-Müllges et al. 1987 [13], collected algorithms from CACM [54]). The zeros located in the vicinity of the wavenumber in the absence of scattering are determined. A valid root is selected such that the difference between the wave number with scattering and without scattering is minimum. Further, in case of transverse waves, for the valid roots, polarization directions (eigenvectors) are determined. Based on the polarization directions the roots are assigned.

4.3 Results and discussion

4.3.1 Attenuation

Attenuation coefficients[5] have been calculated (Munikoti et al. 1998-99 [117, 118]) as a function of

- wave vector to Z-direction of the crystallographic system X, Y, Z, which is generally composed of layback in the welding direction by an angle Ψ and grain tilt in the perpendicular plane by an angle Φ,
- frequency,
- grain shape parameter $\frac{\overline{d}}{h}$. [6]

[3] Reportedly some standard definite integrals (**not used in this work**) are printed wrongly. The correct forms can be found at *http://www.mathsource.com/Content/Publications/Other/0205-557*

[4] The computer code for evaluation is written in FORTRAN 77 which uses mathematical routines from the commercially available "International Mathematical Society Library" (IMSL).

[5] Material elastic constants have been chosen for an austenitic CrNi 18 12 stainless steel as given by Bradfield 1964 [53]: $C_{11} = 2.16$, $C_{12} = 1.45$, and $C_{44} = 1.29\,[10^{11} N/m^2]$.

[6] $\overline{d}$ corresponds to the cross-section of the grain, also in the case of elongated grains

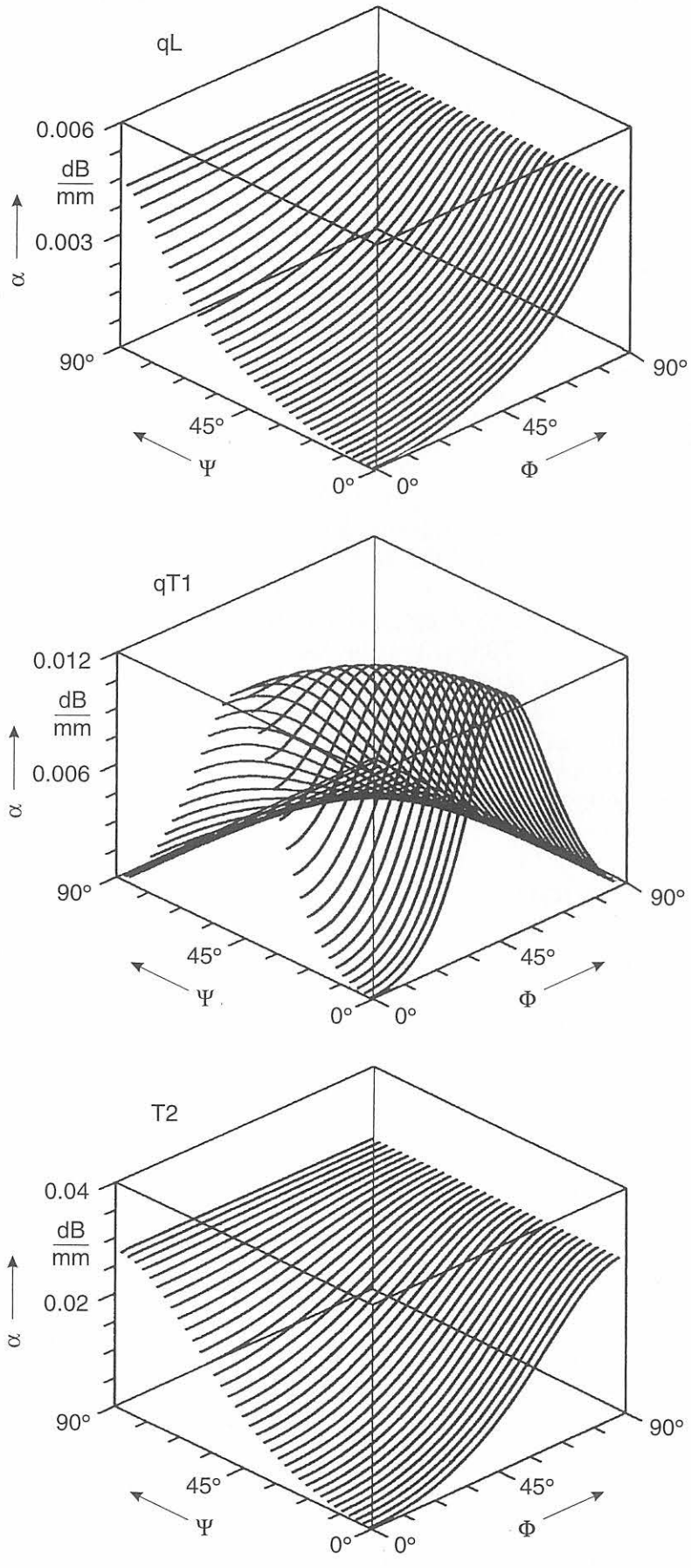

Figure 4.3: *Attenuation coefficients of the three wave modes qL, $qT1$, $T2$ as a function of the grain orientation.*
Grain shape: equiaxed,
grain size $\overline{\mathbf{d}} = 100\ \mu\mathbf{m}$,
Frequency: 2 MHz
(Munikoti et al. 1998-99 [117, 118])

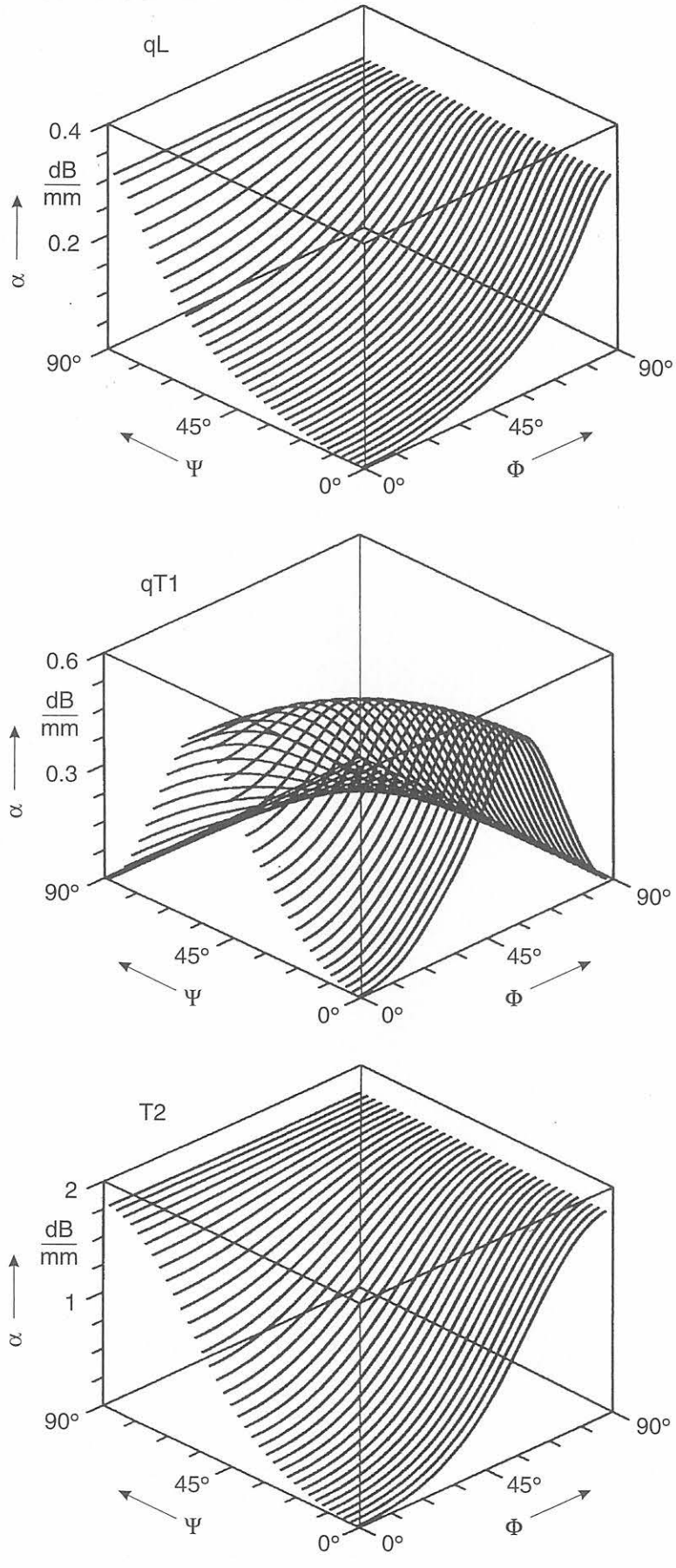

Figure 4.4: *Attenuation coefficients of the three wave modes qL, $qT1$, $T2$ as a function of the grain orientation.*
Grain shape: equiaxed,
grain size $\overline{d} = 800\ \mu m$,
Frequency: 2 MHz
(Munikoti et al. 1998-99 [117, 118])

4.3.1.1 Dependence on propagation direction

The attenuation coefficients of the three wave modes as a function of the wave vector to Z-direction of the crystallographic system X, Y, Z are shown in figs. 4.3 and 4.4.

Attenuation of the quasi longitudinal wave has been measured in the meridian plane of columnar grained austenitic cast X 5 CrNi 18 10 and Ni-based weld metal NiCr 19 Nb (Ernst et al. 1999 [60] - [62], Seldis 1999 [169], Panetta et al. 1998 [148]). The meridian plane is characterized by the layback angle = 0°. Taking into account, that according to metallurgical investigations of these specimens (s. section 1.1.1) the average grain size is measured in the range between 0.5 mm and 3 mm, the agreement between measured attenuation coefficients (fig. 4.5) and theoretical predictions (figs. 4.3 and 4.4.) is satisfying.

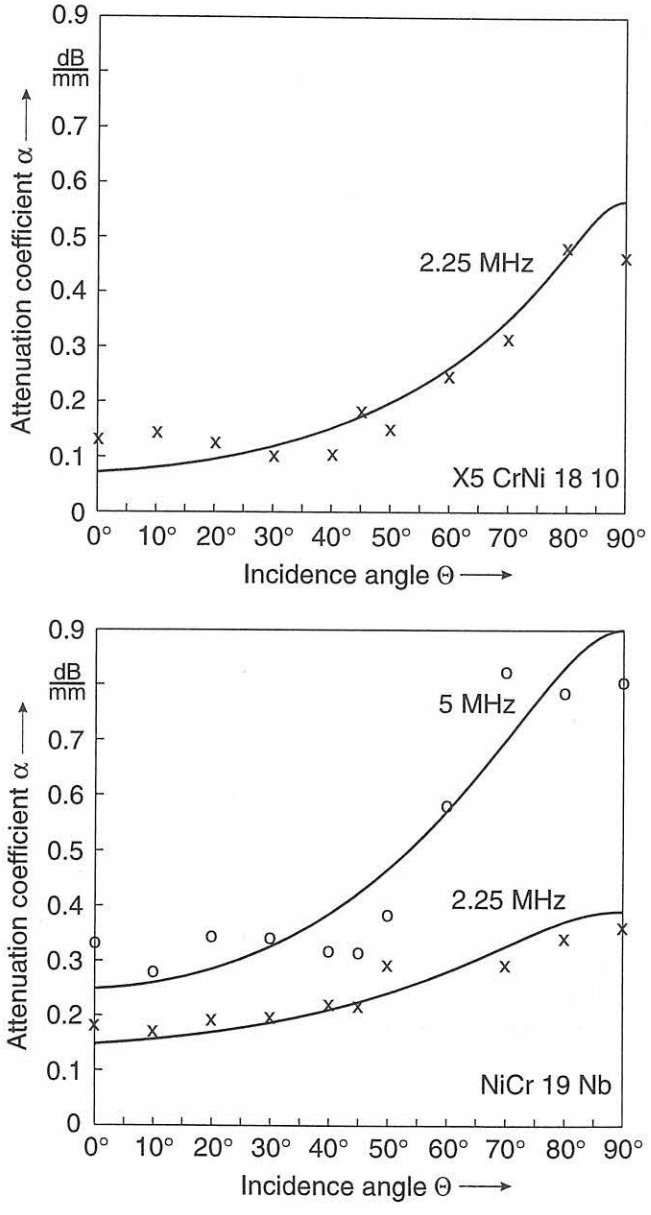

Figure 4.5: *Attenuation coefficients of the quasi-longitudinal wave qL as a function of the wave vector to columnar grain direction angle Θ measured on austenitic weld metal specimens which have been cut in the meridian plane (Ernst 1999 [62]).*

The measured attenuation coefficient deviates from the theoretical prediction at low wave vector to grain angles Θ. This is due to deviations of the columnar grains in the austenitic weld specimens from parallel alignment which yields already theoretically attenuation

larger than zero.

Whereas for quasi-longitudinal and pure transverse waves attenuation theoretically vanishes when propagating in the columnar grain direction and reaches a maximum when propagating perpendicular to the columnar grain direction for the quasi transverse wave maximum attenuation is occurrs at about 45° and both, at normal incidence and at 90°, no attenuation is predicted.

Moreover, it is noteworthy that attenuation of the quasi transverse wave is comparatively lesser than for quasi longitudinal and pure transverse waves. This has also been experimentally validated (e. g. Neumann 1995 [25]). Therefore it is not attenuation that renders the quasi transverse wave inappropriate for austenitic weld testing. It is rather because of the beam splitting this wave type undergoes in austenitic weld metal, s. chapters 2 and 3.

Certain observations concerning coherence of wave vector and polarization on the one hand and attenuation on the other hand are summarized in table 4.1.

Relative to texture	Attenuation		
	Wave mode		
	qL	qT1	T2
$k \parallel p \parallel$	Min	———	———
$k \parallel p \perp$	———	Min	Min
$k \perp p \perp$	Max	Min	Max
$k \perp p \parallel$	———	Min	———
$k <$ $p <$	Interm.	Max	Interm.

Table 4.1: *Dependence of attenuation on wave vector (k) and polarization direction (p) (Munikoti et al. 1998-99 [117, 118])*

4.3.1.2 Dependence on frequency

The unified theory yields unique results of calculation of attenuation for all frequency ranges, viz. subdividing analysis of attenuation into Rayleigh region, stochastic region, and geometric region is no longer necessary.

The grain tilt in the example of figs. 4.6 and 4.7 is restricted to the meridian plane, which is the propagation plane (grain angle Φ varying between 0° and 90°). However, the frequency dependence of the attenuation coefficient can be calculated for each grain tilt composed of the grain angle Φ in the YZ-plane and the layback angle Ψ in the XZ-plane, see also section 4.2.2. As an example for this an incidence plane with a layback angle $\Psi = 20°$ being typical for austenitic welds has been chosen, fig. 4.8.

The figs. 4.6 - 4.8 are incorporating the three frequency regions of ultrasonic scattering (e. g. Hecht 1986 [75]):

- Rayleigh region: $0.02 \leq \frac{\bar{d}}{\lambda} \leq 0.2$
- stochastic region: $\frac{\bar{d}}{\lambda} \approx 1$
- $\frac{\bar{d}}{\lambda} \gg 1$

Generally, attenuation by scattering reaches a high level with $\frac{\bar{d}}{\lambda}$ increasing, becomes independent on $\frac{\bar{d}}{\lambda}$ in the stochastic region though on a high level and decreases in the geometric region.

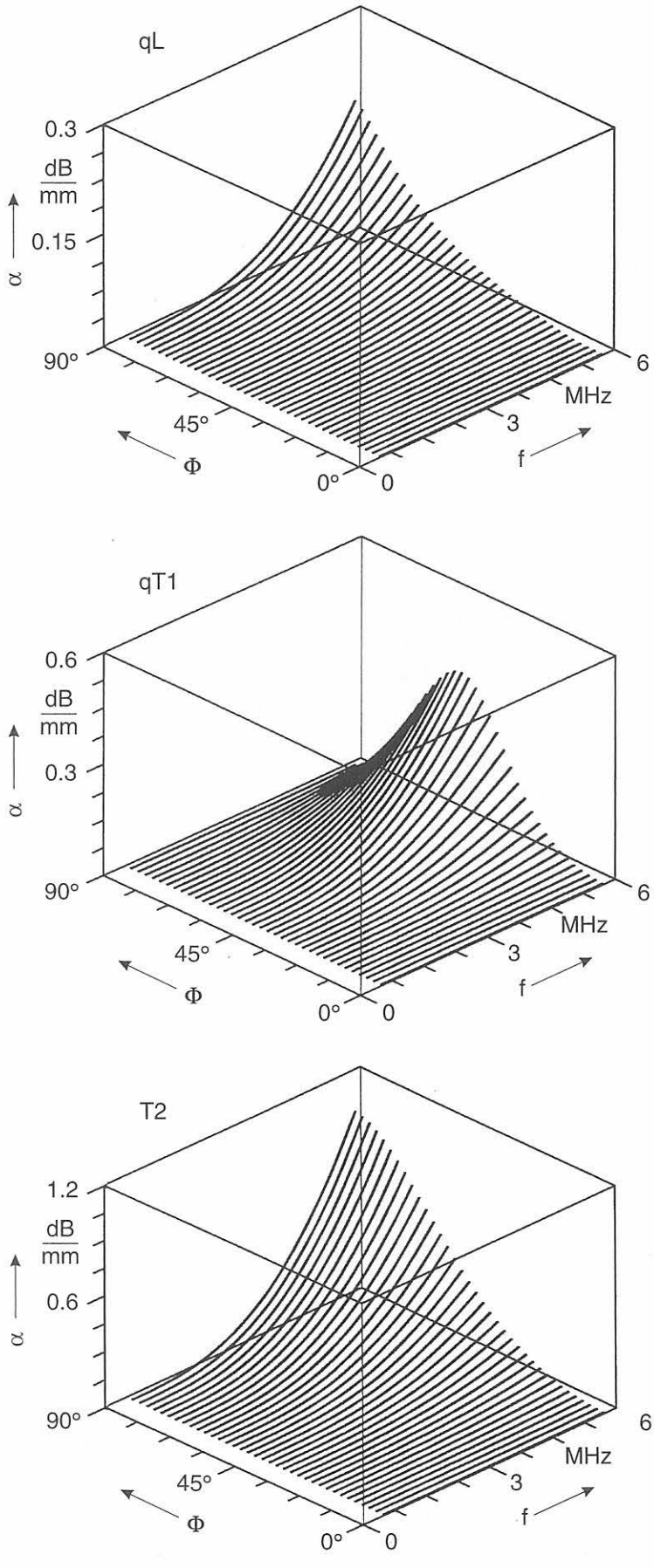

Figure 4.6: *Attenuation coefficients of the three wave modes qL, $qT1$, $T2$ in the* **meridian plane** *as a function of frequency and grain angle.*
Grain shape: equiaxed, **grain size** $\overline{\mathbf{d}} = \mathbf{100}\ \boldsymbol{\mu}\mathbf{m}$, *(Munikoti et al. 1998-99 [117, 118]).*

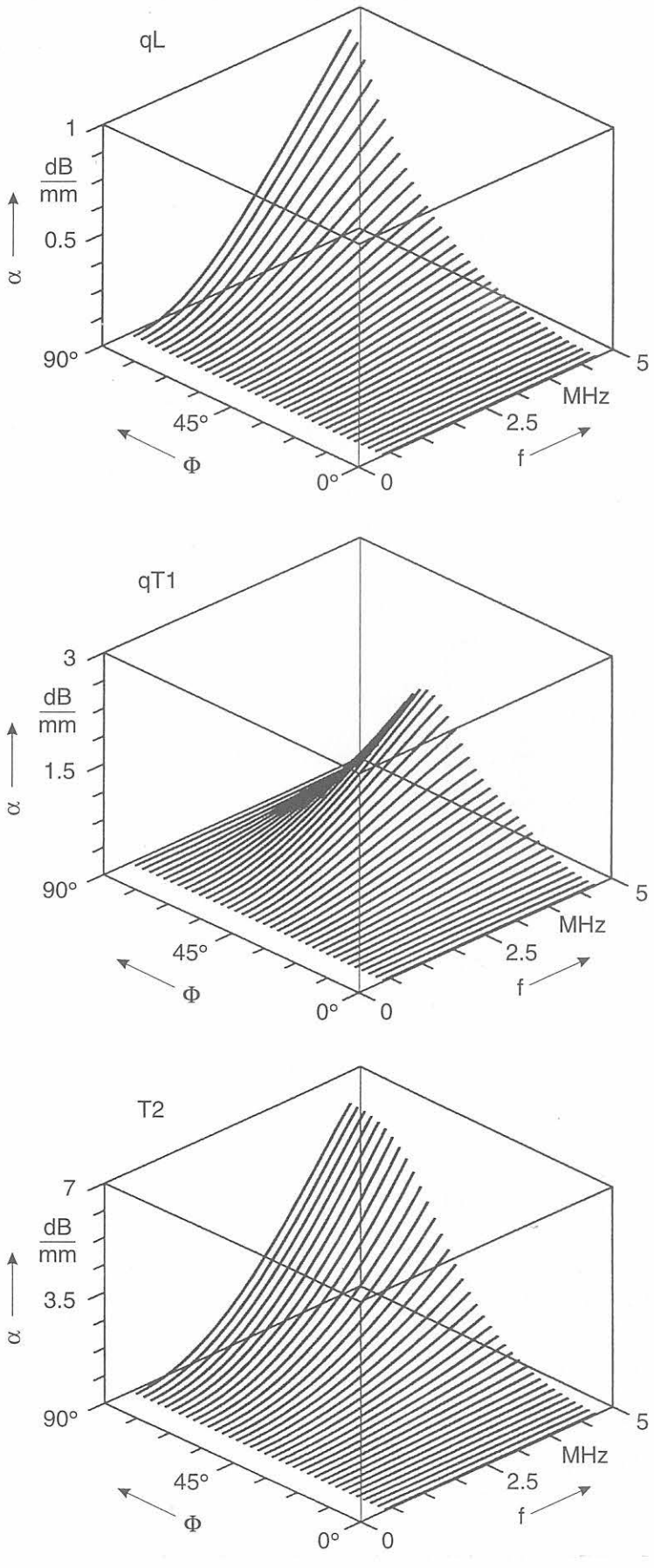

Figure 4.7: *Attenuation coefficients of the three wave modes qL, qT1, T2 in the* **meridian plane** *as a function of frequency and grain angle.*
Grain shape: equiaxed, **grain size** $\overline{\mathbf{d}} = \mathbf{500}\ \mu\mathbf{m}$ *(Munikoti et al. 1998-99 [117, 118]).*

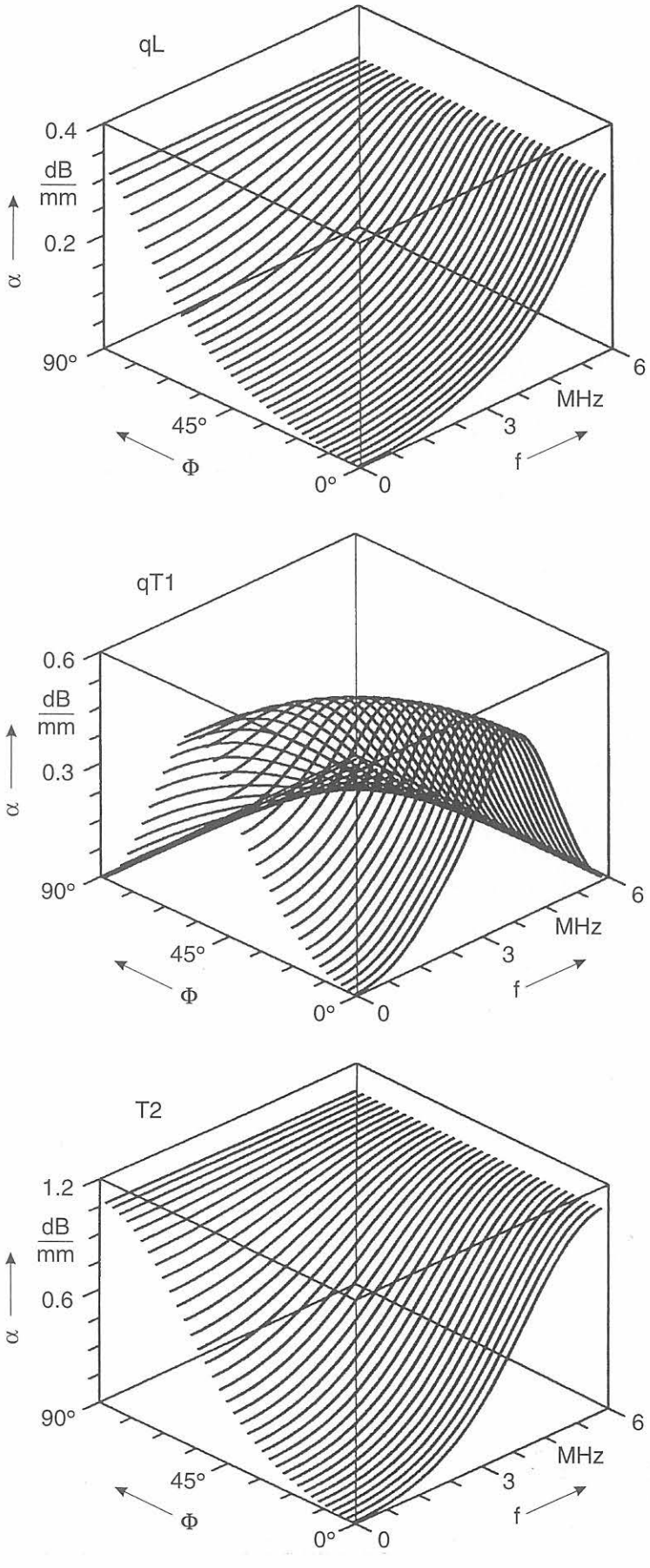

Figure 4.8: *Attenuation coefficients of the three wave modes qL, $qT1$, $T2$ in an* **arbitrary plane** *(Layback angle $\Psi = 20°$) as a function of frequency and grain angle.*
Grain shape: equiaxed, **grain size** $\overline{\mathbf{d}} = \mathbf{100}\ \boldsymbol{\mu}\mathbf{m}$ *(Munikoti et al. 1998-99 [117, 118]).*

Related to the same wavelength attenuation of the pure transverse wave with increasing frequency reaches a level of attenuation, which is three times higher than those of the both other waves. This confirms once more that it is not attenuation that renders the quasi-transverse wave inappropriate for austenitic weld testing but beam splitting this wave type undergoes in austenitic weld metal, s. chapters 2 and 3.

4.3.2 Phase velocity variation due to scattering

In the presence of ultrasound scattering the phase velocity varies. The normalized phase velocity variation, which is the phase velocity variation in the presence of scattering with respect to the phase velocity in the absence of scattering, is presented in fig. 4.9 as a function of the columnar grain orientation.

It turns out that the phase velocity variation of scattered waves does not differ greatly from that of the phase velocity in the medium without scattering, viz. by maximum 0.5% (at 2 MHz ultrasound frequency). This could be analytically explained as described in appendix H.

Furthermore, in the presence of ultrasound scattering dispersion of phase velocity occurs, fig. 4.10. It reaches up to 4%.

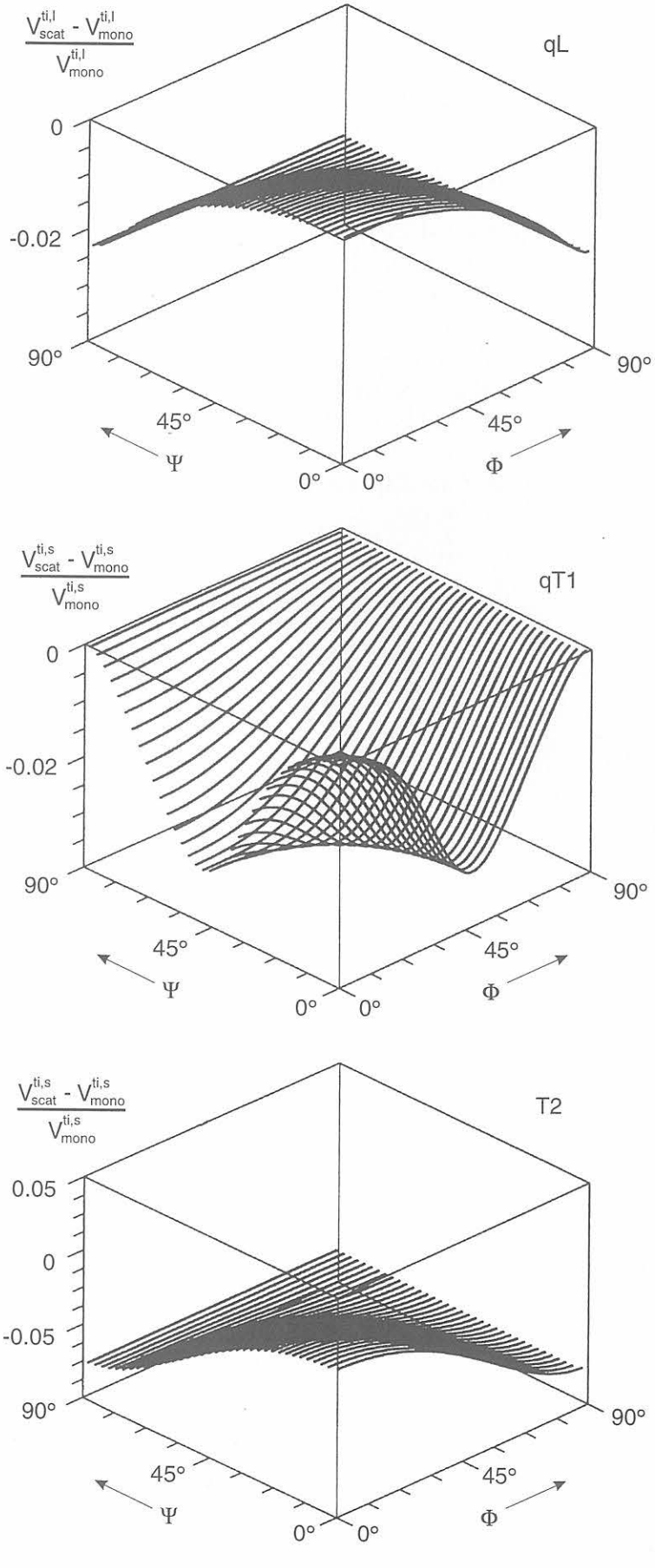

Figure 4.9: *Phase velocity variation* $\frac{V^{ti,l,s}_{scat} - V^{ti,l,s}_{mono}}{V^{ti,l,s}_{mono}}$ *of the three wave modes* qL, $qT1$, $T2$ *due to ultrasound scattering in polycrystalline austenitic weld metal relative to the velocity in the transverse isotropic monocrystal as a function of the columnar grain orientation. Frequency = 2 MHz, Grain shape: equiaxed, grain size* $\overline{d} = 100\mu m$ *(Munikoti et al. 1998-99 [117, 118]).*

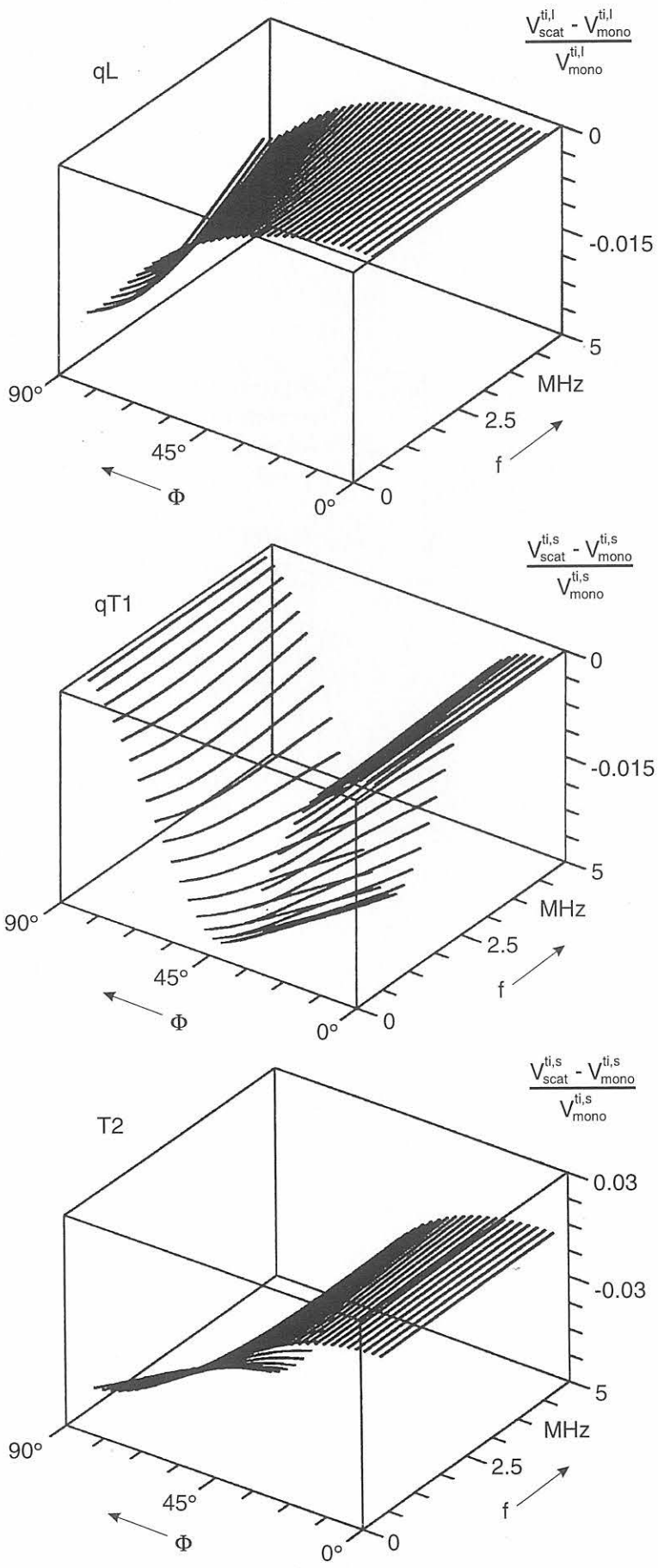

Figure 4.10: *Phase velocity variation* $\frac{V^{ti,l,s}_{scat} - V^{ti,l,s}_{mono}}{V^{ti,l,s}_{mono}}$ *of the three wave modes* qL, $qT1$, $T2$ *in the meridian plane due to ultrasound scattering in polycrystalline austenitic weld metal relative to the velocity in the transverse isotropic monocrystal as a function of frequency* **(dispersion)** *and grain angle. Grain shape: equiaxed, grain size* $\overline{d} = 100\mu m$ *(Munikoti et al. 1998-99 [117, 118]).*

4.3.3 Polarization deviation in the presence of scattering

As discussed in section 2.2.3, the quasi character of the waves in anisotropic media is due to the polarization deviation with respect to the wave vector direction. In the presence of attenuation due to ultrasound scattering the polarization deviation is changed. Fig. 4.11 shows this extra deviation as a function of the columnar grain orientation.

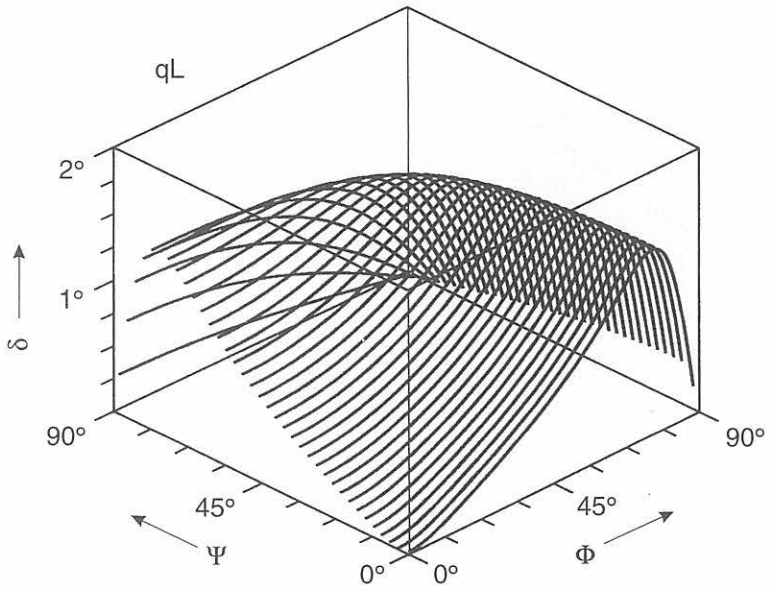

Figure 4.11: *Polarization deviation δ_{scat} of the quasi longitudinal (qL) and the quasi transverse (qT1) waves due to ultrasound scattering as a function of the columnar grain orientation. Frequency = 2 MHz, Grain shape: equiaxed, grain size $\overline{d}$ = 100μm (Munikoti et al. 1998-99 [117, 118]).*

Whereas the polarization of the pure transverse (T2) wave remains unaffected by scattering which is always perpendicular to the wave vector, the other waves (qL and qT1) exhibit an extra (same) deviation up to 2°.

Chapter 5

Conclusion

5.1 Contributions

In this work the propagation behaviour of ultrasound in austenitic weld metal has been analyzed by the time-harmonic plane wave approach. Bounded beam and pulse propagation as occurring in ultrasonic testing can be sufficiently dealt with by this approach. More sophisticated approaches principally do not offer any improvements in the results of plane wave modeling except for diffraction and aperture effects and, therefore, the subject matter of this work has been limited to plane wave propagation in the bulk of the medium and at different types of interfaces.
Inspite of the fact, that the individual columnar grains of the weld metal have cubic symmetry, the austenitic weld metal as a whole exhibits cylinder-symmetrical texture, as substantiated by metallurgical examination, and therefore has been treated as an anisotropic poly-crystalline medium with transverse isotropic symmetry.

5.1.1 Wave modes

Generally three wave types occur in anisotropic materials. In media with transverse isotropic symmetry these are one with predominantly longitudinal character, one with predominantly transverse character, and one pure transverse wave. They are found as solutions of the eigenvalue problem represented by the Christoffel equation for the infinite space yielding direction-dependent phase and group velocities, and direction-dependent polarizations of the three wave modes, all of which have been calculated for ultrasound propagation in three-dimensional space:

- Generally in anisotropic materials the group velocity direction deviates from the direction of the wave vector. The practical consequence of this is beam skewing, so that in ultrasonic testing of anisotropic specimens the transducer has to be offset to effectively intercept the beam. Furthermore, an ultrasonic beam entering the anisotropic medium spreads due to the effect of beam skewing. It has been shown, that in the range of incidence angles relevant for ultrasonic weld testing

  - the divergence of a quasi longitudinal beam is predominantly reduced,
  - on the contrast the divergence of a quasi transverse beam is predominantly increased,
  - the divergence of a pure transverse beam is least affected compared to the other wave types.

- The particle displacement polarizations form an orthogonal trihedral. If the columnar grain direction is not contained in the plane of wave propagation, the particle displacement polarizations are neither restricted to the plane of propagation nor perpendicular to it, respectively. The directions of polarizations rather vary in the three dimensional space as a function of the wave vector direction. Therefore the character of the waves which is described by the particle displacement polarizations is changed. In particular the character of the transverse waves, viz. vertically and horizontally polarized in the meridian plane, generally is not maintained.

  Following details have been shown:

  1. The properties of the T2 wave are as follows:
     - The polarization direction of the transverse wave T2 is invariant, i.e. always perpendicular to the columnar grain direction Z.
     - It is always perpendicular to the **k** vector. Therefore T2 has been defined as a pure wave.
     - The polarization of the T2 wave varies as a function of the **k** vector direction in the plane transverse to it. This means that it is not perpendicular to the plane of sound propagation and therefore T2 is generally not horizontally polarized.
  2. The polarization direction of the transverse wave qT1 is not in the plane of sound propagation and therefore qT1 generally is no longer vertically polarized.
  3. Increasing tilt of the columnar grain direction Z relative to the plane of wave propagation causes the transverse wave polarizations to change their 'roles':
     3.1 If the grain tilt reaches 90°, the polarization of the pure transverse wave T2 is contained in the plane of wave propagation, therefore being now vertically polarized, though as before perpendicular to **k** vector and columnar grain direction Z.
     3.2 If the grain tilt reaches 90°, the polarization of the now pure transverse wave T1 becomes independent of the wave vector direction, and will be perpendicular to the plane of wave propagation, i. e. horizontally polarized.

  Since polarization determines mode coupling at interfaces it can be concluded that

  - in the case of an interface between two *isotropic* materials, the horizontally polarized wave (T_H) does not couple with the other two waves, viz. with the vertically polarized shear wave (T_V) and the longitudinal wave (L) and vice versa,
  - in the case of an interface between two *anisotropic* materials, always all three wave modes couple.

5.1.2 Reflection and transmission

Plane wave reflection and transmission between two generally anisotropic materials has been analyzed. The analysis was divided into three sections:

- Reflection and transmission at perfect interfaces, which is a defect free rigid contact interface,
- Reflection and transmission at imperfect interfaces including the thin viscoelastic layer between perspex and anisotropic medium (i. e. the coupling of the ultrasonic transducer to the anisotropic weld and cladding metal),

- Reflection of bounded beams at an interface between fluid and anisotropic solid.

At the interfaces columnar grain orientations in the anisotropic weld metal were chosen as encountered in typical non-destructive testing problems. The computer codes to calculate reflection and transmission energy coefficients are written in FORTRAN 77 with graphics integrated. The types of interfaces considered were:

- **Isotropic base metal - anisotropic weld metal**, representing the weld fusion face and the cladding interface.

  The transparency of the **perfect interface** for all three wave modes is fairly high and approximately independent of the columnar grain orientation. Mode conversion only marginally exceeds 10%, generally it is much lower. However, transverse waves exhibit mutual mode conversion at the fusion face, which depends on the columnar layback angle and can reach up to 100%. The energy of the transmitted transverse waves depends on the polarization of the incident transverse wave, because only modes with (at least partially) identical polarizations couple to the incident wave.

  Conventional ultrasonic probes generate either vertically polarized transverse waves or horizontally polarized transverse waves. These waves incident from the isotropic face are split at the fusion face. In the anisotropic medium only two orthogonally polarized transverse waves, qT1 and T2, exist. In the case that the columnar grains are tilted relative to the plane of incidence, this decreases the energy of transverse waves considerably during examination of austenitic welds and cladded components. Both the transverse waves do not superpose due to different refraction angles.

  In the isotropic base material, however, the both transmitted components, T_H and T_V, are degenerated and therefore form a resulting transverse wave T with polarization according to the intensities of both superposed components.

- **Anisotropic base metal - anisotropic weld metal**, represent the weld fusion face in welded austenitic cast components and the interface between adjacent columnar grain bundles.

  Again for all three wave modes the transparency of the **perfect interfaces** made up by adjacent different crystallographic orientations is fairly high and is approximately independent of the columnar grain orientation. Mode conversion of the incident energy exceeds 10% only at certain points, generally it is much lower.

  However, direction dependent mutual mode conversion of transverse waves can reach 100% as before.

  At boundaries between two general transverse isotropic media with different grain orientations, when the propagation plane is not the meridian plane but an arbitrary plane, always both transverse wave modes couple simultaneously - with complementary energy distributions in reflection and transmission -, both with considerable energy, because the particle displacement polarization direction of the incident wave is not restricted by any crystallographic symmetry conditions.

  Whereas the grain angle, which denotes the tilt of the columnar grains *in* the incidence plane, does not influence the transverse wave mode conversion at large scales, it is the layback angle denoting the tilt of the columnar grains *out of* the incidence plane, which governs the transverse wave mode conversion. In austenitic stainless steel weld testing with layback angles in the welding direction up to $\approx 20°$ and even more between adjacent dendritic bundles, large transverse wave mode conversion rates are to be predicted even in the low angle range, attenuating considerably the transverse wave actually used for testing.

In the special case where the columnar grains are contained in the meridian plane, i. e. no layback of the columnar grains in the incident plane, (medium 1), mutual mode conversion of the transverse waves in medium 2 is similar to what is observed at the fusion face at wave incidence from the isotropic face.

Also the transparency of solid **imperfect interfaces** for all wave modes is still fairly high, though the crack area fraction comprises 75% of the interface. However, in contrast to the solid perfect interface a larger portion of the incident energy is reflected, mainly in the range below 45° incident angle Θ. In this region reflection increases with frequency, and may be used to characterize the interface.

Similarly it is observed that a larger portion of the incident wave energy, quasi longitudinal and quasi transverse, is mode converted reaching 15% at incidence angles larger than 45°, both, in reflection and refraction. However, mode conversion to the pure transverse wave T2 generally does not exceed 1%.

- The transparency of **thin viscoelastic layers** between isotropic and anisotropic materials, which represents the coupling layer between ultrasonic probe and austenitic material, basically is similar to that obtained during coupling on isotropic material. The columnar grain direction in the weld metal relative to the coupling surface only has little influence on the echo transparency.

  Generally, as a matter of fact, transverse waves do not pass through a fluid coupling layer due to its vanishing viscosity. However, the viscosity of glycerine and even fresh water, though very small, is not zero. Therefore transverse waves are transmitted at a corresponding low level into the weld metal. High viscosity couplants provide transparencies up to 50% for transverse waves, whereas solid coupling between perspex and weld metal only yields slightly increased transparency.

Splitting of the slowness surface domain of permissible wave vector angles of the quasi transverse wave: Due to the concave parts of the slowness surface of the quasi transverse wave in anisotropic austenite for certain incidence planes the slowness surface splits into disjoint sectors of "permissible" wave vectors.

This is because the existence criterion for reflected and transmitted ultrasonic waves is, that their energy flow direction (group velocity) vectors should be real and point away from the boundary, thus defining the sectors of the slowness surface containing the permissible wave vectors. The remaining sectors of the slowness surface contain "forbidden" wave vectors, because reflected and transmitted sound rays would be directed towards the interface: such rays do not exist.

This splitting phenomenon occurs both in transmission and reflection, when upon incidence of the quasi transverse wave qT1 and also of the pure transverse wave T2 the wave vector of the mode converted quasi-longitudinal wave qL reaches its critical angle. The incident energy then is redistributed and a second qT1(2) wave is transmitted instead of the qL wave, the phase velocity having continuously decreased as a function of the incidence angle Θ from the value of the qL wave to the value of the quasi-transverse qT1(2) wave. Both qT1 waves have almost the same phase and group velocities with slightly different polarization directions. This poses special problems in testing of materials with transverse waves, making them less suitable for inspection.

The **Schoch-effect**, viz. the lateral displacement and splitting of an reflected ultrasound beam upon incidence of a beam onto a liquid-solid interface at an angle around the Rayleigh angle has been calculated for a beam with Gaussian profile for the liquid-*anisotropic* solid. Apart from the effect that the Rayleigh angle and the phase velocity of Rayleigh waves vary with the columnar grain orientation, lateral displacement of the

reflected beam relative to its position predicted by geometrical acoustics and splitting of the reflected beam are observed qualitatively similar to the isotropic case.

5.1.3 Ray tracing

Determining the columnar grain distribution by an empirical function, interfaces could be defined between neighbouring grain boundaries. A numerical procedure has been developed describing the transmission of ultrasound as it propagates through numerous grain boundaries and the energy flow direction associated with the wave of interest. Since the energy flow direction (direction of group velocity) is skewed with respect to the wave vector direction, ray paths generally are three dimensional in nature. The procedure developed allows to trace the most probable paths of ultrasound in anisotropic weld metal *three dimensionally*. The ray tracing code is written in FORTRAN 77 with graphics integrated.

Results for quasi longitudinal, quasi transverse and pure transverse waves are presented for different incidence angles, transducer positions, and microstructures (textures). To simulate a beam, seven rays are assumed to be generated at the probe index point. The divergence of the rays increases (decreases) by one degree steps with respect to the central ray direction.

Beam paths of quasi longitudinal and pure transverse waves are generally more straightforward than the paths of quasi transverse waves. However, it can be observed that beam paths are generally highly sensitive to the weld texture. This is due to the form of the slowness surfaces. The slowness surface of the quasi transverse wave exhibits concave and convex areas with cusps which results in largely varying group velocity (energy flow) directions and ray splitting.

When the quasi transverse wave is incident obliquely at the parent-weld metal interface, for a particular angle of incidence, the transmitted quasi longitudinal wave may not be propagating (evanescent). Then, due to the energy balance criterion the incident energy would be redistributed to the other propagating waves. Under these conditions there are two quasi transverse waves and one pure transverse wave propagating. The two quasi transverse waves, however, have different phase velocities, polarization directions and energy contents.

At every iterative step, there could be two quasi transverse waves branches, one with higher energy than the other. In this work both the possible rays have been traced. If the ray paths of both the quasi transverse waves are not significantly apart, then at the receiving end of the transducer, both the waves could *interfere* making it experimentally difficult to identify them.

5.1.4 Scattering of ultrasound

By assuming the weld metal to be mono-crystalline with transverse isotropic symmetry, the attenuation which is inherent in such materials can not be accounted for. The weld metal, therefore, has been assumed to be an anisotropic, polycrystalline material with cylinder-symmetric texture (transverse isotropy). Such material exhibits grain scattering depending on elastic anisotropy and geometric features of the grains and on the grain boundaries. To determine attenuation for an arbitrarily oriented columnar grain texture *three-dimensionally* the unified theory on elastic wave propagation in polycrystalline materials as proposed by Stanke and Kino in the Keller's approximation for equiaxed grains has been extended to austenitic weld metal. No restrictive assumptions are made with respect to the polarization direction of waves, viz. polarization deviation is taken into account stringently.

Attenuation coefficients in an austenitic CrNi 18 12 stainless steel have been calculated as a function of the wave vector to Z-direction of the crystallographic system X, Y, Z, and as a function of frequency. The computer code for evaluation of reflection and transmission energy coefficients is written in FORTRAN 77 which uses mathematical routines from the commercially available "International Mathematical Society Library" (IMSL).

Whereas for quasi-longitudinal and pure transverse waves attenuation theoretically vanishes when propagating in the columnar grain direction and reaches a maximum when propagating perpendicular to the columnar grain direction, for the quasi transverse wave maximum attenuation occurs at about 45° and, both, at normal incidence and at 90°, no attenuation is predicted.

Generally, attenuation by scattering reaches a high level with the grain size to wavelength ratio increasing and becomes independent on this ratio in the stochastic region though on a high level.

Attenuation of the quasi transverse wave is lesser than for quasi longitudinal and pure transverse waves related to the same wavelength. With increasing frequency the pure transverse wave reaches a level of attenuation, which is three times higher than those of the both other waves. Therefore it is not attenuation that renders the quasi transverse wave inappropriate for austenitic weld testing. It is rather because of the beam splitting this wave type undergoes in austenitic weld metal.

In the presence of ultrasound scattering the phase velocity varies by a maximum of 7% at 2 MHz and 100 μm grain size. Also dispersion of phase velocity occurs, which reaches 6% in the range up to 5 MHz at 100 μm grain size. Furthermore, in the presence of ultrasound scattering the polarization deviation is changed. Whereas the polarization of the pure transverse (T2) wave remains unaffected by scattering being always perpendicular to the wave vector, the other waves (qL and qT1) exhibit an extra deviation up to 2°.

5.2 Areas for continued research

5.2.1 Modeling

The theory of scattering in spherical grains has been extended to ellipsoidal grains using the correlation function (4.4) suggested by Ahmed, see section 4.2.1. The necessary mathematical programming has been done and is in final stages of implementation.

5.2.2 Software

For the present work ultrasound propagation softwares have been developed which use a macroscopic material model based on the result from averaging the microscopic anisotropy of the single grains. However, since grain growth simulation software is available, which uses the welding input parameters and weld pool data, as well as the data of 'Orientation Imaging Microscopy' (s. section 1.1), it would be worthwhile to integrate this simulation software with the software dealing with ultrasound propagation in such simulated structures in order to validate the predictions of ray tracing.

5.2.3 Experimental validation

Measurements of the attenuation of the three wave modes in real materials comprising the full scale of industrially relevant stainless steels (austenitic stainless CrNi-steels, fully austenitic stainless steels with increased Ni-content, Nickel based-alloys, and Duplex steels

(Ferritic-austenitic steels)) can determine how generally useful the plane wave ansatz and the present material model is. The theoretically predicted attenuation of quasi longitudinal waves could be already verified (see section 4.3.1.1). The experience gained hereby showed that any procedure that does not fully account for the anisotropic nature of the material is bound to yield disputable results: if energy losses due to mode conversion, due to beam skewing and beam spreading, which are characteristic for the anisotropic nature of the media considered in this work, are not taken into account, apparent attenuation due to these effects adds to the scattering-induced attenuation.

It is this apparent attenuation that renders measurement and evaluation of scattering-induced attenuation of shear waves in austenitic steel samples more difficult, because it may reduce the amplitude of the reflected signal to the noise level.

Experimental ray tracing also can determine how useful the plane wave ansatz and the present material model is. This needs a series of weld metal specimens, which allow to measure contour maps of the sound field distribution at increasing sound path lengths. Specimens of an austenitic stainless CrNi-weld are already available.

Bibliography

[A] Textbooks and Monographs

[1] J. D. Achenbach, *Wave propagation in elastic solids*, Elsevier, North Holland, Amsterdam, 1987

[2] K. Aki, P. G. Richards, *Quantitative seismology, theory and methods*, Vol. 1 & 2, W. H. Freeman and Company, San Fransisco, 1980

[3] B. A. Auld, *Acoustic fields and waves in solids*, Volume I and II, 2nd edition, Robert E. Krieger Publishing Company, Malabar, Florida 1990

[4] W. Bergmann, *Werkstofftechnik, Teil 1 & Teil 2*, Carl Hanser Verlag, München, Wien, 1989

[5] Léon Brillouin, *Wave propagation in periodic structures* Dover publications Inc., New York, 1953

[6] Léon Brillouin, *Wave propagation and group velocity* Academic press Inc., New York, 1960

[7] L. M. Brekhovskikh, *Waves in layered media*, Academic Press, Inc., San Diego, New York, Berkeley, Boston, London, Sydney, Tokyo, Toronto 1980

[8] L. M. Brekhovskikh, O. A. Godin, *Waves in layered media I*, Springer-Verlag, Berlin, Heidelberg, New York, London, Paris, Tokyo, Hongkong 1990

[9] L. M. Brekhovskikh, O. A. Godin, *Waves in layered media II*, Springer-Verlag, Berlin, Heidelberg, New York, London, Paris, Tokyo, Hongkong 1992

[10] H.-J. Bunge, *Texture analysis in materials science*, Butterworths, London, 1983

[11] *Mathematical modeling of weld phenomena,* Edt. H. Cerjak, K. E. Easterling, The University Press, Cambridge, Vol. 1 (1993), Vol. 2 (1995), Vol. 3 (1997)

[12] V. Červený, I. A. Molotkov, I. Pšenčík, *Ray method in seismology*, Univerzita Karlova, Praha 1977

[13] G. Engeln-Müllges, F. Reutter, *Numerische Mathematik für Ingenieure*, Wissenschaftsverlag, Mannheim / Wien / Zürich, 1987

[14] W. M. Ewing, W. S. Jardetzky, F. Press, *Elastic waves in layered media*, McGraw-Hill Book Company; New York, Toronto, London, 1957

[15] F. I. Fedorov, *Theory of elastic waves in crystals*, Plenum Press, New York, 1968

[16] I. S. Gradshteyn and I. M. Ryzhik, *Table of Integrals, Series, and Products*, Academic Press, New York, San Francisco, London, 1965

[17] A. H. Harker, *Elastic waves in solids*, British Gas, Adam Hilger, 1988

[18] R. A. Kline, *Nondestructive characterization of composite media*, Technomic Publication Co., 1992

[19] J. Krautkrämer, H. Krautkrämer, *Werkstoffprüfung mit Ultraschall*, 5. Aufl., Springer-Verlag, Berlin, Heidelberg, New York, London, Paris, Tokyo 1986, ISBN 3-540-15754-9

[20] W. Kurz, D. J. Fischer, *Fundamentals of solidification*, 1992, Trans Tech Publications Ltd., Switzerland, ISBN 0-87849-522-3

[21] L. D. Landau, E. M. Lifschitz, *Hydrodynamik*, Lehrbuch der theoretischen Physik, Band VI, 4. Aufl., Akademie-Verlag, Berlin, 1981

[22] T. Mura, *Micromechanics of defects in solids*, 2nd Edt., Kluwer Academic Publishers, Dordrecht, Boston, London, 1987

[23] M. J. P. Musgrave, *Crystal acoustics*, Holden-Day, San Francisco, Cambridge, London, Amsterdam, 1970.

[24] A. H. Nayfeh, *Wave propagation in layered anisotropic media with applications to composites*, Elsevier; Amsterdam, Lausanne, New York, 1995

[25] E. Neumann, S. Hirsekorn, G. Hübschen, T. Just, R. Schmid, *Ultraschallprüfung von austenitischen Plattierungen, Mischnähten und austenitischen Schweißnähten, Theorie - Praxis - Regelwerke*, Renningen - Malmsheim, Expert-Verlag, 1995, ISBN 3-8169-1078-5

[26] J. A. Ogilvy, *Theory of wave scattering from random rough surfaces*, Institute of Physics Publishing, Bristol, 1991

[27] R. G. Payton, *Elastic wave propagation in transversely isotropic media*, Martinus Nijhoff Publishers, The Hague, Boston, Lancaster, 1983

[28] S. I. Rokhlin (Edt.), *Theoretical and experimental aspects of models of ultrasonic wave interaction with imperfect interfaces,* Special Issue of the Journal of Nondestructive Evaluation, **11** Numbers 3/4 (1992)

[29] J. F. Rosenbaum, *Bulk acoustic wave theory and devices*, Artech House, London, 1988

[30] R. E. Sheriff, L. P. Geldart, *Exploration Seismology*, Second Edition, Cambridge University Press, 1995

[31] E. Skudrzyk, *The foundations of Acoustics*, Springer-Verlag, Wien, New York, 1971

[32] A. H. Stroud, D. Secrest, *Gaussian quadrature formulas*, Prentice-Hall Inc., Englewood Cliffs, N. J. 1966

[33] H. Tada, P. Paris, G. Irwin, *The stress analysis of cracks handbook*, Del Research Corporation, Hellertown, Pennsylvania, 1973

[34] R. Truell, Ch. Elbaum, B. B. Chick, *Ultrasonic methods in solid state physics*, Academic Press, New York, London, 1969

[35] I. A. Viktorov, *Rayleigh and Lamb waves*, Plenum Press, New York, 1967

[36] S. Wolfram, *The Mathematica*, Third edition, Cambridge University Press, 1996

[B] STANDARDS, REGULATIONS, GUIDELINES

[37] *The evaluation of ultrasonic signals. Guidance and recommendations on evaluation of ultrasonic signals in manual weld examination and on defect acceptance/rejection criteria*, Document I. I. S. /I. I. W.-850-86, Commission V 'Testing, measurement and control of welds' of the International Institute of Welding (IIW), The Welding Institute, Abington Hall, Abington, Cambridge CB1 6AL, UK (1987)

[38] Ultraschallprüfung von austenitischen Werkstoffen - Fortbildungsseminar Deutsche Gesellschaft für Zerstörungsfreie Prüfung (DGZfP), 1999.

[C] ORIGINAL PAPERS

[39] B. L. Adams, St. I. Wright, K. Kunze, *Orientation imaging: The emergence of a new microscopy*, Met. Trans. **24A** (1993) 819-831

[40] S. Ahmed, R. B. Thompson, *Unified theory for elastic waves propagation in polycrystalline materials*, J. Acoust. Soc. Am. **75** (1984) 665-681

[41] S. Ahmed, R. B. Thompson, *Propagation of elastic waves in equiaxed stainless-steel polycrystals with aligned [001] axes*, J. Acoust. Soc. Am. **99** (1996) 2086-2096

[42] S. Ahmed, R. B. Thompson, *On the observation of elliptic polarization of quasi-P and quasi-SV waves propagating in highly oriented equiaxed stainless steel polycrystals*, Proc. 1^{st} USA-Japan Symp. Adv. in NDT (1996) 150-155, ASNT Columbus, ISBN 1-57117-021-9

[43] S. Ahmed, R. B. Thompson, *Influence of columnar microstructure on ultrasonic backscattering*, Review of Progress in Quantitative Nondestructive Evaluation **14** (1995) 1617-1624

[44] S. Ahmed, *Personal communication*

[45] J.-M. Baik, R. B. Thompson, *Ultrasonic scattering from imperfect interfaces: A quasi-static model*, JNDE **4** (1984) 177-196

[46] S. Bauer, *Metallography* in the project SMT4-CT95-2012 "Effect of Ultrasonic Scattering on Inspection of Austenitic Welds" funded by the Commission of the European Communities under the Standards, Measurements & Testing Programme, 1996 - 1999, DG XII, Brussels; BAM, Lab. VIII.42, D-12200 Berlin

[47] H. L. Bertoni, T. Tamir, *Unified theory of Rayleigh angle phenomena for acoustic beams at liquid-solid interfaces*, J. Appl. Phys. **2** (1973) 157-172

[48] T. Tamir, H. L. Bertoni, *Lateral displacement of optical beams at multilayered and periodic structures*, J. Op. Soc. Am. **10** (1971) 1397-1413

[49] R. Boehm, T. Hauser, P. Le Gal, B. Rotter, A. Bleck, W. Hesselmann, *Richtungsabhängigkeit der Schallgeschwindigkeit in austenitischen Plattierungen; Aspekte zur anisotropen Schallausbreitung*, Fortschr.-Ber. der Jahrestagung 1992 der Deutschen Gesellschaft für Zerstörungsfreie Prüfung e. V. (DGZfP), Fulda, **33.2** (1992) 627-637

[50] R. Boehm, A. Erhard, W. Möhrle, *Beeinflussung des Gruppenstrahler-Schallfeldes durch Anisotropie*, Fortschr.-Ber. der Jahrestagung 1993 der Deutschen Gesellschaft für Zerstörungsfreie Prüfung e. V. (DGZfP), Garmisch-Partenkirchen, **37.2** (1993) 638-647

[51] R. Boehm, A. Erhard, H. Wüstenberg, *Sound field distribution in a simulated polycrystal*, Proc. 6^{th} European Conf. on NDT, Nice, France, 1994

[52] W. L. Bond, *The mathematics of the physical properties of crystals*, The Bell system technical journal (BSTJ), American telephone and telegraph company, New York, **22** (1943) 1-72

[53] G. Bradfield, *Comparison of the elastic anisotropy of two austenitic steels*, Journal of the Iron and steel Institute **202** (1964) 616

[54] *Collected algorithms from CACM*, www.netlib.org, 196-P1 - 196-P4

[55] F. Champigny, B. Nouailhas, *Modeling the propagation of an acoustic beam from a focussed transducer through a bimetallic weld*, Proc. 4^{th} Eur. Conf. NDT, London 1987, Vol. 1, 695-703, Pergamon Press

[56] G. J. Davies, D. J. Goodwill, J. S. Kallend, *Elastic and plastic anisotropy in sheets of cubic metals*, Metallurgical transactions **3** (1972) 1627-1631

[57] U. Dilthey, V. Pavlik, T. Reichel, *Struktursimulation von Schweißgut und Wärmeeinflußzone*, DVS-Berichte **176**,(1996) 26-28

[58] U. Dilthey, T. Reichel, V. Pavlik, *A modified cellular automata model for grain growth simulation* in *Mathematical modeling of weld phenomena,* Edt. H. Cerjak, The University Press, Cambridge, Vol. 3 (1997) 106-113

[59] W. Dreyer, *Personal communication*

[60] H. Ernst, *Measurement of ultrasonic wave attenuation: Evaluation of frontface- and backwall-echoes*, in the project SMT4-CT95-2012 "Effect of Ultrasonic Scattering on Inspection of Austenitic Welds" funded by the Commission of the European Communities under the Standards, Measurements & Testing Programme, 1996 - 1999, DG XII, Brussels; BAM, Lab. VIII.42, D-12200 Berlin

[61] H. Ernst, *Messung der Ultraschallschwächung in akustisch anisotropen polykristallinen Werkstoffen*, Diplomarbeit, Technische Universität Bergakademie Freiberg, Fakultät Werkstoffwissenschaften und -technologie; BAM, Lab. VIII.42, D-12200 Berlin, 1999

[62] H. Ernst, V. Munikoti, E. Neumann, *Messung der Schwächung von longitudinalen Ultraschallwellen in austenitischem stengelkristallinem Gefüge*, Fortschr.-Ber. der Jahrestagung 1999 der Deutschen Gesellschaft für Zerstörungsfreie Prüfung e. V. (DGZfP), Celle, **68.2** (1992) 615-626

[63] P. Fellinger, *Ein Verfahren zur numerischen Lösung elastischer Wellenausbreitungsprobleme im Zeitbereich durch direkte Diskretisierung der elastodynamischen Grundgleichungen*, Ph. D. Thesis, Gesamthochschule, Kassel, Germany, 1991

[64] P. Fellinger, R. Marklein, K. J. Langenberg, S. Klaholz, *Numerical modeling of elastic wave propagation and scattering with EFIT - elastodynamic finite integration technique*, Wave Motion **21** (1995) 47-66

[65] D. P. Field, D. J. Dingley, *Microstructure mapping of interconnects by orientation imaging microscopy*, J. of Electronic Matls. **25** (1996) 1767-1771

[66] *UltraSIM*, FORCE Institute, Brøndby, Denmark, *http://www. ultrasim. dk//*

[67] T. Furukawa, K. Date, *Ray-modeling for computer simulation of ultrasonic testing*, Review of Progress in Quantitative Nondestructive Evaluation **14** (1995)

[68] T. Furukawa, G. Yotsuya, K. Date, *Simple modeling of ultrasonic beam incidence in immersion testing*, Materials Evaluation, June 1995

[69] Ch.-A. Gandin, J.-L. Desbiolles, M. Rappaz, M. Swierkosz, Ph. Thévoz, *3 D Modelling of grain structure formation during solidification*, Supercomputing Review (Nov. 1996) 11-15

[70] S. Gripp, *Beitrag zur Verbesserung der Ultraschallprüfung glasfaserverstärkter Polymere auf der Grundlage analytischer Modellierung*, Dissertation, Technische Universität Berlin, 1999, D 83

[71] J. E. Gubernatis, E. Domany, J. A. Krumhansl, *Formal aspects of the theory of the scattering of ultrasound by flaws in elastic materials*, J. Appl. Phys. **48** (1977) 2804-2811

[72] A.H. Harker, J. A. Ogilvy, J. A.G. Temple, *Modeling ultrasonic inspection of austenitic welds.* J. NDE. **9** (1990) 155-165

[73] A.H. Harker, J. A. Ogilvy, *Coherent wave propagation in inhomogeneous materials: a comparison of theoretical models.* Ultrasonics **29** (1991) 235-244

[74] M. Haubold, *Metallurgical Investigation by Acoustic Microscopy* in the project SMT4-CT95-2012 "Effect of Ultrasonic Scattering on Inspection of Austenitic Welds" funded by the Commission of the European Communities under the Standards, Measurements & Testing Programme, 1996 - 1999, DG XII, Brussels; BAM, Lab. VIII.42, D-12200 Berlin

[75] A. Hecht, *Zerstörungsfreie Korngrößenbestimmung an austenitischen Feinblechen mit Hilfe der Ultraschallrückstreung*, Dissertation, Technische Universität Berlin, 1986, D 83; Forschungsbericht 120, Bundesanstalt für Materialforschung und -prüfung (BAM) Berlin, Wirtschaftsverlag NW, Bremerhaven, 1986, ISBN 3-88314-514-9

[76] E. G. Henneke II, *Reflection-refraction of a stress wave at a plane boundary between anisotropic media*, J. Acoust. Soc. Am. **51** (1972) 210-217

[77] W. Hesselmann, R. Boehm, T. Hauser, H. Wüstenberg, *Einfluß des Anisotropie-Effektes bei der Ultraschallprüfung plattierter Bauteile.* Fortschr.-Ber. der Jahrestagung 1993 der Deutschen Gesellschaft für Zerstörungsfreie Prüfung e. V. (DGZfP), Garmisch-Partenkirchen, **37.1** (1993) 249-263

[78] W. Hesselmann, *Zum Einfluß der elastischen Anisotropie bei der Ultraschallprüfung von Plattierungen*, Dissertation, Technische Universität Berlin, D 83, Berlin 1994

[79] S. Hirsekorn, *Ultraschallausbreitung in mehrphasigen Polykristallen*, Report 860447 - TW, Fraunhofer-Institut für zerstörungsfreie Prüfverfahren, Saarbrücken

[80] S. Hirsekorn, *Personal communication*

[81] S. Hirsekorn, *The scattering of ultrasonic waves by polycrystals*, J. Acoust. Soc. Am. **72** (1982) 1021-1031

[82] S. Hirsekorn, *The scattering of ultrasonic waves by polycrystals. II. Shear waves*, J. Acoust. Soc. Am. **73** (1983) 1160-1163

[83] S. Hirsekorn, *The scattering of ultrasonic waves in polycrystalline materials with texture*, J. Acoust. Soc. Am. **77** (1985) 832-843

[84] S. Hirsekorn, *Directional dependence of ultrasonic propagation in textured polycrystals*, J. Acoust. Soc. Am. **79** (1986) 1269-1279

[85] S. Hirsekorn, *The scattering of ultrasonic waves by multiphase polycrystals*, J. Acoust. Soc. Am. **83** (1988) 1231-1242

[86] S. Hirsekorn, *Ultraschallausbreitung in Metall-Matrix-Verbundwerkstoffen*, Fraunhofer-Institut für Zerstörungsfreie Prüfverfahren Report Nr. 880117-TW (1988)

[87] B. E. Hornby, L. M. Schwartz, J. A. Hudson, *Anisotropic effective-medium modelling of the elastic properties of shales*, Geophysics **59** (1994) 1570-1583

[88] W. Huang, S. I. Rokhlin, *Interface waves along an anisotropic imperfect interface between anisotropic solids*, J. NDE **11** (1992) 185-198

[89] W. Huang, S. I. Rokhlin, *Generalized spring boundary conditions and scattering coefficients for interface imperfections with arbitrary orientations*, Review of Progress in QNDE **14** (1995) 107-114

[90] J. A. Hudson, *Wave speeds and attenuation of elastic waves in material containing cracks*, Geophys. J. R. astr. Soc. **64** (1981) 133-150

[91] *IMSL FORTRAN and C application development tools*, Visual Numerics Inc., 1994

[92] C. A. Issa, K. Balasubramaniam, *P-version Finite Element modelling for NDE*, Rev. of Progr. in QNDE **11** (1992) 2307-2314

[93] J. B. Keller, *Stochastic equations and wave propagation in random media*, Proc. 16th Symp. Applied Mathematics, American Mathematical Society, New York, 1964, 145-179

[94] S. Klaholz, K. J. Langenberg, R. Bärmann, R. Marklein, S. Irmer, H. Müller, F. Walte, *Ultraschallmodellierung mit dem EFIT-Code zur zerstörungsfreien Prüfung an Beton und anisotropen Schweißnähten*, Fortschr.-Ber. der DGZfP-Jahrestagung 'Zerstörungsfreie Materialprüfung', Aachen, **47** (1995) 597-606

[95] S. Klaholz, F. Walte, K. J. Langenberg, P. Baum, *Elastic wave propagation and scattering in austenitic steel*, Rev. Progr. Quant. NDE **14** (1995) 219-226, Plenum Press, New York

[96] C. G. Knott, *Reflection and refraction of elastic waves with seismological applications*, Phil. Mag. **48** (1899) 64-97

[97] P. Krarup, *Experimental sound ray tracing* in the project SMT4-CT95-2012 "Effect of Ultrasonic Scattering on Inspection of Austenitic Welds" funded by the Commission of the European Communities under the Standards, Measurements & Testing Programme, 1996 - 1999, DG XII, Brussels; BAM, Lab. VIII.42, D-12200 Berlin

[98] E. A. Kraut, *Advances in the theory of anisotropic elastic wave propagation*, Review of Geophysics **1** (1963) 401-448

[99] E. M. Lifshits, G. D. Parkhomovski, *Eine Theorie der Ausbreitung von Ultraschallwellen im polykristallinen Medium* (in Russisch), Zh. Eksp. Teor. Fiz. **20** (1950) 176-182

[100] M. J. Lighthill, *Studies on magneto-hydrodynamic waves and other anisotropic wave motions*, Phil. Trans. Roy. Soc. London A, **252** (1960) 397-470

[101] F. J. Margetan, R. B. Thompson, T. A. Gray, *Interfacial spring model for ultrasonic interactions with imperfect interfaces: Theory of oblique incidence and application to diffusion-bonded butt joints*, JNDE **7** (1988) 131-152

[102] F. J. Margetan, *Personal communication*

[103] R. Marklein, S. Klaholz, P. Fellinger, K. J. Langenberg, *Der US-Modellierungscode EFIT für anisotrope Materialien*, Fortschr.-Ber. der DGZfP-Jahrestagung 'Zerstörungsfreie Materialprüfung', Timmendorfer Strand, **43.2** (1994) 395-407

[104] R. Marklein, R. Bärmann, K. J. Langenberg, *The ultrasonic modeling code EFIT as applied to inhomogeneous dissipative isotropic and anisotropic media*, Rev. Progr. Quant. NDE **14** (1995) 251-258, Plenum Press, New York

[105] R. Marklein, *Numerische Verfahren zur Modellierung von akustischen, elektromagnetischen, elastischen und piezoelektrischen Wellenausbreitungsproblemen im Zeitbereich basierend auf der Finite Integrationstechnik*, Ph. D. Thesis, Universität Gesamthochschule Kassel, Germany, Kassel 1997

[106] A. Minachi, R. B. Thompson, *Ultrasonic beam propagation through a bimetallic weld - a comparison of predictions of the Gauss-Hermite beam model and Finite Element Method*, J. NDE, **12** (1993) 151-158

[107] V. Munikoti, E. Neumann, *Reflexions- und Durchlässigkeitsfaktoren des Schalldrucks an Grenzflächen zwischen akustisch isotropen und anisotropen Materialien*, Fortschr.-Ber. der Jahrestagung 1991 der Deutschen Gesellschaft für Zerstörungsfreie Prüfung e. V. (DGZfP), Luzern, **28** (1991) 607-615

[108] V. Munikoti, E. Neumann, S. Gripp, *Über die Ankopplung bei der Ultraschallprüfung akustisch anisotroper Werkstoffe*, Fortschr.-Ber. der Jahrestagung 'Zerstörungsfreie Materialprüfung' der Deutschen Gesellschaft für zerstörungsfreie Prüfung **33** (1992) 638-646, Fulda

[109] V. Munikoti, E. Neumann, *Über Polarisationsabweichungen bei der Ultraschallprüfung akustisch anisotroper Werkstoffe und Auswirkungen auf die Prüfergebnisse*, Fortschr.- Ber. des 2. Koll. 'Qualitätssicherung durch Werkstoffprüfung', 1992, Zwickau, Deutsche Gesellschaft für Zerstörungsfreie Prüfung e. V. (DGZfP), **34** (1992) 152-160

[110] V. Munikoti, E. Neumann, *Reflection and transmission energy coefficients at the interface between austenitic base and weld metal*, J. Phys. D, Appl. Phys. **25** (1992) 1504-1512

[111] V. Munikoti, E. Neumann, R. Boehm, *Über die Polarisation der Ultraschallwellen bei der Ultraschallprüfung von akustisch anisotropen Werkstoffen mit Textur*, Fortschr.-Ber. der Jahrestagung 'Zerstörungsfreie Materialprüfung' der Deutschen Gesellschaft für Zerstörungsfreie Prüfung e. V. (DGZfP) **37** (1993) 225-240, Garmisch-Partenkirchen,

[112] V. Munikoti, E. Neumann, *Ultraschall-Polarisation in Werkstoffen mit Textur; Physikalische Grundlagen der Ultraschallprüfung von austenitischen Schweißverbindungen.* Materialprüfung **35** (1993) 260-264

[113] V. Munikoti, R. Schmid, K. Matthies, E. Neumann, *Über die Veränderung der Ultraschallwellen in akustisch anisotropen Werkstoffen und über Konsequenzen für die Prüfung, dargestellt am Beispiel der austenitisch-ferritischen Mischverbindungen.* Fortschr.-Ber. des 3. Koll. 'Qualitätssicherung durch Werkstoffprüfung' **39** (1993) 137-150, Zwickau

[114] V. Munikoti, R. Schmid, K. Matthies, E. Neumann, *Prüfmethoden für Werkstoffe mit Fasertextur - Darstellung am Beispiel der Austenite*, Fortschr.-Ber. der Jahrestagung 'Zerstörungsfreie Materialprüfung' der Deutschen Gesellschaft für Zerstörungsfreie Prüfung e. V. (DGZfP), **43** (1994) 39-52, Timmendorfer Strand

[115] V. Munikoti, R. Schmid, G. Hübschen, K. Matthies, E. Neumann, *Über den Einfluß von Nahtflanke und Plattierungsgrenzfläche austenitischer Schweißungen auf transversale Ultraschallwellen*, Fortschr.-Ber. der DGZfP-Jahrestagung 'Zerstörungsfreie Materialprüfung', der Deutschen Gesellschaft für Zerstörungsfreie Prüfung e. V. (DGZfP) **47** (1995) 403-416, Aachen

[116] V. Munikoti, E. Neumann, *Über Probleme der Ortung mit Ultraschall in austenitischem Schweißgut - Das scheinbare Schielen des Prüfkopfs*, Fortschr.-Ber. der DGZfP-Jahrestagung 'Zerstörungsfreie Materialprüfung' **52** (1996) 461-478, Lindau, 13. - 15. 5. 1996

[117] V. K. Munikoti, E. Neumann, *Extension of Ahmed & Thompson theory to general elastic plane quasi-wave propagation in textured polycrystalline material*, Review of Progress in QNDE **17** (1998) 1657-1664

[118] V. K. Munikoti, *Application and extension of the unified theory for elastic wave propagation by Stanke & Kino to general elastic plane quasi-wave propagation in textured polycrystalline material* in the project SMT4-CT95-2012 "Effect of Ultrasonic Scattering on Inspection of Austenitic Welds" funded by the Commission of the European Communities under the Standards, Measurements & Testing Programme, 1996 - 1999, DG XII, Brussels; BAM, Lab. VIII.42, D-12200 Berlin

[119] P. B. Nagy, *Personal communication*

[120] P. B. Nagy, L. Adler, *Reflection of ultrasonic waves at imperfect boundaries*, Review of Progress in QNDE **10A** (1991) 177-184

[121] P. B. Nagy, *Ultrasonic classification of imperfect interfaces*, J. NDT Eval. **11** (1992) 127-139

[122] A. H. Nayfeh, P. B. Nagy, *Excess attenuation of leaky Lamb waves due to viscous fluid loading*, J. Acoust. Soc. Am. **101** (1997) 2649-2658

[123] E. Neumann, M. Römer, T. Just, K. Matthies et al., *Development and improvement of ultrasonic testing techniques for austenitic nuclear components*, Proc. Int. Conf. NDE in the Nuclear Industry, 84-105, 1978, Salt Lake City, Utah/USA, ASM, Metals Park, Ohio, ISBN 0-87170-029-8

[124] E. Neumann, *Über den Stand der Entwicklung von Ultraschallprüfverfahren für grobkörnige austenitische Werkstoffe*, in L. Dorn u. a., *Schadensfälle und Fehler an Schweißbauteilen, Ursachen und Vermeidung*, Expert Verlag, (1985) 159-187, ISBN 3-88508-962-9

[125] E. Neumann, V. Munikoti, K. Matthies, R. Schmid, G. Hübschen, *Über den Einfluß von Texturinhomogenität von austenitischem Schweißgut auf transversale Ultraschallwellen und über Konsequenzen für die Prüfung*, Fortschr.-Ber. des 4. Koll. 'Qualitätssicherung durch Werkstoffprüfung', Deutsche Gesellschaft für Zerstörungsfreie Prüfung e. V. (DGZfP), **49** (1995) 61-74, Zwickau

[126] E. Neumann, V. Munikoti, *Fortschritte bei der kritischen Auswahl der Parameter für die Ultraschallprüfung von austenitischen Schweißnähten*, Fortschr.-Ber. des DGZfP-Querschnittseminars Methodische Ansätze zur Lösung von speziellen Prüfproblemen **56** (1996) 21-44

[127] Project SMT4-CT95-2012, *Effect of ultrasonic scattering on inspection of austenitic welds* funded by the Commission of the European Communities under the Standards, Measurements & Testing Programme, 1996 - 1999, DG XII, Brussels; BAM, Lab. VIII. 42, D-12200 Berlin

[128] T. D. K. Ngoc, W. G. Mayer, *Numerical integration method for reflected beam profiles near Rayleigh angle*, J. Acoust. Soc. Am. **67** (1980) 1149-1152

[129] T. D. K. Ngoc, W. G. Mayer, *A general description of ultrasonic nonspecular reflection and transmission effects for layered media*, IEEE Transactions and Ultrasonics **27** (1980) 229-236

[130] T. D. K. Ngoc, W. G. Mayer, *Influence of plate mode structure and Gaussian beam profile characteristics on ultrasonic reflection and transmission*, IEEE Transactions and Ultrasonics **29** (1982) 112-114

[131] G. Nolze, *Determination of the Crystallographic Orientation in Austenitic Weld Metal by Means of X-Ray Diffraction Investigation* in the project SMT4-CT95-2012 "Effect of Ultrasonic Scattering on Inspection of Austenitic Welds" funded by the Commission of the European Communities under the Standards, Measurements & Testing Programme, 1996 - 1999, DG XII, Brussels; BAM, Lab. VIII.42, D-12200 Berlin

[132] G. Nolze, *Determination of the Crystallographic Structure in Austenitic Weld Metal X 6 CrNi 18 11 by Measurement of Kikuchi-Diagrams at the Scanning Electron Microscope* in the project SMT4-CT95-2012 "Effect of Ultrasonic Scattering on Inspection of Austenitic Welds" funded by the Commission of the European Communities under the Standards, Measurements & Testing Programme, 1996 - 1999, DG XII, Brussels; BAM, Lab. VIII.42, D-12200 Berlin

[133] A. N. Norris, *A theory of pulse propagation in anisotropic elastic solids*, Wave Motion **9** (1987) 509-532

[134] B. Nouailhas, F. Champigny, S. Vermersch, F. Pons, G. Nguyen, *Modeling studies of bimetallic weld*, Proc. 10^{th} Int. Conf. NDE in the Nucl. & Pressure Vessel Ind., Glasgow 1990, 633-639, ASM International

[135] B. Nouailhas, G. van Chi Nguyen, F. Pons, S. Vermersch, *Ultrasonic modeling and experiments; an industrial case: bimetallic weld in nuclear power plant*, J. NDE **9** (1990) 145-153

[136] B. Nouailhas, G. Nguyen van Chi, *Modeling study of ultrasonic propagation in bimetallic weld*, Ultrasonics International 91 Conf. Proc., 563-566

[137] J. A. Ogilvy, *A model for elastic wave propagation in anisotropic media with applications to ultrasonic inspection through austenitic steel*, Br. J. NDT **27** (1985) 13-21

[138] J. A. Ogilvy, *Modeling of ultrasonic wave behaviour in austenitic steel*, Proc. 7^{th} Int. Conf. on NDE in the Nuclear Industry, 431-434, Grenoble, 1985

[139] J. A. Ogilvy, *Computerized ultrasonic ray tracing in austenitic steel*, NDT International **18** (1985) 67-77

[140] J. A. Ogilvy, *Ultrasonic propagation in anisotropic welds and cast materials*, Proc. Conf. Math. Mod. in NDT, Cambridge (UK) (1986) 191-208, Clarendon Press, Oxford (UK) 1988

[141] J. A. Ogilvy, *Ultrasonic beam profiles and beam propagation in an austenitic weld using a theoretical ray tracing model*, Ultrasonics **24** (1986) 337-347

[142] J. A. Ogilvy, *The influence of austenitic weld geometry and manufacture on ultrasonic inspection of welded joints*, Brit. J. NDT **29** (1987) 147-156

[143] J. A. Ogilvy, *On the use of focused beams in austenitic welds*, Brit. J. NDT **29** (1987) 238-246

[144] J. A. Ogilvy, *Ultrasonic reflection properties of planar defects within austenitic welds*, Ultrasonics **26** (1988) 318-327

[145] J. A. Ogilvy, *A user guide and manual for the computer program* RAYTRAIM, *AERE-R.13426, Harwell Lab., Theoretical Physics Div., Oxfordshire OX11 0RA, 1989*

[146] J. A. Ogilvy, *A layered media model for ray propagation in anisotropic inhomogeneous materials*, Appl. Math. Modelling **14** (1990) 237-247

[147] J. A. Ogilvy, *An iterative ray tracing model for ultrasonic nondestructive testing*, NDT & E Int. **25** (1992) 3-10

[148] P. D. Panetta, R. B. Thompson, F. J. Margetan, *Use of electron backscatter diffraction in understanding texture and the mechanisms of backscattered noise generation in titanium alloys*, Review of Progress in QNDE **17** (1998) 89-96

[149] V. Pavlik, T. Reichel, *Modellierung und Computersimulation des Schweissens*, ISF Direkt 12 (Nov. 1995) 2

[150] Claudio Pecorari, Piaras A. Kelly, *The quasi-static approximation for a cracked interface between a layer and a substrate*, J.Acoust.Soc.Am. **107** (2000) 2454 - 2461

[151] R. A. Roberts, *Ultrasonic beam transmission at the interface between an isotropic and a transversely isotropic solid half-space*, Ultrasonics **26** (1988) 139-147

[152] R. J. Roe, W. R. Krigbaum, *Description of crystallite orientation in polycrystalline materials having fiber texture*, J. of Chemical Physics, **40** (1964) 2608 -2615

[153] R. J. Roe, *Description of crystallite orientation in polycrystalline materials III: General solution to pole figure inversion*, J. Appl. Phys., **36** (1964) 2024-2031

[154] S. I. Rokhlin, M. Hefets, M. Rosen, *An elastic interface wave guided by a thin film between two solids*, J. Appl. Phys. **51** (1980) 3579-3582

[155] S. I. Rokhlin, T. K. Bolland, L. Adler, *Reflection and refraction of elastic waves on a plane interface between two generally anisotropic media*, J. Acoust. Soc. Am. **79** (1986) 906-917

[156] S. I. Rokhlin, T. K. Bolland, L. Adler, *Splitting of domain of angles for incident wave vectors in elastic anisotropic media*, J. Appl. Phys. **59** (1986) 3672-3677

[157] S. I. Rokhlin, D. Marom, *Study of adhesive bonds using low-frequency obliquely incident ultrasonic waves*, J. Acoust. Soc. Am. **80** (1986) 585-590

[158] S. I. Rokhlin, Y. J. Wang, *Analysis of boundary conditions for elastic wave interaction with an interface between two solids*, J. Acoust. Soc. Am. **89** (1991) 503-515

[159] S. I. Rokhlin, Y. J. Wang, *Equivalent boundary conditions for thin orthotropic layer between two solids: Reflection,refraction and interface waves*, J. Acoust. Soc. Am. **91** (1992) 1875-1887

[160] S. I. Rokhlin, *Ultrasonic characterization of interfaces*, J. Acoust. Soc. Am. **92** (1992) 1729-1742

[161] S. I. Rokhlin (Edt.), *Modelling and ultrasonic characterization of interfaces*, Special Issue of J. NDE **11** (1992) No. 3/4, 107-278

[162] S. I. Rokhlin, W. Huang, *Ultrasonic wave interaction with a thin anisotropic layer between two anisotropic solids: Exact and asymptotic boundary condition methods*, J. Acoust. Soc. Am. **92** (1992) 1729-1742

[163] S. I. Rokhlin, W. Huang, *Ultrasonic wave interaction with a thin anisotropic layer between two anisotropic solids. II. Second-order asymptotic boundary conditions*, J. Acoust. Soc. Am. **94** (1993) 3405-3420

[164] S. I. Rokhlin, *Ultrasonic characterization of interfaces*, Ultrasonics International 93 Conference Proceedings, p. 25-39, Butterworth-Heinemann Ltd., Wien, 1993

[165] J. H. Rose, R. A. Roberts, F. J. Margetan, *Time-domain analysis of ultrasonic reflection from imperfect Interfaces*, J. NDE **11** (1992) 151-166

[166] A. Schoch, *Seitliche Versetzung eines total reflektierten Strahls bei Ultraschallwellen*, Acoustics **2** (1952) 18-19

[167] M. Schoenberg, *Elastic wave behaviour across linear slip interfaces*, J. Acoust. Soc. Am. **68** (1980) 1516-1521

[168] A. Schumm, *Using CAD representations in transient sound field calculations through curved surfaces*, Dissertation, 1997, Paris

[169] Th. Seldis, *Measurement of ultrasonic wave attenuation: C-scan integration technique*, in the project SMT4-CT95-2012 "Effect of Ultrasonic Scattering on Inspection of Austenitic Welds" funded by the Commission of the European Communities under the Standards, Measurements & Testing Programme, 1996 - 1999, DG XII, Brussels; BAM, Lab. VIII.42, D-12200 Berlin

Th. Seldis, C. Pecorari, *Scattering-induced attenuation of an ultrasonic beam in austenitic steel*, J. Acoust. Soc. Am. **108** (2000) 580-587

[170] M. G. Silk, *A computer model for ultrasonic propagation in complex orthotropic structures*, Ultrasonics **19** (1981) 208-212

[171] M. Spies, *Elastische Wellen in transversal-isotropen Medien: Ebene Wellen, Gaußsche Wellenpakete, Greensche Funktionen, elastische Holographie*, Fraunhofer-Institut für zerstörungsfreie Prüfverfahren, Ber.-Nr. 920175-TW, 06. 11. 1992; Dissertation, Universität des Saarlandes, Saarbrücken, 1992

[172] M. Spies, *Elastic waves in homogeneous and layered transversely isotropic media: plane waves and Gaussian wave packets. A general approach*, JASA **95** (1994) 1748-1760

[173] M. Spies, F. Walte, *Application-directed modeling of radiation and propagation of elastic waves in anisotropic media: GPSS and OPOSSM*, Rev. Progr. Quant. NDE **14** (1995) 1013-1020, Plenum Press, New York

[174] M. Spies, F. Walte, H. Rieder, H. Wüstner, *Computer aided design and modeling for ultrasonic applications, CADMUS-on-PC*, IEEE Ultrasonics Symposium, 1996, Vol. **1** (1996) 677-680

[175] M. Spies, *Elastische Wellen in austenitischen Schweißstrukturen. Modellierung mittels generalisierter Punktquellensynthese*, Materialpr. **38** (1996) 354-359

[176] M. Spies, M. Kröning, *A computationally efficient modeling code for SH-wave propagation in austenitic welds using an explicit space-time Green's function*, Rev. Progr. Quant. NDE **15** (1996) 145-152, Plenum Press, New York

[177] F. E. Stanke, *Unified theory and measurements of elastic waves in polycrystalline materials*, Ph. D. Thesis, Stanford University, Stanford, CA (1983)

[178] F. E. Stanke, G. S. Kino, *A unified theory for elastic wave propagation in polycrystalline materials*, J. Acoust. Soc. Am. **75** (1984) 665-681

[179] A. M. Stansfield, *A Ray tracing model for the propagation of ultrasound through an austenitic weld*, Central Electricity Generating Board, Report No. OED/STN/87/20031/R, Jan. 1987

[180] T. H. Tan, *Reciprocity relations for scattering of plane, elastic waves*, J. Acoust. Soc. Am. **61** (1977) 928-931

[181] J. A. Turner, *Elastic wave propagation and scattering in heterogeneous, anisotropic media: Textured polycrystalline materials*, J. Acoust. Soc. Am. **106** (1999) 541-552

[182] K. Wu, P. B. Nagy, L. Adler, *A general technique for wave propagation problems in anisotropic media*, Review of Progress in QNDE **10A** (1991) 137-144

[183] H. Wüstenberg, *Untersuchungen zum Schallfeld von Winkelprüfköpfen für die Materialprüfung mit Ultraschall*, Dissertation, Technische Universität Berlin, 1974, D 83

[184] I. Yalda-Mooshabad, R. B. Thompson, *Influence of texture and grain morphology on the two-point correlation of elastic constants: Theory and implications on ultrasonic attenuation and backscattering*, Review of progress in QNDE, **14** (1995) 1939-1946

[185] S. Zeroug, L. B. Felsen, *Nonspecular reflection of beams from liquid-solid interfaces*, J. NDE **11** (1992) 263-278

Appendix A

Equivalence of group and energy velocities

As defined in (2.1), the plane wave is of the form

$$\begin{aligned} u_k &= A\, p_k\, \exp\left(\mathbf{k}.\mathbf{r} - \omega\, t\right) \\ &= A\, p_k\, \cos\phi_p \end{aligned} \tag{A.1}$$

where $(\mathbf{k}.\mathbf{r} - \omega\, t) = \phi_p$ is the phase.

$$\dot{u}_k = A\, p_k\, \omega\, \sin\phi \tag{A.2}$$

Now, according to Hooke's law

$$T_{ij} = C_{ijmn}\, S_{mn} \tag{A.3}$$

$$S_{kl} = \frac{1}{2}\left(\frac{\partial u_k}{\partial u_l} + \frac{\partial u_l}{\partial u_k}\right) \tag{A.4}$$

Substituting the equation A.4 in the equation A.3 yields

$$T_{ij} = \frac{1}{2}\, C_{ijmn}\, \left(\frac{\partial u_m}{\partial u_n} + \frac{\partial u_n}{\partial u_m}\right) \tag{A.5}$$

In equation A.5, k, l are dummy indices, therefore they have to be summed up according to Einstein's summation convention. Therefore, the equation A.5 can be written as

$$T_{ij} = C_{ijmn}\, \frac{\partial u_m}{\partial u_n} \tag{A.6}$$

where

$$\frac{\partial u_m}{\partial u_n} = -k_m\, p_n\, \sin\phi \tag{A.7}$$

$$\begin{aligned} E_{kin} &= \frac{1}{2}\, \rho\, \dot{u}^2 \\ &= \frac{1}{2}\, A^2\, \omega^2\, p_k^2\, \sin\phi_p^2 \end{aligned} \tag{A.8}$$

The kinetic energy E_{kin} and the potential energy E_{pot} for a plane wave is equal (Federov 1968, Kline 1992 [15, 18]). This can be shown as follows:
The equation of motion is given by

$$\rho\, \ddot{u}_i = C_{ijmn}\, \frac{\partial^2 u_n}{\partial x_j \partial x_m} \tag{A.9}$$

Substituting the equation A.1 in A.9 yields

$$\rho\, \omega^2\, p_i = C_{ijmn}\, k_j\, k_m\, p_n \tag{A.10}$$

The expression for the potential energy is

$$\begin{aligned} E_{pot} &= \frac{1}{2}\, T_{ij}\, S_{kl} \\ &= \frac{1}{2}\, C_{ijmn}\, S_{mn}\, S_{kl} \end{aligned} \tag{A.11}$$

Using the relation derived in the equations A.5, A.7, and A.10, the expression for the potential energy simplifies to

$$\begin{aligned} E_{pot} &= \frac{1}{2}\, C_{ijmn}\, k_i\, k_m\, p_j\, p_n\, \sin^2\phi \\ &= \frac{1}{2}\, A^2\, \rho\, \omega^2\, {p_n}^2\, \sin^2\phi \end{aligned} \tag{A.12}$$

The expressions A.12 and A.8 are equal, which means, that for the plane wave kinetic and potential energies are equal. The total energy is $E_{tot} = 2\, E_{kin} = 2\, E_{pot}$.
The time average (taken per one stress cycle) of the energy density is

$$\begin{aligned} \overline{E_{tot}} &= \frac{1}{2\pi} \int_0^{2\pi} A^2\, \rho\, \omega^2\, {u^2}_k\, \sin^2\phi\, d\phi \\ &= \frac{1}{2} A^2\, \rho\, \omega^2 \end{aligned} \tag{A.13}$$

Now the energy flux density vector is given by:

$$E_i = -T_{ij}\, \dot{u}_j \tag{A.14}$$

Substituting the equations A.2 and A.6 in A.14 yields

$$E_i = A^2\, \omega\, C_{ijmn}\, k_m\, p_n\, p_j \sin^2\phi \tag{A.15}$$

Performing time averaging of the energy flux density vector over one stress cycle the equation A.15 yields

$$\overline{E}_i = \frac{1}{2\pi} \int_0^{2\pi} A^2\, \omega\, C_{ijmn}\, k_m\, p_n\, p_j \sin^2\phi\, d\phi \tag{A.16}$$

$$= \frac{1}{2} A^2\, \omega\, C_{ijmn}\, k_m\, p_n\, p_j \tag{A.17}$$

Now, dividing the equation A.16 by A.13 yields the energy velocity vector:

$$\mathbf{V}_e = \frac{\overline{E_i}}{\overline{E_{tot}}} = \frac{C_{ijmn}\, k_m\, p_n\, p_j}{\rho\, \omega} \tag{A.18}$$

The Christoffel equation can be written as

$$\rho\alpha_i = C_{ijkl}\, k_j\, k_l\, \alpha_k \tag{A.19}$$

The group velocity as defined before can be obtained as a partial derivative of ω with respect to $\mathbf{k}$.
Expressing the equation A.10 as a function of frequency yields

$$\omega^2 = \frac{C_{ijmn}}{\rho}\, k_j\, k_m\, p_n\, p_i \tag{A.20}$$

$$\frac{\partial \omega^2}{\partial k_q} = \frac{C_{ijmn}}{\rho}\, k_j\, \delta_{mq}\, p_n\, p_i + \frac{C_{ijmn}}{\rho}\, k_m\, \delta_{jq}\, p_n\, p_i \tag{A.21}$$

$$= \frac{C_{ijqn}}{\rho}\, k_j\, p_n\, p_i + \frac{C_{iqmn}}{\rho}\, k_m\, p_n\, p_i \tag{A.22}$$

$$2\,\omega\, \frac{\partial \omega}{\partial k_q} = \frac{2\, C_{iqmn}}{\rho}\, k_m\, p_n\, p_i \tag{A.23}$$

$$\frac{\partial \omega}{\partial k_q} = \frac{C_{iqmn}\; k_m\, p_n\, p_i}{\rho\, \omega} \tag{A.24}$$

It can be seen that the equation (A.24) is equivalent to (A.18). Therefore, for plane waves in lossless media, the direction of energy flow is equivalent to the direction of group velocity.

Appendix B

The transverse components of reflected and transmitted waves

The following procedure is adopted to determine the transverse components of reflected and transmitted waves. The Christoffel's matrix is split into three (3×3) matrices.
The first matrix A consists of terms containing K_x^2, K_y^2 and $K_x \cdot K_y$. That means that all the terms are independent of K_z.
The second matrix B consists of terms containing $K_x \cdot K_z$, $K_y \cdot K_z$, and finally the third matrix D consists of terms connected only with K_z^2.

$$A = \begin{bmatrix} \alpha_A & \delta_A & \epsilon_A \\ \delta_A & \beta_A & \zeta_A \\ \epsilon_A & \zeta_A & \gamma_A \end{bmatrix}$$

$$B = \begin{bmatrix} \alpha_B & \delta_B & \epsilon_B \\ \delta_B & \beta_B & \zeta_B \\ \epsilon_B & \zeta_B & \gamma_B \end{bmatrix}$$

$$D = \begin{bmatrix} c_{55} & c_{45} & c_{35} \\ c_{45} & c_{44} & c_{34} \\ c_{35} & c_{34} & c_{33} \end{bmatrix} \tag{B.1}$$

with

$$\begin{aligned}
\alpha_A &= c_{11}K_x^2 + c_{66}K_y^2 + 2 \cdot c_{16}K_x \cdot K_y \\
\beta_A &= c_{66}K_x^2 + c_{22}K_y^2 + 2 \cdot c_{26}K_x \cdot K_y \\
\gamma_A &= c_{55}K_x^2 + c_{44}K_y^2 + 2 \cdot c_{45}K_x \cdot K_y \\
\delta_A &= c_{16}K_x^2 + c_{26}K_y^2 + (c_{12} + c_{66})K_x \cdot K_y \\
\epsilon_A &= c_{15}K_x^2 + c_{46}K_y^2 + (c_{14} + c_{56})K_x \cdot K_y \\
\zeta_A &= c_{56}K_x^2 + c_{24}K_y^2 + (c_{25} + c_{46})K_x \cdot K_y
\end{aligned}$$

$$\begin{aligned}
\alpha_B &= 2 \cdot (c_{56}K_y + c_{15}K_x) \\
\beta_B &= 2 \cdot (c_{24}K_y + c_{46}K_x) \\
\gamma_B &= 2 \cdot (c_{34}K_y + c_{35}K_x) \\
\delta_B &= (c_{46} + c_{25})K_y + (c_{14} + c_{56})K_x \\
\epsilon_B &= (c_{45} + c_{36})K_y + (c_{13} + c_{55})K_x \\
\zeta_B &= (c_{44} + c_{23})K_y + (c_{36} + c_{45})K_x
\end{aligned}$$

The characteristic sixth degree polynomial in K_z, $\Omega\,(\mathbf{K})$, is as follows:

$$\begin{aligned}
\Omega\,(K_i, K_j) &= |A_1A_2A_3| \\
&+ \left[|A_1A_2B_3| + |A_1B_2A_3| + |B_1A_2A_3|\right]\, K_z \\
&+ \left[|A_1A_2D_3| + |A_1B_2B_3| + |A_1D_2A_3|\right. \\
&+ \left.|B_1A_2B_3| + |B_1B_2A_3| + |D_1A_2A_3|\right]\, K_z^2 \\
&+ \left[|A_1B_2D_3| + |A_1D_2B_3| + |B_1A_2D_3| + |B_1B_2B_3|\right. \\
&+ \left.|B_1D_2A_3| + |D_1A_2B_3| + |D_1B_2A_3|\right]\, K_z^3 \\
&+ \left[|A_1D_2D_3| + |B_1B_2D_3| + |B_1D_2B_3|\right. \\
&+ \left.|D_1A_2D_3| + |D_1B_2B_3| + |D_1D_2A_3|\right]\, K_z^4 \\
&+ \left[|B_1D_2D_3| + |D_1B_2D_3| + |D_1D_2B_3|\right]\, K_z^5 \\
&+ |D_1D_2D_3|\, K_z^6 \;=\; 0
\end{aligned} \tag{B.2}$$

Appendix C

Acoustic analogue to Snell's law

Fig. C.1 shows a ray of an acoustic plane wave travelling from the point A at an angle θ_1 to the point O at the interface in a distance d_1. The point A is at a horizontal distance s_1 from the point O at the interface. The wave gets refracted at the point O by an angle θ_2. The horizontal distance OB is s_2. The total horizontal distance from A to B is $s = s_1 + s_2$.

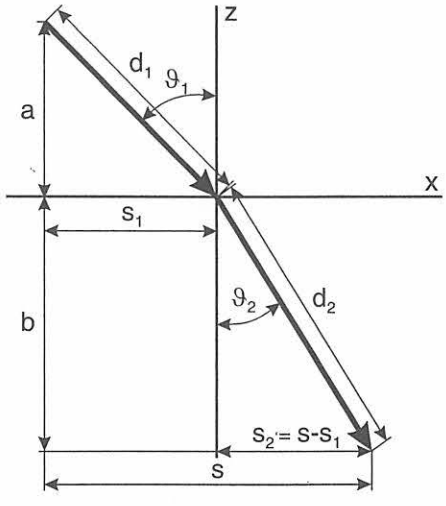

Figure C.1: *Acoustic equivalent to Snell's law*

The total time taken for the wave to travel (AOB) is the sum of the time taken to travel from A to O (t_1) and from O to B (t_2).

$$t = t1 + t2 = \frac{d1}{V_{p1}} + \frac{d2}{V_{p2}} \tag{C.1}$$

where V_{p1}, V_{p2} are the corresponding phase velocities for medium 1 and 2 respectively.

$$t = \frac{\sqrt{s_1^2 + a^2}}{V_{p1}} + \frac{\sqrt{s - {s_1}^2}}{V_{p2}} \tag{C.2}$$

From the Fermat's principle follows

$$\begin{aligned} \frac{\partial t}{\partial s_1} = 0 &= \frac{\sqrt{s_1^2 + a^2}}{V_{p1}} + \frac{\sqrt{s - {s_1}^2}}{V_{p2}} \\ &= \frac{s_1}{\sqrt{a^2 + {s^2}_1}\, V_{p1}} - \frac{s - s_1}{\sqrt{b^2 + s - {s_1}^2}\, V_{p1}} \end{aligned} \tag{C.3}$$

From fig. C.1 it can be read

$$s_1 = a \ \tan\theta_1 \tag{C.4}$$
$$s = a \ \tan\theta_1 + b \ \tan\theta_2 \tag{C.5}$$

Substituting the transformations (C.4) and (C.5) in the equation (C.3) yields:

$$V_{p1} \ \sin\theta_2 = V_{p2} \ \sin\theta_2 \tag{C.6}$$
$$\frac{V_{p1}}{\sin\theta_1} = \frac{V_{p2}}{\sin\theta_2} \tag{C.7}$$

Expressions C.6 and C.7 are equivalent to Snell's law.

Appendix D

Reflection and transmission energy coefficients at perfect interfaces

D.1 Interface between isotropic and transverse isotropic media (fusion face): Wave incidence from the isotropic base metal

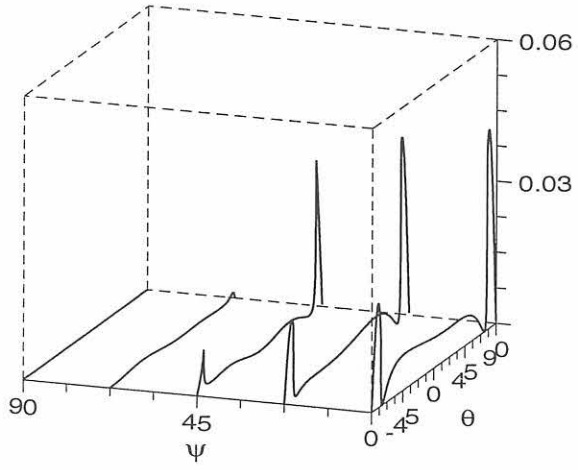

a) z-axis: r_{TvL}

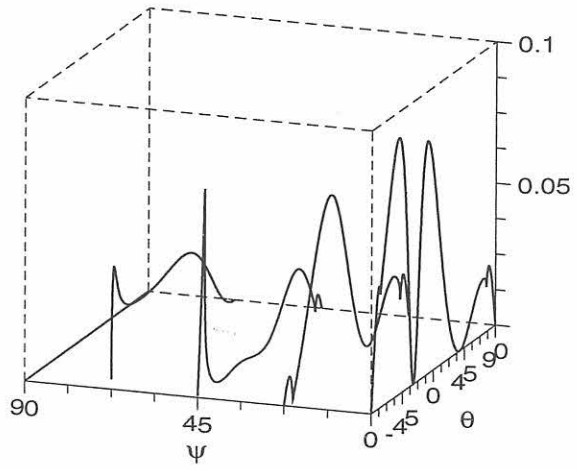

b) z-axis: t_{qT1L}

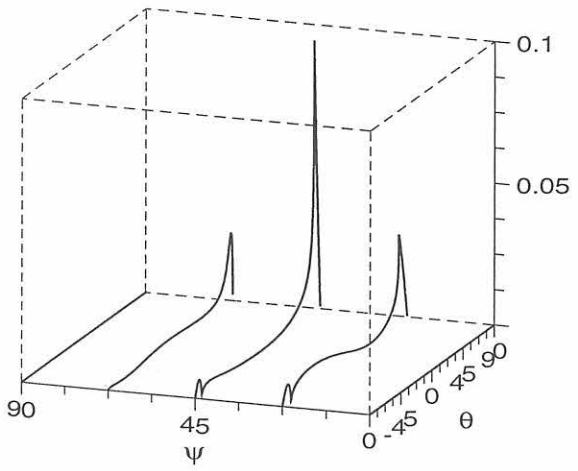

c) z-axis: r_{ThL}

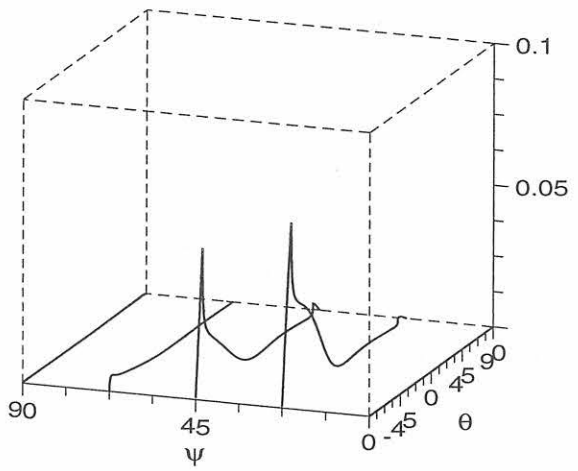

d) z-axis: t_{T2L}

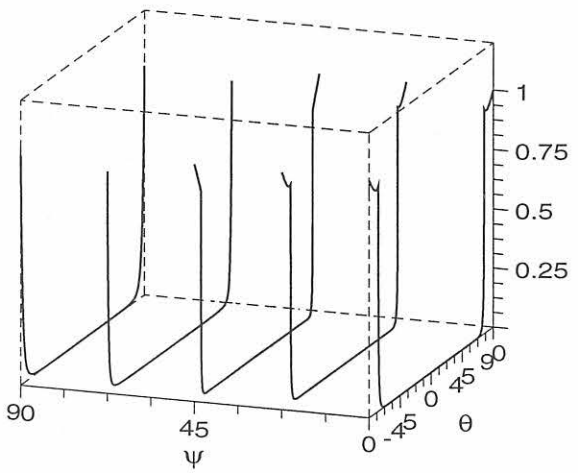

e) z-axis: r_{LL}

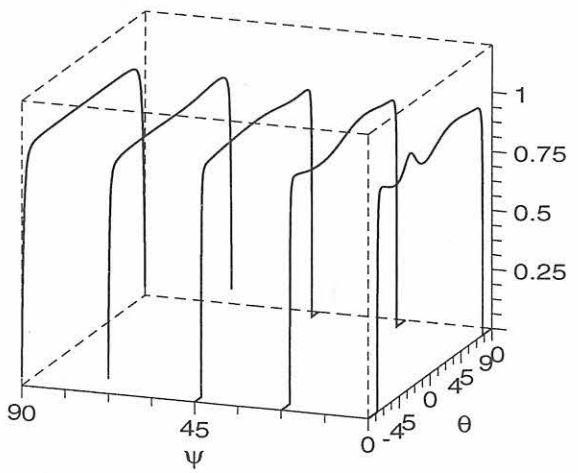

f) z-axis: t_{qLL}

Figure D.1: *Reflection and transmission energy coefficients of the three waves at the interface between isotropic and transverse isotropic media (fusion face) as a function of the incidence angle* Θ *and the layback angle* Ψ. **Longitudinal (L)** *wave incidence from the isotropic base metal. Columnar grain tilt angle* $\Phi = 22,5°$

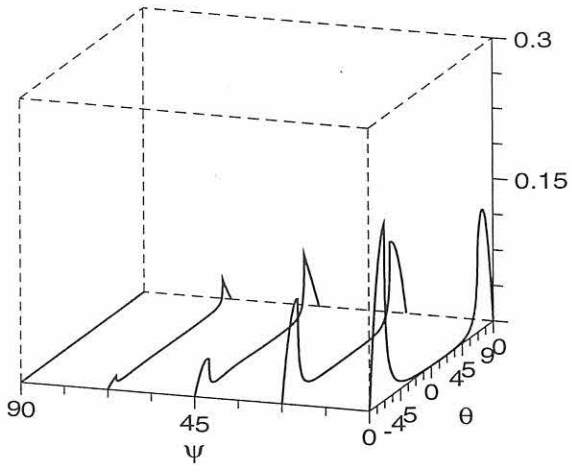

a) z-axis: r_{TvL}

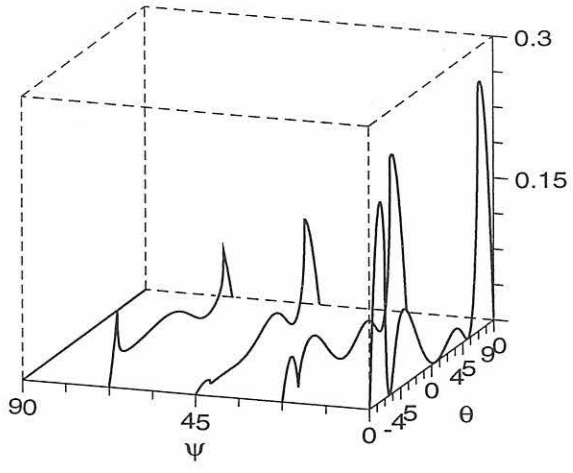

b) z-axis: t_{qT1L}

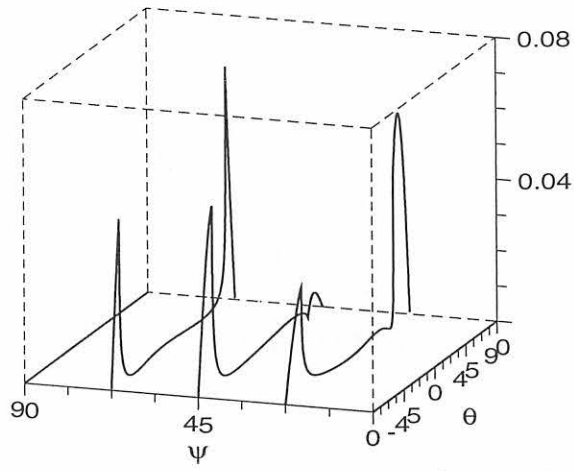

c) z-axis: r_{ThL}

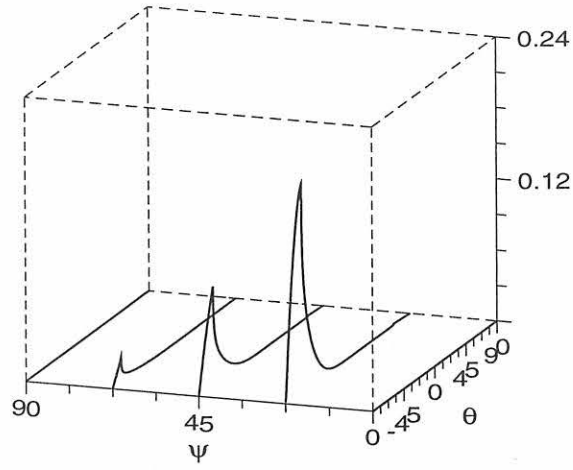

d) z-axis: t_{T2L}

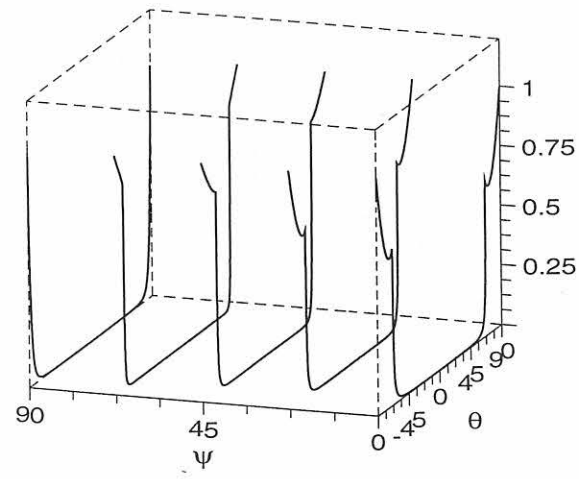

e) z-axis: r_{LL}

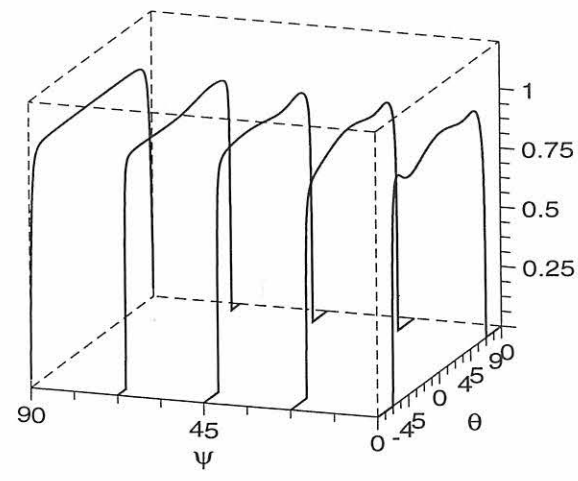

f) z-axis: t_{qLL}

Figure D.2: *Reflection and transmission energy coefficients of the three waves at the interface between isotropic and transverse isotropic media (fusion face) as a function of the incidence angle* Θ *and the layback angle* Ψ. **Longitudinal (L)** *wave incidence from the isotropic base metal. Columnar grain tilt angle* $\Phi = 45°$

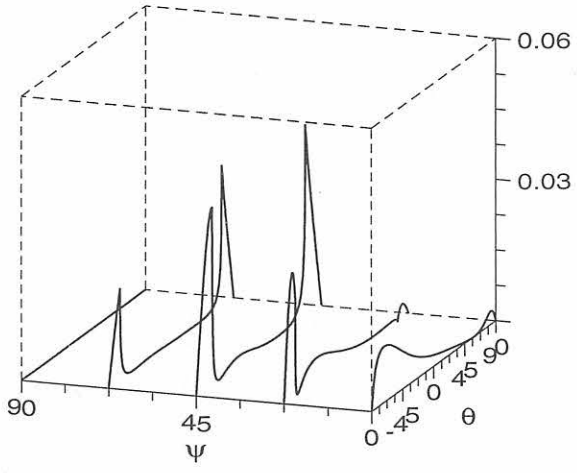

a) z-axis: r_{TvL}

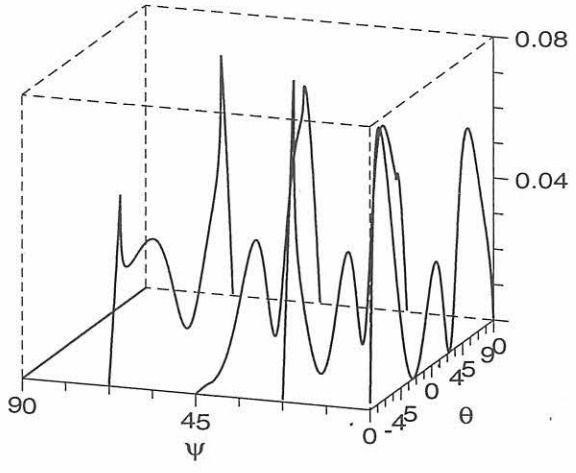

b) z-axis: t_{qT1L}

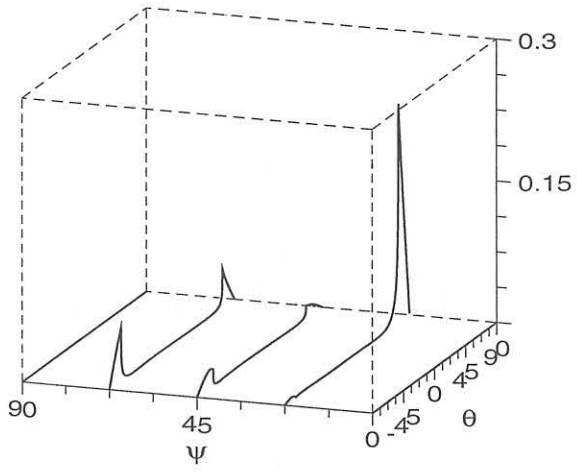

c) z-axis: r_{ThL}

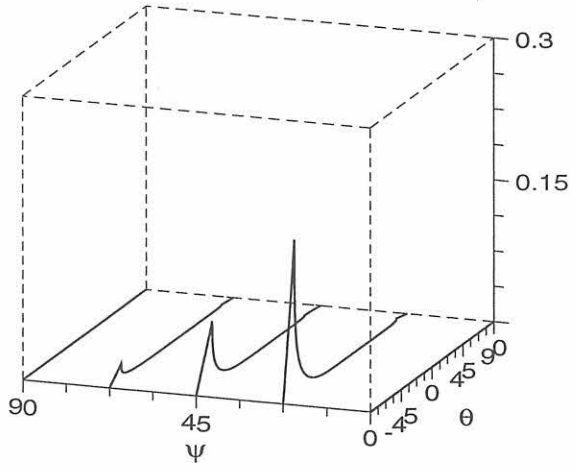

d) z-axis: t_{T2L}

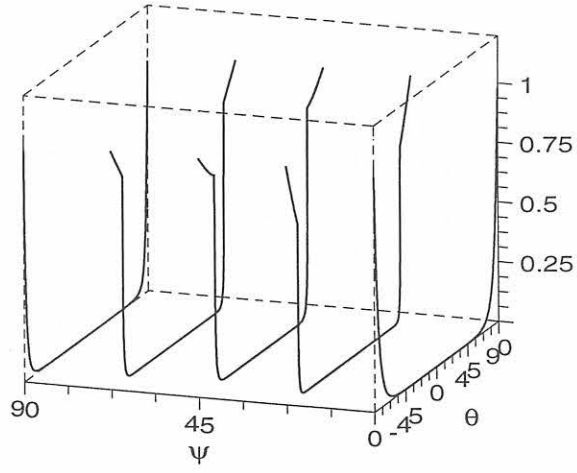

e) z-axis: r_{LL}

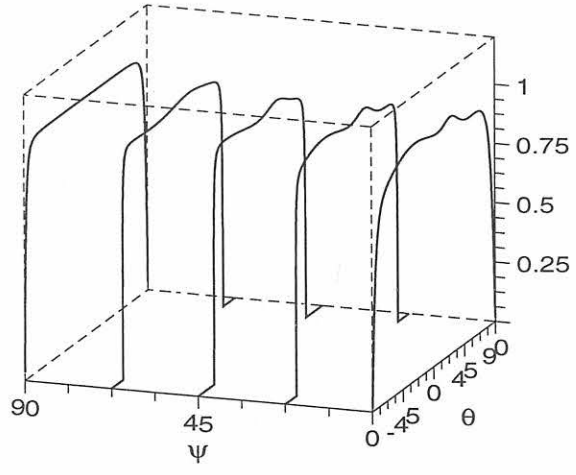

f) z-axis: t_{qLL}

Figure D.3: *Reflection and transmission energy coefficients of the three waves at the interface between isotropic and transverse isotropic media (fusion face) as a function of the incidence angle* Θ *and the layback angle* Ψ. **Longitudinal (L)** *wave incidence from the isotropic base metal. Columnar grain tilt angle* $\Phi = 67,5°$

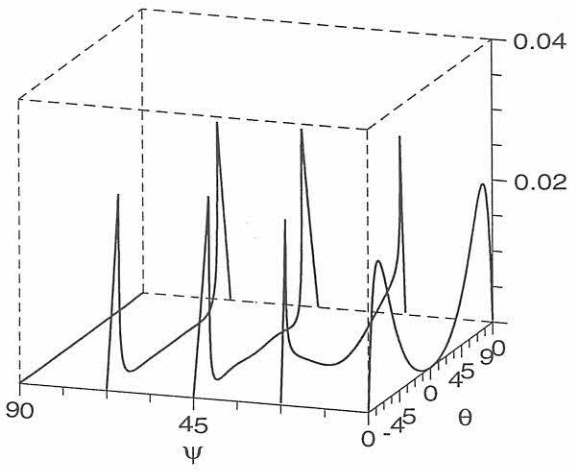

a) z-axis: r_{TvL}

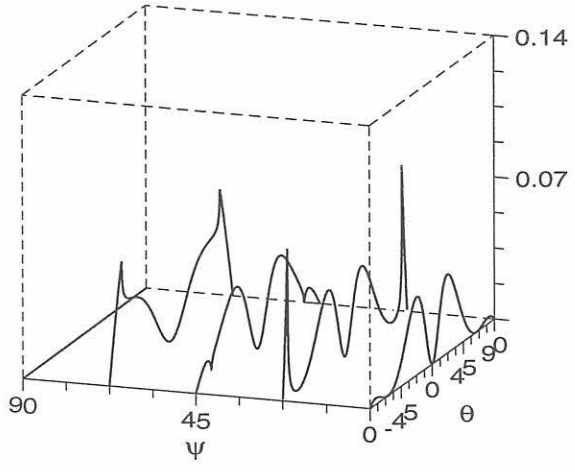

b) z-axis: t_{qT1L}

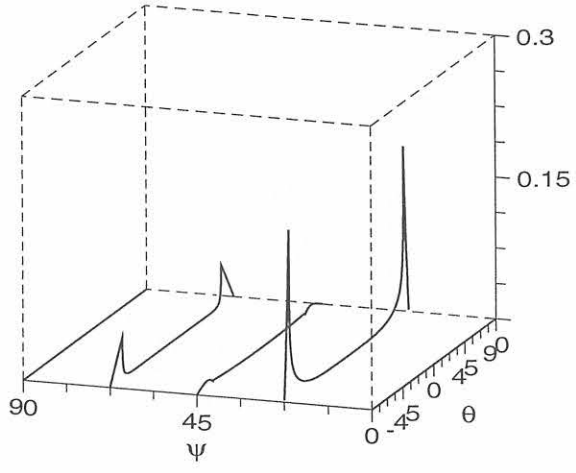

c) z-axis: r_{ThL}

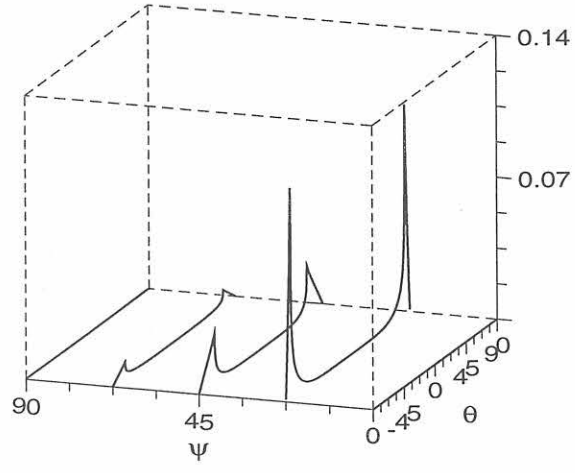

d) z-axis: t_{T2L}

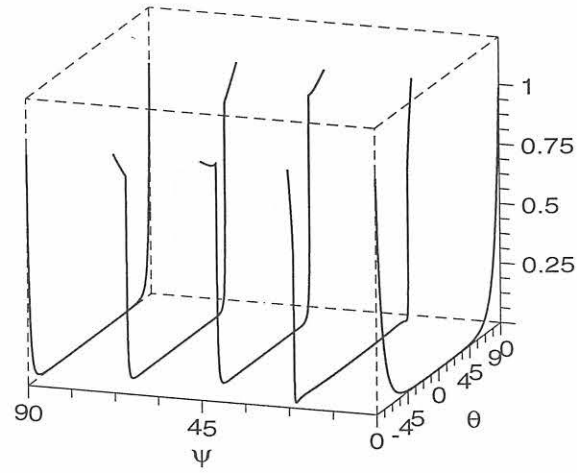

e) z-axis: r_{LL}

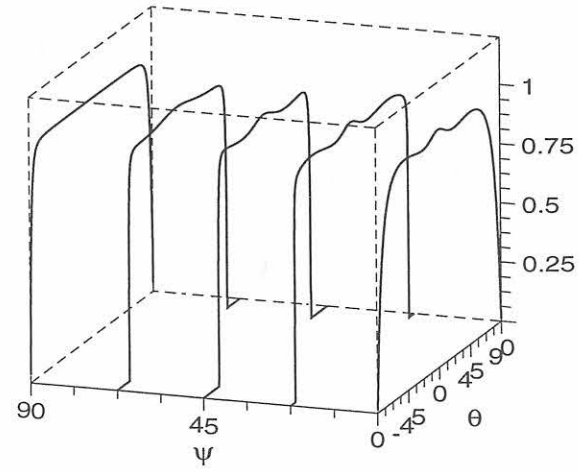

f) z-axis: t_{qLL}

Figure D.4: *Reflection and transmission energy coefficients of the three waves at the interface between isotropic and transverse isotropic media (fusion face) as a function of the incidence angle* Θ *and the layback angle* Ψ. **Longitudinal (L)** *wave incidence from the isotropic base metal. Columnar grain tilt angle* $\Phi = 90°$

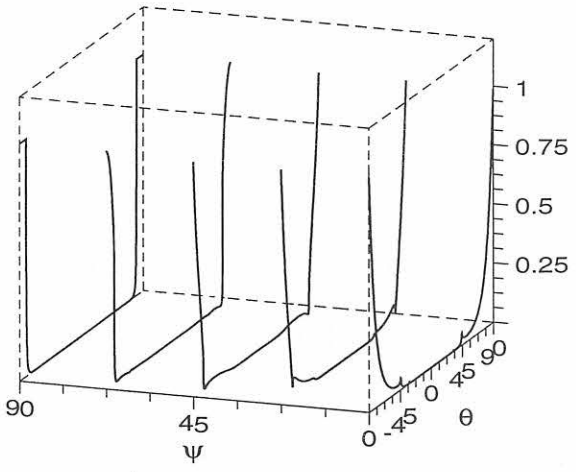

a) z-axis: r_{TvTv}

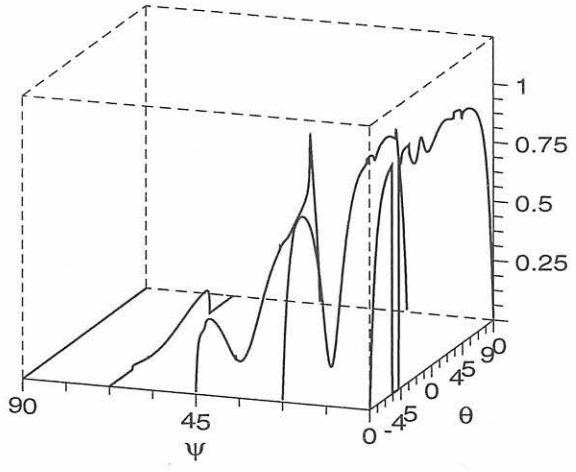

b) z-axis: t_{qT1Tv}

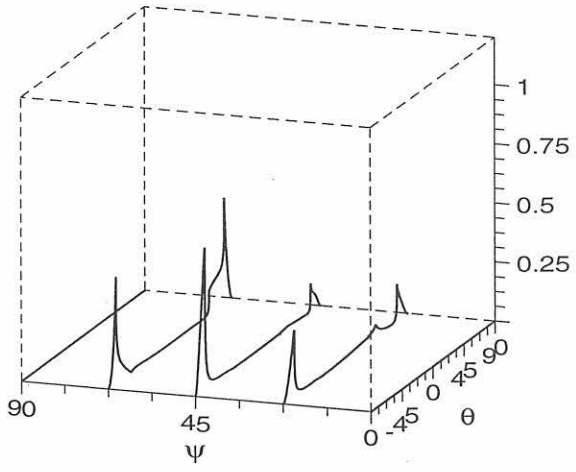

c) z-axis: r_{ThTv}

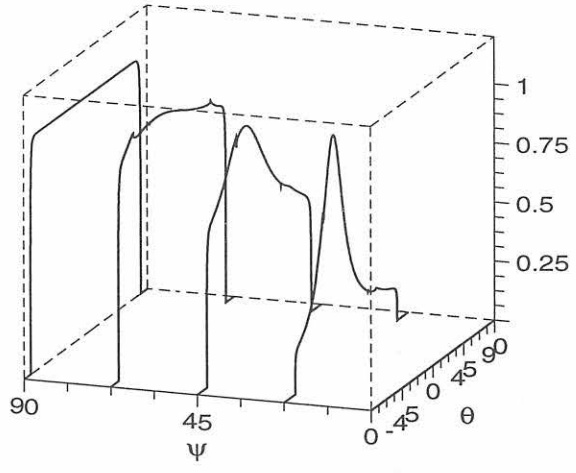

d) z-axis: t_{T2Tv}

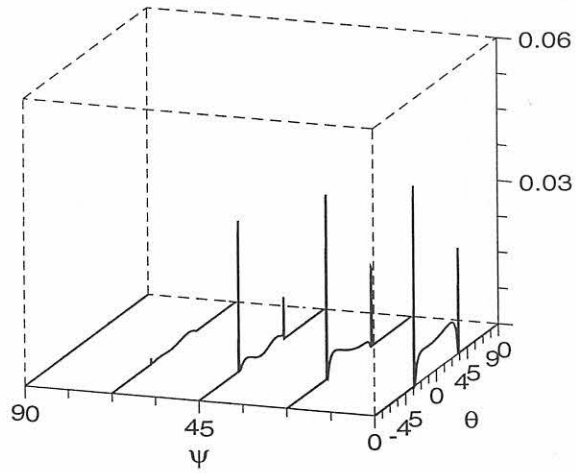

e) z-axis: r_{LTv}

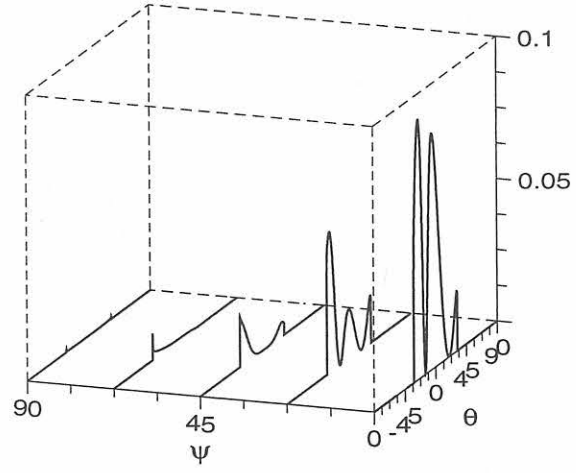

f) z-axis: t_{qLTv}

Figure D.5: *Reflection and transmission energy coefficients of the three waves at the interface between isotropic and transverse isotropic media (fusion face) as a function of the incidence angle* Θ *and the layback angle* Ψ. **Transverse vertically polarized (Tv)** *wave incidence from the isotropic base metal. Columnar grain tilt angle* $\Phi = 22,5°$

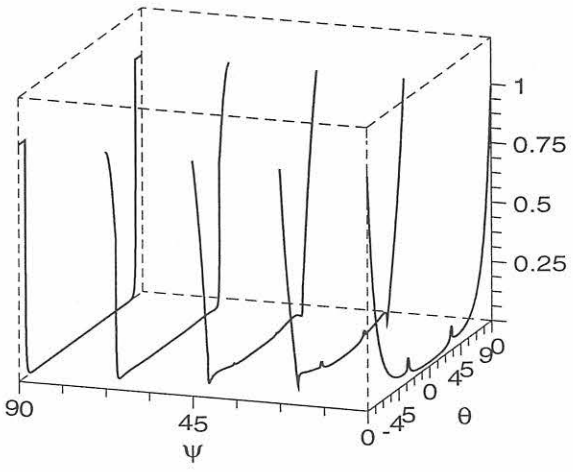

a) z-axis: r_{TvTv}

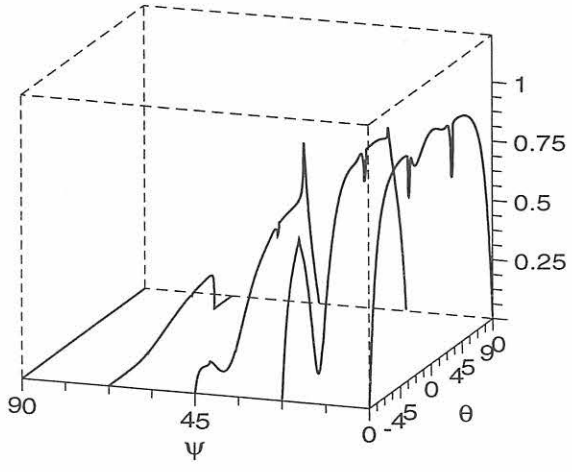

b) z-axis: t_{qT1Tv}

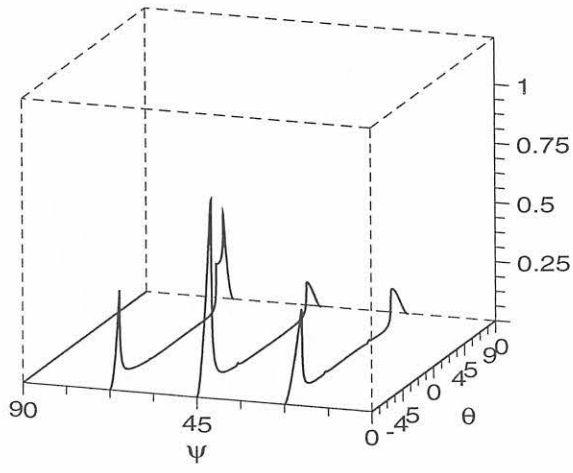

c) z-axis: r_{ThTv}

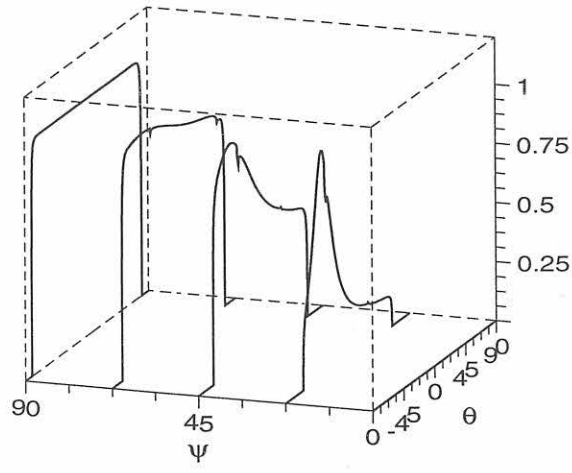

d) z-axis: t_{T2Tv}

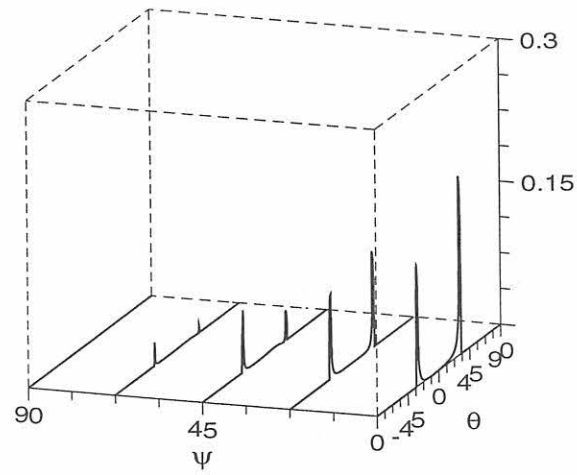

e) z-axis: r_{LTv}

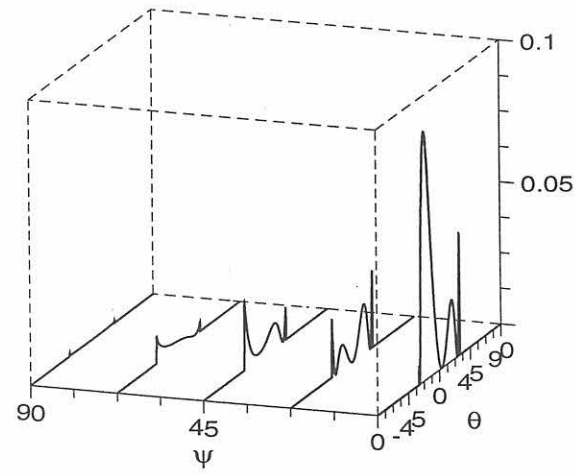

f) z-axis: t_{qLTv}

Figure D.6: *Reflection and transmission energy coefficients of the three waves at the interface between isotropic and transverse isotropic media (fusion face) as a function of the incidence angle* Θ *and the layback angle* Ψ. **Transverse vertically polarized (Tv)** *wave incidence from the isotropic base metal. Columnar grain tilt angle* $\Phi = 45°$

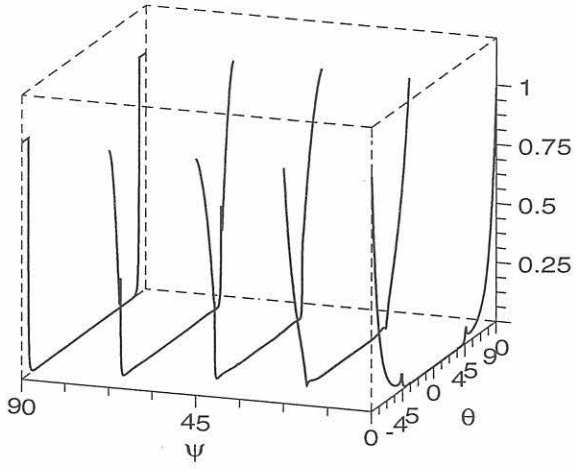

a) z-axis: r_{TvTv}

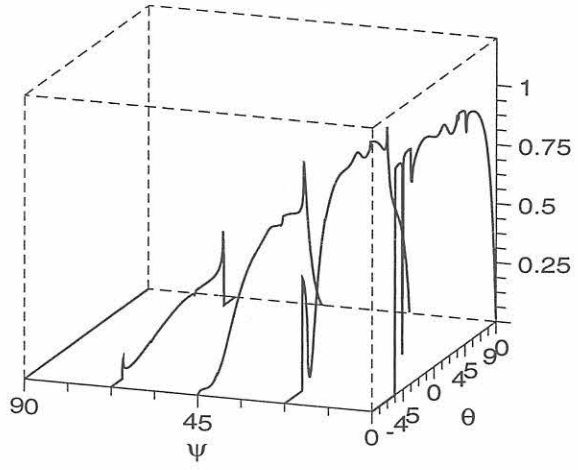

b) z-axis: t_{qT1Tv}

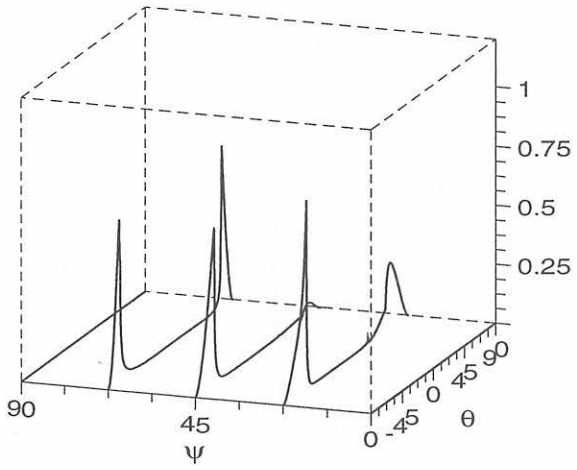

c) z-axis: r_{ThTv}

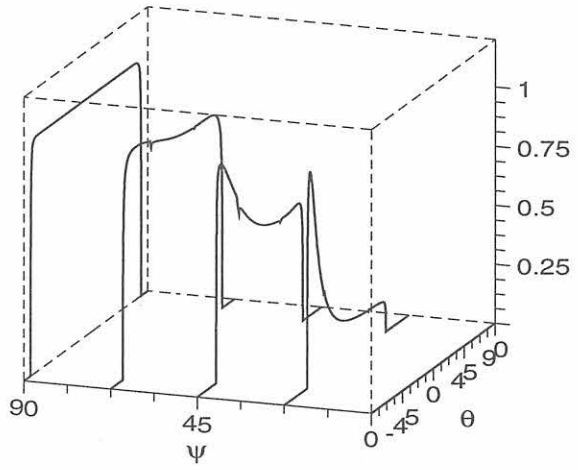

d) z-axis: t_{T2Tv}

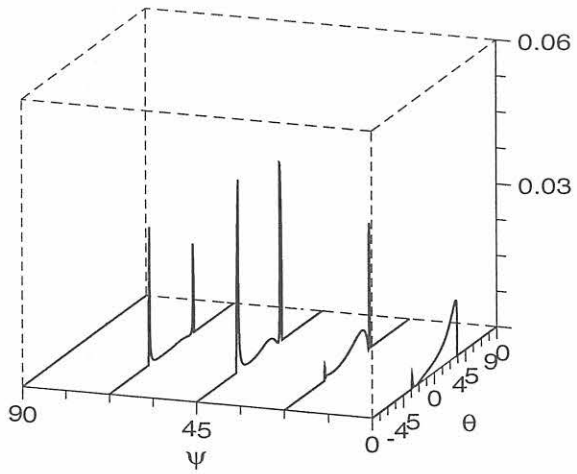

e) z-axis: r_{LTv}

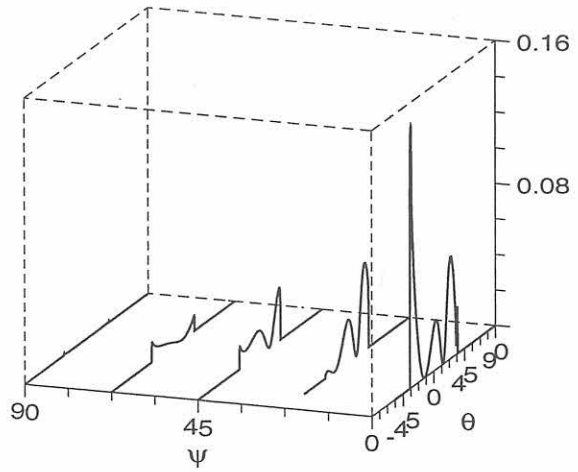

f) z-axis: t_{qLTv}

Figure D.7: *Reflection and transmission energy coefficients of the three waves at the interface between isotropic and transverse isotropic media (fusion face) as a function of the incidence angle* Θ *and the layback angle* Ψ. **Transverse vertically polarized (Tv)** *wave incidence from the isotropic base metal. Columnar grain tilt angle* $\Phi = 67,5°$

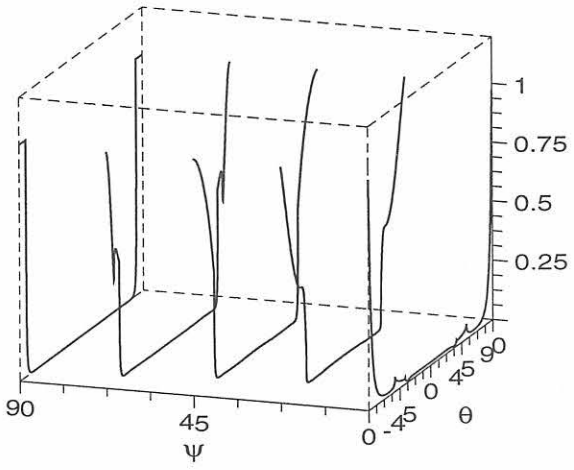

a) z-axis: r_{TvTv}

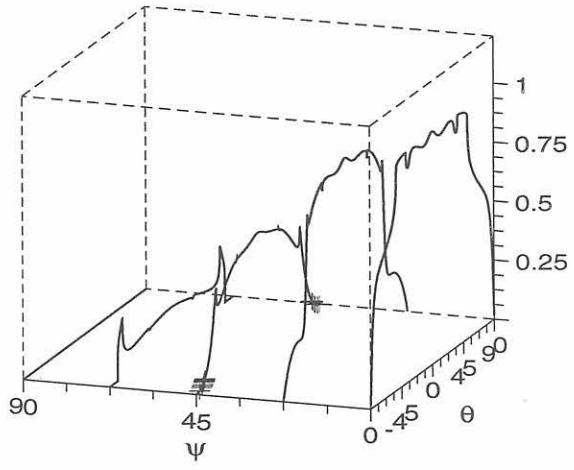

b) z-axis: t_{qT1Tv}

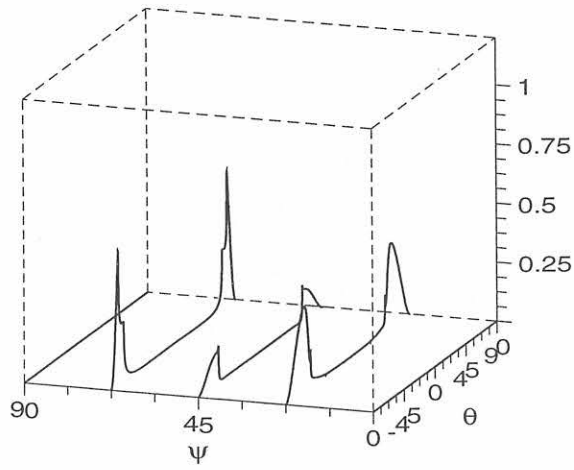

c) z-axis: r_{ThTv}

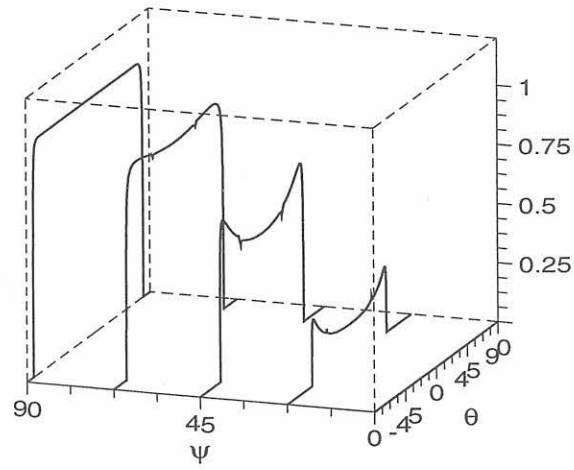

d) z-axis: t_{T2Tv}

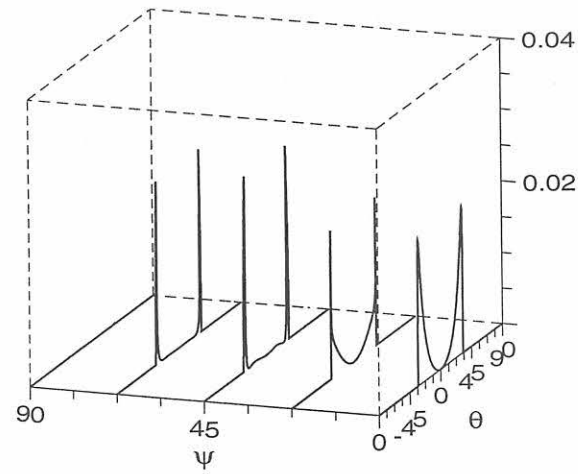

e) z-axis: r_{LTv}

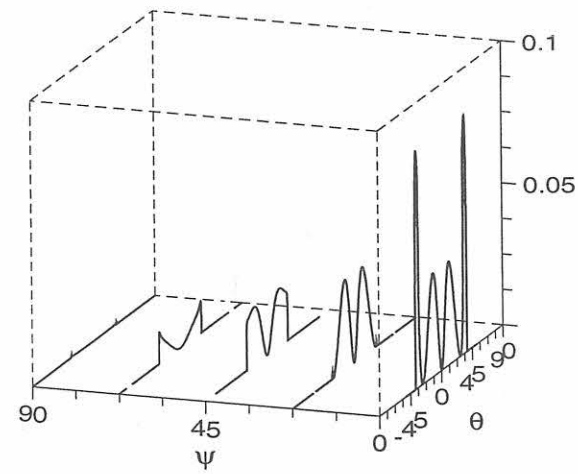

f) z-axis: t_{qLTv}

Figure D.8: *Reflection and transmission energy coefficients of the three waves at the interface between isotropic and transverse isotropic media (fusion face) as a function of the incidence angle* Θ *and the layback angle* Ψ. **Transverse vertically polarized (Tv)** *wave incidence from the isotropic base metal. Columnar grain tilt angle* $\Phi = 90°$

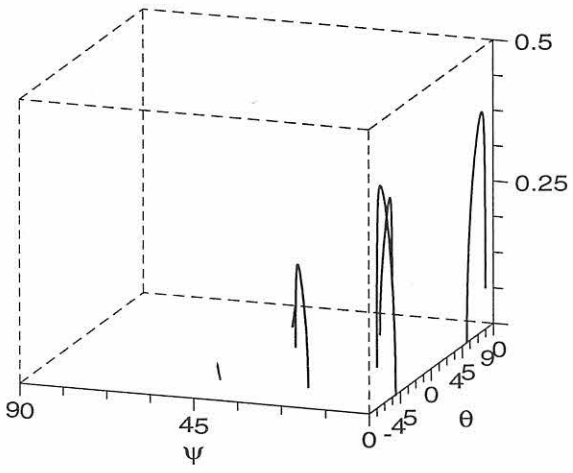

g) z-axis: $t_{qT1(2)Tv}$

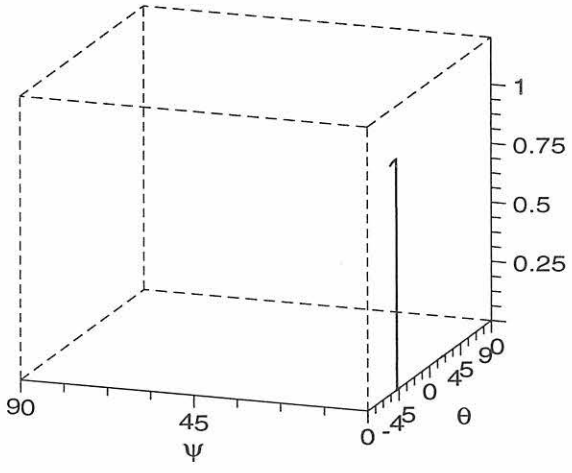

h) z-axis: $t_{qT1(2)Tv}$

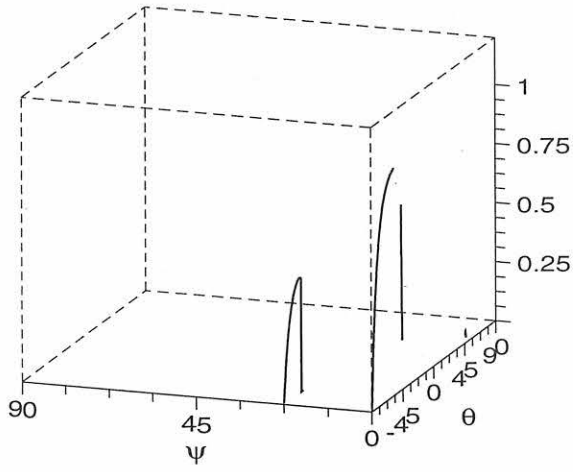

i) z-axis: $t_{qT1(2)Tv}$

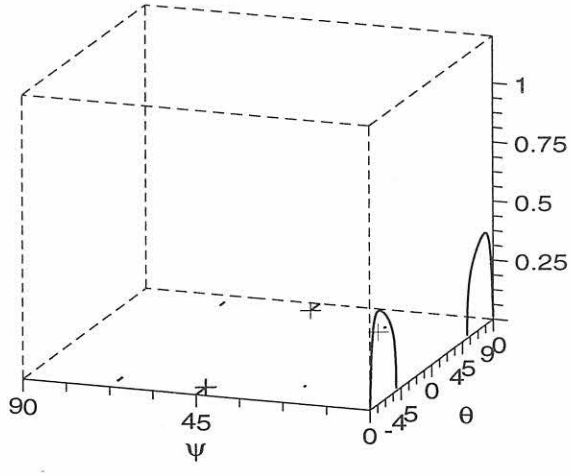

j) z-axis: $t_{qT1(2)Tv}$

Figure D.9: *Energy transmission coefficients of the second branch of the quasi transverse wave qT1(2) at the interface between isotropic and transverse isotropic media (fusion face) as a function of the incidence angle* Θ *and the layback angle* Ψ. **Transverse vertically polarized (Tv)** *wave incidence from the isotropic base metal. Columnar grain tilt angle* Φ : *a*) $0°$; *b*) $22,5°$; *c*) $67,5°$; *d*) $90°$

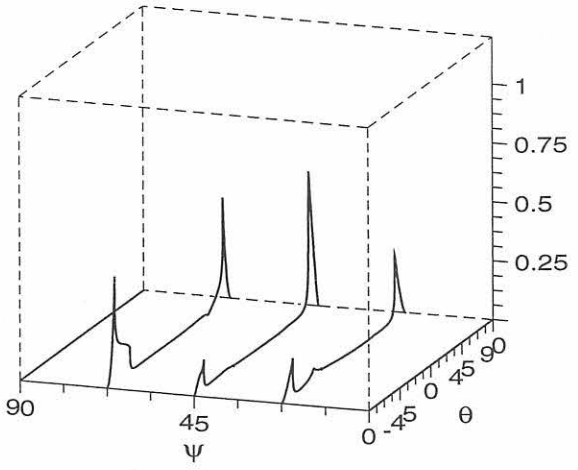

a) z-axis: r_{TvTh}

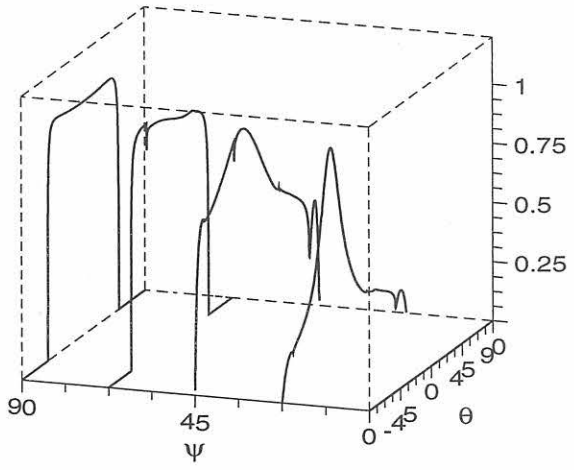

b) z-axis: t_{qT1Th}

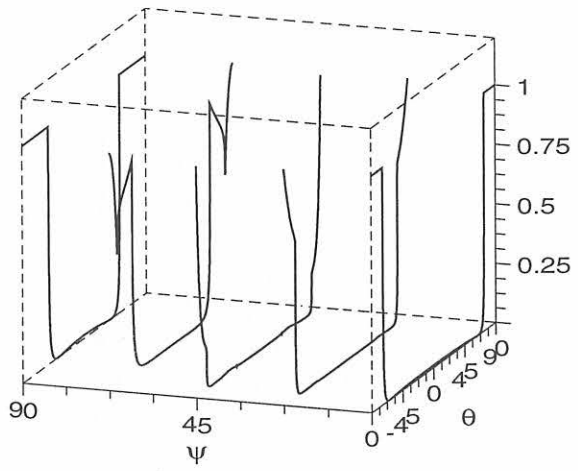

c) z-axis: r_{ThTh}

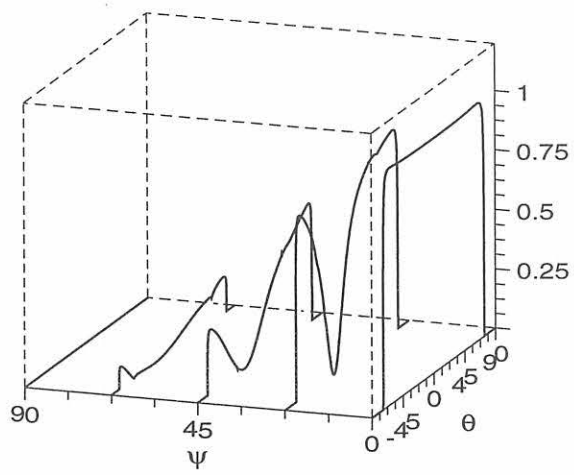

d) z-axis: t_{T2Th}

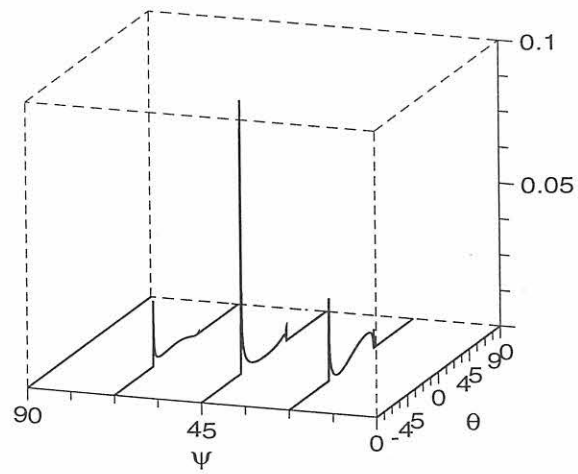

e) z-axis: r_{LTh}

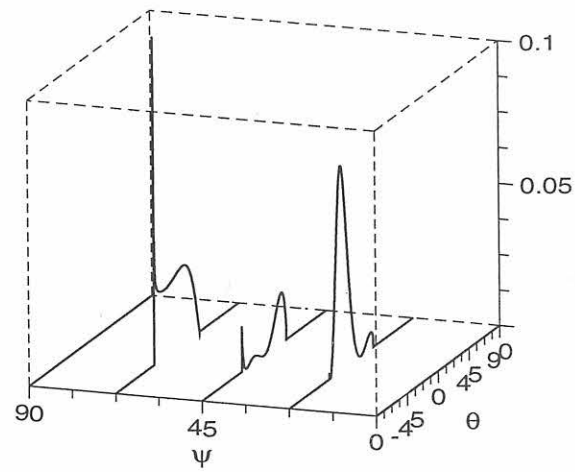

f) z-axis: t_{qLTh}

Figure D.10: *Reflection and transmission energy coefficients of the three waves at the interface between isotropic and transverse isotropic media (fusion face) as a function of the incidence angle* Θ *and the layback angle* Ψ. **Transverse horizontally polarized (Th)** *wave incidence from the isotropic base metal. Columnar grain tilt angle* $\Phi = 22,5°$

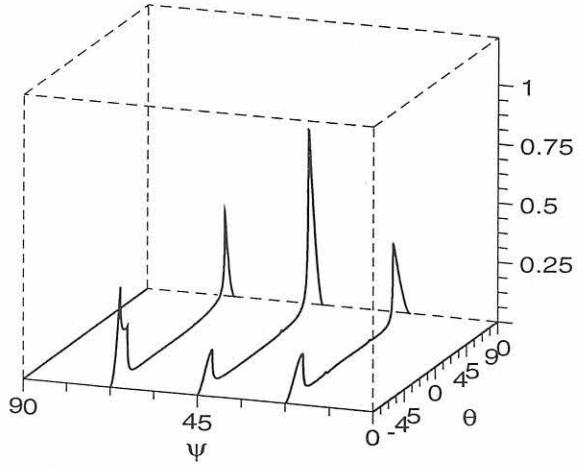

a) z-axis: r_{TvTh}

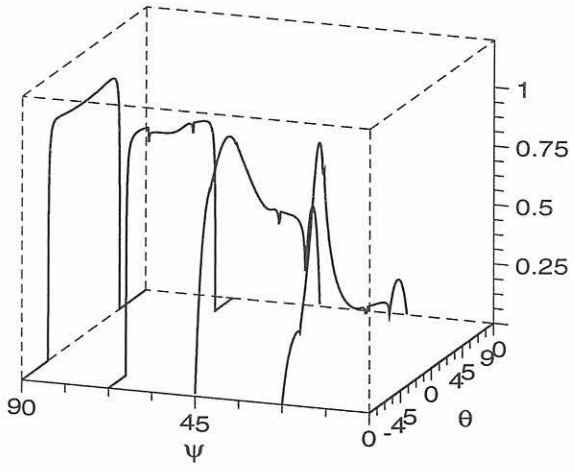

b) z-axis: t_{qT1Th}

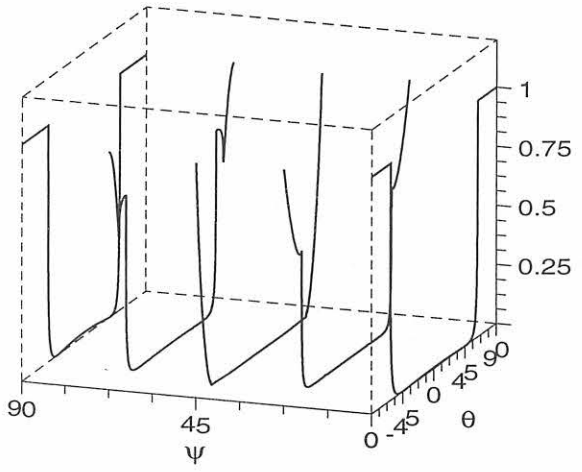

c) z-axis: r_{ThTh}

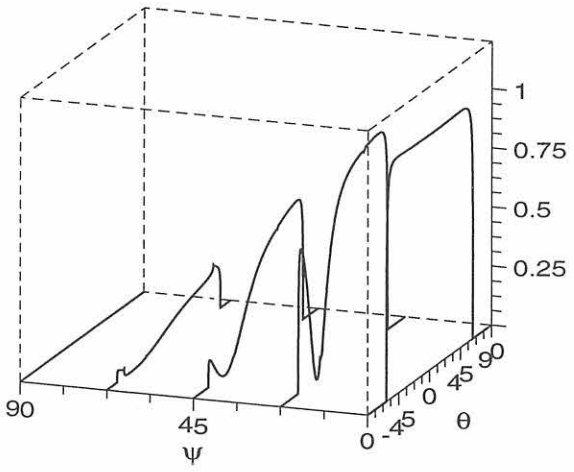

d) z-axis: t_{T2Th}

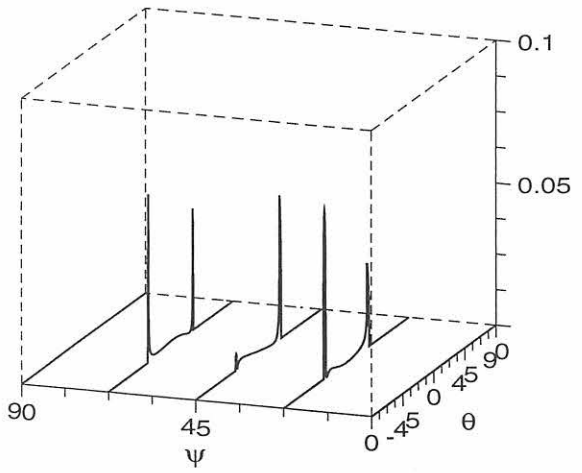

e) z-axis: r_{LTh}

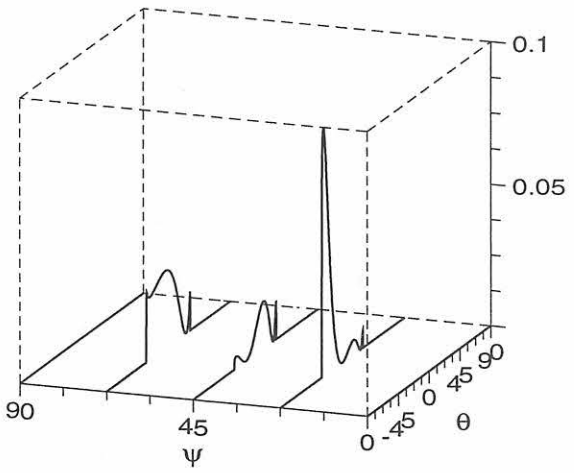

f) z-axis: t_{qLTh}

Figure D.11: *Reflection and transmission energy coefficients of the three waves at the interface between isotropic and transverse isotropic media (fusion face) as a function of the incidence angle* Θ *and the layback angle* Ψ. **Transverse horizontally polarized (Th)** *wave incidence from the isotropic base metal. Columnar grain tilt angle* $\Phi = 45°$

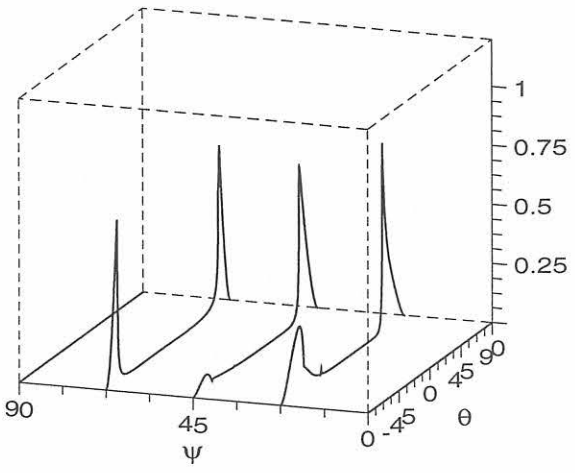

a) z-axis: r_{TvTh}

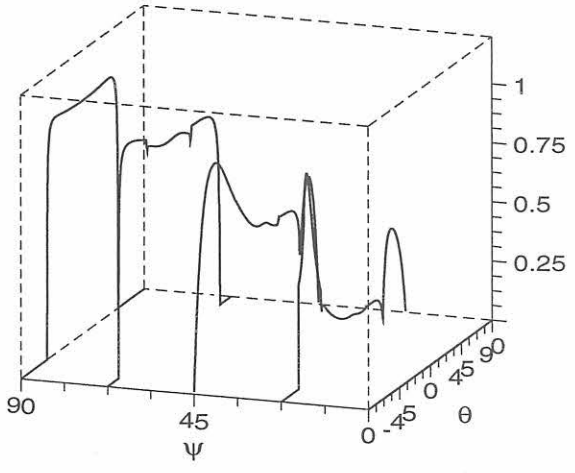

b) z-axis: t_{qT1Th}

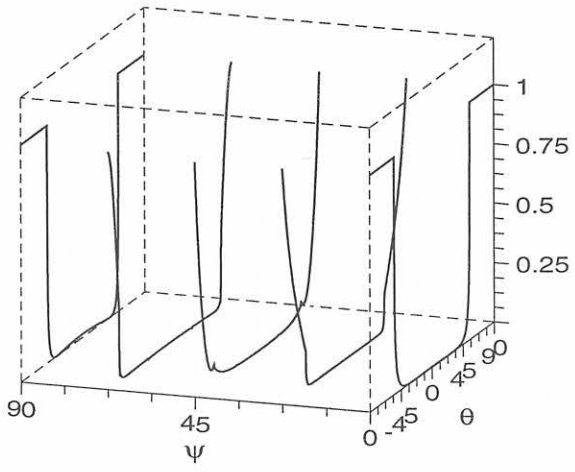

c) z-axis: r_{ThTh}

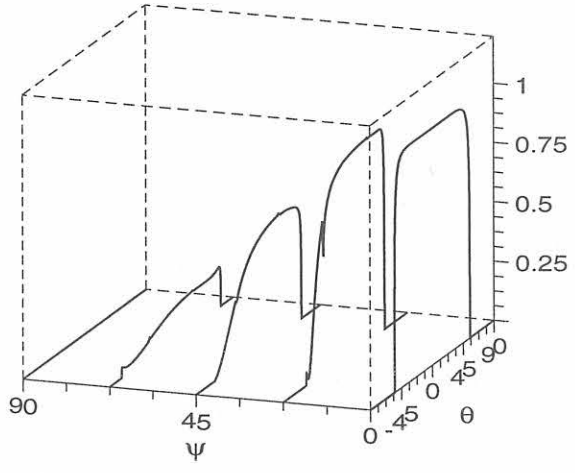

d) z-axis: t_{T2Th}

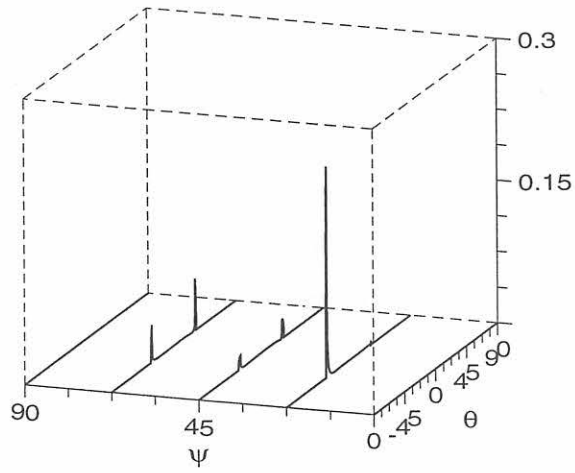

e) z-axis: r_{LTh}

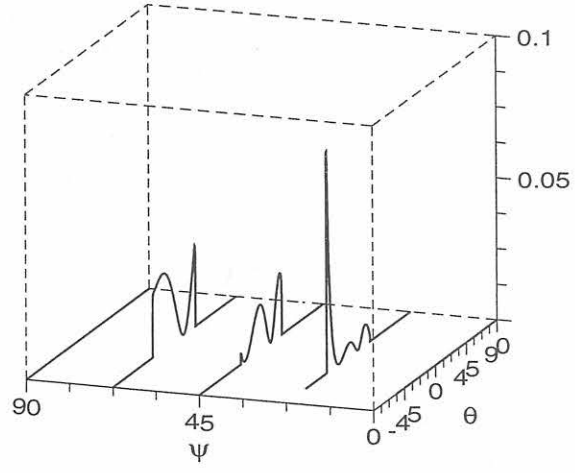

f) z-axis: t_{qLTh}

Figure D.12: *Reflection and transmission energy coefficients of the three waves at the interface between isotropic and transverse isotropic media (fusion face) as a function of the incidence angle* Θ *and the layback angle* Ψ. **Transverse horizontally polarized (Th)** *wave incidence from the isotropic base metal. Columnar grain tilt angle* $\Phi = 67,5°$

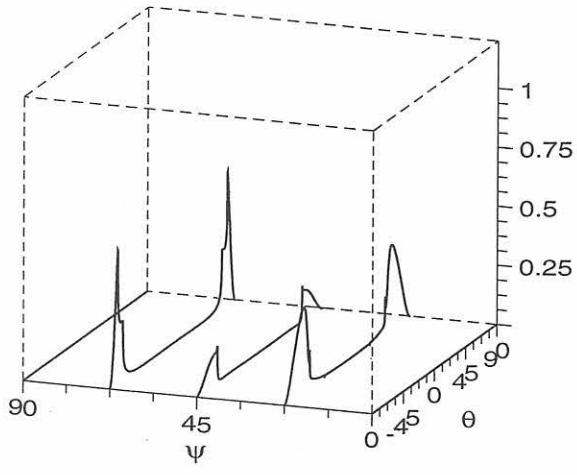

a) z-axis: r_{TvTh}

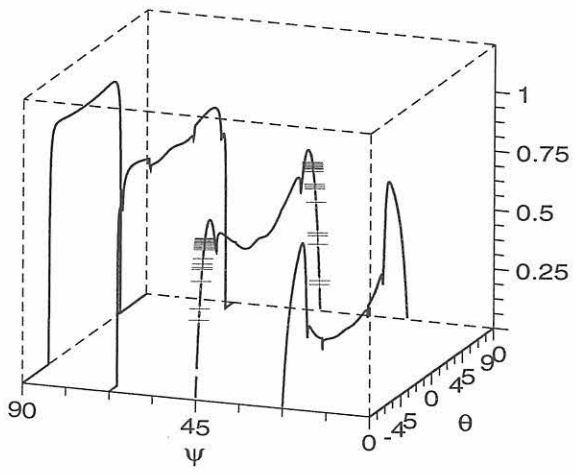

b) z-axis: t_{qT1Th}

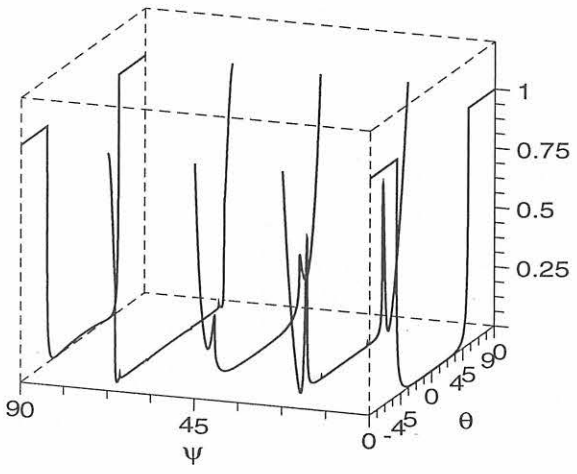

c) z-axis: r_{ThTh}

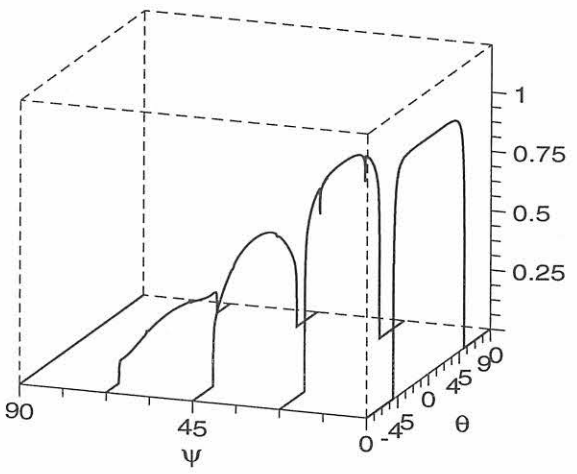

d) z-axis: t_{T2Th}

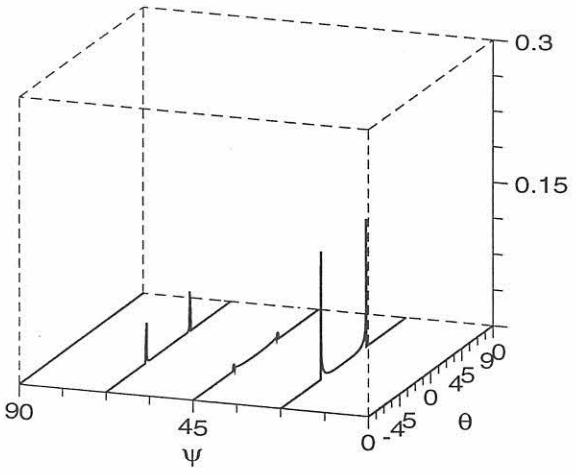

e) z-axis: r_{LTh}

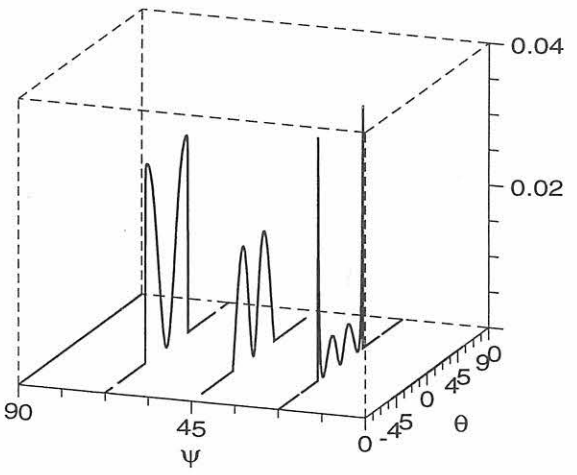

f) z-axis: t_{qLTh}

Figure D.13: *Reflection and transmission energy coefficients of the three waves at the interface between isotropic and transverse isotropic media (fusion face) as a function of the incidence angle* Θ *and the layback angle* Ψ. **Transverse horizontally polarized (Th)** *wave incidence from the isotropic base metal. Columnar grain tilt angle* $\Phi = 90°$

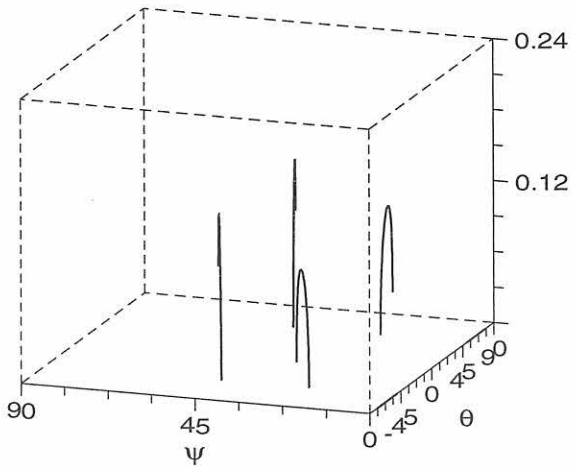

g) z-axis: $t_{qT1(2)Th}$

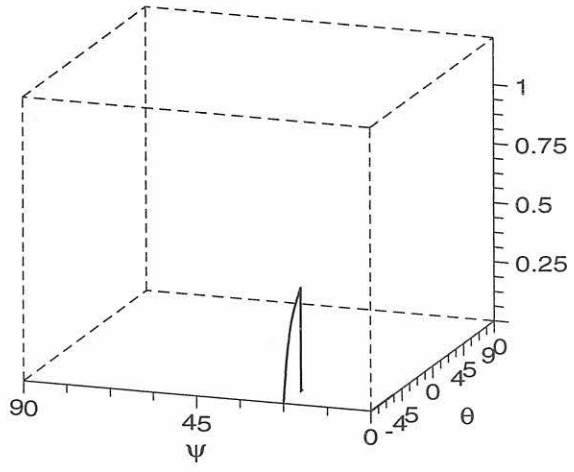

h) z-axis: $t_{qT1(2)Th}$

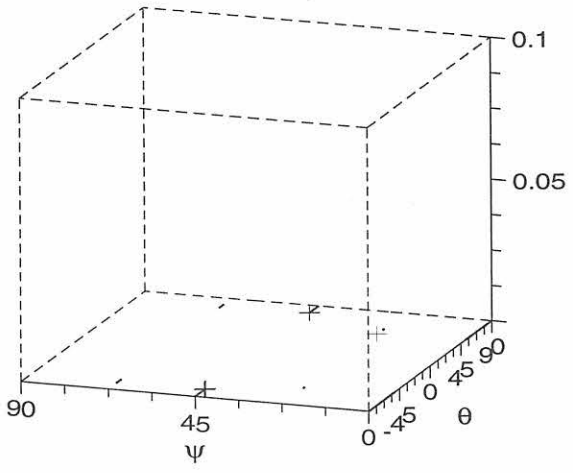

i) z-axis: $t_{qT1(2)Th}$

Figure D.14: *Energy transmission coefficients of the second branch of the quasi transverse wave qT1(2) at the interface between isotropic and transverse isotropic media (fusion face) as a function of the incidence angle* Θ *and the layback angle* Ψ. **Transverse horizontally polarized (Th)** *wave incidence from the isotropic base metal. Columnar grain tilt angle* Φ : *a*) $0°$; *b*) $67,5°$; *c*) $90°$

D.2 Interface between transverse isotropic and isotropic media (fusion face): Wave incidence from the anisotropic weld metal

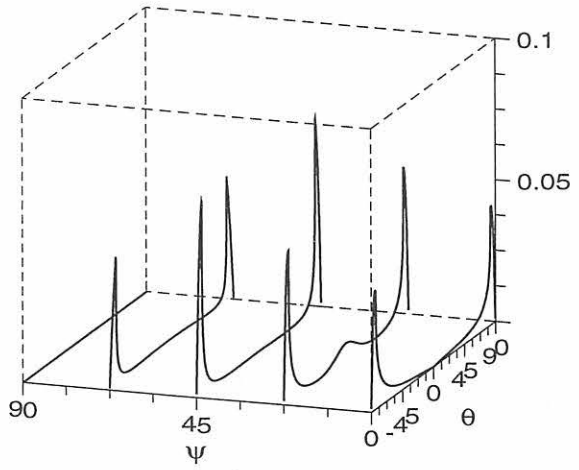

a) z-axis: r_{qT1qL}

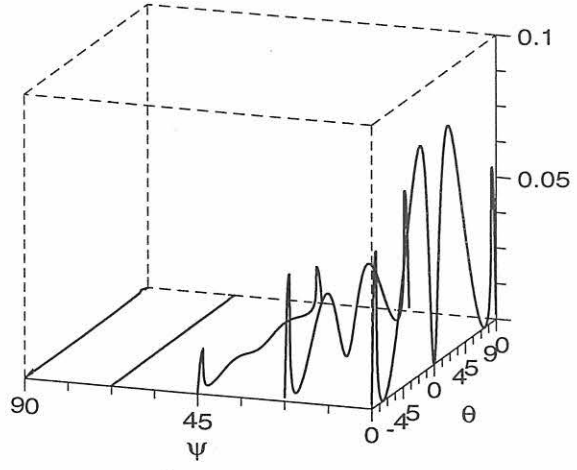

b) z-axis: t_{TvqL}

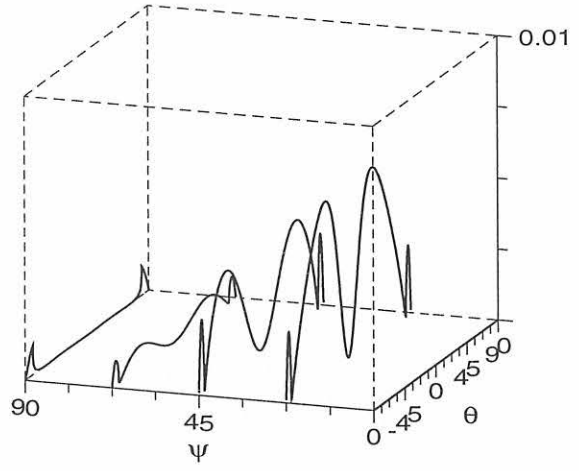

c) z-axis: r_{T2qL}

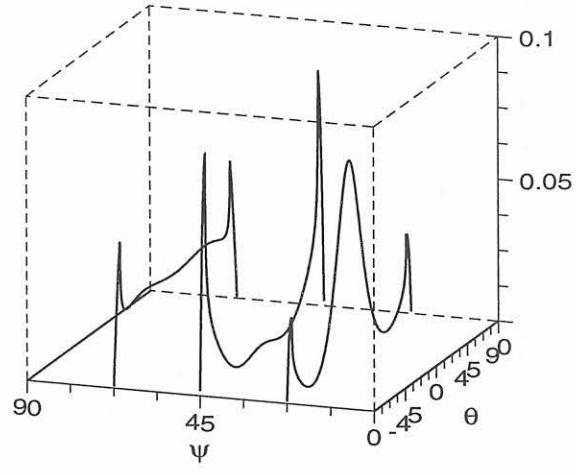

d) z-axis: t_{ThqL}

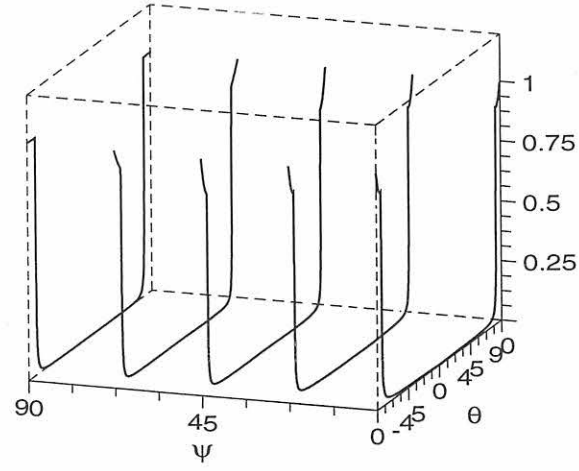

e) z-axis: r_{qLqL}

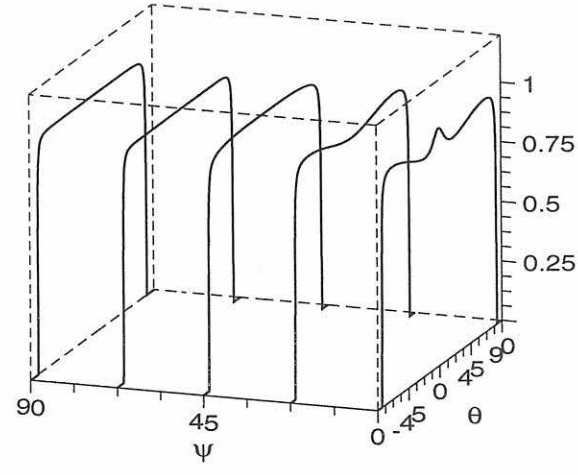

f) z-axis: t_{LqL}

Figure D.15: *Reflection and transmission energy coefficients of the three waves at the interface between transverse isotropic and isotropic media (fusion face) as a function of the incidence angle* Θ *and the layback angle* Ψ. **Quasi longitudinal (qL)** *wave incidence from the anisotropic weld metal. Columnar grain tilt angle* $\Phi = 0°$

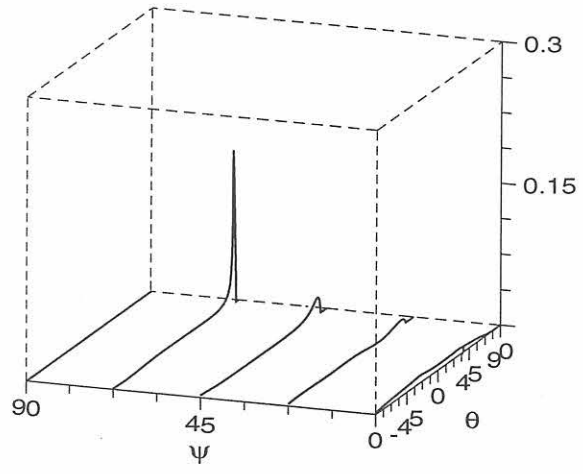

a) z-axis: r_{qT1qL}

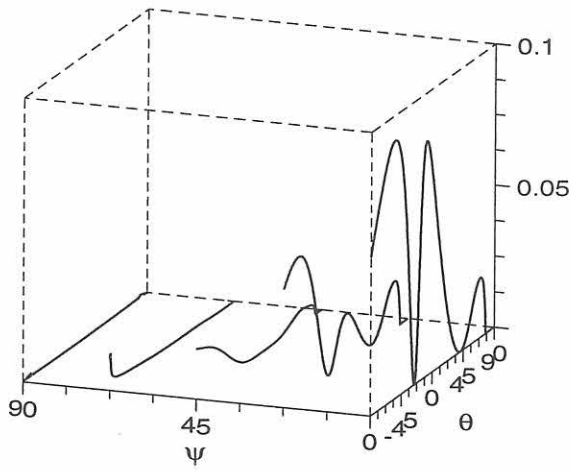

b) z-axis: t_{TvqL}

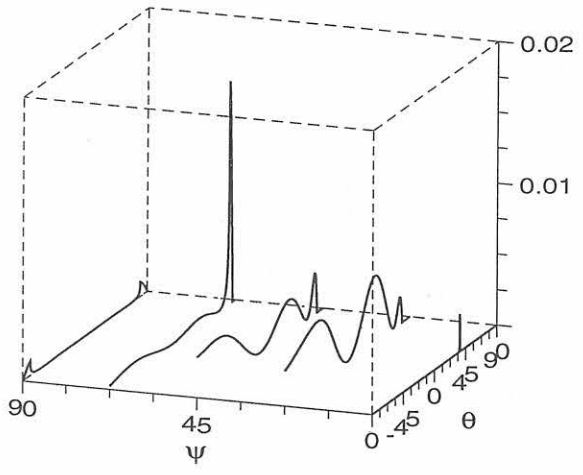

c) z-axis: r_{T2qL}

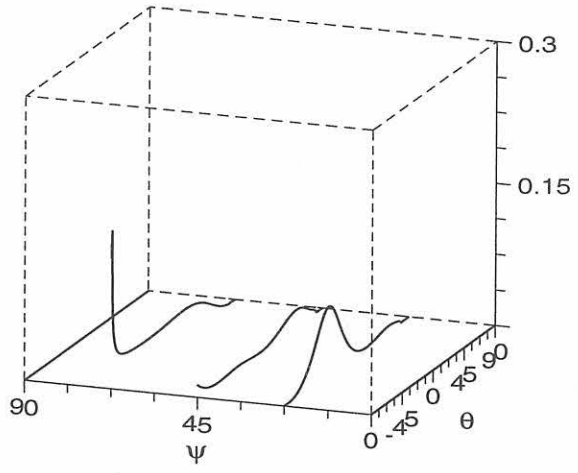

d) z-axis: t_{ThqL}

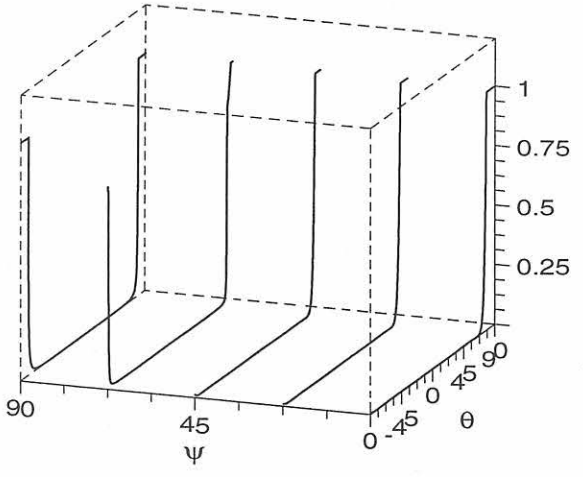

e) z-axis: r_{qLqL}

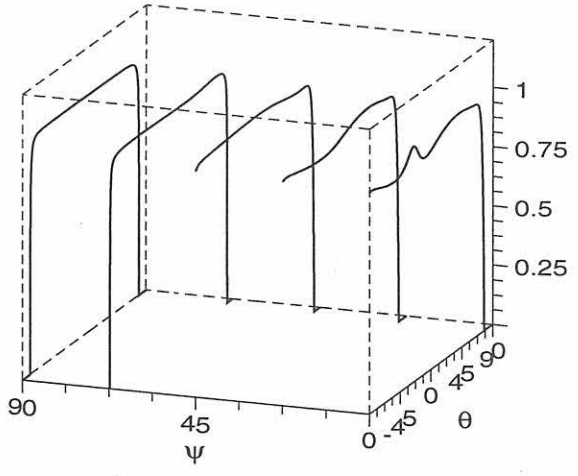

f) z-axis: t_{LqL}

Figure D.16: *Reflection and transmission energy coefficients of the three waves at the interface between transverse isotropic and isotropic media (fusion face) as a function of the incidence angle* Θ *and the layback angle* Ψ. **Quasi longitudinal (qL)** *wave incidence from the anisotropic weld metal. Columnar grain tilt angle* $\Phi = 22,5°$

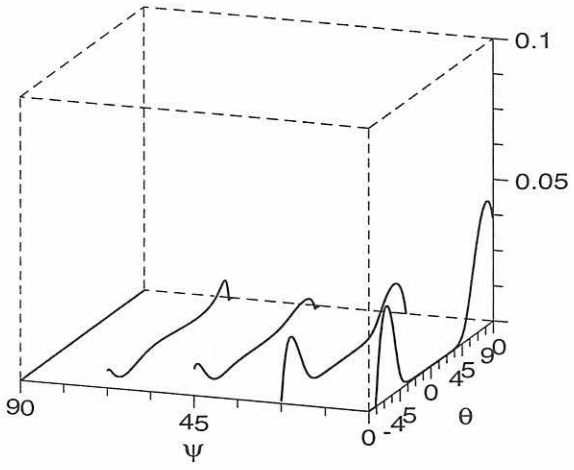

a) z-axis: r_{qT1qL}

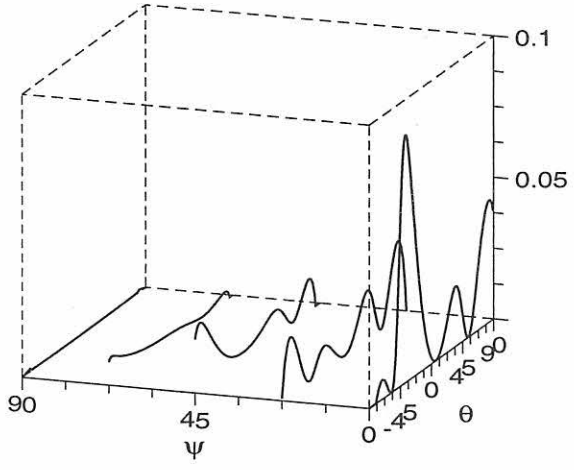

b) z-axis: t_{TvqL}

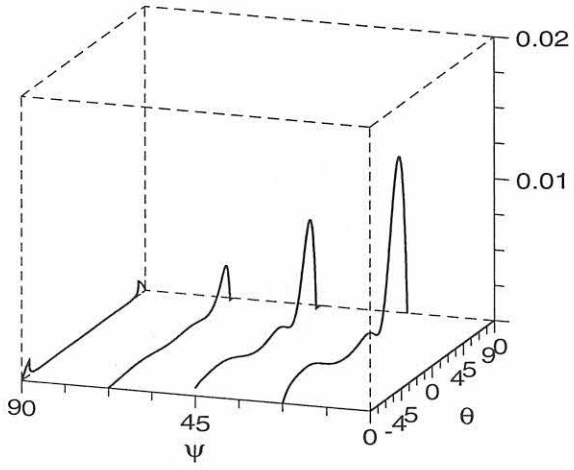

c) z-axis: r_{T2qL}

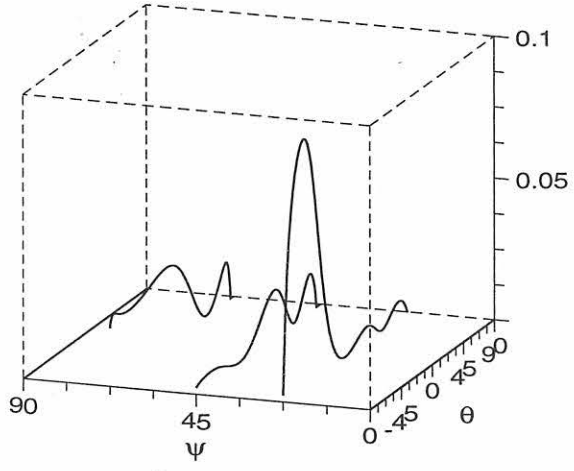

d) z-axis: t_{ThqL}

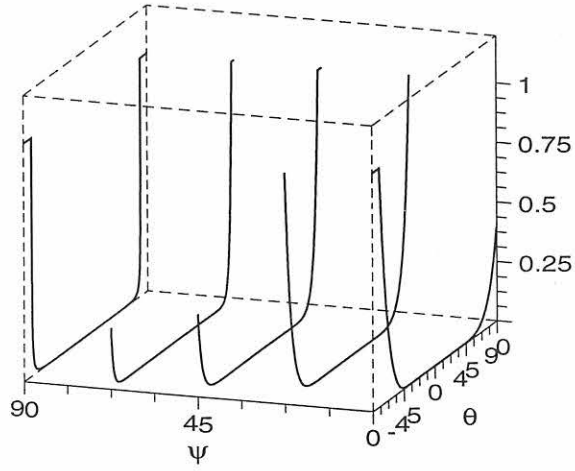

e) z-axis: r_{qLqL}

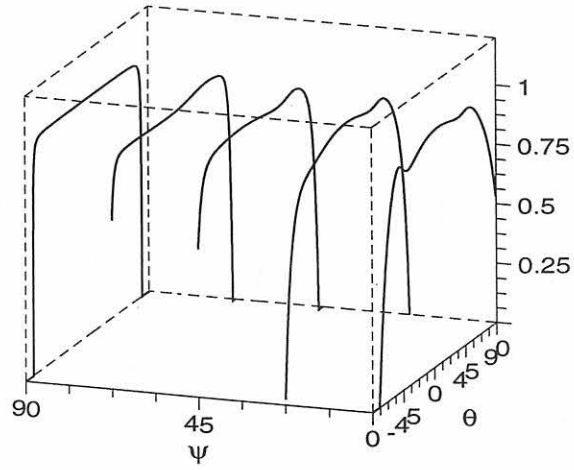

f) z-axis: t_{LqL}

Figure D.17: *Reflection and transmission energy coefficients of the three waves at the interface between transverse isotropic and isotropic media (fusion face) as a function of the incidence angle* Θ *and the layback angle* Ψ. **Quasi longitudinal (qL)** *wave incidence from the anisotropic weld metal. Columnar grain tilt angle* $\Phi = 45°$

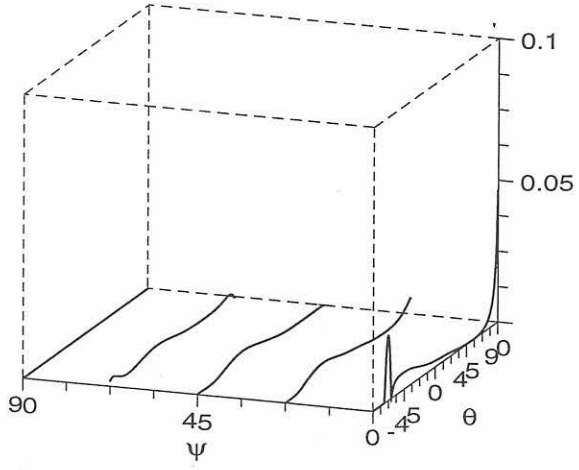

a) z-axis: r_{qT1qL}

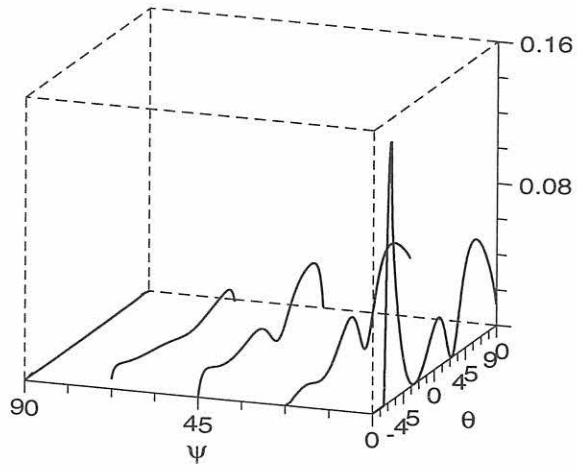

b) z-axis: t_{TvqL}

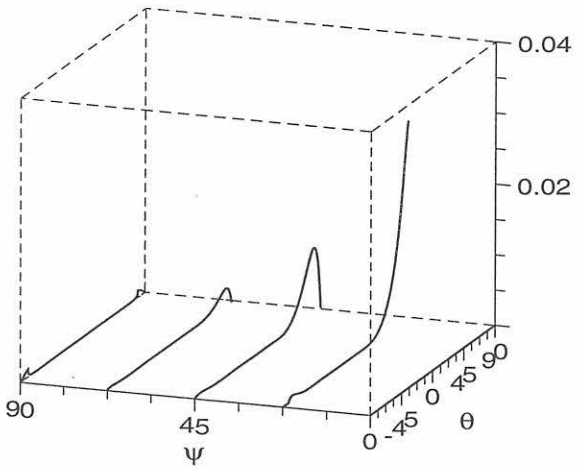

c) z-axis: r_{T2qL}

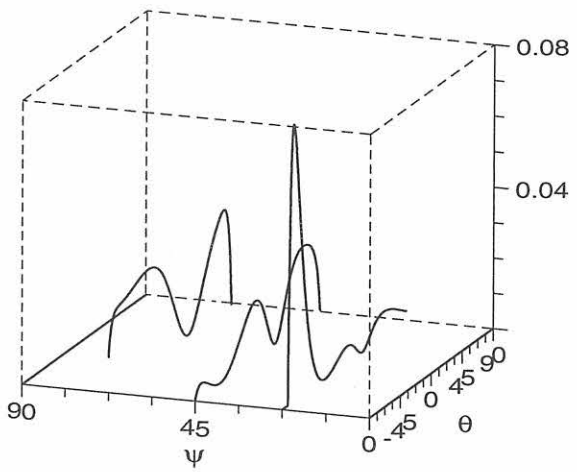

d) z-axis: t_{ThqL}

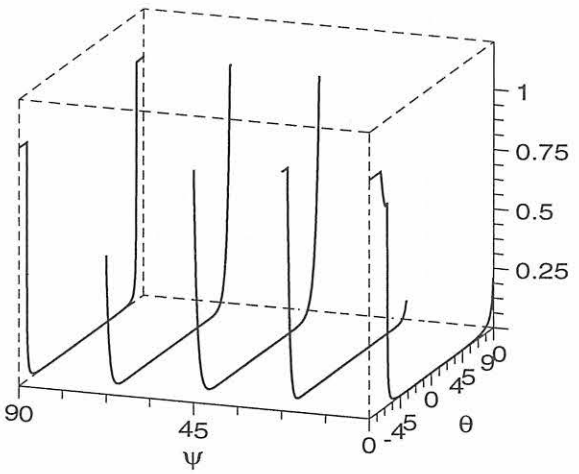

e) z-axis: r_{qLqL}

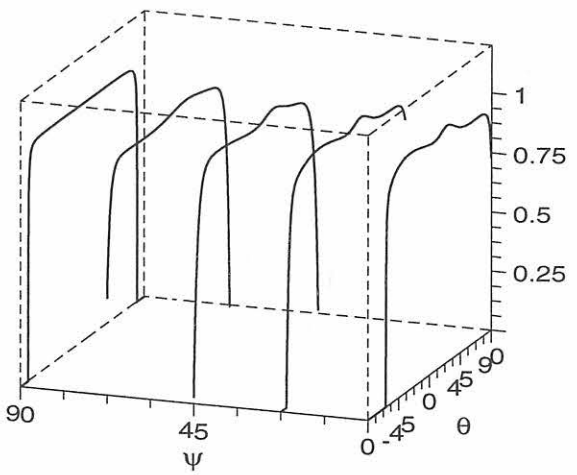

f) z-axis: t_{LqL}

Figure D.18: *Reflection and transmission energy coefficients of the three waves at the interface between transverse isotropic and isotropic media (fusion face) as a function of the incidence angle* Θ *and the layback angle* Ψ. **Quasi longitudinal (qL)** *wave incidence from the anisotropic weld metal. Columnar grain tilt angle* $\Phi = 67,5°$

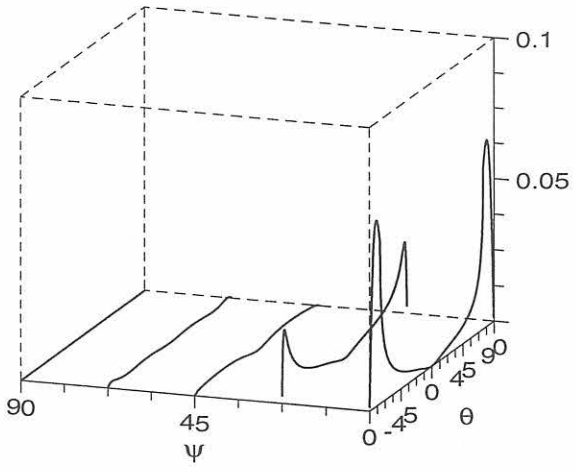

a) z-axis: r_{qT1qL}

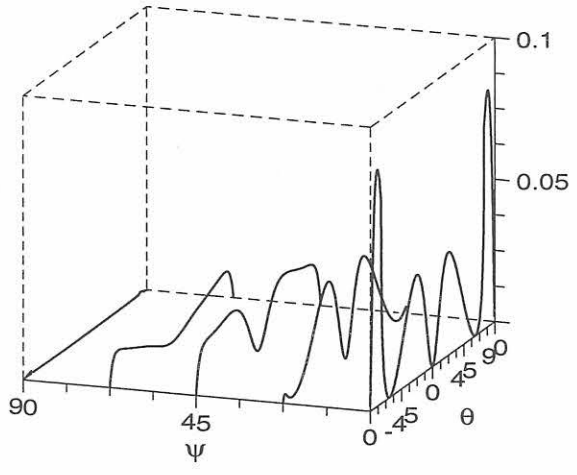

b) z-axis: t_{TvqL}

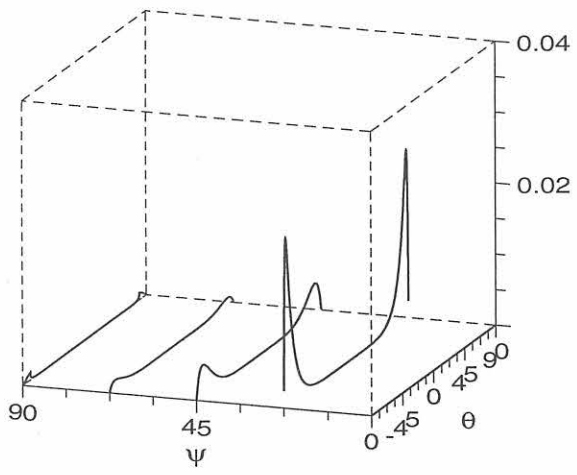

c) z-axis: r_{T2qL}

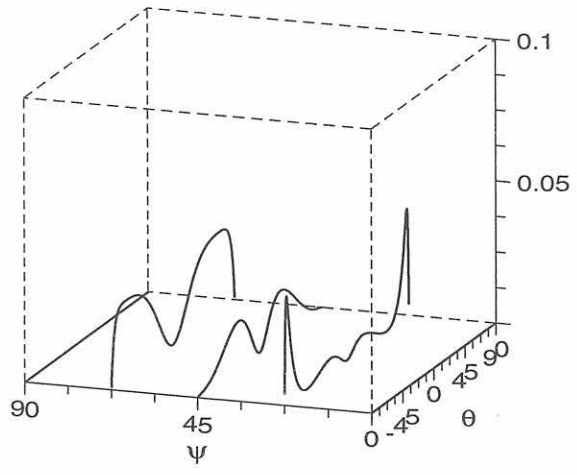

d) z-axis: t_{ThqL}

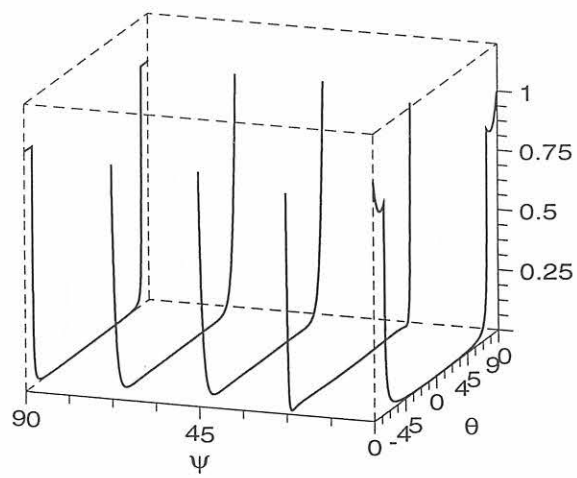

e) z-axis: r_{qLqL}

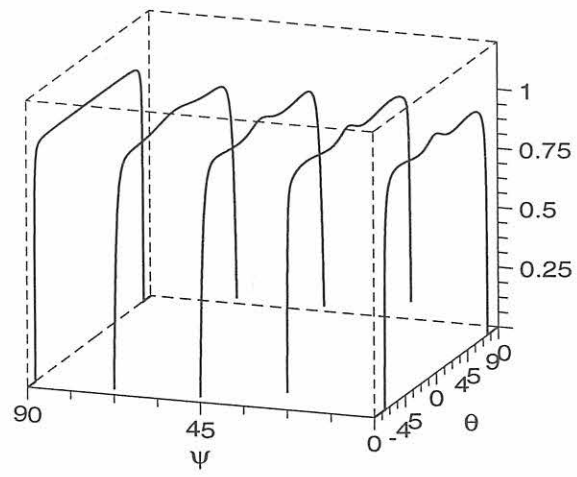

f) z-axis: t_{LqL}

Figure D.19: *Reflection and transmission energy coefficients of the three waves at the interface between transverse isotropic and isotropic media (fusion face) as a function of the incidence angle* Θ *and the layback angle* Ψ. **Quasi longitudinal (qL)** *wave incidence from the anisotropic weld metal. Columnar grain tilt angle* $\Phi = 90°$

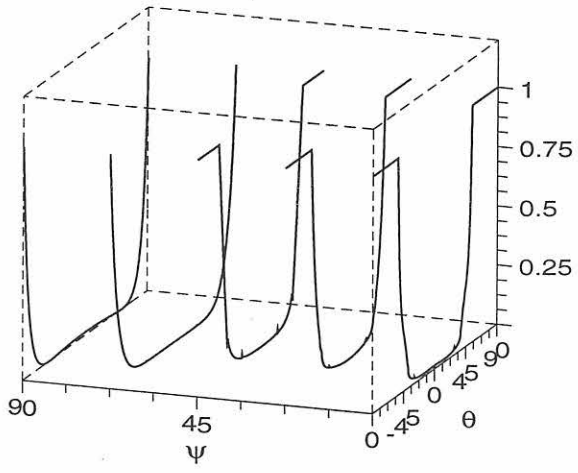

a) z-axis: r_{qT1qT1}

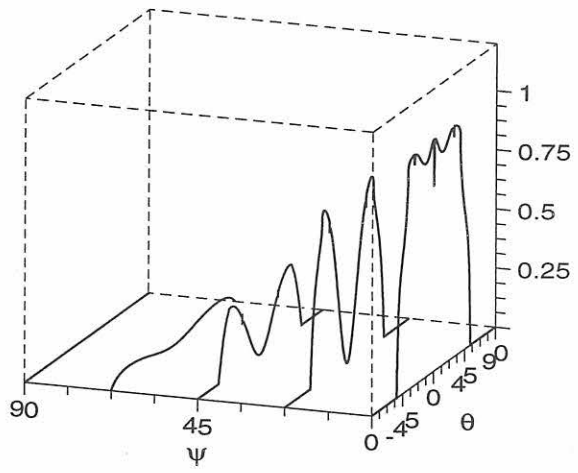

b) z-axis: t_{TvqT1}

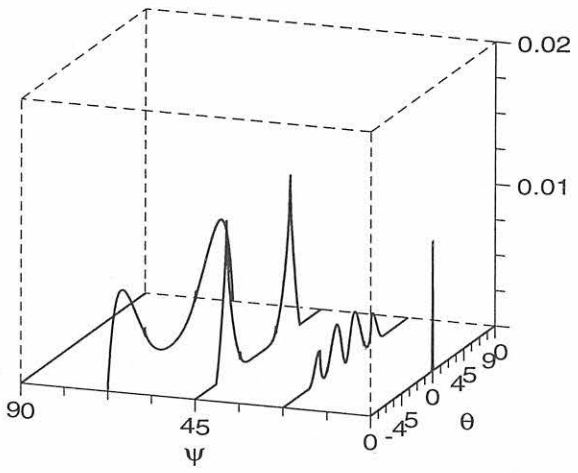

c) z-axis: r_{T2qT1}

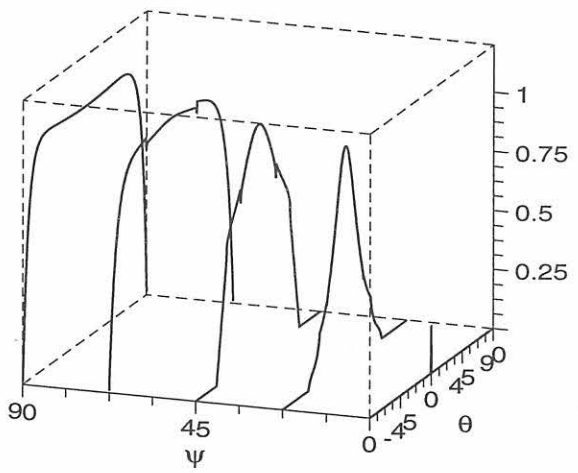

d) z-axis: t_{ThqT1}

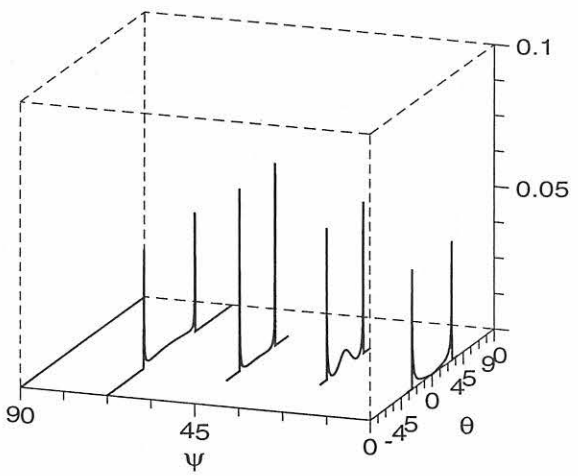

e) z-axis: r_{qLqT1}

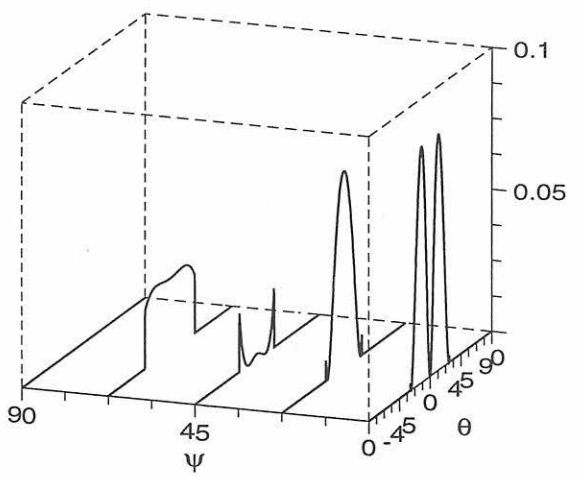

f) z-axis: t_{LqT1}

Figure D.20: *Reflection and transmission energy coefficients of the three waves at the interface between transverse isotropic and isotropic media (fusion face) as a function of the incidence angle* Θ *and the layback angle* Ψ. **Quasi transverse (qT1)** *wave incidence from the anisotropic weld metal. Columnar grain tilt angle* $\Phi = 0°$

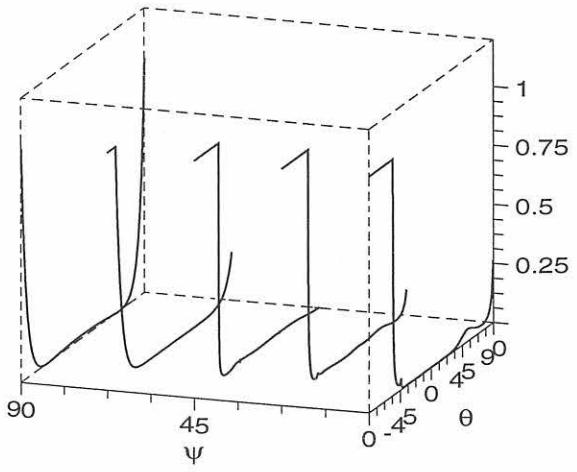

a) z-axis: r_{qT1qT1}

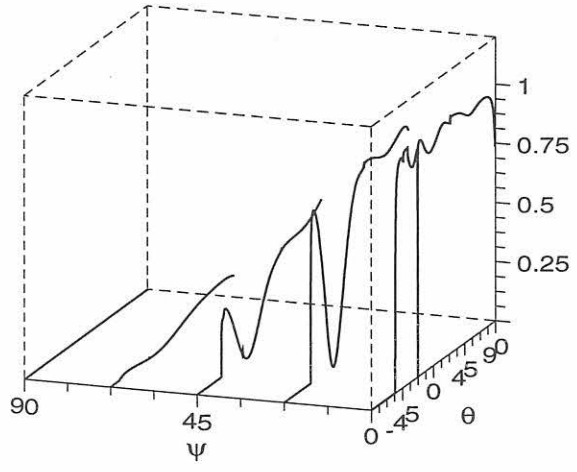

b) z-axis: t_{TvqT1}

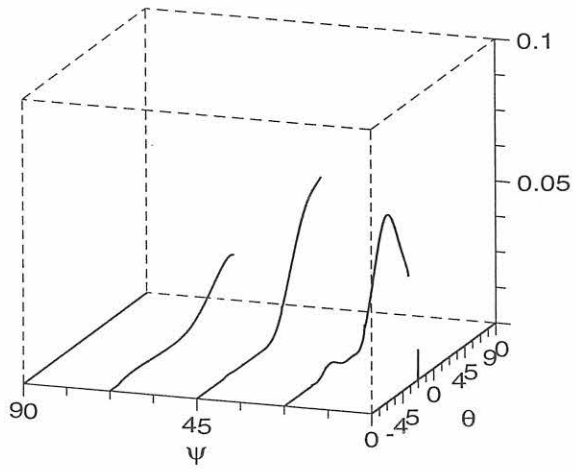

c) z-axis: r_{T2qT1}

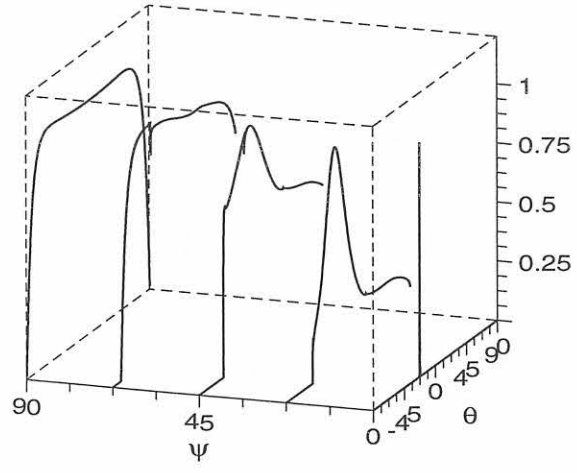

d) z-axis: t_{ThqT1}

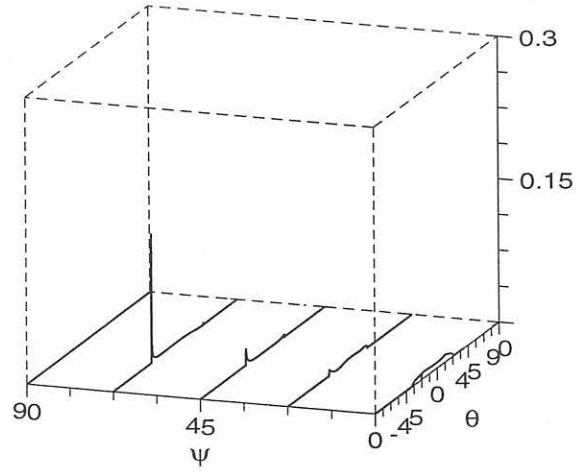

e) z-axis: r_{qLqT1}

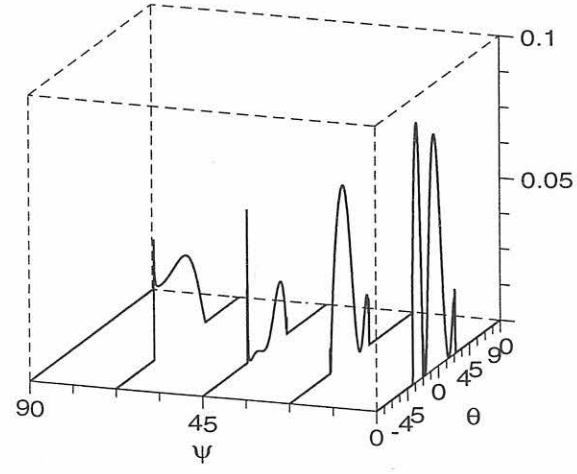

f) z-axis: t_{LqT1}

Figure D.21: *Reflection and transmission energy coefficients of the three waves at the interface between transverse isotropic and isotropic media (fusion face) as a function of the incidence angle* Θ *and the layback angle* Ψ. **Quasi transverse (qT1)** *wave incidence from the anisotropic weld metal. Columnar grain tilt angle* $\Phi = 22,5°$

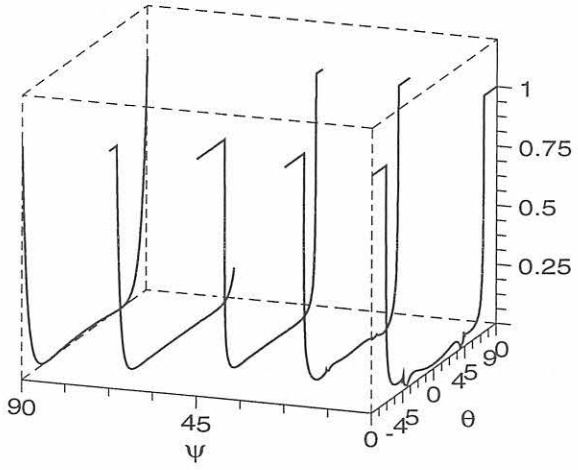

a) z-axis: r_{qT1qT1}

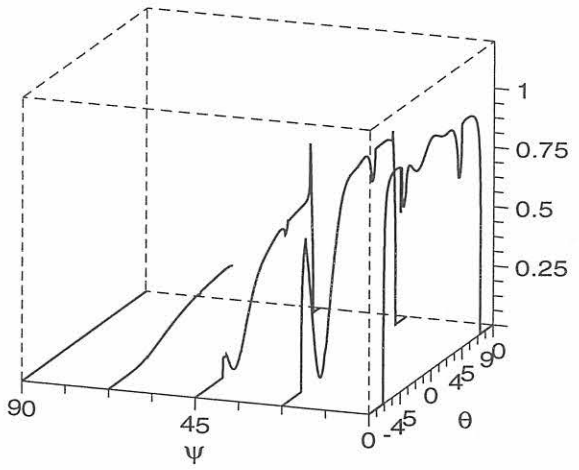

b) z-axis: t_{TvqT1}

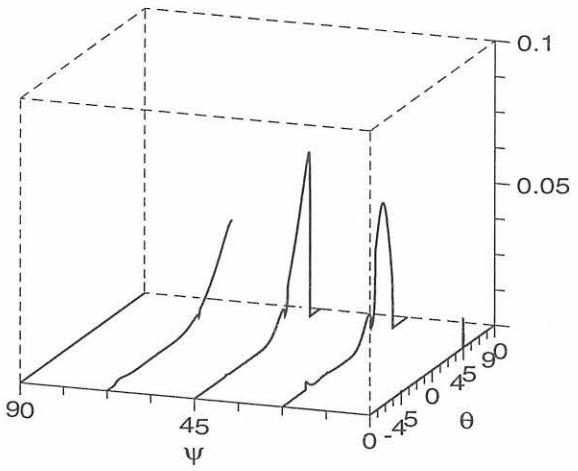

c) z-axis: r_{T2qT1}

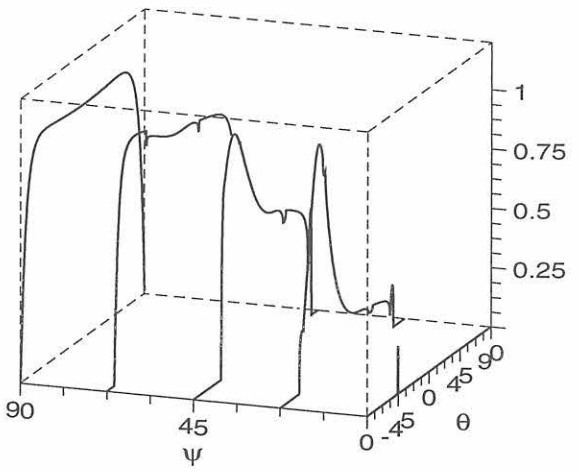

d) z-axis: t_{ThqT1}

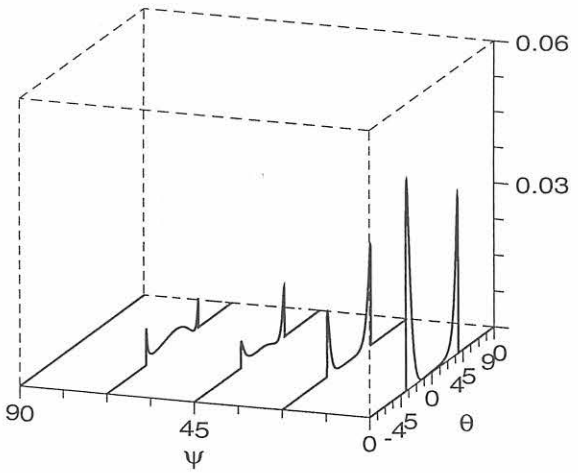

e) z-axis: r_{qLqT1}

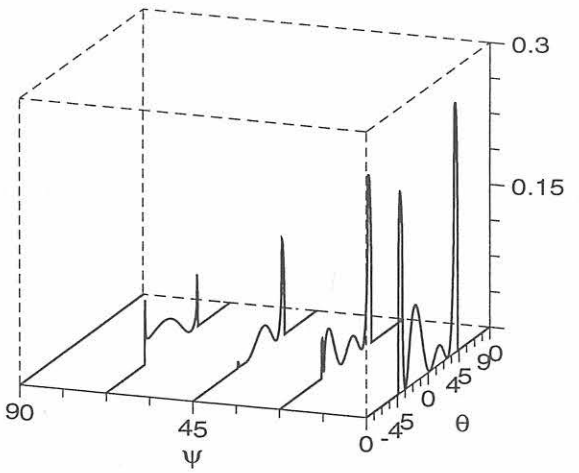

f) z-axis: t_{LqT1}

Figure D.22: *Reflection and transmission energy coefficients of the three waves at the interface between transverse isotropic and isotropic media (fusion face) as a function of the incidence angle* Θ *and the layback angle* Ψ. **Quasi transverse (qT1)** *wave incidence from the anisotropic weld metal. Columnar grain tilt angle* $\Phi = 45°$

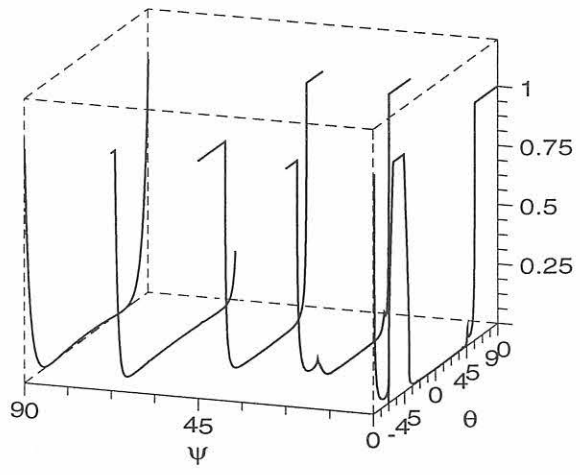

a) z-axis: r_{qT1qT1}

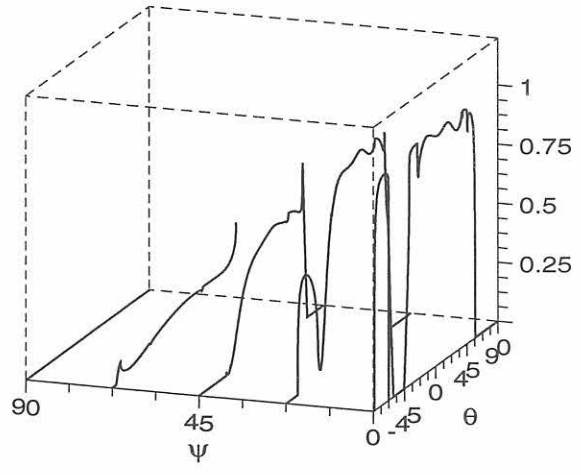

b) z-axis: t_{TvqT1}

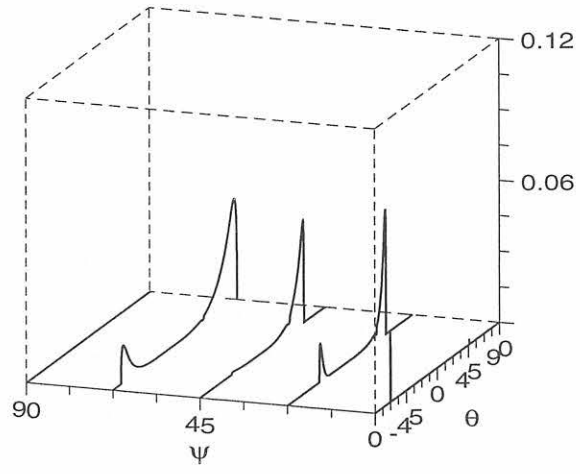

c) z-axis: r_{T2qT1}

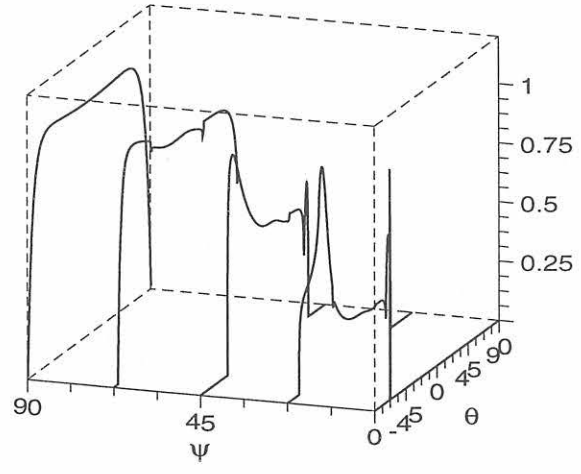

d) z-axis: t_{ThqT1}

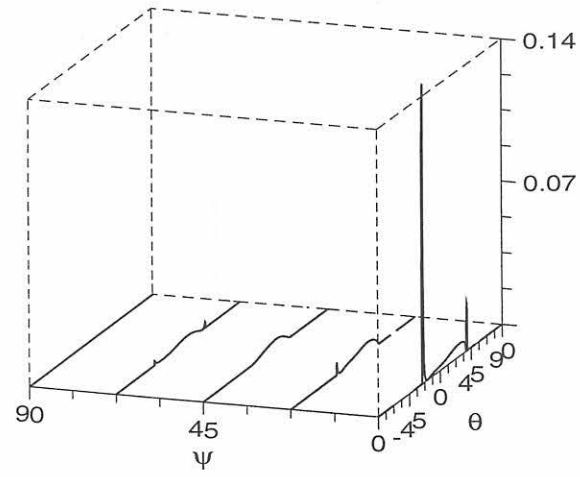

e) z-axis: r_{qLqT1}

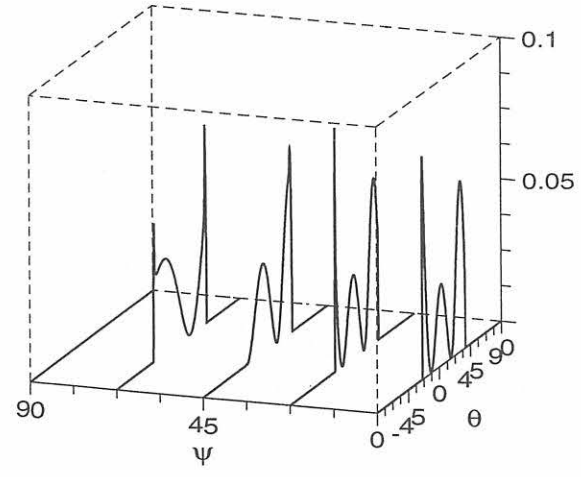

f) z-axis: t_{LqT1}

Figure D.23: *Reflection and transmission energy coefficients of the three waves at the interface between transverse isotropic and isotropic media (fusion face) as a function of the incidence angle* Θ *and the layback angle* Ψ. **Quasi transverse (qT1)** *wave incidence from the anisotropic weld metal. Columnar grain tilt angle* $\Phi = 67,5°$

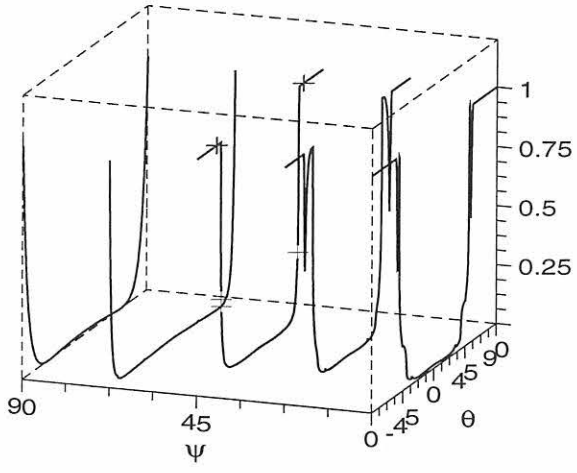

a) z-axis: r_{qT1qT1}

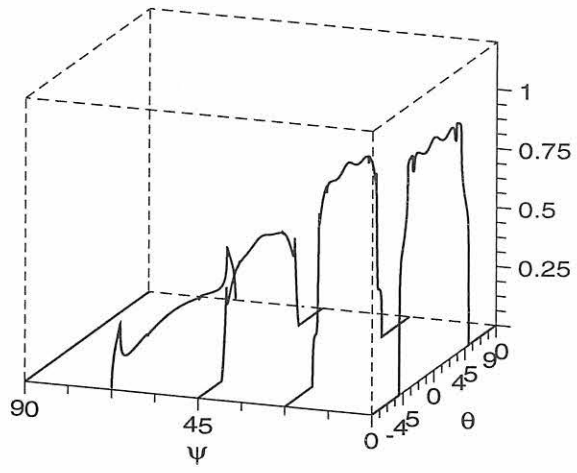

b) z-axis: t_{TvqT1}

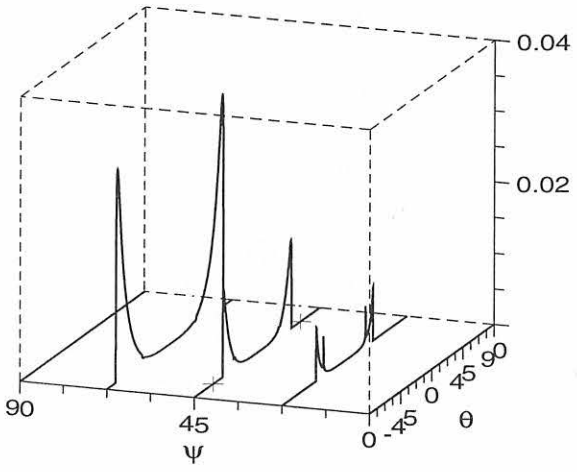

c) z-axis: r_{T2qT1}

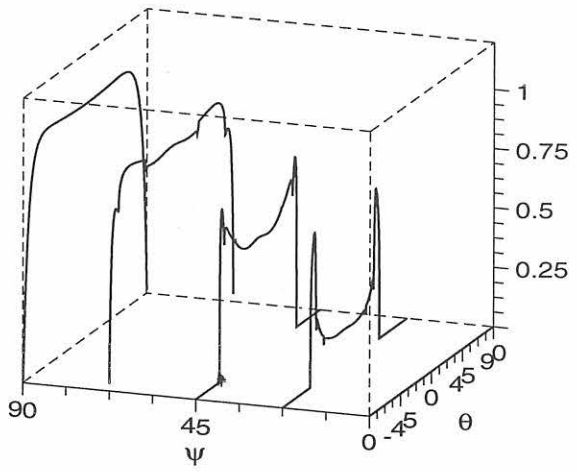

d) z-axis: t_{ThqT1}

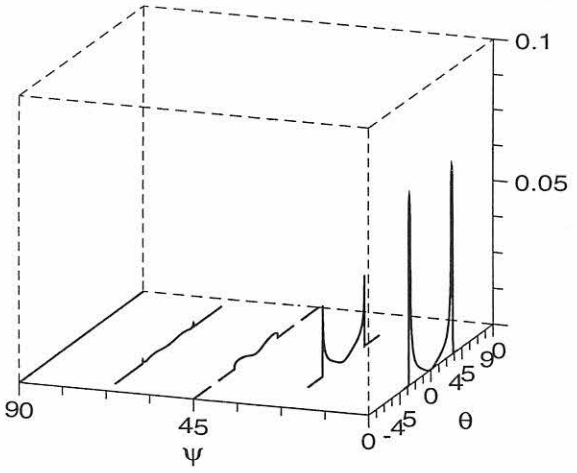

e) z-axis: r_{qLqT1}

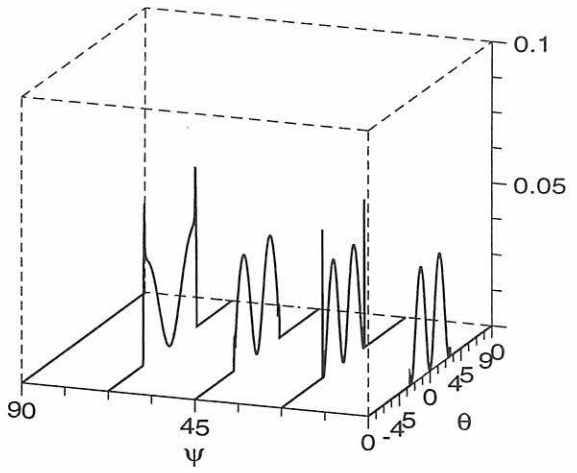

f) z-axis: t_{LqT1}

Figure D.24: *Reflection and transmission energy coefficients of the three waves at the interface between transverse isotropic and isotropic media (fusion face) as a function of the incidence angle* Θ *and the layback angle* Ψ. **Quasi transverse (qT1)** *wave incidence from the anisotropic weld metal. Columnar grain tilt angle* $\Phi = 90°$

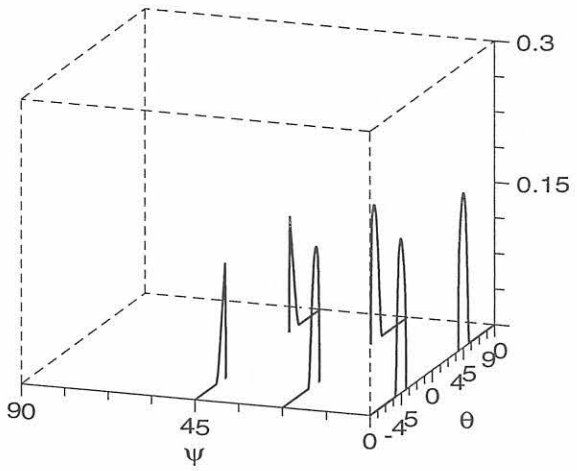

g) z-axis: $r_{qT1(2)qT1}$

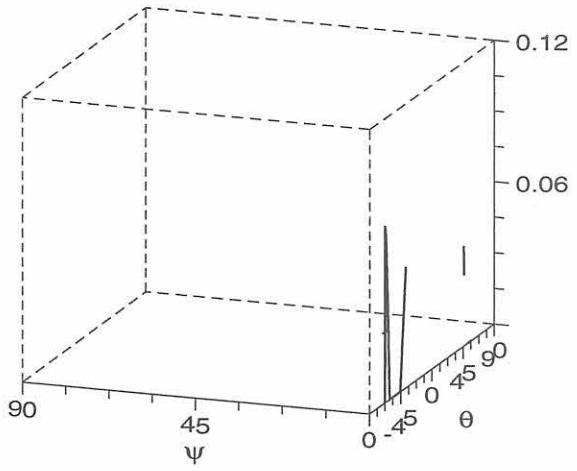

h) z-axis: $r_{qT1(2)qT1}$

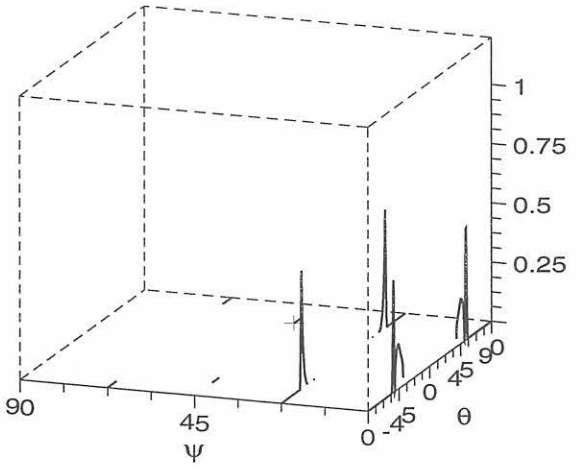

i) z-axis: $r_{qT1(2)qT1}$

Figure D.25: *Energy reflection coefficients of the second branch of the quasi transverse wave qT1(2) at the interface between transverse isotropic and isotropic media (fusion face) as a function of the incidence angle* Θ *and the layback angle* Ψ. **Quasi transverse (qT1)** *wave incidence from the anisotropic weld metal. Columnar grain tilt angle* Φ : *a*) $0°$; *b*) $67,5°$; *c*) $90°$

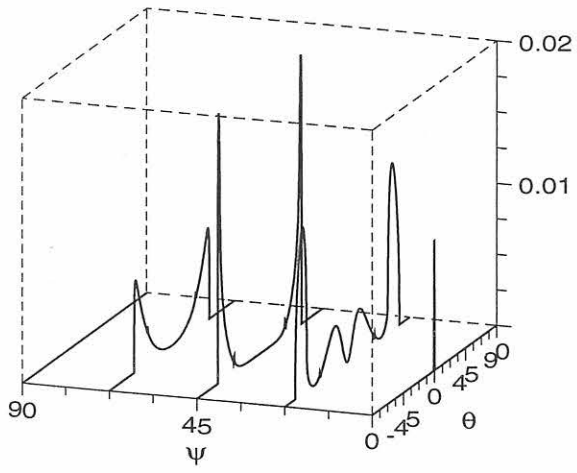

a) z-axis: r_{qT1T2}

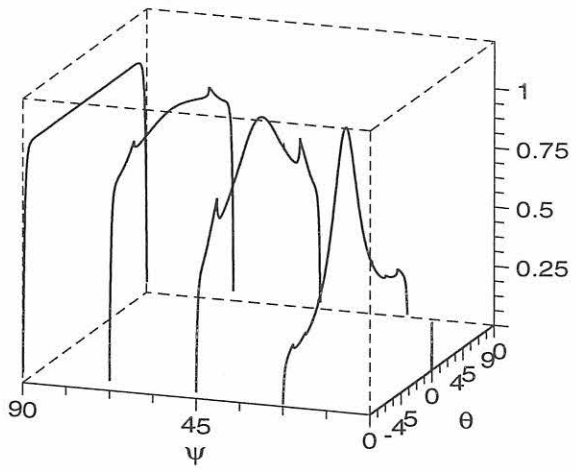

b) z-axis: t_{TvT2}

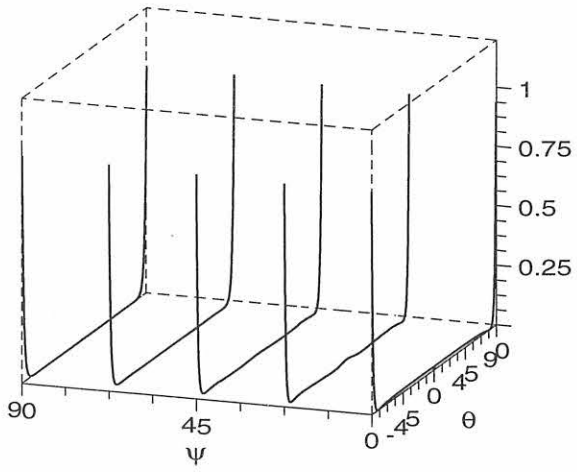

c) z-axis: r_{T2T2}

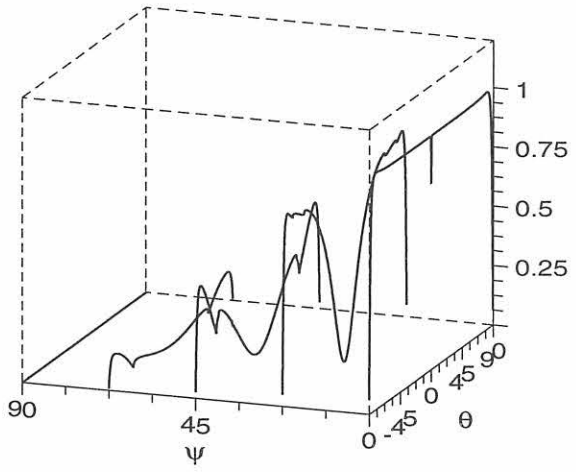

d) z-axis: t_{ThT2}

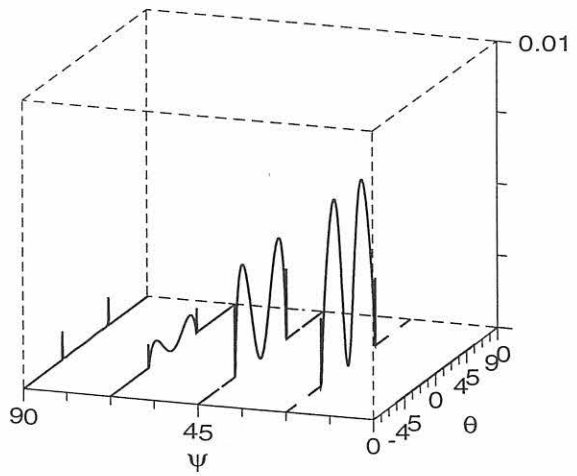

e) z-axis: r_{qLT2}

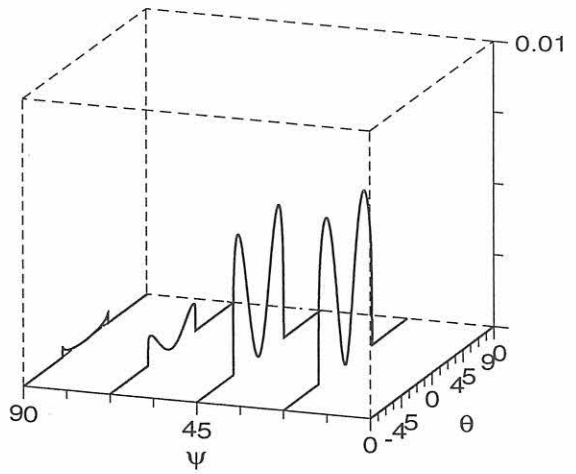

f) z-axis: t_{LT2}

Figure D.26: *Reflection and transmission energy coefficients of the three waves at the interface between transverse isotropic and isotropic media (fusion face) as a function of the incidence angle* Θ *and the layback angle* Ψ. **pure transverse (T2)** *wave incidence from the anisotropic weld metal. Columnar grain tilt angle* $\Phi = 0°$

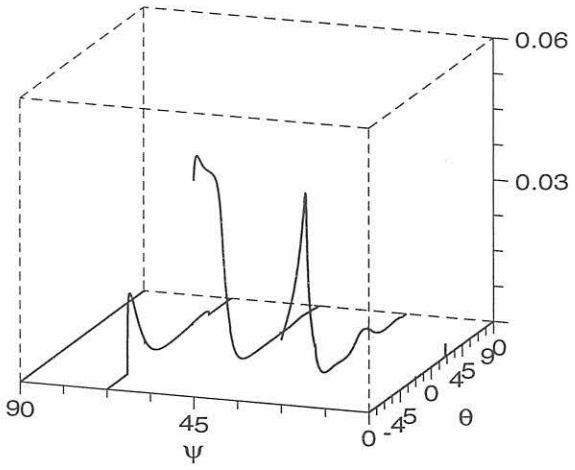

a) z-axis: r_{qT1T2}

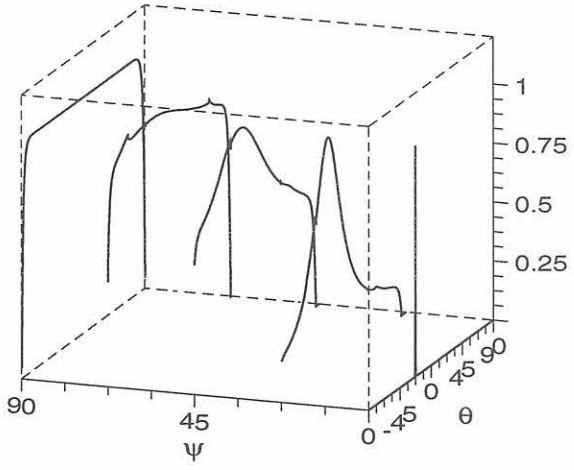

b) z-axis: t_{TvT2}

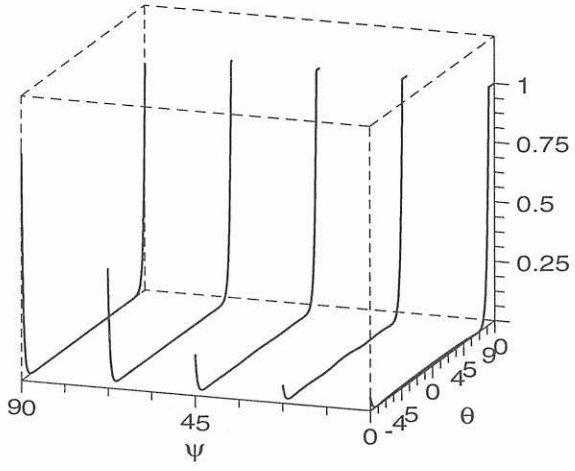

c) z-axis: r_{T2T2}

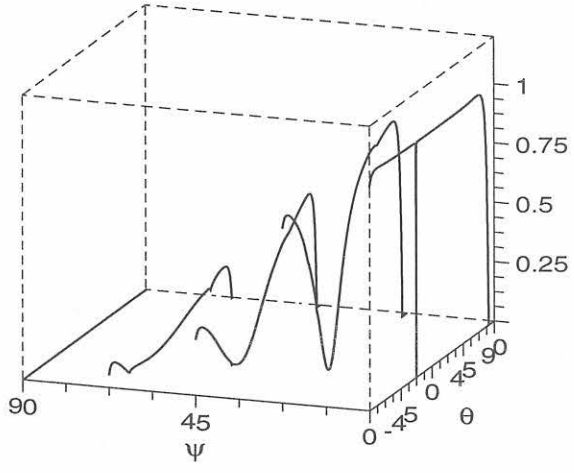

d) z-axis: t_{ThT2}

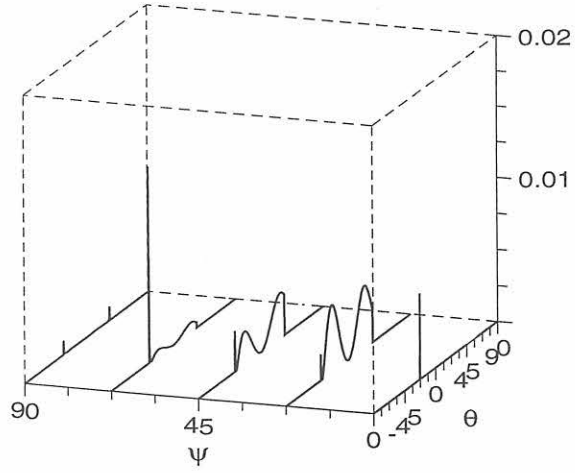

e) z-axis: r_{qLT2}

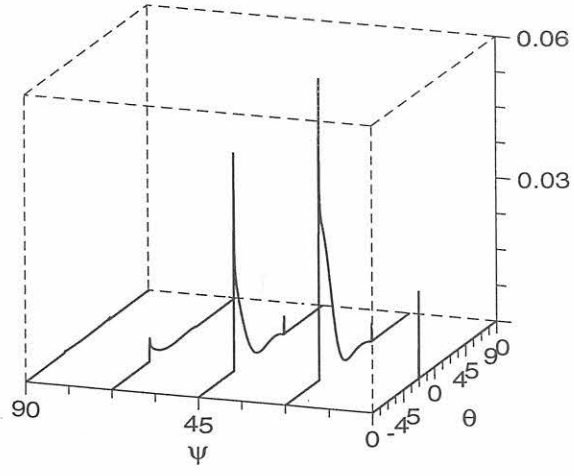

f) z-axis: t_{LT2}

Figure D.27: *Reflection and transmission energy coefficients of the three waves at the interface between transverse isotropic and isotropic media (fusion face) as a function of the incidence angle* Θ *and the layback angle* Ψ. **Pure transverse (T2)** *wave incidence from the anisotropic weld metal. Columnar grain tilt angle* $\Phi = 22,5°$

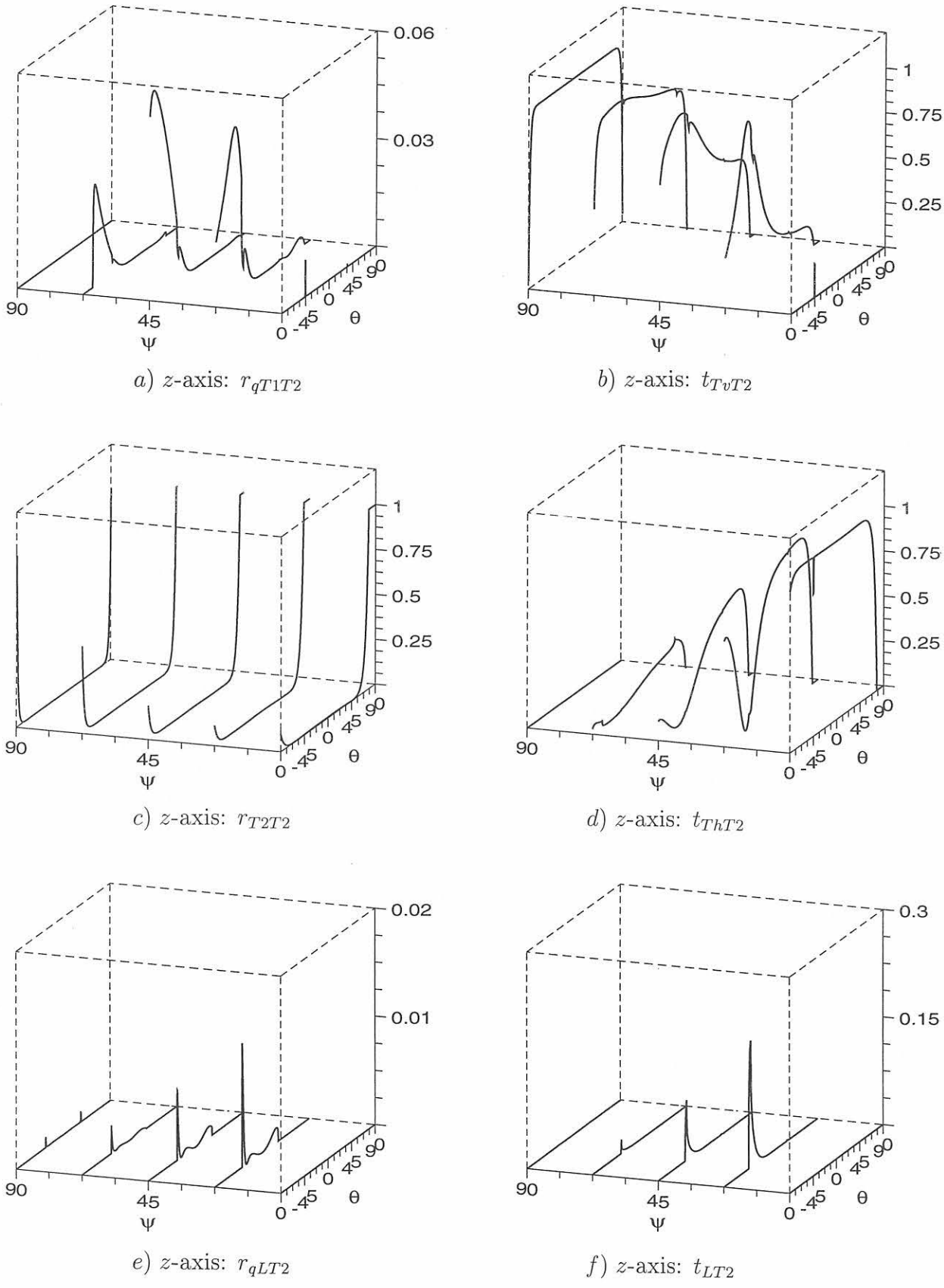

a) z-axis: r_{qT1T2} *b*) z-axis: t_{TvT2}

c) z-axis: r_{T2T2} *d*) z-axis: t_{ThT2}

e) z-axis: r_{qLT2} *f*) z-axis: t_{LT2}

Figure D.28: *Reflection and transmission energy coefficients of the three waves at the interface between transverse isotropic and isotropic media (fusion face) as a function of the incidence angle* Θ *and the layback angle* Ψ. **Pure transverse (T2)** *wave incidence from the anisotropic weld metal. Columnar grain tilt angle* $\Phi = 45°$

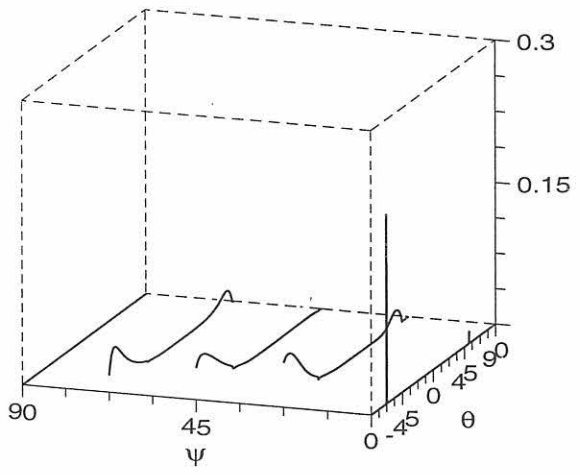

a) z-axis: r_{qT1T2}

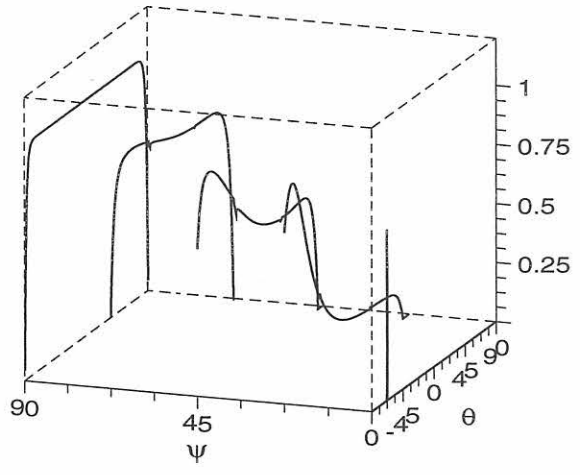

b) z-axis: t_{TvT2}

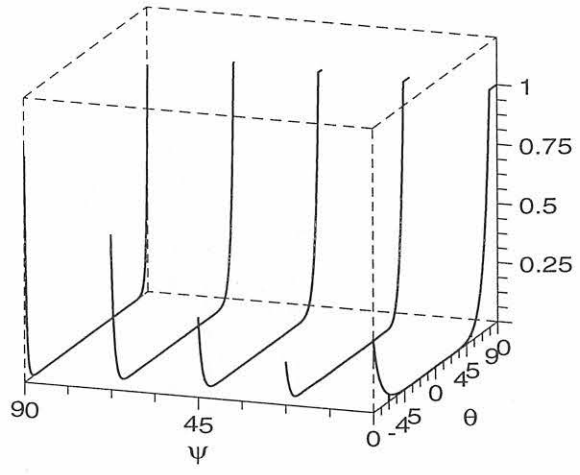

c) z-axis: r_{T2T2}

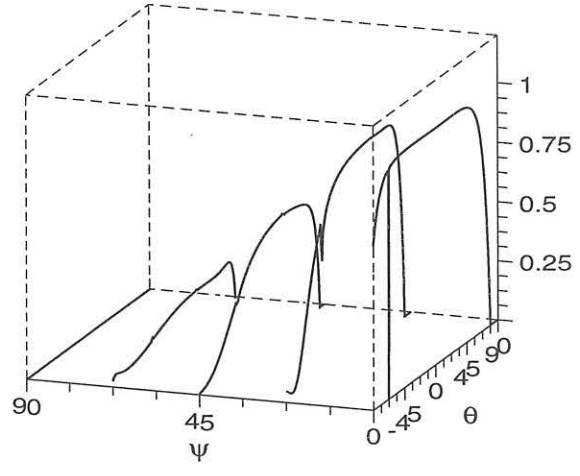

d) z-axis: t_{ThT2}

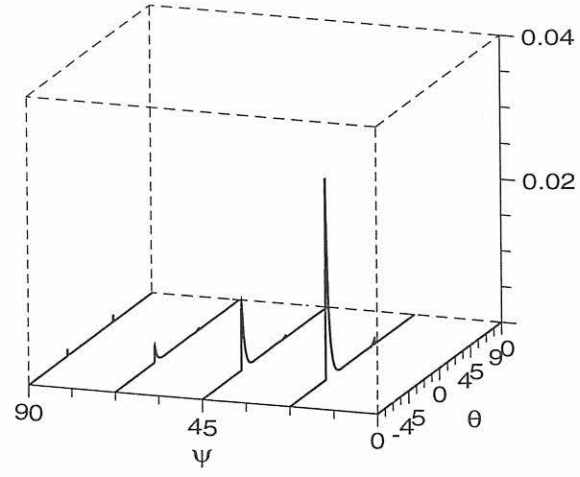

e) z-axis: r_{qLT2}

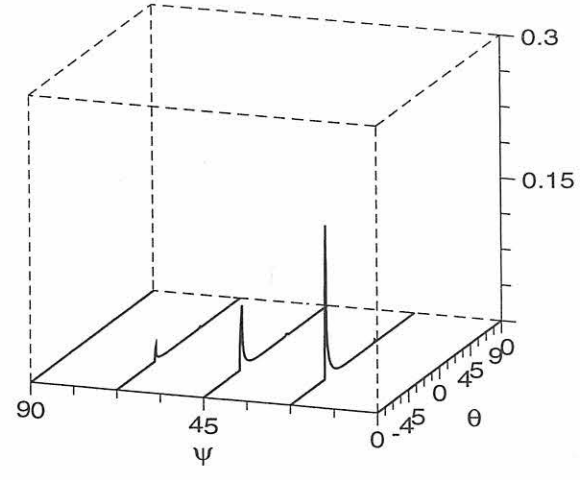

f) z-axis: t_{LT2}

Figure D.29: *Reflection and transmission energy coefficients of the three waves at the interface between transverse isotropic and isotropic media (fusion face) as a function of the incidence angle* Θ *and the layback angle* Ψ. **Pure transverse (T2)** *wave incidence from the anisotropic weld metal. Columnar grain tilt angle* $\Phi = 67,5°$

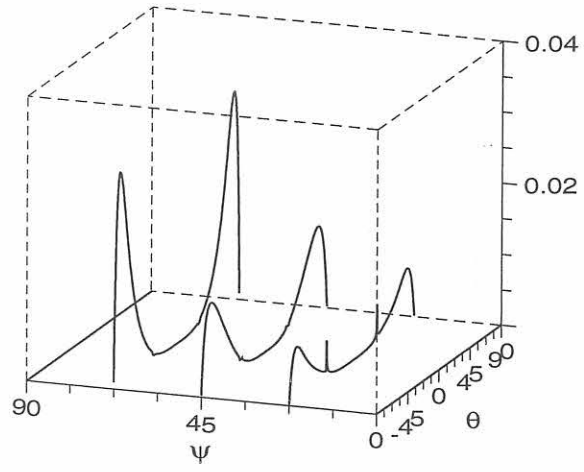

a) z-axis: r_{qT1T2}

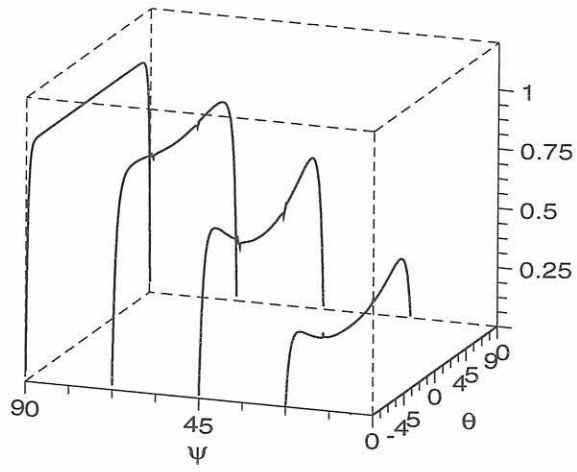

b) z-axis: t_{TvT2}

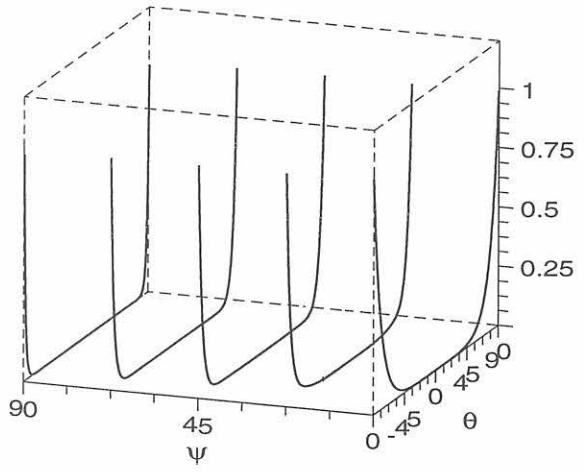

c) z-axis: r_{T2T2}

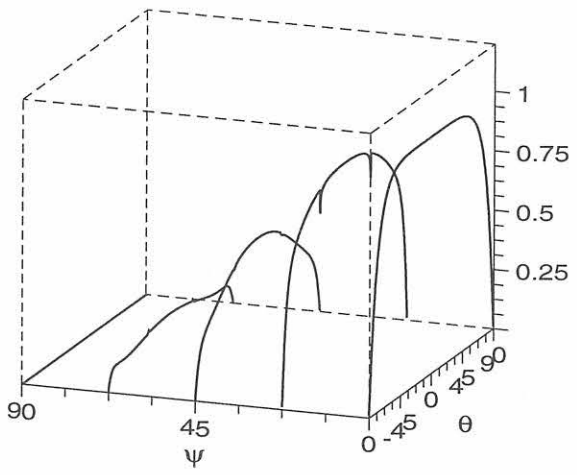

d) z-axis: t_{ThT2}

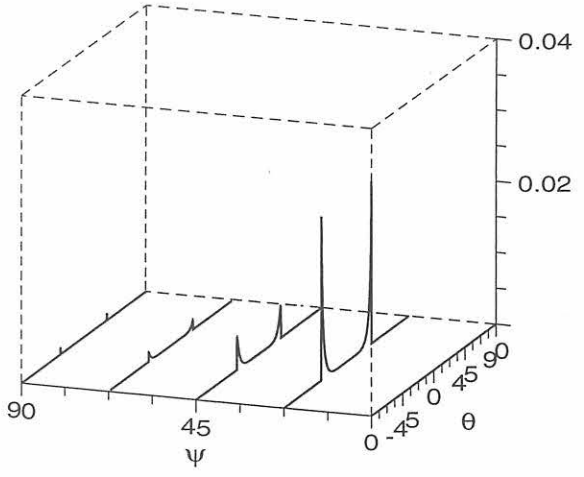

e) z-axis: r_{qLT2}

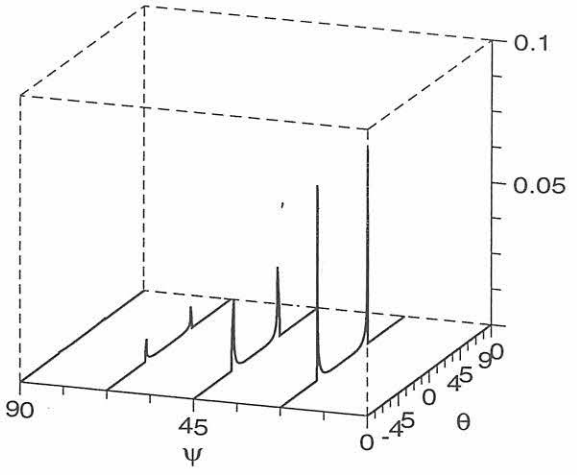

f) z-axis: t_{LT2}

Figure D.30: *Reflection and transmission energy coefficients of the three waves at the interface between transverse isotropic and isotropic media (fusion face) as a function of the incidence angle* Θ *and the layback angle* Ψ. **Pure transverse (T2)** *wave incidence from the anisotropic weld metal. Columnar grain tilt angle* $\Phi = 90°$

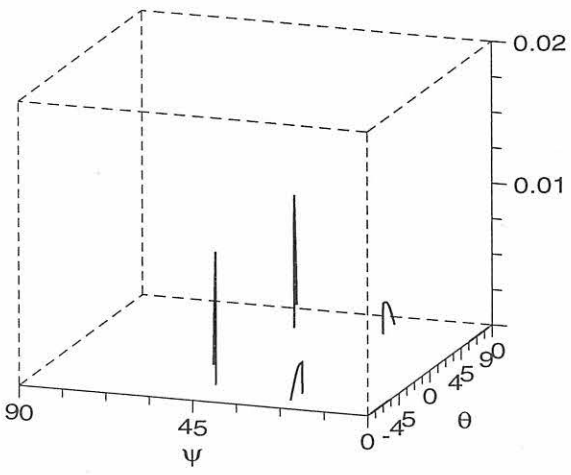

g) z-axis: $r_{qT1(2)T2}$

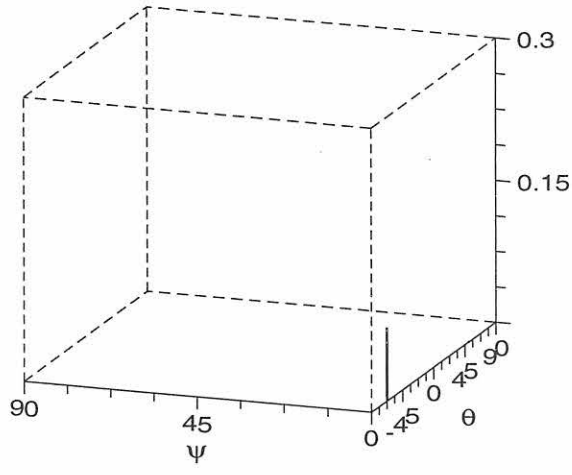

h) z-axis: $r_{qT1(2)T2}$

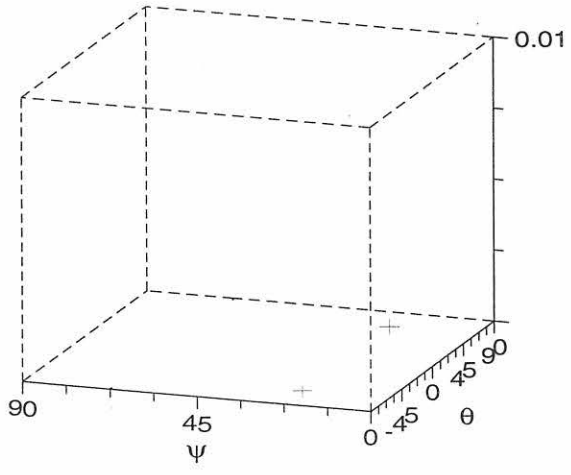

i) z-axis: $r_{qT1(2)T2}$

Figure D.31: *Energy reflection coefficients of the second branch of the quasi transverse wave qT1(2) at the interface between transverse isotropic and isotropic media (fusion face) as a function of the incidence angle* Θ *and the layback angle* Ψ. **Pure transverse (T2)** *wave incidence from the anisotropic weld metal. Columnar grain tilt angle* Φ : *a*) $0°$; *b*) $67,5°$; *c*) $90°$

D.3 Interface between two transverse isotropic media; Special case: Ultrasound propagation in the meridian plane

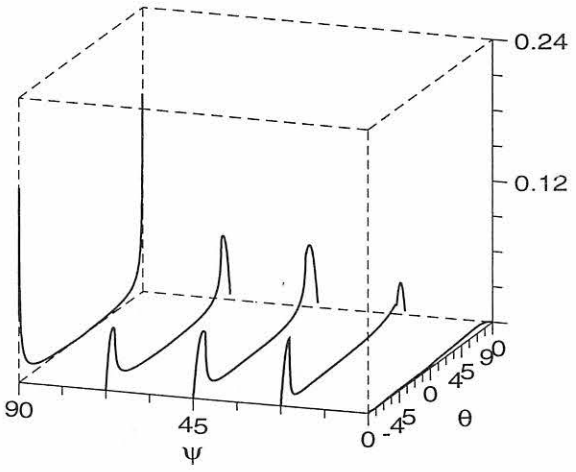

a) z-axis: r_{qT1qL}

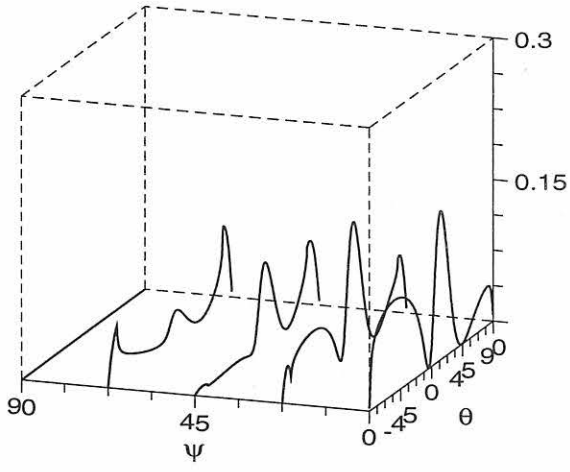

b) z-axis: t_{qT1qL}

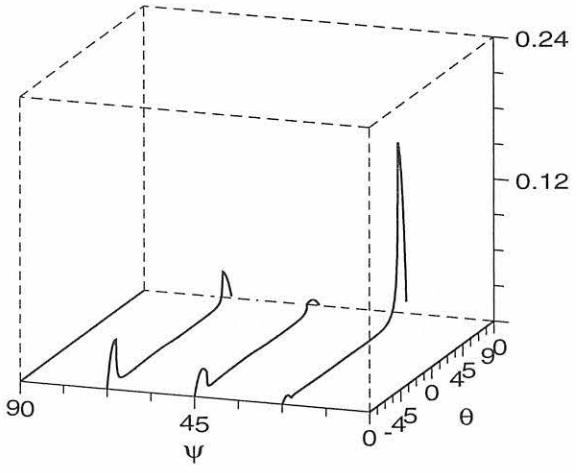

c) z-axis: r_{T2qL}

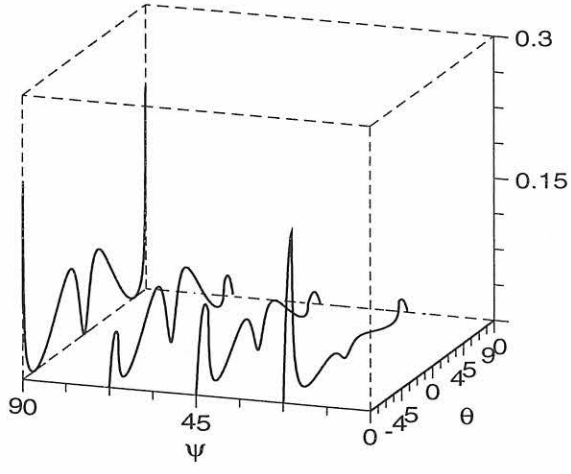

d) z-axis: t_{T2qL}

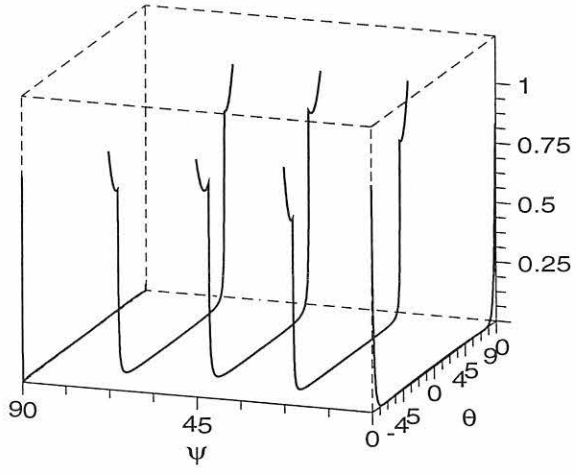

e) z-axis: r_{qLqL}

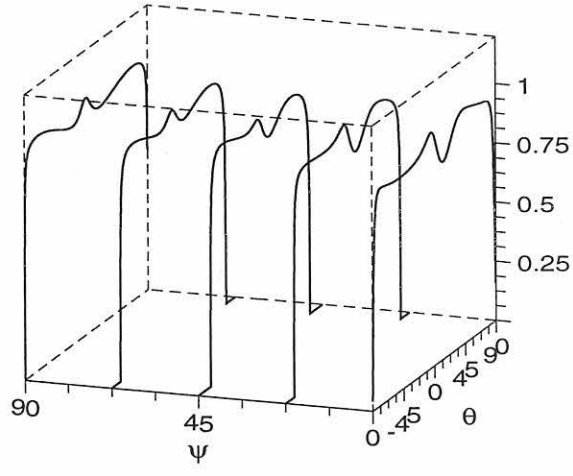

f) z-axis: t_{qLqL}

Figure D.32: *Reflection and transmission energy coefficients of the three waves at the interface between two transverse isotropic media as a function of the incidence angle* Θ *and the layback angle* Ψ *of medium 2.* **Quasi longitudinal (qL)** *wave incidence in the meridian plane from medium 1. Medium 1: Columnar grains perpendicular to the interface. Medium 2: Columnar grain tilt angle* $\Phi = 67,5°$.

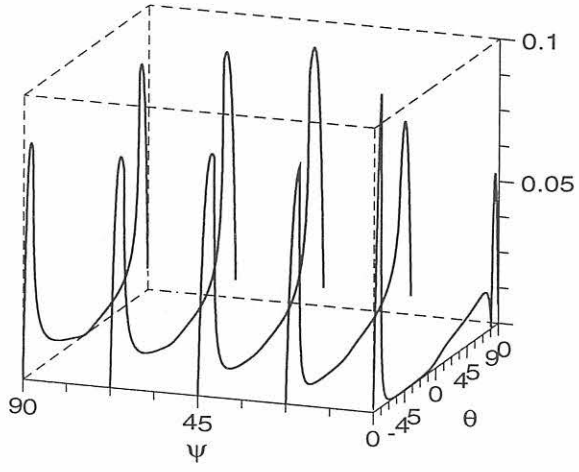

a) z-axis: r_{qT1qL}

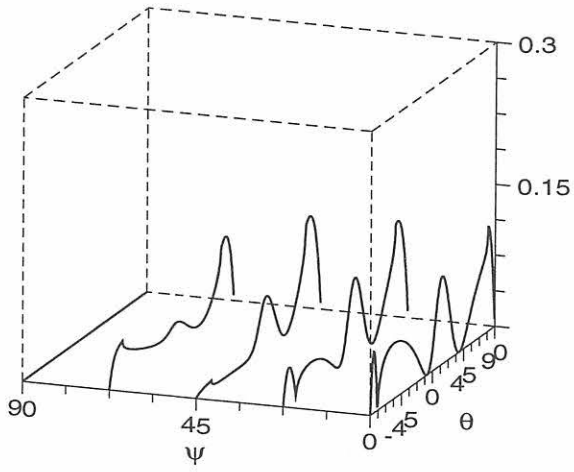

b) z-axis: t_{qT1qL}

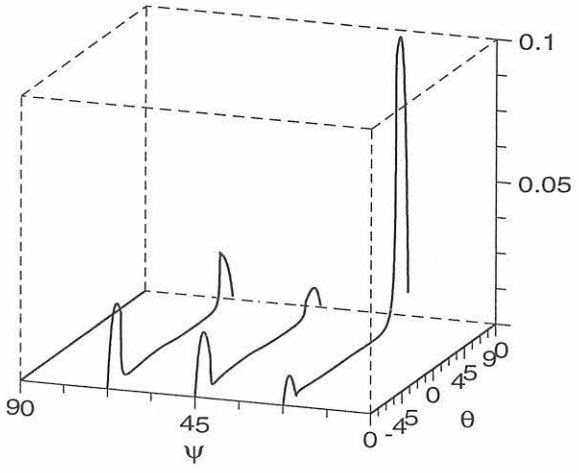

c) z-axis: r_{T2qL}

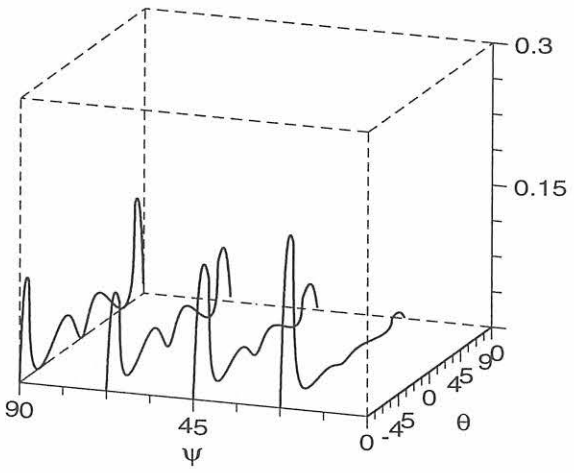

d) z-axis: t_{T2qL}

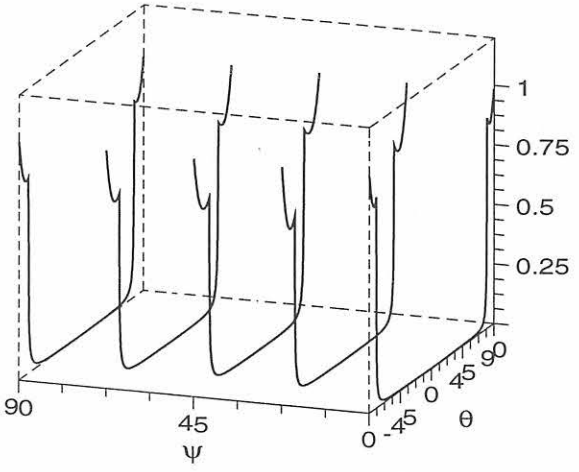

e) z-axis: r_{qLqL}

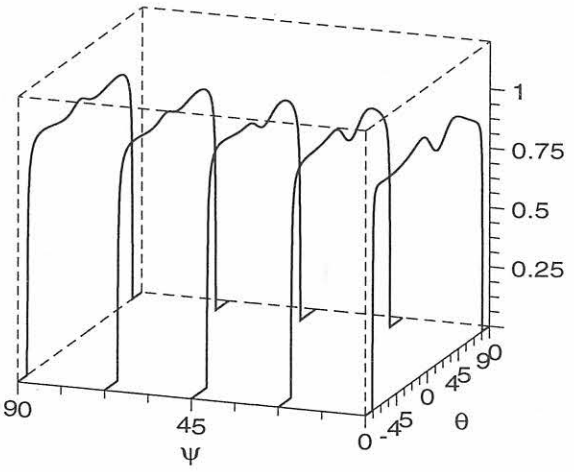

f) z-axis: t_{qLqL}

Figure D.33: *Reflection and transmission energy coefficients of the three waves at the interface between two transverse isotropic media as a function of the incidence angle* Θ *and the layback angle* Ψ *of medium 2.* **Quasi longitudinal (qL)** *wave incidence in the meridian plane from medium 1. Medium 1: Columnar grains parallel to the interface. Medium 2: Columnar grain tilt angle* $\Phi = 67,5°$.

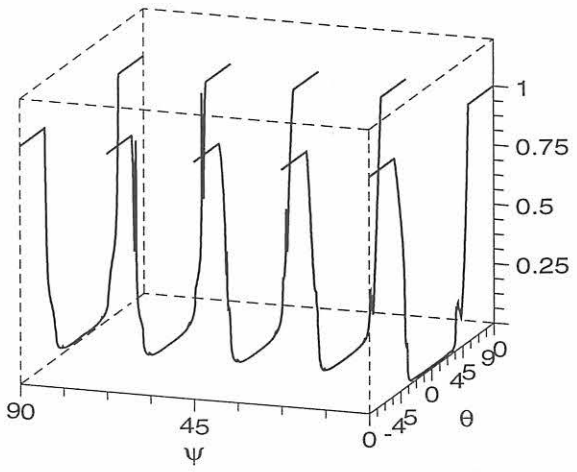

a) z-axis: r_{qT1qT1}

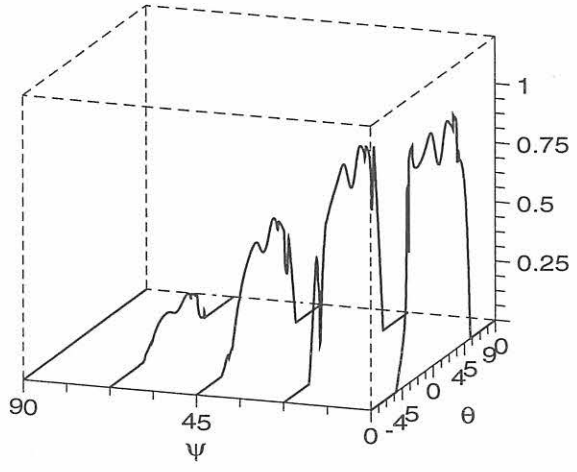

b) z-axis: t_{qT1qT1}

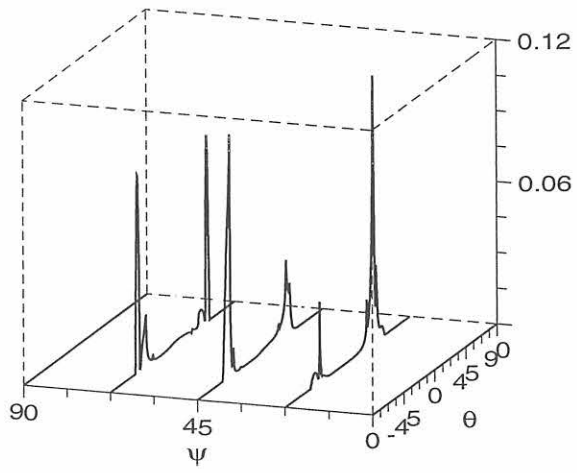

c) z-axis: r_{T2qT1}

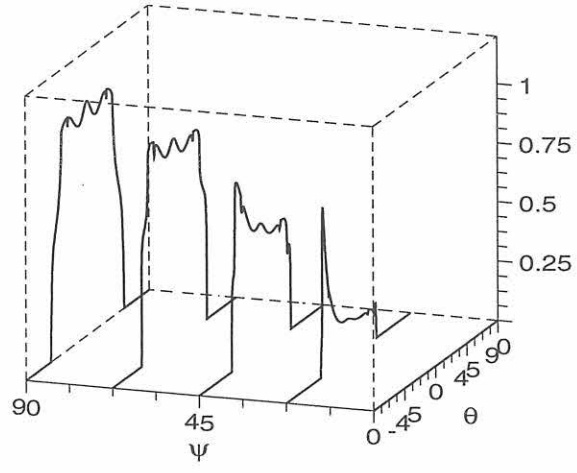

d) z-axis: t_{T2qT1}

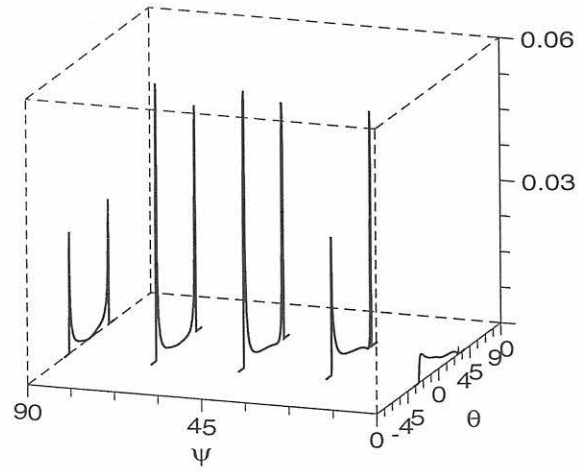

e) z-axis: r_{qLqT1}

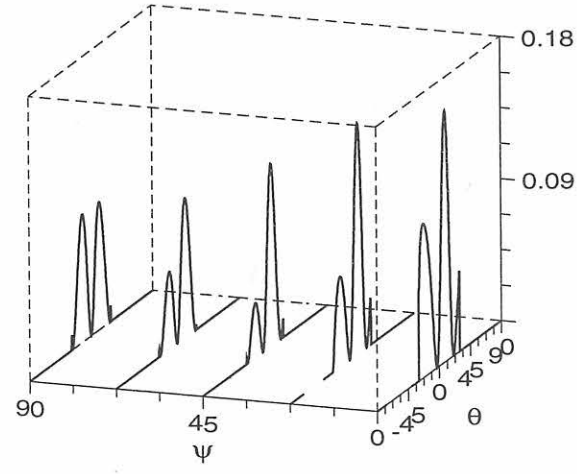

f) z-axis: t_{qLqT1}

Figure D.34: *Reflection and transmission energy coefficients of the three waves at the interface between two transverse isotropic media as a function of the incidence angle* Θ *and the layback angle* Ψ *of medium 2.* **Quasi transverse (qT1)** *wave incidence in the meridian plane from medium 1. Medium 1: Columnar grains perpendicular to the interface. Medium 2: Columnar grain tilt angle* $\Phi = 67,5°$.

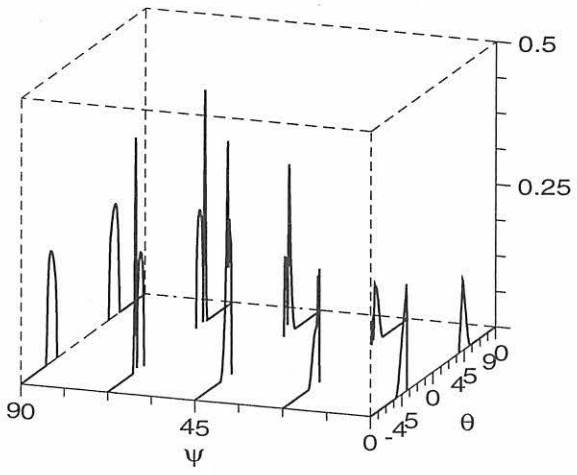

g) z-axis: $r_{qT1(2)qT1}$; Grain angle 67.5°

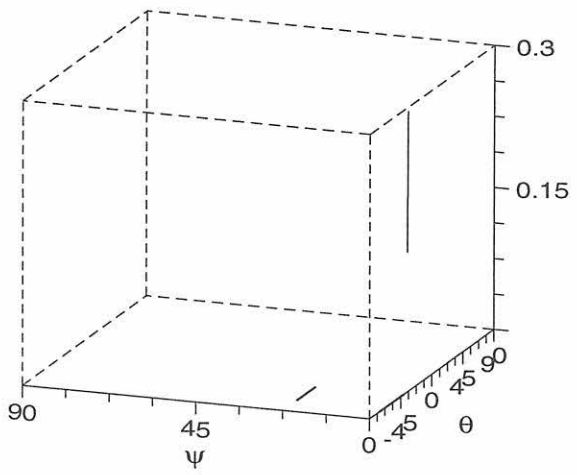

h) z-axis: t_{qT1qT1}; Grain angle 67.5°

Figure D.35: *Reflection and transmission energy coefficients of the second branch of the quasi transverse wave qT1(2) at the interface between two transverse isotropic media as a function of the incidence angle* Θ *and the layback angle* Ψ *of medium 2.* **Quasi transverse (qT1)** *wave incidence in the meridian plane from medium 1. Medium 1: Columnar grains perpendicular to the interface. Medium 2: Columnar grain tilt angle* $\Phi = 67,5°$.

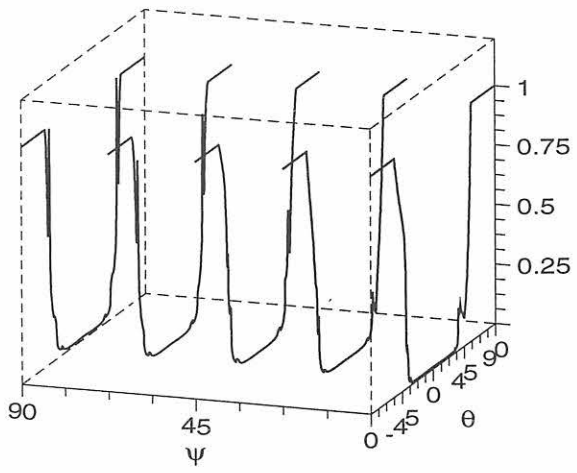

a) z-axis: r_{qT1qT1}

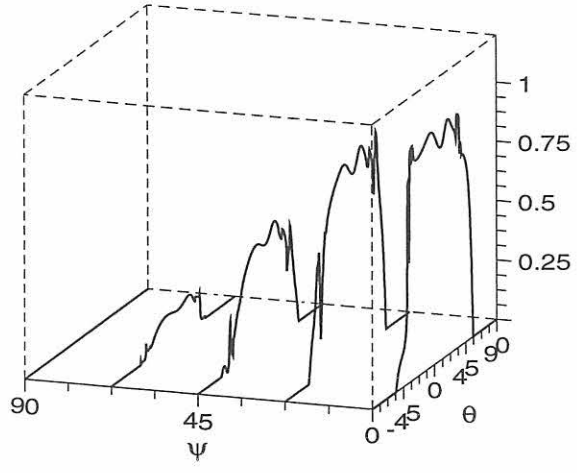

b) z-axis: t_{qT1qT1}

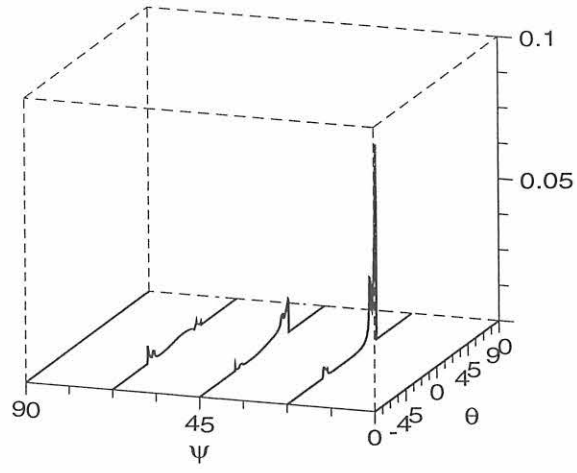

c) z-axis: r_{T2qT1}

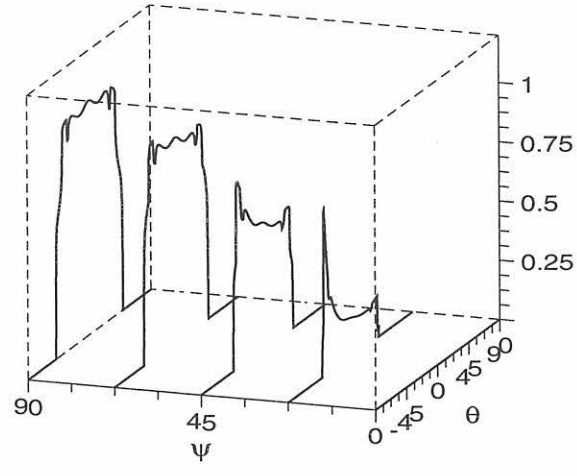

d) z-axis: t_{T2qT1}

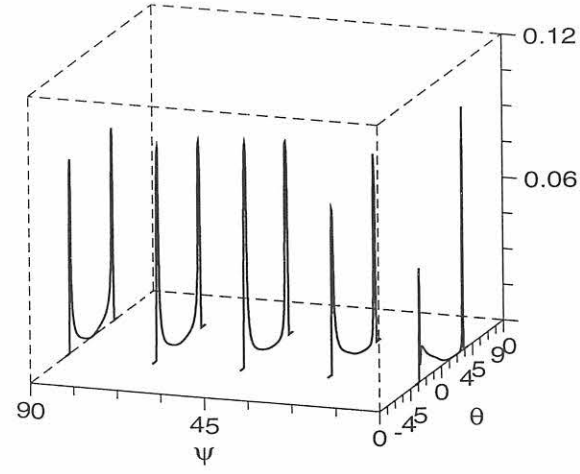

e) z-axis: r_{qLqT1}

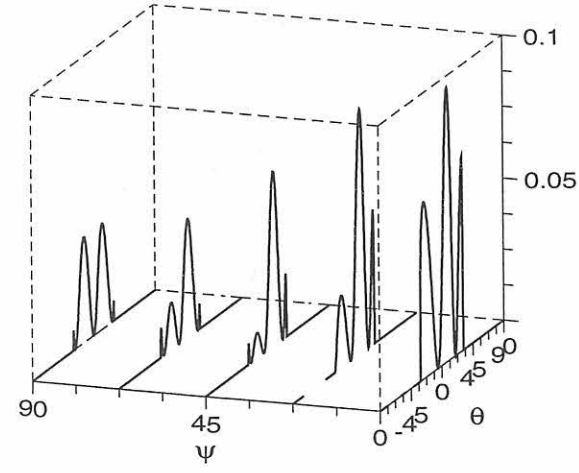

f) z-axis: t_{qLqT1}

Figure D.36: *Reflection and transmission energy coefficients of the three waves at the interface between two transverse isotropic media as a function of the incidence angle* Θ *and the layback angle* Ψ *of medium 2.* **Quasi transverse (qT1)** *wave incidence in the meridian plane from medium 1. Medium 1: Columnar grains parallel to the interface. Medium 2: Columnar grain tilt angle* $\Phi = 67,5°$.

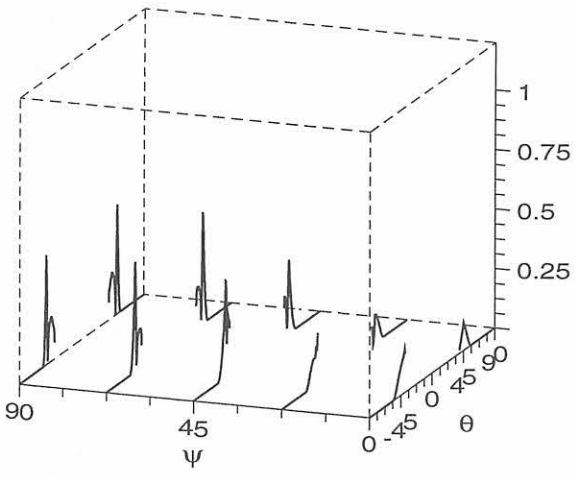

g) z-axis: $r_{qT1(2)qT1}$; Grain angle 67.5°

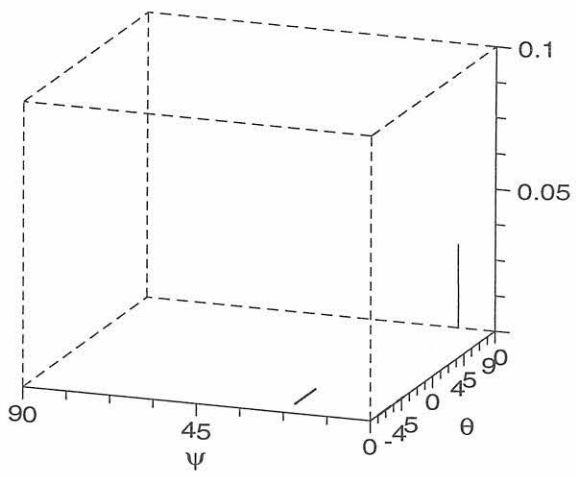

h) z-axis: t_{qT1qT1}; Grain angle 67.5°

Figure D.37: *Reflection and transmission energy coefficients of the second branch of the quasi transverse wave qT1(2) at the interface between two transverse isotropic media as a function of the incidence angle* Θ *and the layback angle* Ψ *of medium 2.* **Quasi transverse (qT1)** *wave incidence in the meridian plane from medium 1. Medium 1: Columnar grains parallel to the interface. Medium 2: Columnar grain tilt angle* $\Phi = 67,5°$.

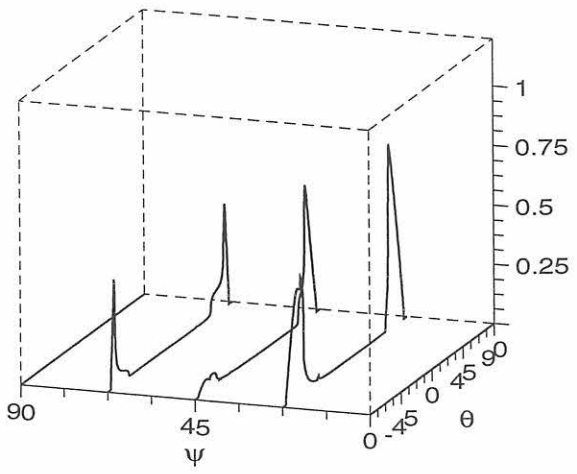

a) z-axis: r_{qT1T2}

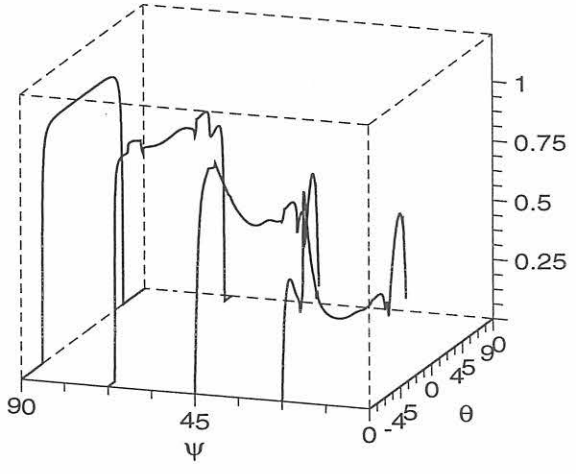

b) z-axis: t_{qT1T2}

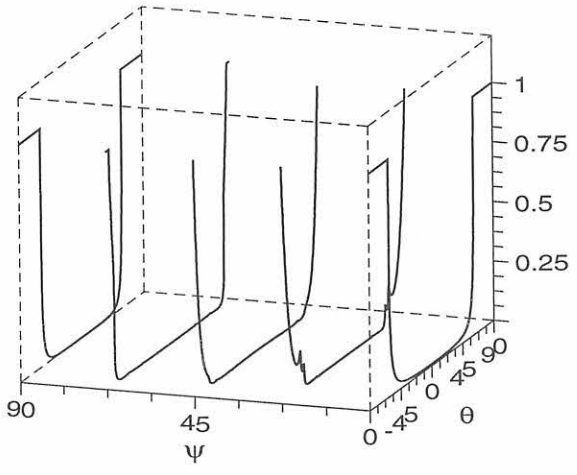

c) z-axis: r_{T2T2}

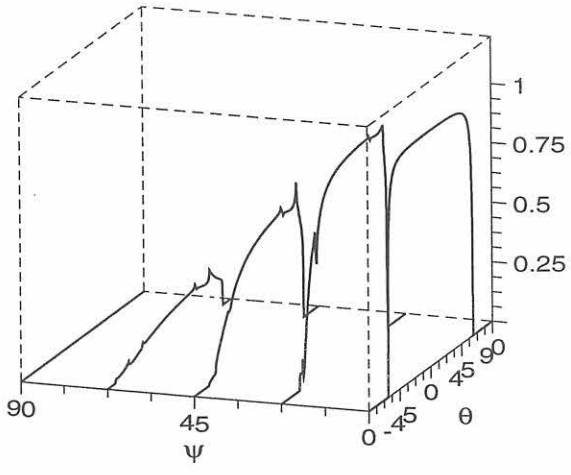

d) z-axis: t_{T2T2}

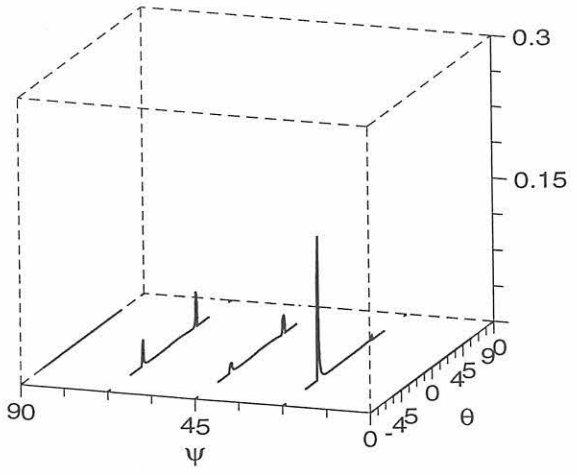

e) z-axis: r_{qLT2}

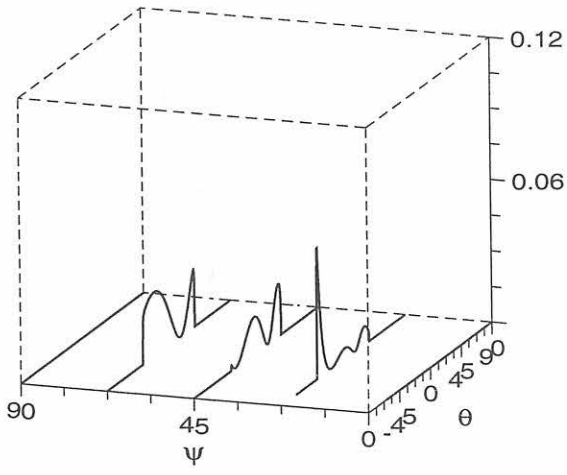

f) z-axis: t_{qLT2}

Figure D.38: *Reflection and transmission energy coefficients of the three waves at the interface between two transverse isotropic media as a function of the incidence angle* Θ *and the layback angle* Ψ *of medium 2.* **Pure transverse (T2)** *wave incidence in the meridian plane from medium 1. Medium 1: Columnar grains perpendicular to the interface. Medium 2: Columnar grain tilt angle* $\Phi = 67,5°$.

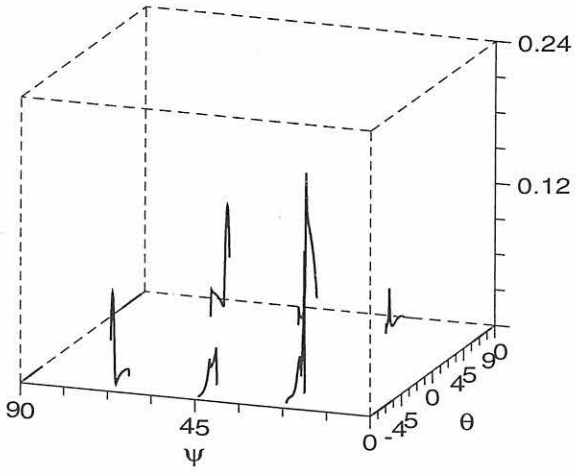

g) z-axis: $r_{qT1(2)T2}$; Grain angle 67.5°

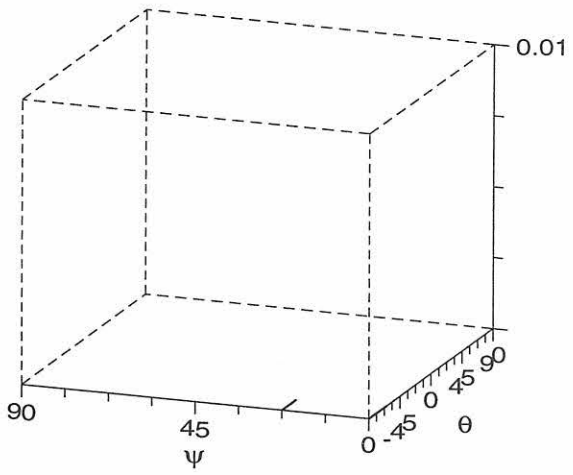

h) z-axis: $t_{qT1(2)T2}$; Grain angle 67.5°

Figure D.39: *Reflection and transmission energy coefficients of the second branch of the quasi transverse wave qT1(2) at the interface between two transverse isotropic media as a function of the incidence angle* Θ *and the layback angle* Ψ *of medium 2.* **Pure transverse (T2)** *wave incidence in the meridian plane from medium 1. Medium 1: Columnar grains perpendicular to the interface. Medium 2: Columnar grain tilt angle* $\Phi = 67,5°$.

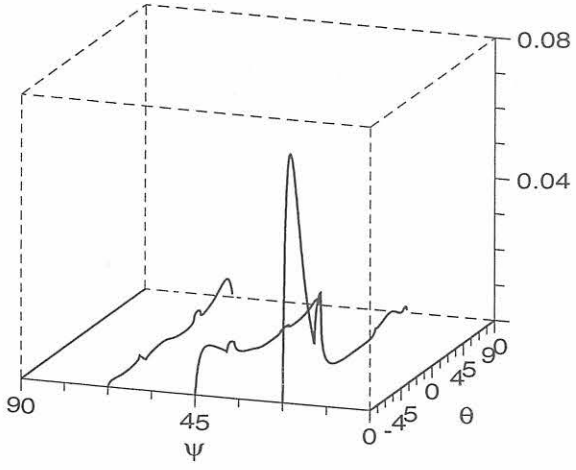

a) z-axis: r_{qT1T2}

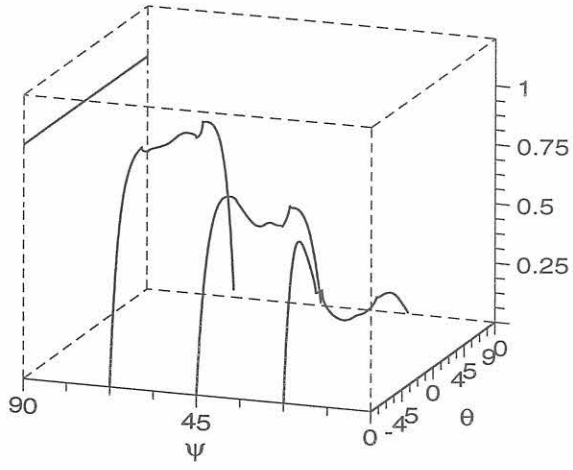

b) z-axis: t_{qT1T2}

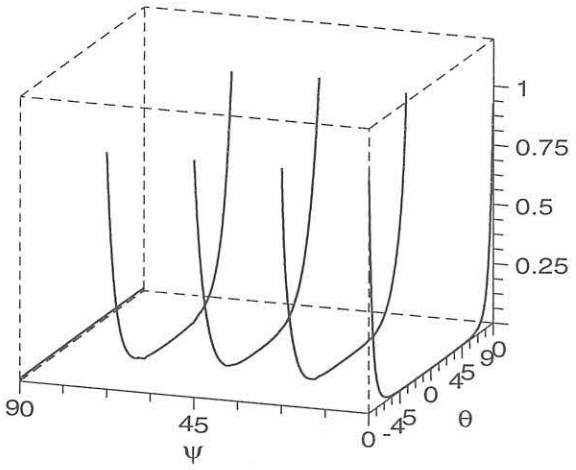

c) z-axis: r_{T2T2}

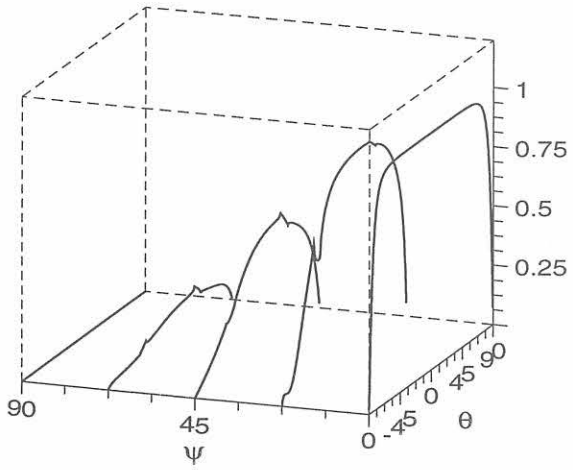

d) z-axis: t_{T2T2}

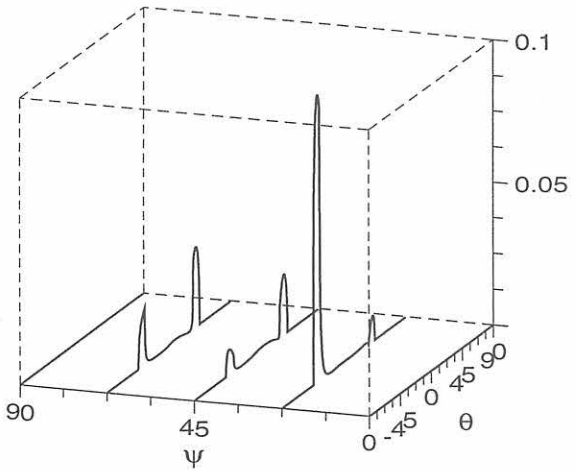

e) z-axis: r_{qLT2}

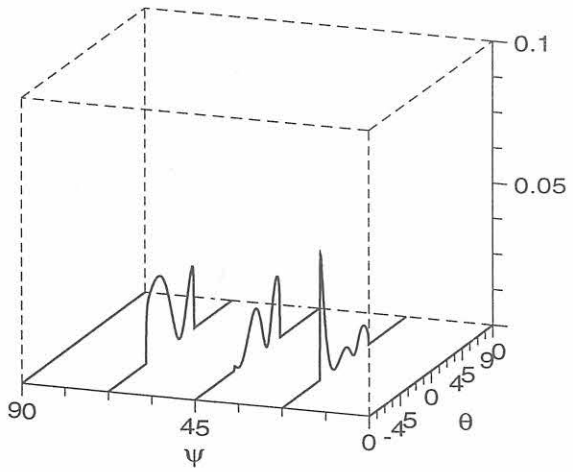

f) z-axis: t_{qLT2}

Figure D.40: *Reflection and transmission energy coefficients of the three waves at the interface between two transverse isotropic media as a function of the incidence angle* Θ *and the layback angle* Ψ *of medium 2.* **Pure transverse (T2)** *wave incidence in the meridian plane from medium 1. Medium 1: Columnar grains parallel to the interface. Medium 2: Columnar grain tilt angle* $\Phi = 67,5°$.

D.4 Interface between two transverse isotropic media; General case: Ultrasound propagation in an arbitrary plane

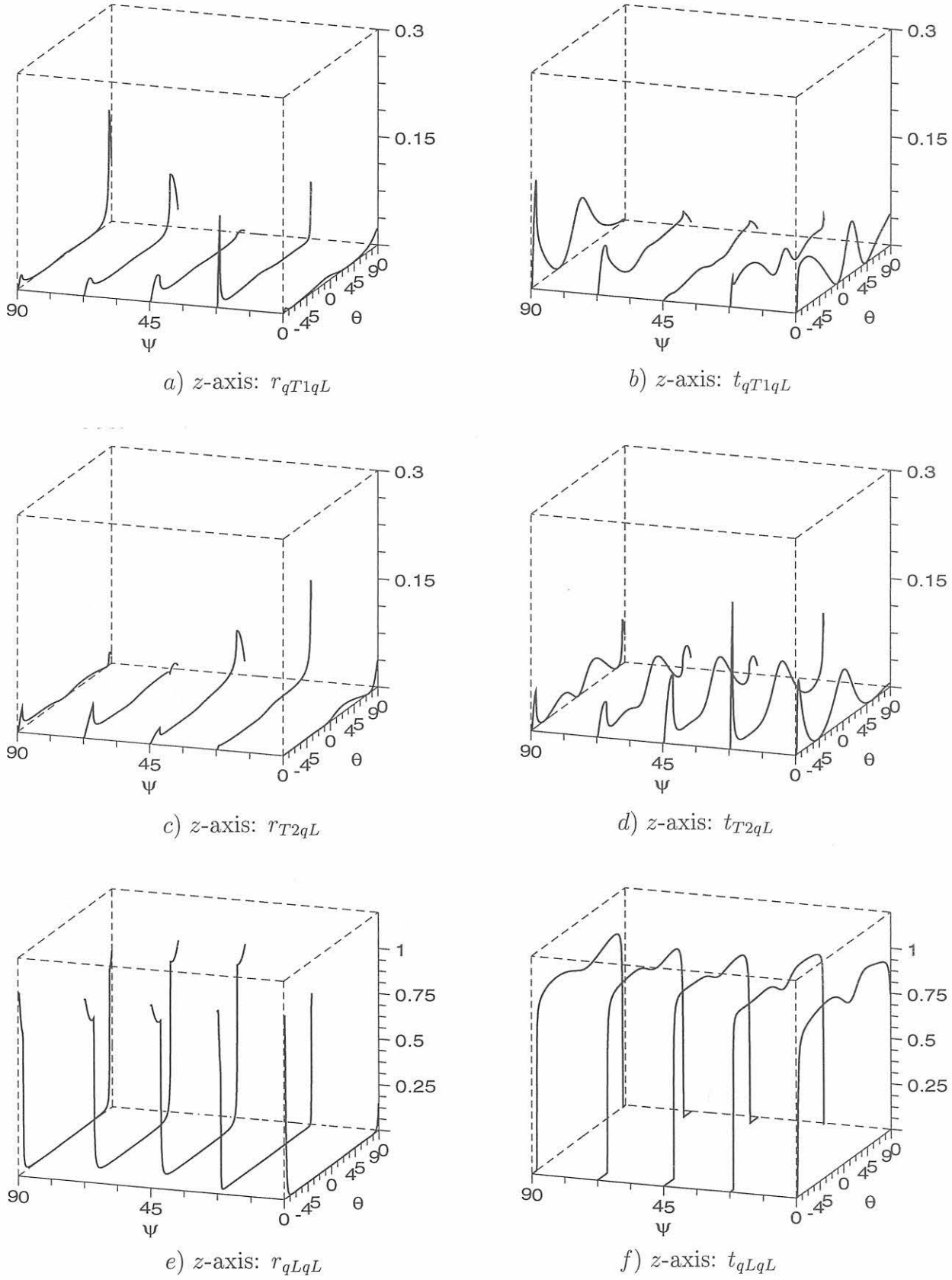

a) z-axis: r_{qT1qL}

b) z-axis: t_{qT1qL}

c) z-axis: r_{T2qL}

d) z-axis: t_{T2qL}

e) z-axis: r_{qLqL}

f) z-axis: t_{qLqL}

Figure D.41: *Reflection and transmission energy coefficients of the three waves at the interface between two transverse isotropic media as a function of the incidence angle* Θ *and the layback angle* Ψ *of medium 2.* **Quasi longitudinal (qL)** *wave incidence from medium 1. Medium 1: Grain angle* $\Phi = 0°$*; layback angle* $\Psi = -22,5°$*. Medium 2: Columnar grain tilt angle* $\Phi = 67,5°$*.*

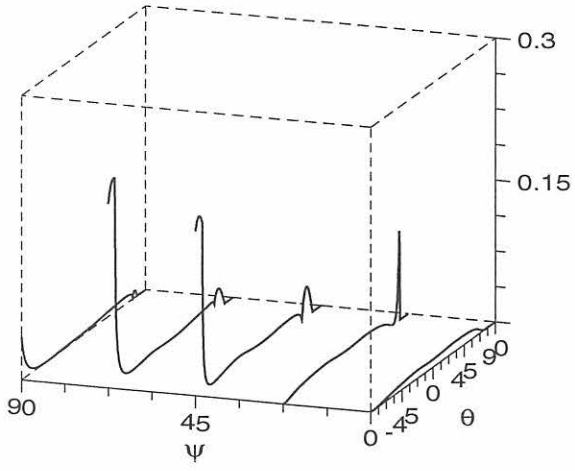

a) z-axis: r_{qT1qL}

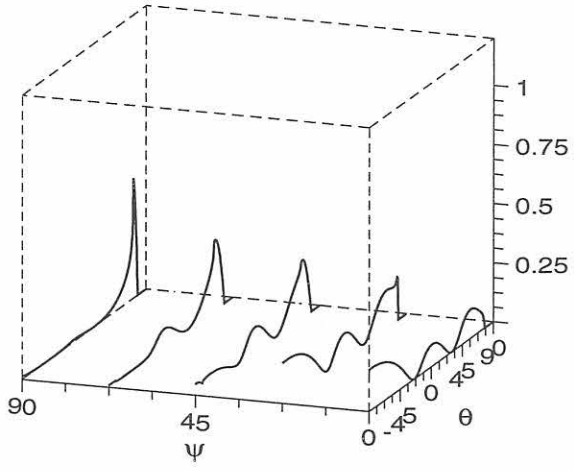

b) z-axis: t_{qT1qL}

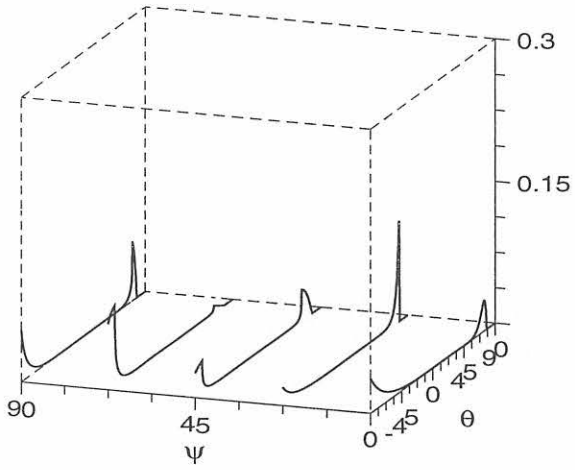

c) z-axis: r_{T2qL}

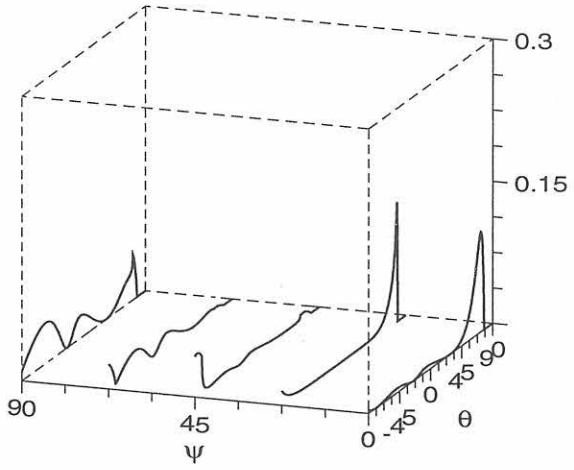

d) z-axis: t_{T2qL}

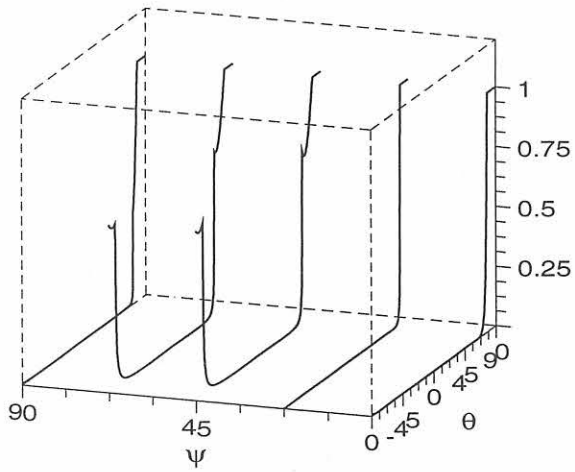

e) z-axis: r_{qLqL}

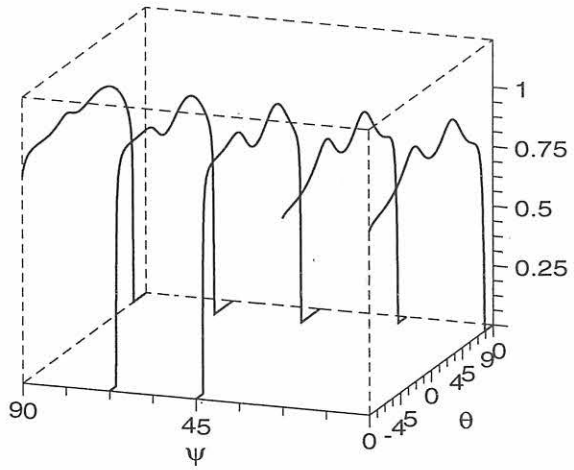

f) z-axis: t_{qLqL}

Figure D.42: *Energy reflection and transmission coefficients of the three waves at the interface between two transverse isotropic media as a function of the incidence angle* Θ *and the layback angle* Ψ *of medium 2.* **Quasi longitudinal (qL)** *wave incidence from medium 1. Medium 1: Grain angle* $\Phi = -67,5°$*; layback angle* $\Psi = -22,5°$*. Medium 2: Columnar grain tilt angle* $\Phi = 67,5°$*.*

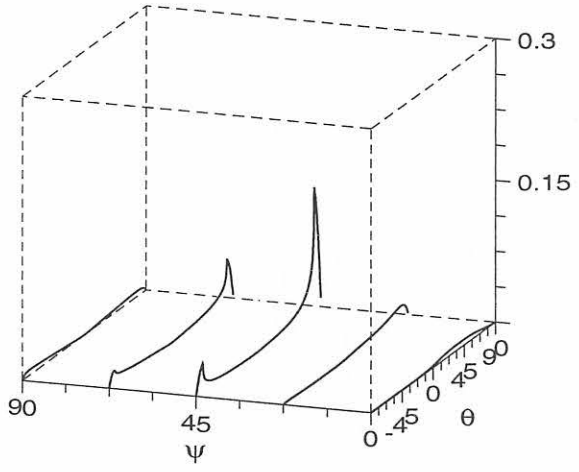

a) z-axis: r_{qT1qL}

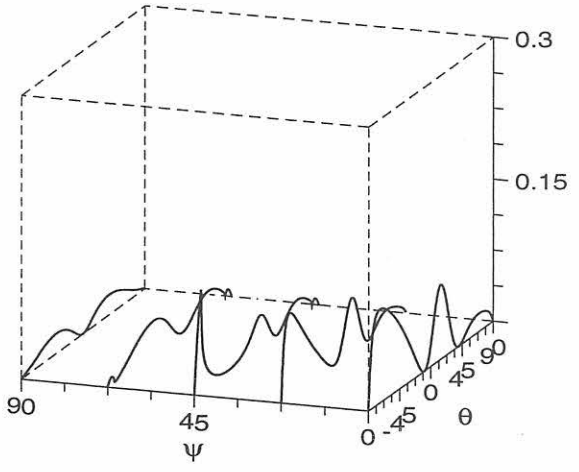

b) z-axis: t_{qT1qL}

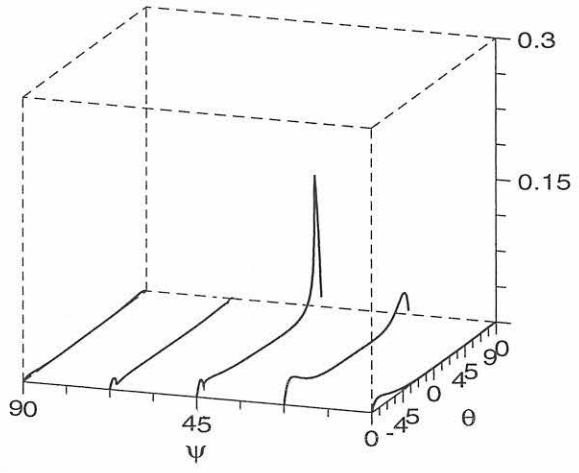

c) z-axis: r_{T2qL}

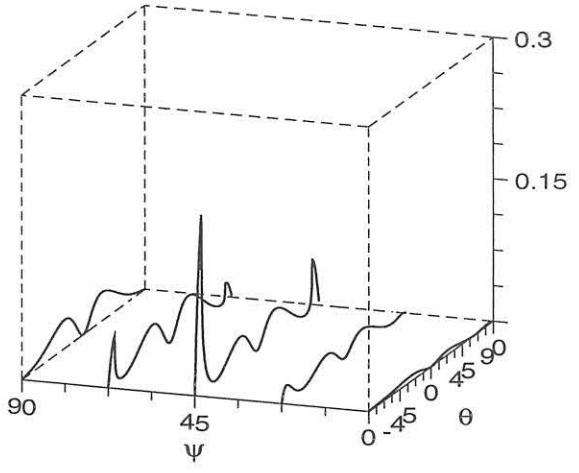

d) z-axis: t_{T2qL}

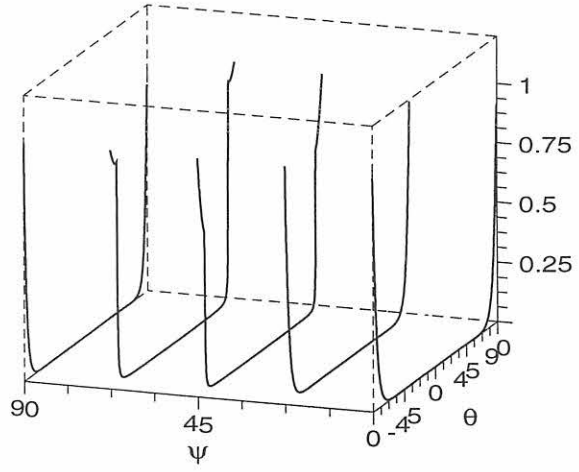

e) z-axis: r_{qLqL}

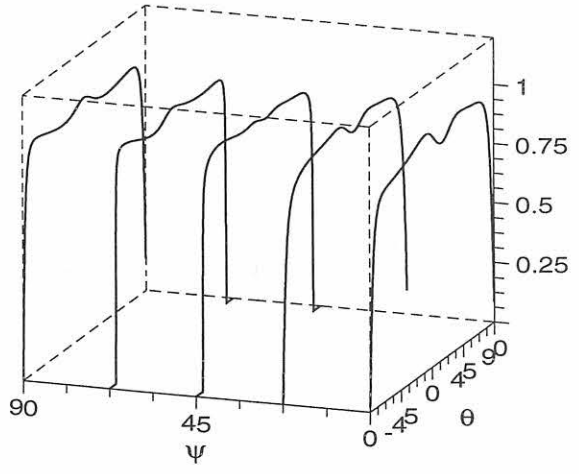

f) z-axis: t_{qLqL}

Figure D.43: *Reflection and transmission energy coefficients of the three waves at the interface between two transverse isotropic media as a function of the incidence angle* Θ *and the layback angle* Ψ *of medium 2.* **Quasi longitudinal (qL)** *wave incidence from medium 1. Medium 1: Grain angle* $\Phi = 90°$*; layback angle* $\Psi = -22,5°$*. Medium 2: Columnar grain tilt angle* $\Phi = 67,5°$*.*

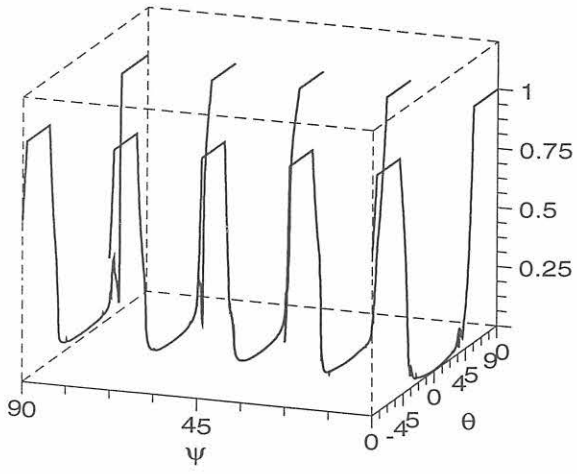

a) z-axis: r_{qT1qT1}

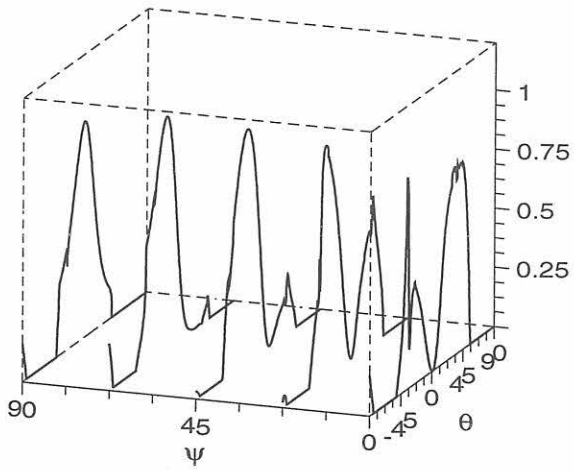

b) z-axis: t_{qT1qT1}

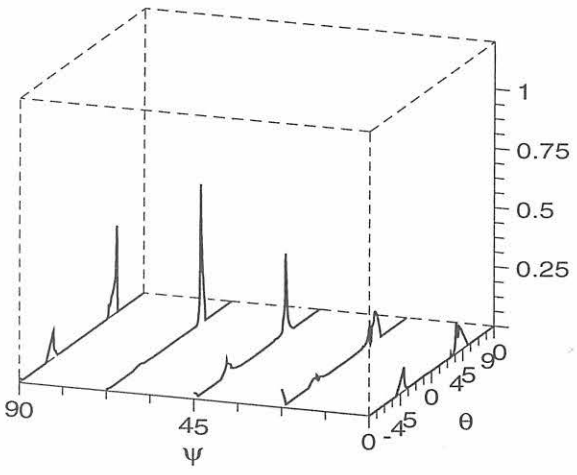

c) z-axis: r_{T2qT1}

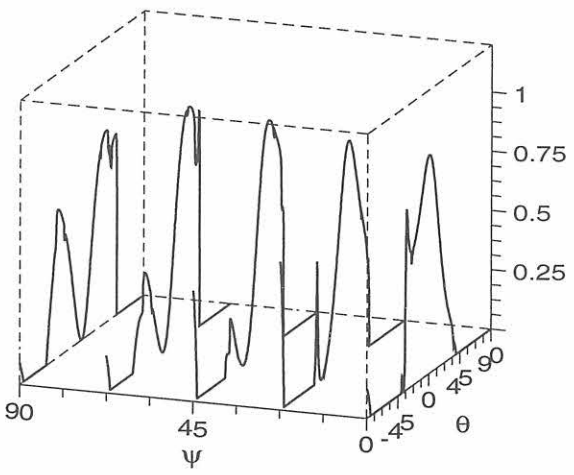

d) z-axis: t_{T2qT1}

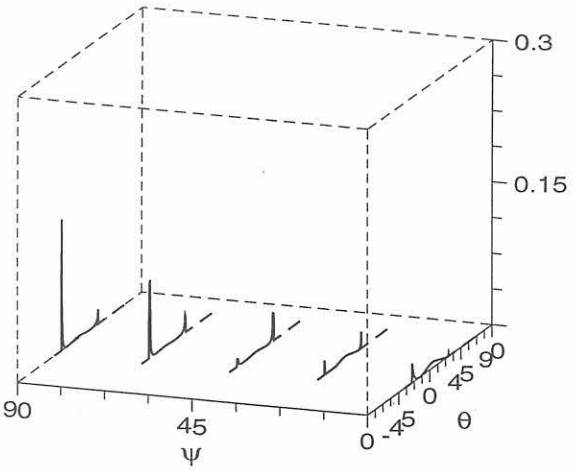

e) z-axis: r_{qLqT1}

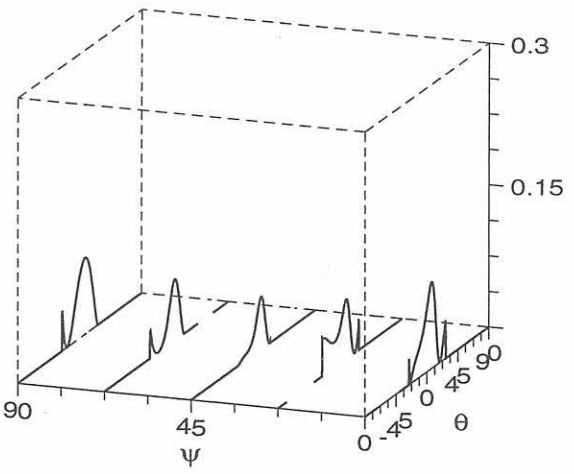

f) z-axis: t_{qLqT1}

Figure D.44: *Reflection and transmission energy coefficients of the three waves at the interface between two transverse isotropic media as a function of the incidence angle* Θ *and the layback angle* Ψ *of medium 2.* **Quasi transverse (qT1)** *wave incidence from medium 1. Medium 1: Grain angle* $\Phi = 0°$*; layback angle* $\Psi = -22,5°$*. Medium 2: Columnar grain tilt angle* $\Phi = 67,5°$*.*

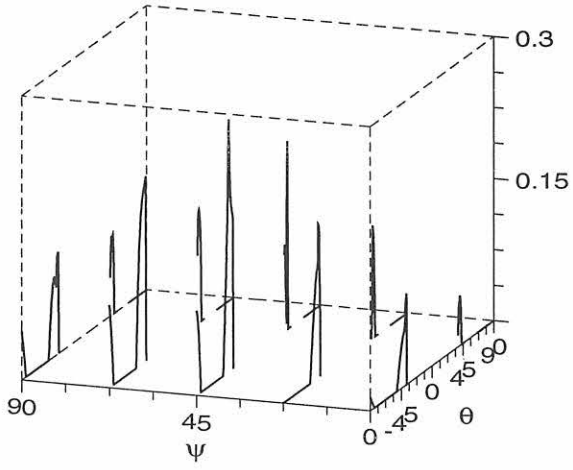

g) z-axis: $r_{qT1(2)qT1}$

Figure D.45: *Energy reflection and transmission coefficients of the second branch of the quasi transverse wave qT1(2) at the interface between two transverse isotropic media as a function of the incidence angle* Θ *and the layback angle* Ψ *of medium 2.* **Quasi transverse (qT1)** *wave incidence from medium 1. Medium 1: Grain angle* $\Phi = 0°$*; layback angle* $\Psi = -22,5°$*. Medium 2: Columnar grain tilt angle* $\Phi = 67,5°$*.*

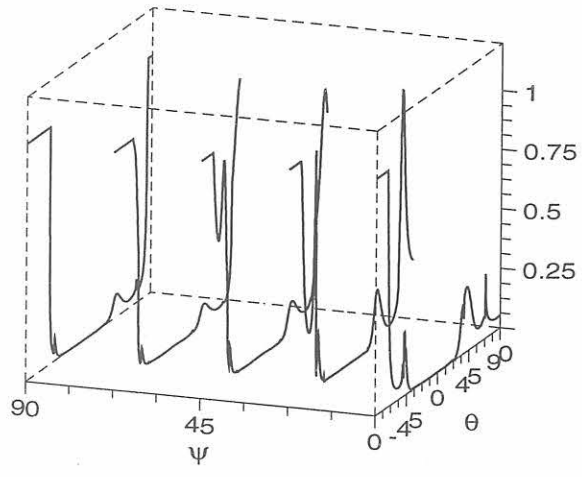

a) z-axis: r_{qT1qT1}

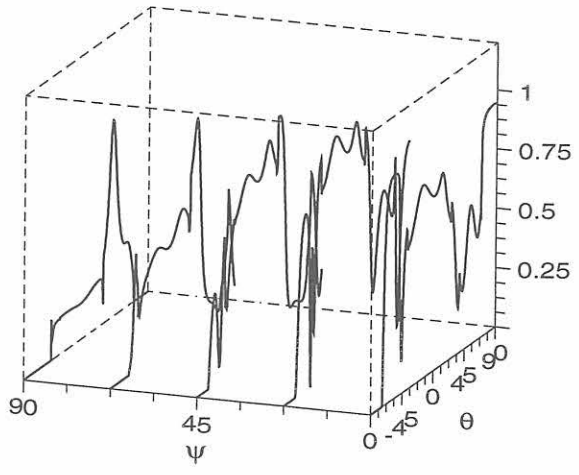

b) z-axis: t_{qT1qT1}

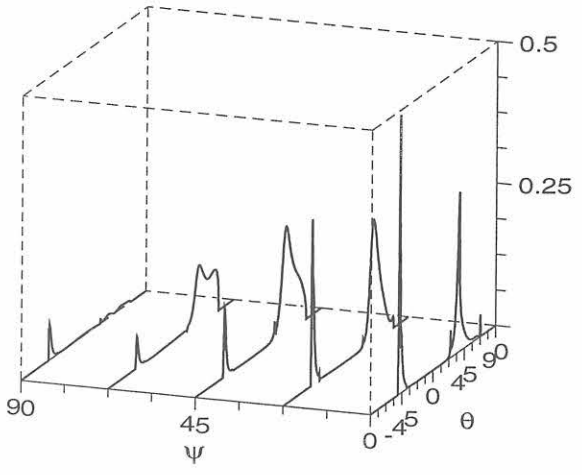

c) z-axis: r_{T2qT1}

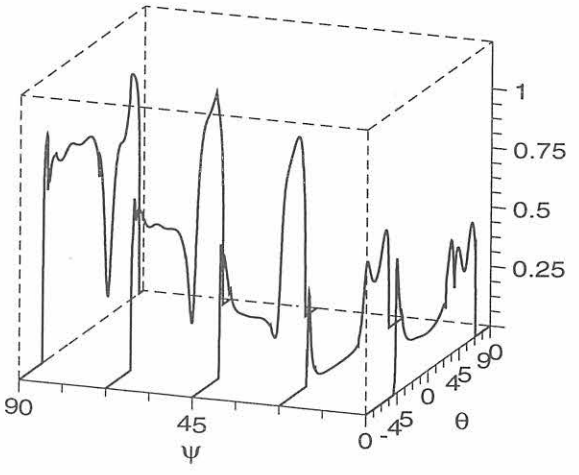

d) z-axis: t_{T2qT1}

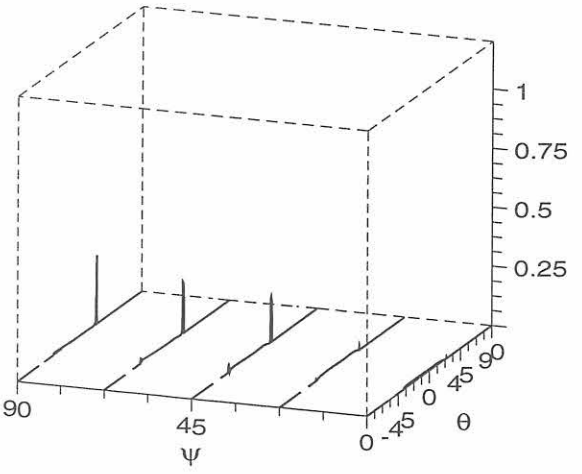

e) z-axis: r_{qLqT1}

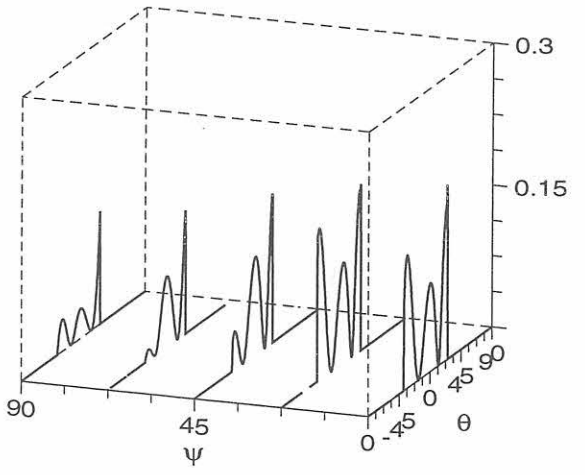

f) z-axis: t_{qLqT1}

Figure D.46: *Energy reflection and transmission coefficients of the three waves at the interface between two transverse isotropic media as a function of the incidence angle* Θ *and the layback angle* Ψ *of medium 2.* **Quasi transverse (qT1)** *wave incidence from medium 1. Medium 1: Grain angle* $\Phi = -67,5°$*; layback angle* $\Psi = -22,5°$*. Medium 2: Columnar grain tilt angle* $\Phi = 67,5°$*.*

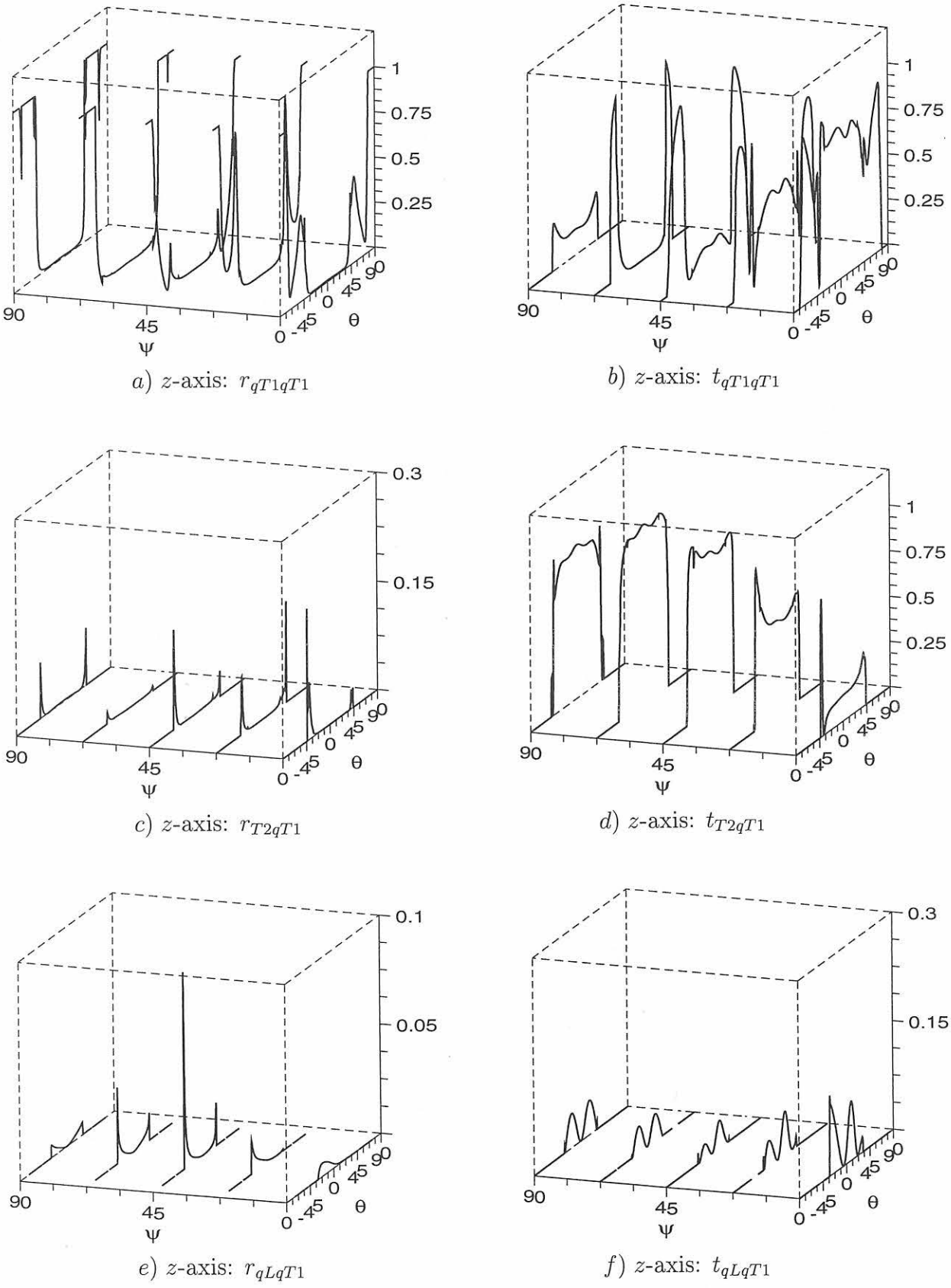

a) z-axis: r_{qT1qT1}

b) z-axis: t_{qT1qT1}

c) z-axis: r_{T2qT1}

d) z-axis: t_{T2qT1}

e) z-axis: r_{qLqT1}

f) z-axis: t_{qLqT1}

Figure D.47: *Reflection and transmission energy coefficients of the three waves at the interface between two transverse isotropic media as a function of the incidence angle* Θ *and the layback angle* Ψ *of medium 2.* **Quasi transverse (qT1)** *wave incidence from medium 1. Medium 1: Grain angle* $\Phi = 90°$*; layback angle* $\Psi = -22,5°$*. Medium 2: Columnar grain tilt angle* $\Phi = 67,5°$*.*

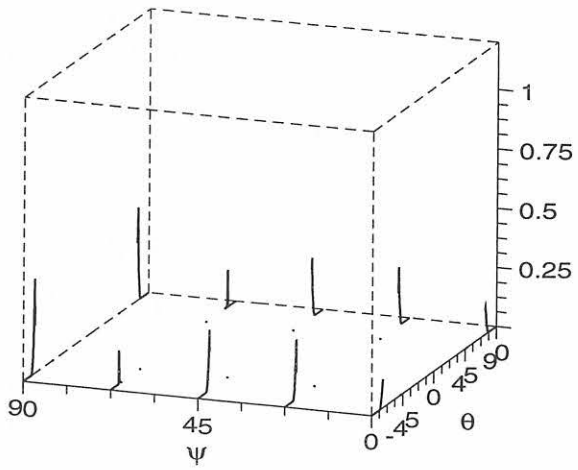

g) z-axis: $r_{qT1(2)qT1}$

Figure D.48: *Energy reflection and transmission coefficients of the second branch of the quasi transverse wave qT1(2) at the interface between two transverse isotropic media as a function of the incidence angle* Θ *and the layback angle* Ψ *of medium 2.* **Quasi transverse (qT1)** *wave incidence from medium 1. Medium 1: Grain angle* $\Phi = 90°$*; layback angle* $\Psi = -22,5°$*. Medium 2: Columnar grain tilt angle* $\Phi = 67,5°$*.*

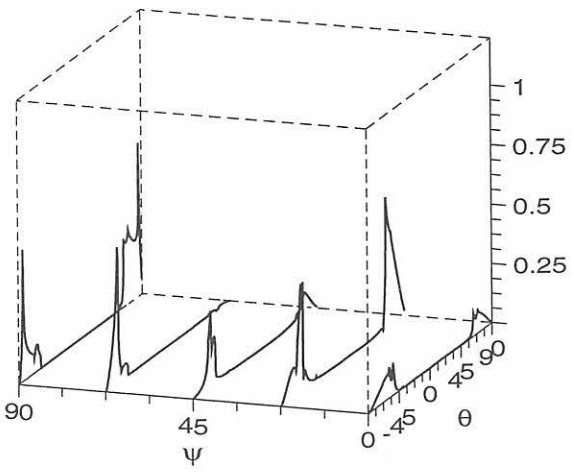

a) z-axis: r_{qT1T2}

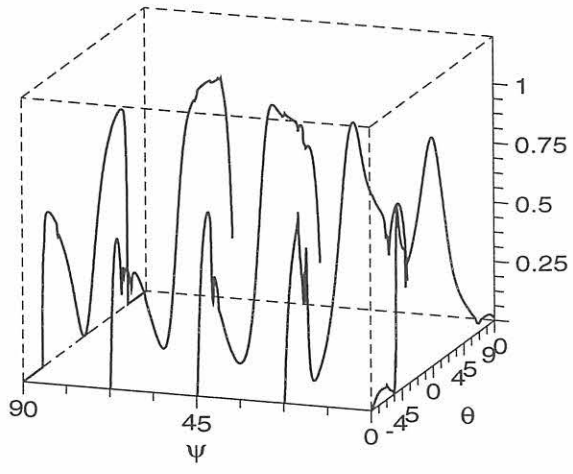

b) z-axis: t_{qT1T2}

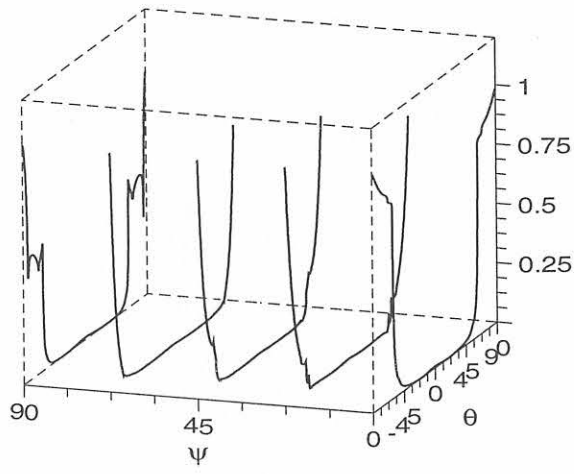

c) z-axis: r_{T2T2}

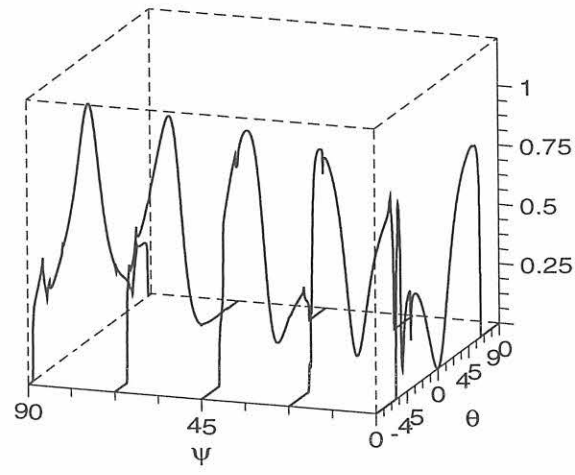

d) z-axis: t_{T2T2}

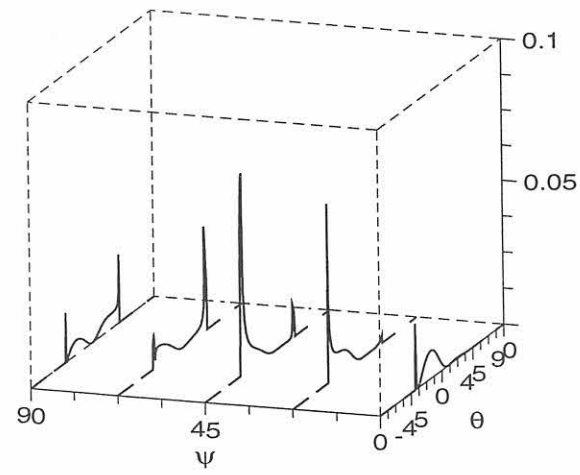

e) z-axis: r_{qLT2}

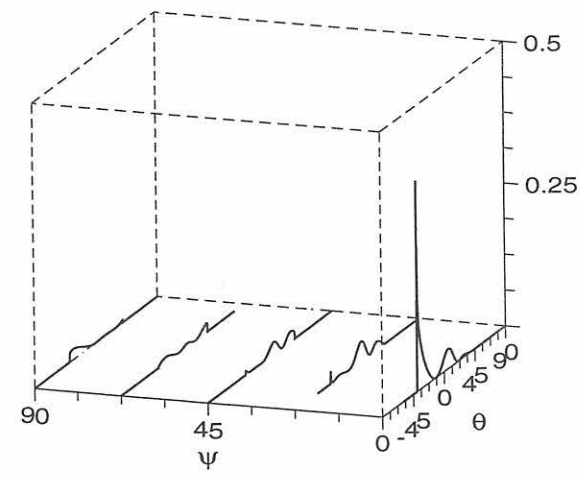

f) z-axis: t_{qLT2}

Figure D.49: *Reflection and transmission energy coefficients of the three waves at the interface between two transverse isotropic media as a function of the incidence angle* Θ *and the layback angle* Ψ *of medium 2.* **Pure transverse (T2)** *wave incidence from medium 1. Medium 1: Grain angle* $\Phi = 0°$*; layback angle* $\Psi = -22,5°$*. Medium 2: Columnar grain tilt angle* $\Phi = 67,5°$*.*

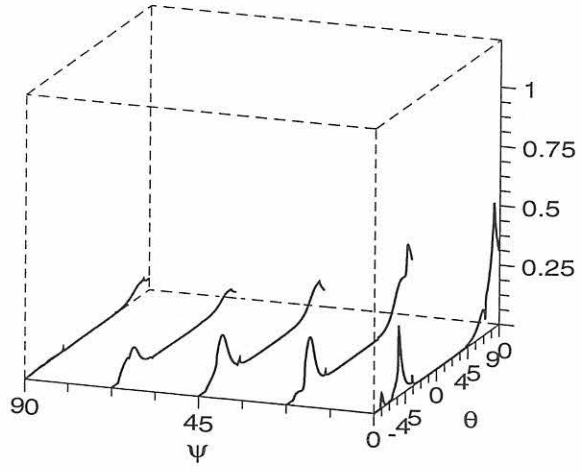

a) z-axis: r_{qT1T2}

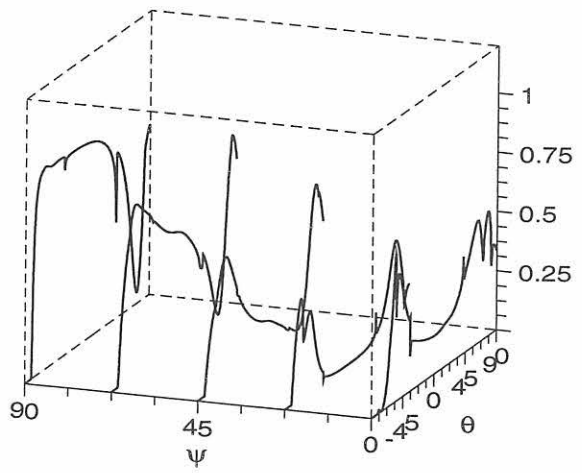

b) z-axis: t_{qT1T2}

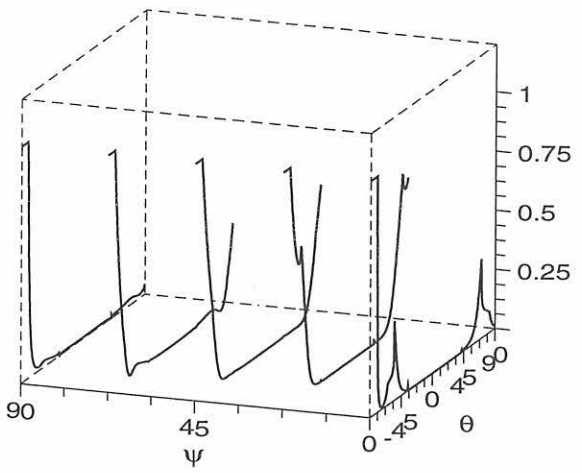

c) z-axis: r_{T2T2}

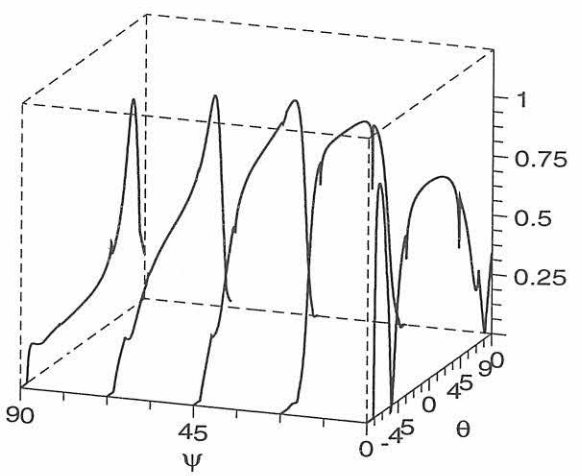

d) z-axis: t_{T2T2}

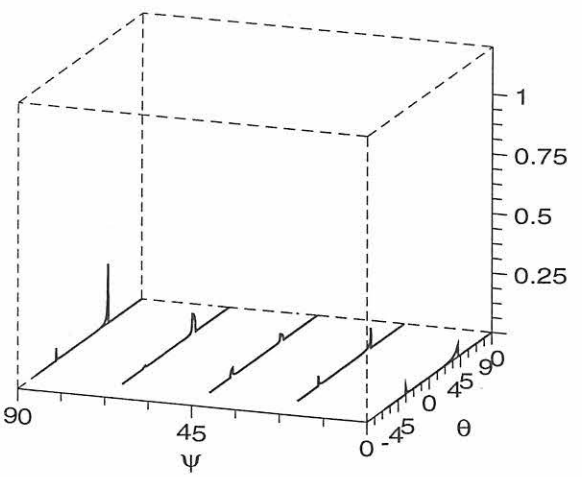

e) z-axis: r_{qLT2}

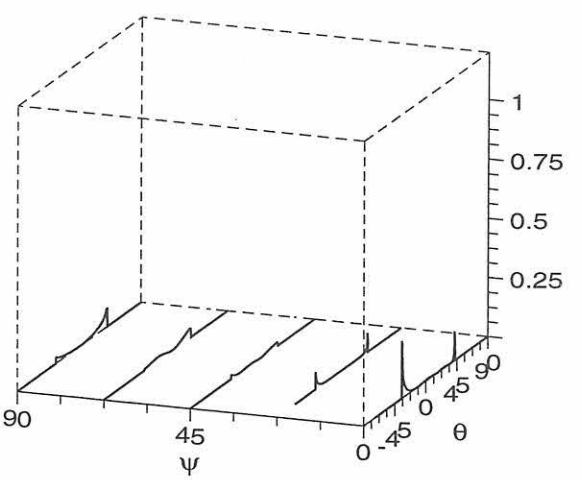

f) z-axis: t_{qLT2}

Figure D.50: *Energy reflection and transmission coefficients of the three waves at the interface between two transverse isotropic media as a function of the incidence angle* Θ *and the layback angle* Ψ *of medium 2.* **Pure transverse (T2)** *wave incidence from medium 1. Medium 1: Grain angle* $\Phi = -67,5°$*; layback angle* $\Psi = -22,5°$*. Medium 2: Columnar grain tilt angle* $\Phi = 67,5°$*.*

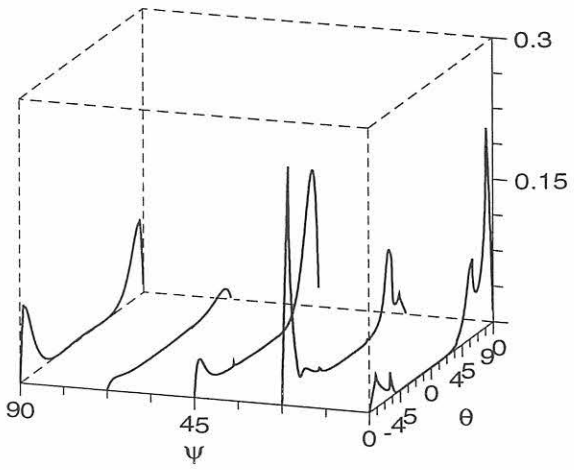

a) z-axis: r_{qT1T2}

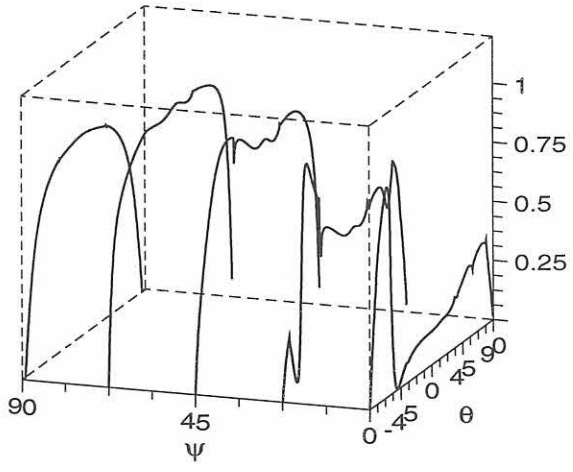

b) z-axis: t_{qT1T2}

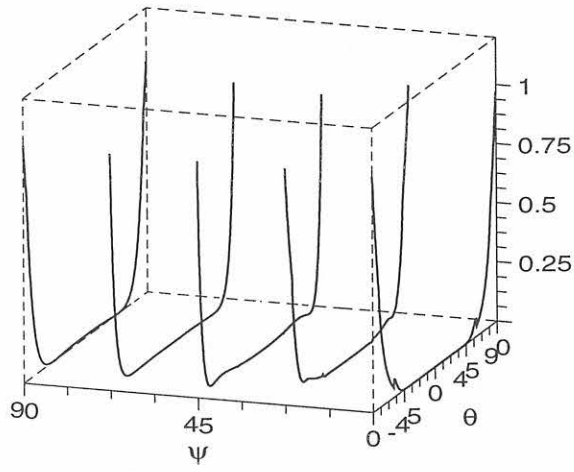

c) z-axis: r_{T2T2}

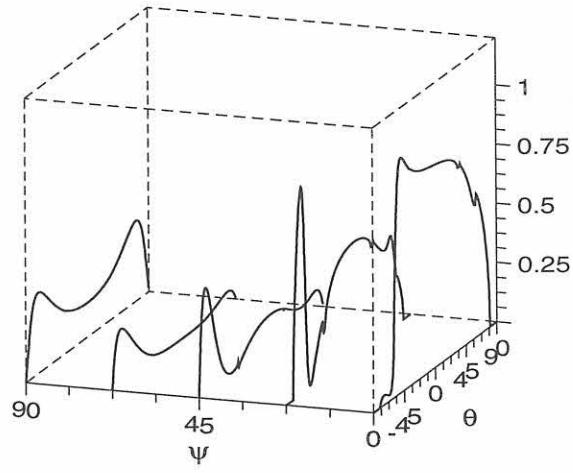

d) z-axis: t_{T2T2}

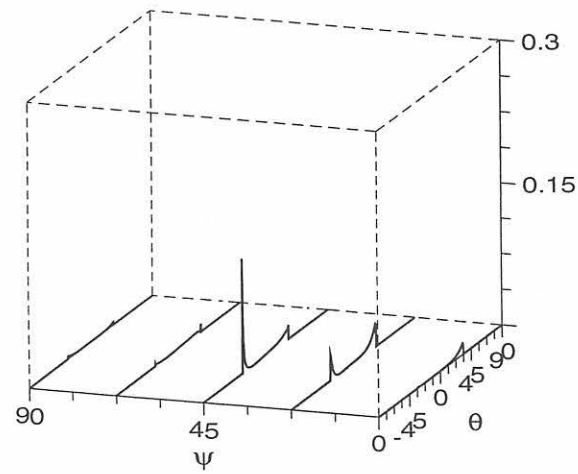

e) z-axis: r_{qLT2}

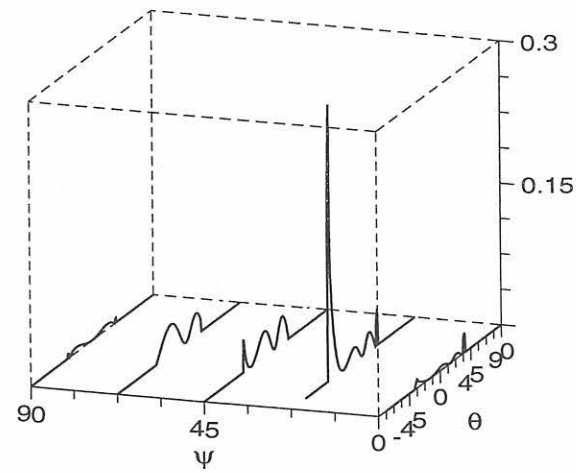

f) z-axis: t_{qLT2}

Figure D.51: *Reflection and transmission energy coefficients of the three waves at the interface between two transverse isotropic media as a function of the incidence angle* Θ *and the layback angle* Ψ *of medium 2.* **Pure transverse (T2)** *wave incidence from medium 1. Medium 1: Grain angle* $\Phi = 90°$*; layback angle* $\Psi = -22,5°$*. Medium 2: Columnar grain tilt angle* $\Phi = 67,5°$*.*

Appendix E

Reflection and transmission energy coefficients at imperfect interfaces

E.1 Solid imperfect interface between two anisotropic media

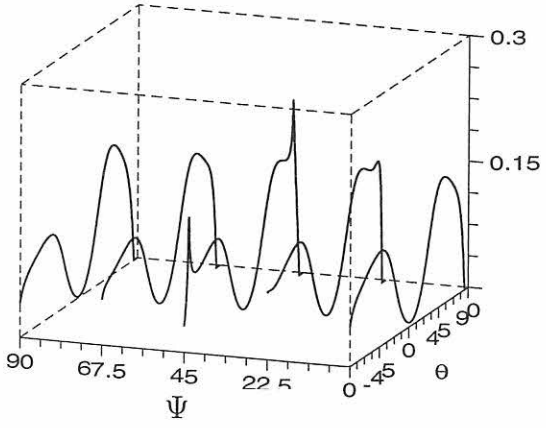

a) z-axis: r_{qT1qL}

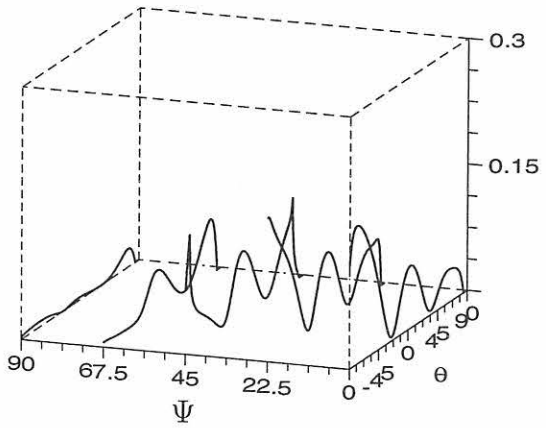

b) z-axis: t_{qT1qL}

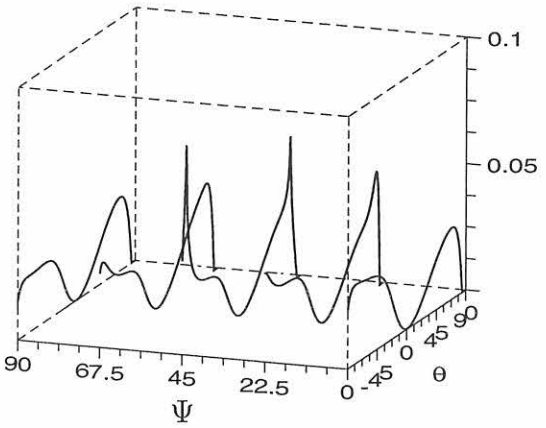

c) z-axis: r_{T2qL}

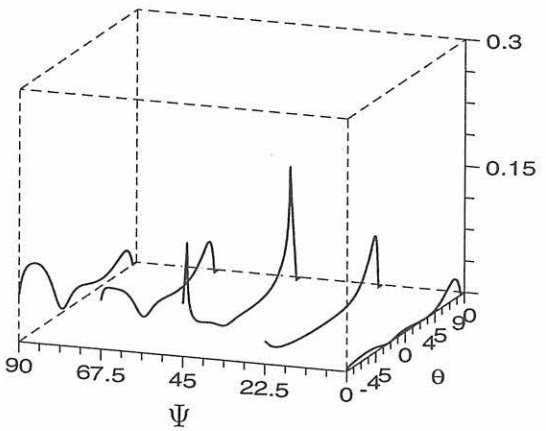

d) z-axis: t_{T2qL}

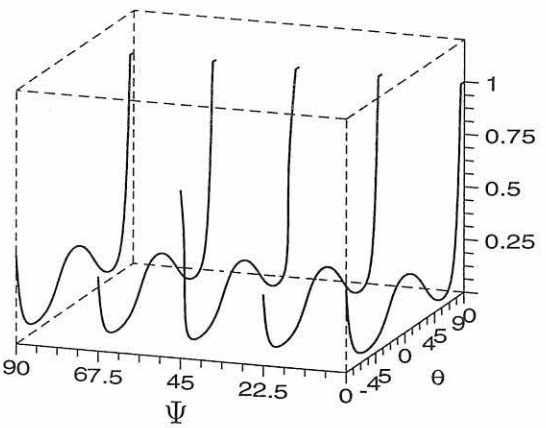

e) z-axis: r_{qLqL}

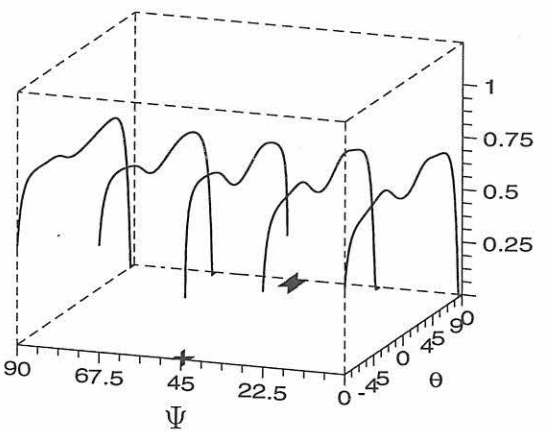

f) z-axis: t_{qLqL}

Figure E.1: *Energy reflection and transmission coefficients of the three waves at the imperfect interface between two transverse isotropic media as a function of the incidence angle* Θ *and the layback angle* Ψ *of medium 2.* **Quasi longitudinal (qL)** *wave incidence from medium 1. Medium 1: Grain angle* $\Phi = -67,5°$*; layback angle* $\Psi = -22,5°$*. Medium 2: Columnar grain tilt angle* $\Phi = 67,5°$*. Interface: Crack area fraction* $A = 0.75$*,* **f = 2 MHz**

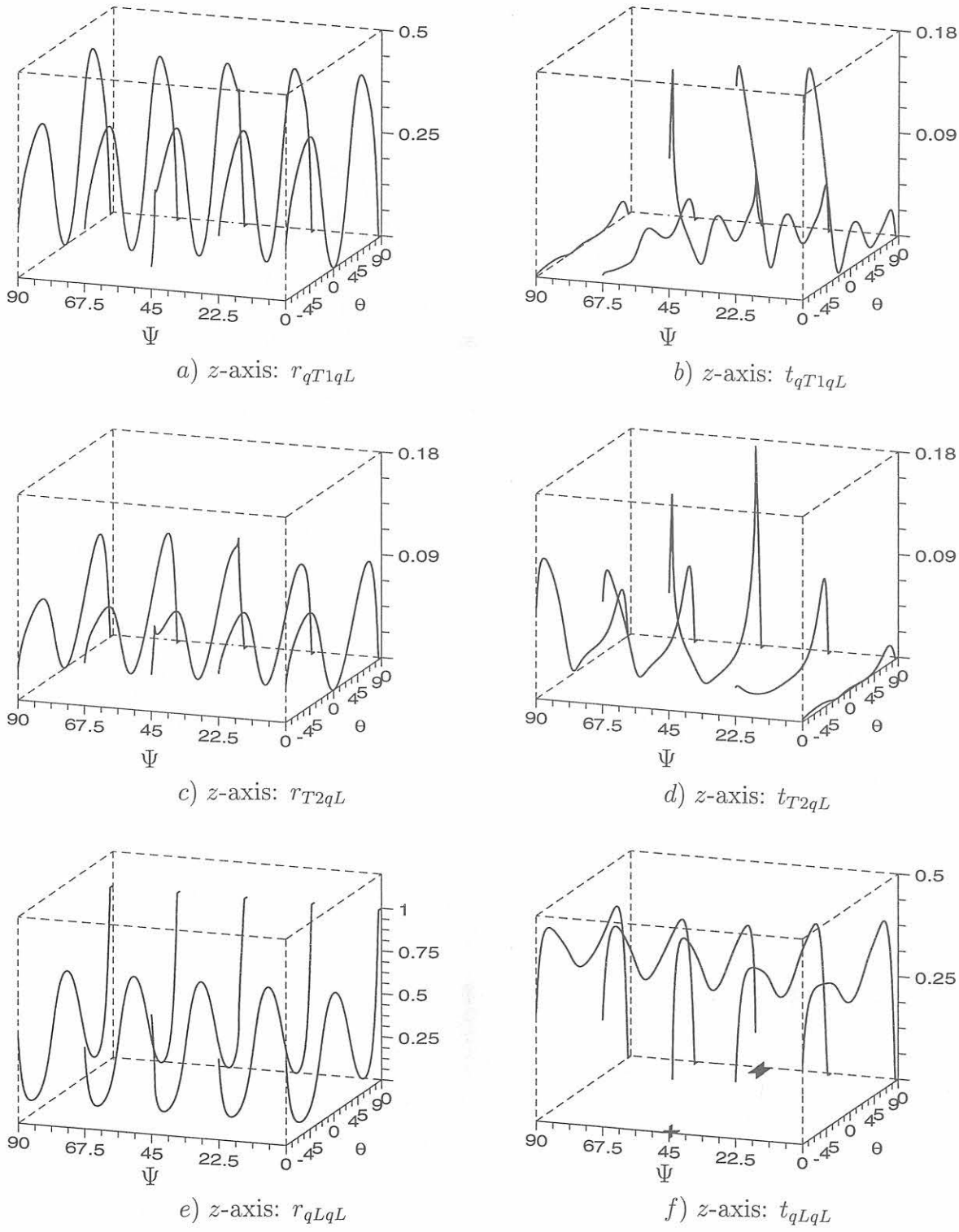

a) z-axis: r_{qT1qL} *b*) z-axis: t_{qT1qL}

c) z-axis: r_{T2qL} *d*) z-axis: t_{T2qL}

e) z-axis: r_{qLqL} *f*) z-axis: t_{qLqL}

Figure E.2: *Energy reflection and transmission coefficients of the three waves at the imperfect interface between two transverse isotropic media as a function of the incidence angle* Θ *and the layback angle* Ψ *of medium 2.* **Quasi longitudinal (qL)** *wave incidence from medium 1. Medium 1: Grain angle* $\Phi = -67,5°$*; layback angle* $\Psi = -22,5°$*. Medium 2: Columnar grain tilt angle* $\Phi = 67,5°$*. Interface: Crack area fraction* $A = 0.75$*,* $\mathbf{f = 5}$ **MHz**

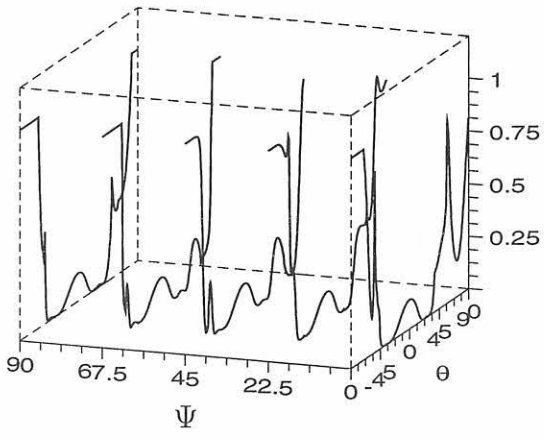

a) z-axis: r_{qT1qT1}

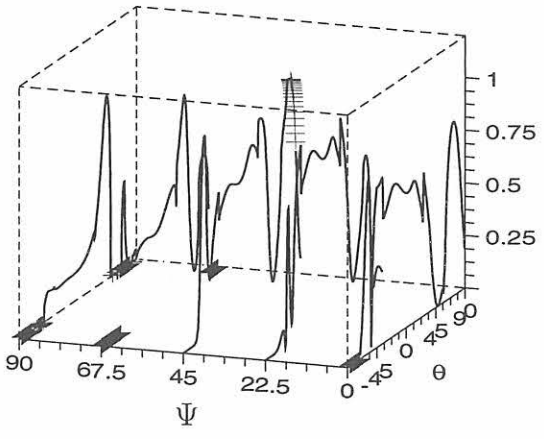

b) z-axis: t_{qT1qT1}

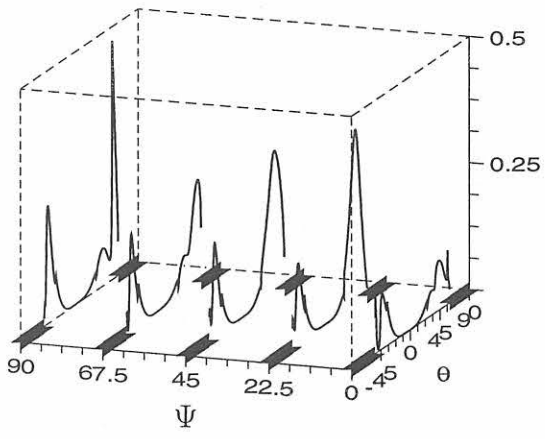

c) z-axis: r_{T2qT1}

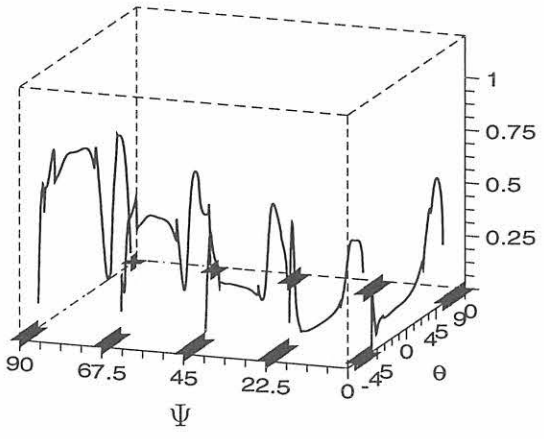

d) z-axis: t_{T2qT1}

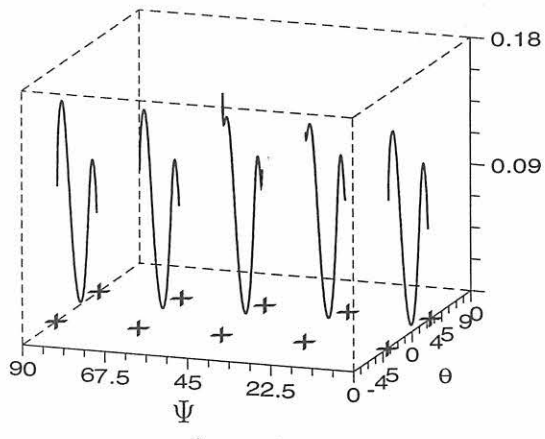

e) z-axis: r_{qLqT1}

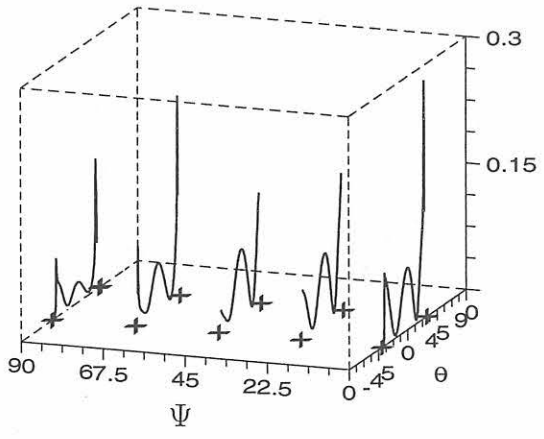

f) z-axis: t_{qLqT1}

Figure E.3: *Energy reflection and transmission coefficients of the three waves at the imperfect interface between two transverse isotropic media as a function of the incidence angle* Θ *and the layback angle* Ψ *of medium 2.* **Quasi transverse (qT1)** *wave incidence from medium 1. Medium 1: Grain angle* $\Phi = 67,5°$*; layback angle* $\Psi = -22,5°$*. Medium 2: Columnar grain tilt angle* $\Phi = 67,5°$*. Interface: Crack area fraction* $A = 0.75$*,* $\mathbf{f = 2}$ **MHz**

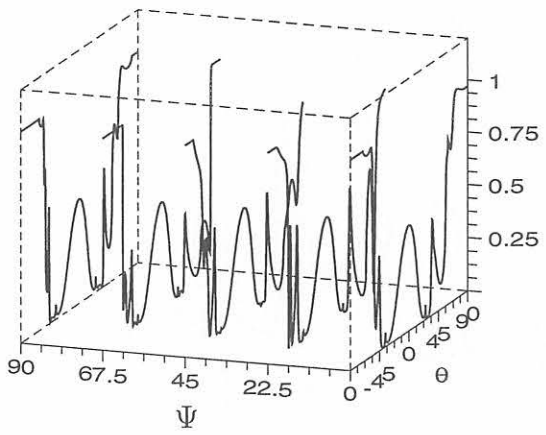

a) z-axis: r_{qT1qT1}

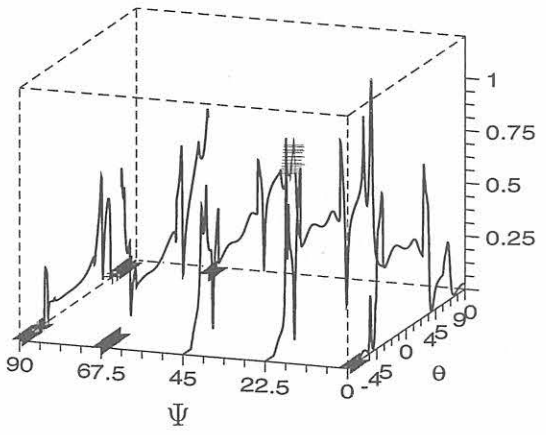

b) z-axis: t_{qT1qT1}

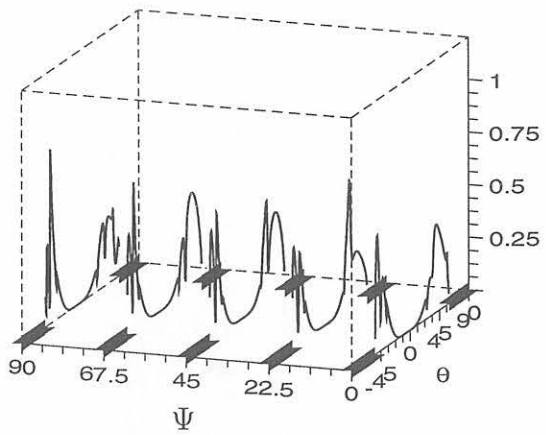

c) z-axis: r_{T2qT1}

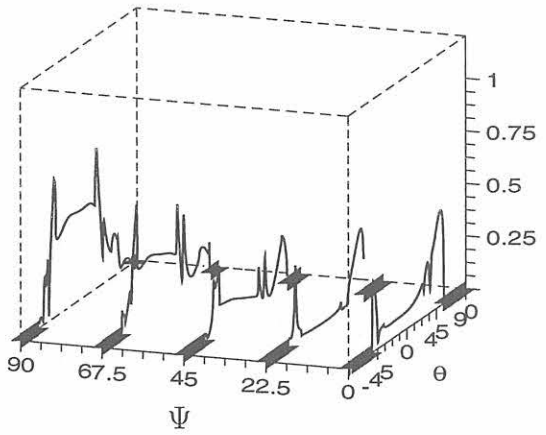

d) z-axis: t_{T2qT1}

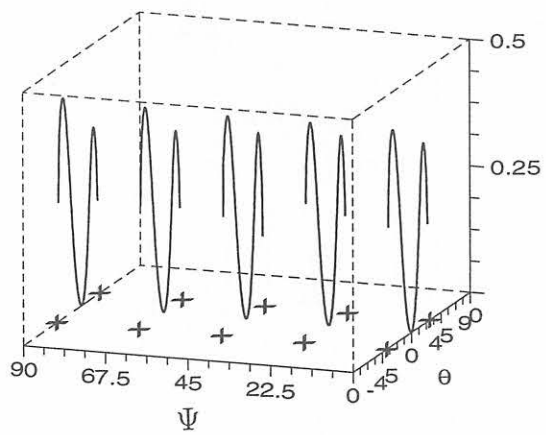

e) z-axis: r_{qLqT1}

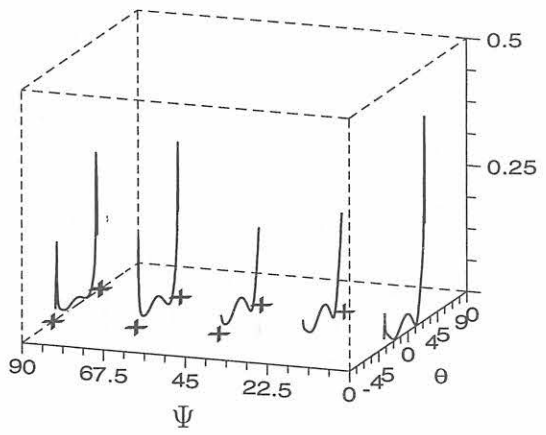

f) z-axis: t_{qLqT1}

Figure E.4: *Energy reflection and transmission coefficients of the three waves at the imperfect interface between two transverse isotropic media as a function of the incidence angle* Θ *and the layback angle* Ψ *of medium 2.* **Quasi transverse (qT1)** *wave incidence from medium 1. Medium 1: Grain angle* $\Phi = 67,5°$*; layback angle* $\Psi = -22,5°$*. Medium 2: Columnar grain tilt angle* $\Phi = 67,5°$*. Interface: Crack area fraction* $A = 0.75$*,* $\mathbf{f = 5}$ **MHz**

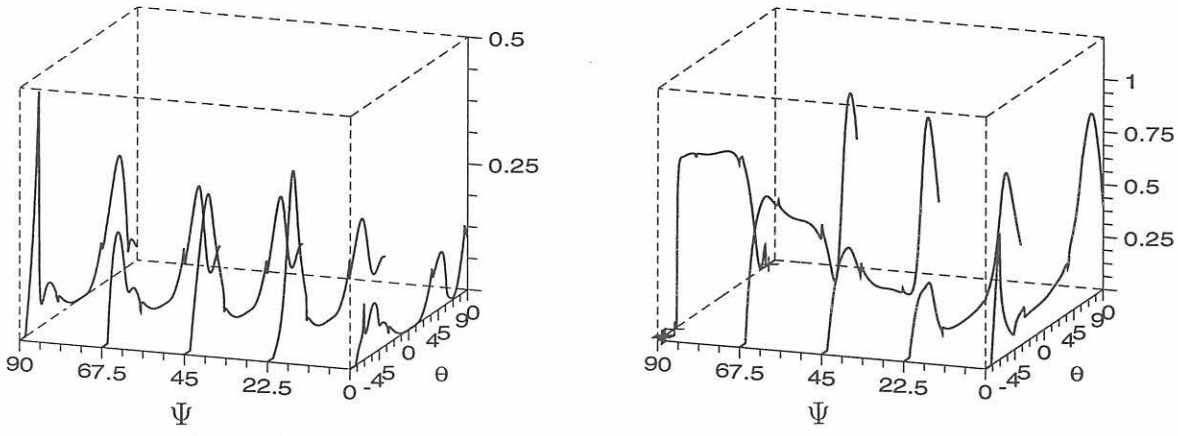

a) z-axis: r_{qT1T2}

b) z-axis: t_{qT1T2}

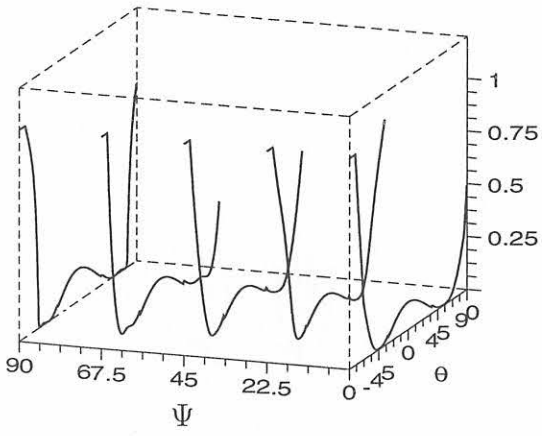

c) z-axis: r_{T2T2}

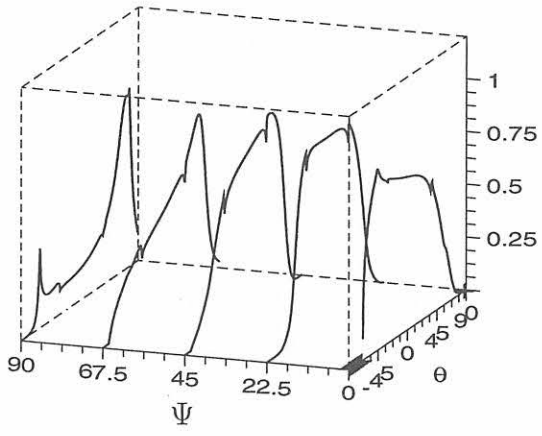

d) z-axis: t_{T2T2}

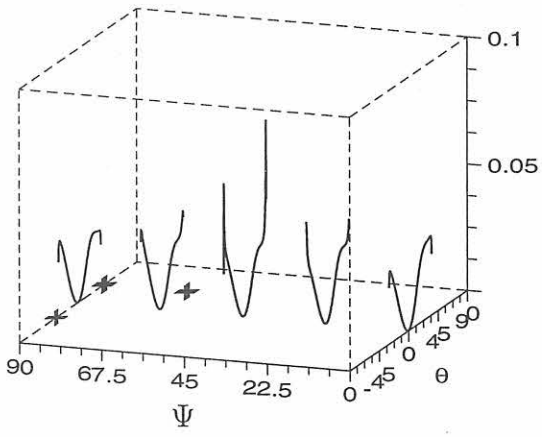

e) z-axis: r_{qLT2}

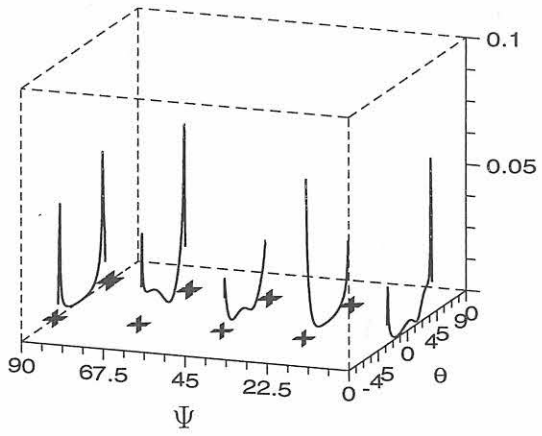

f) z-axis: t_{qLT2}

Figure E.5: *Energy reflection and transmission coefficients of the three waves at the imperfect interface between two transverse isotropic media as a function of the incidencè angle* Θ *and the layback angle* Ψ *of medium 2.* **Pure transverse (T2)** *wave incidence from medium 1. Medium 1: Grain angle* $\Phi = 67,5°$*; layback angle* $\Psi = -22,5°$*. Medium 2: Columnar grain tilt angle* $\Phi = 67,5°$*. Interface: Crack area fraction* $A = 0.75$*,* **f = 2 MHz**

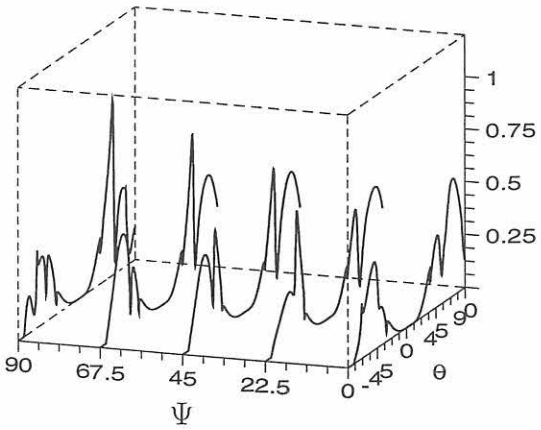

a) z-axis: r_{qT1T2}

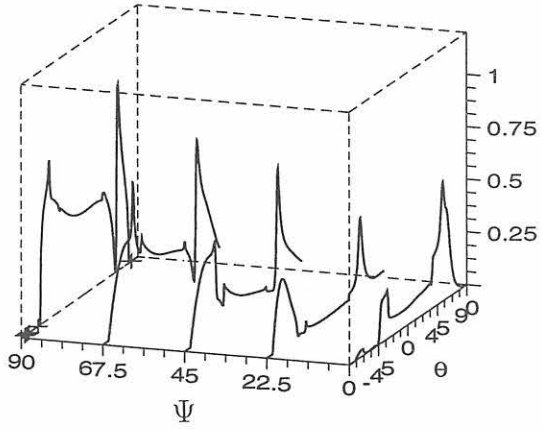

b) z-axis: t_{qT1T2}

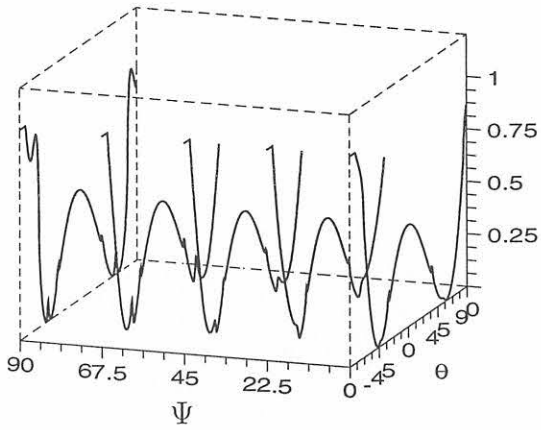

c) z-axis: r_{T2T2}

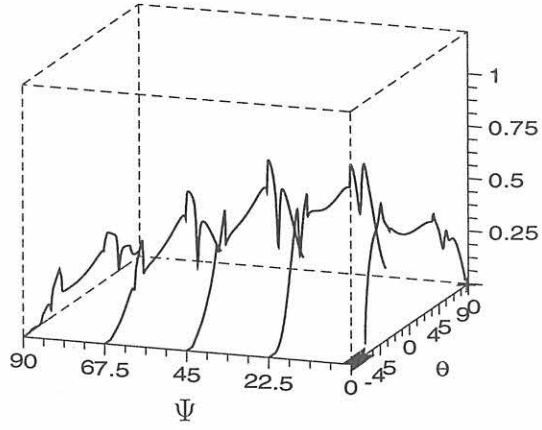

d) z-axis: t_{T2T2}

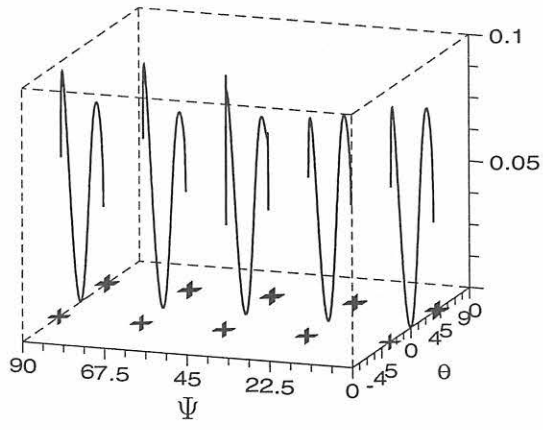

e) z-axis: r_{qLT2}

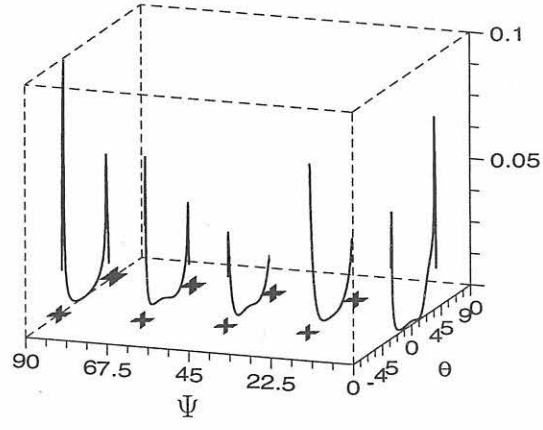

f) z-axis: t_{qLT2}

Figure E.6: *Energy reflection and transmission coefficients of the three waves at the imperfect interface between two transverse isotropic media as a function of the incidence angle* Θ *and the layback angle* Ψ *of medium 2.* **Pure transverse (T2)** *wave incidence from medium 1. Medium 1: Grain angle* $\Phi = 67,5°$*; layback angle* $\Psi = -22,5°$*. Medium 2: Columnar grain tilt angle* $\Phi = 67,5°$*. Interface: Crack area fraction* $A = 0.75$*,* $\mathbf{f = 5}$ **MHz**

E.2 Thin viscoelastic layers between perspex and anisotropic medium

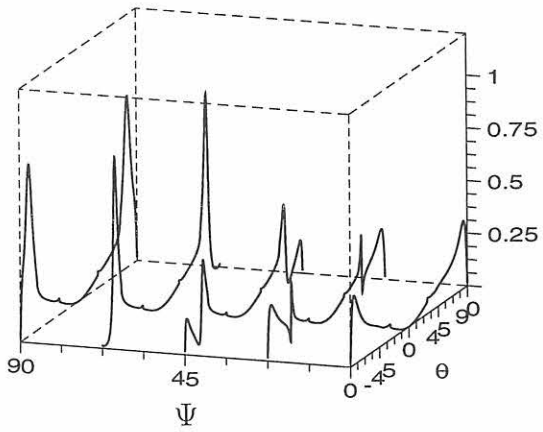

a) z-axis: r_{qT1qL}

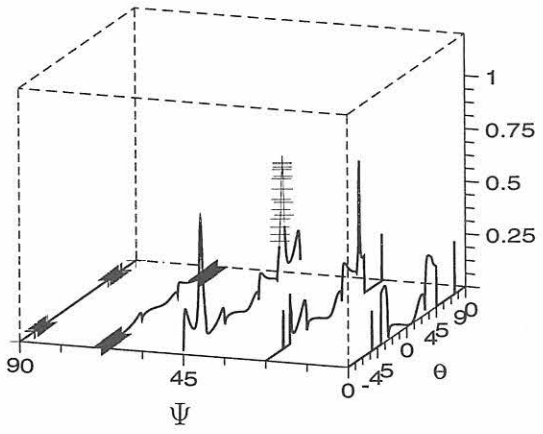

b) z-axis: t_{qT1qL}

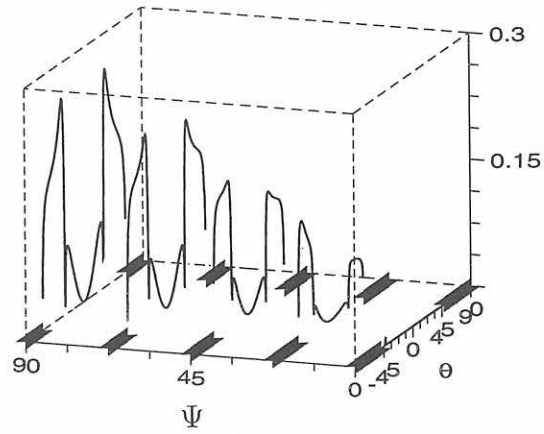

c) z-axis: t_{T2qL}

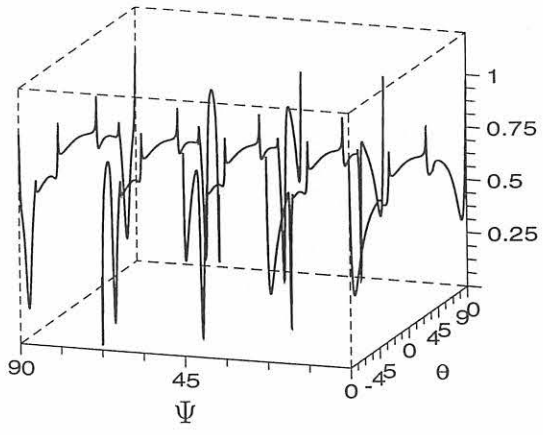

d) z-axis: r_{qLqL}

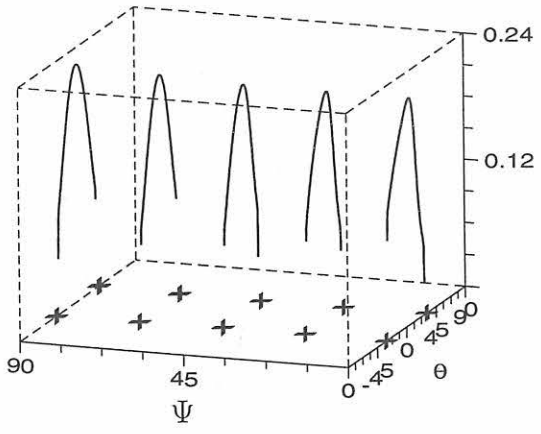

e) z-axis: t_{qLqL}

Figure E.7: *Reflection and transmission energy coefficients of the three waves at the glycerine coupling layer between perspex and the transverse isotropic medium as a function of the incidence angle* Θ *and the layback angle* Ψ *in the transverse isotropic medium 2.* **Longitudinal (L)** *wave incidence. Medium 2: Columnar grain tilt angle* $\Phi = 67,5°$. *Frequency* $f = 2$ *MHz, Layer thickness* $h = 50$ μm

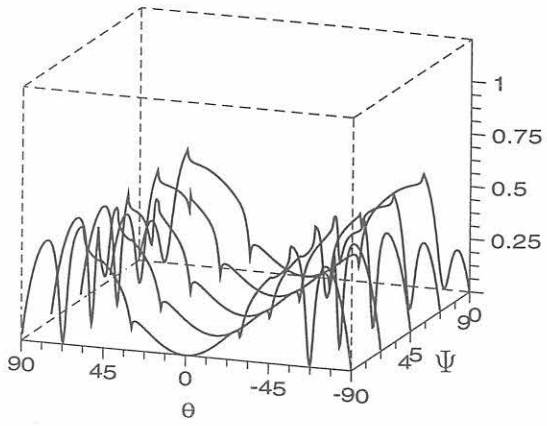

a) z-axis: r_{TvL}

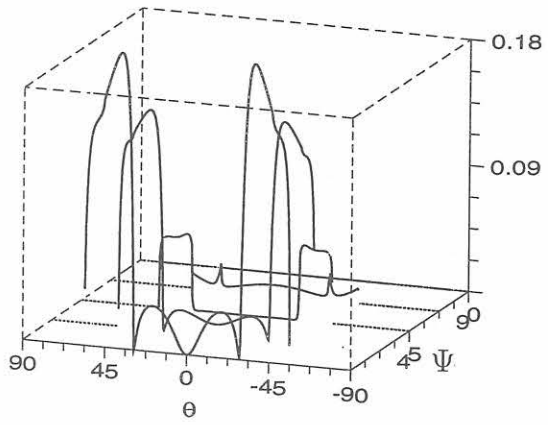

b) z-axis: t_{qT1L}

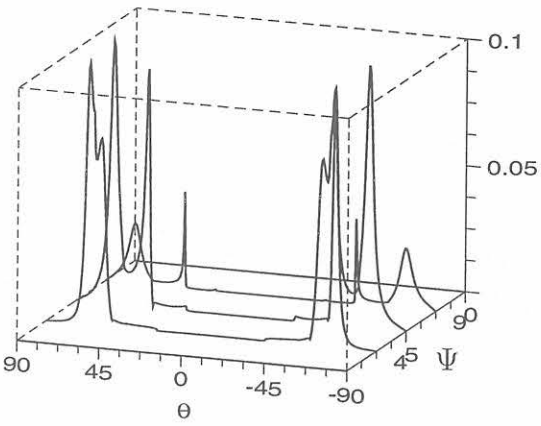

c) z-axis: r_{ThL}

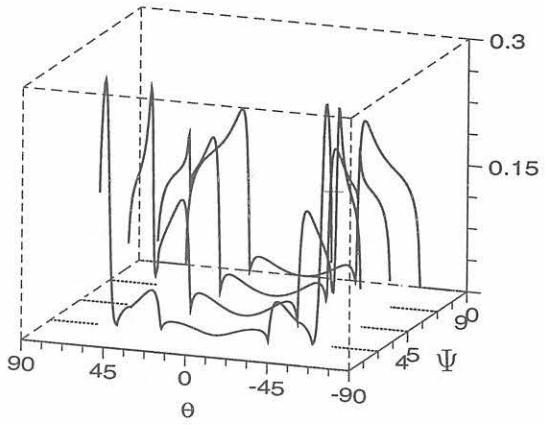

d) z-axis: t_{T2L}

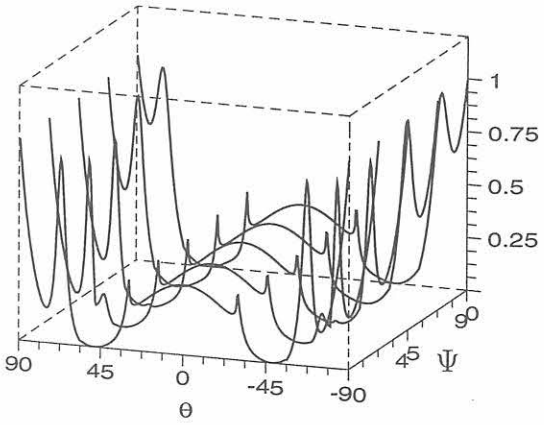

e) z-axis: r_{LL}

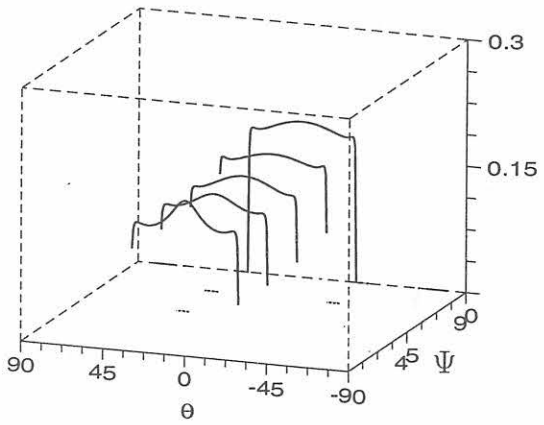

f) z-axis: t_{qLL}

Figure E.8: *Reflection and transmission energy coefficients of the three waves at the high viscosity 'Gel 3000' coupling layer between perspex and the transverse isotropic medium as a function of the incidence angle* Θ *and the layback angle* Ψ *in the transverse isotropic medium 2.* **Longitudinal (L)** *wave incidence. Medium 2: Columnar grain tilt angle* $\Phi = 0°$. *Frequency* $f = 2$ *MHz, Layer thickness* $h = 50$ μm

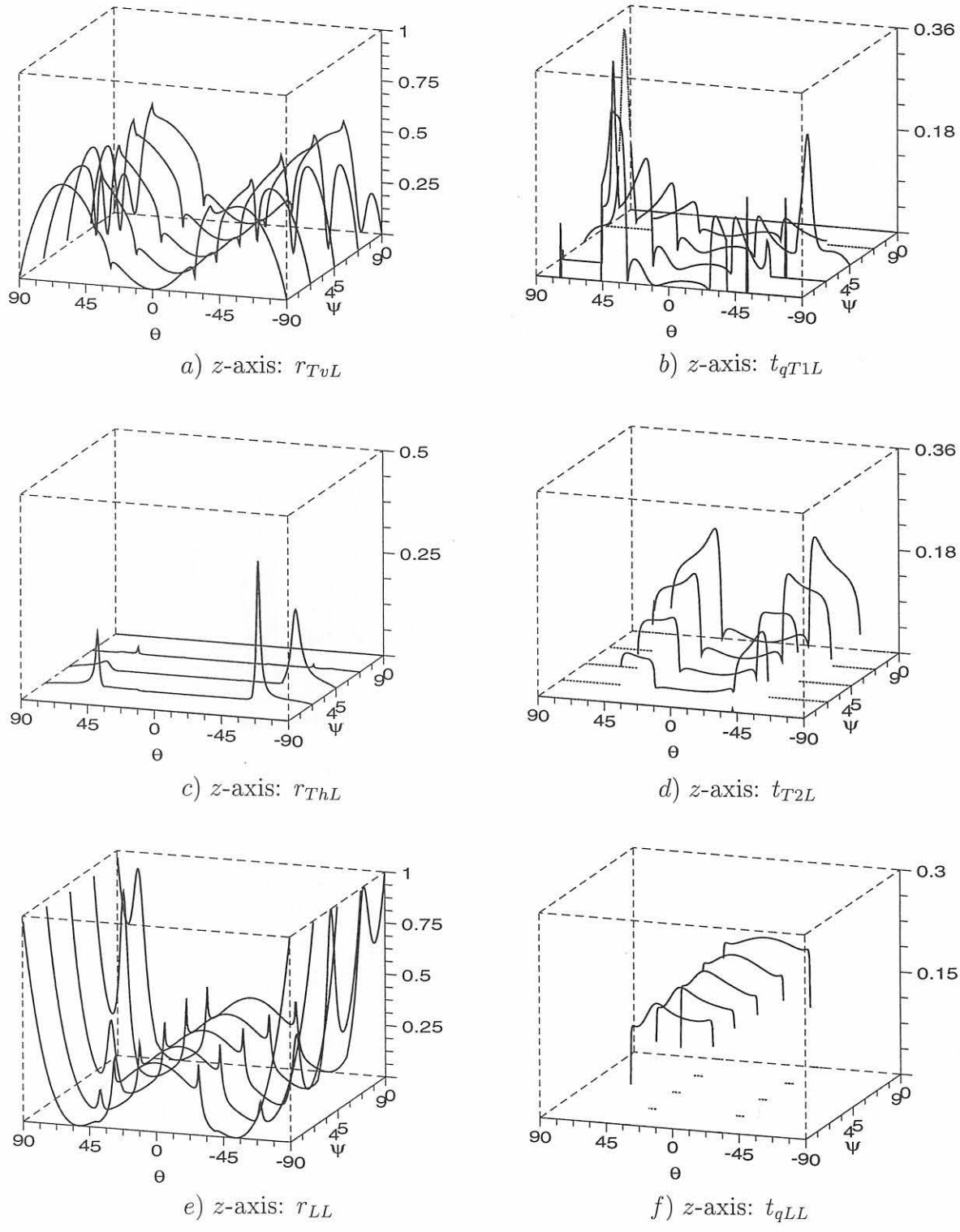

a) z-axis: r_{TvL} *b*) z-axis: t_{qT1L}

c) z-axis: r_{ThL} *d*) z-axis: t_{T2L}

e) z-axis: r_{LL} *f*) z-axis: t_{qLL}

Figure E.9: *Reflection and transmission energy coefficients of the three waves at the high viscosity 'Gel 3000' coupling layer between perspex and the transverse isotropic medium as a function of the incidence angle* Θ *and the layback angle* Ψ *in the transverse isotropic medium 2.* **Longitudinal (L)** *wave incidence. Medium 2: Columnar grain tilt angle* $\Phi = 67,5°$. *Frequency* $f = 2$ *MHz, Layer thickness* $h = 50$ μm

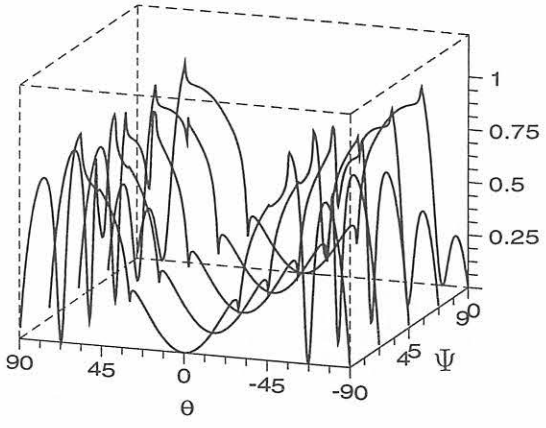

a) z-axis: r_{TvL}

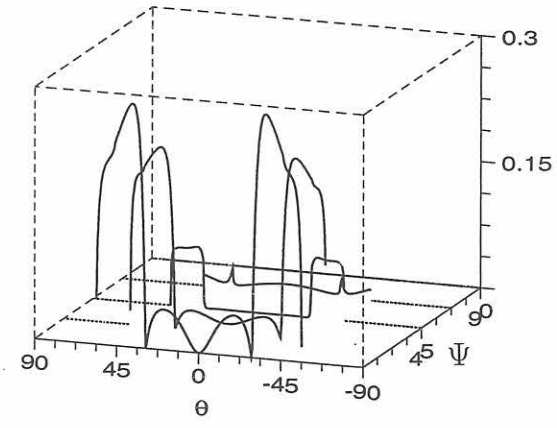

b) z-axis: t_{qT1L}

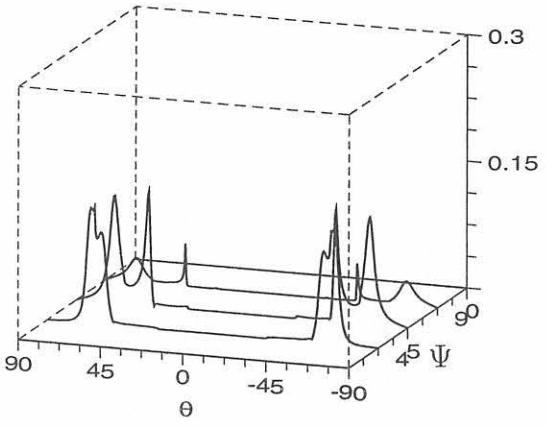

c) z-axis: r_{ThL}

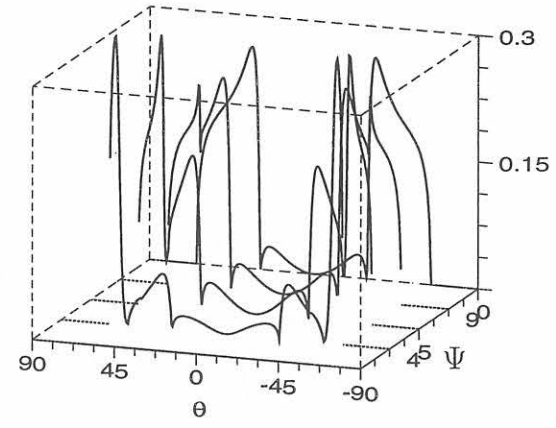

d) z-axis: t_{T2L}

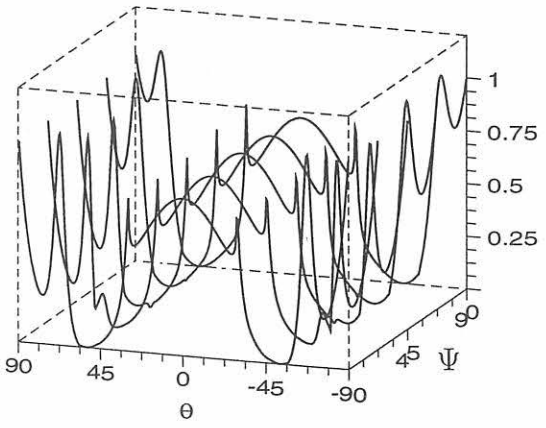

e) z-axis: r_{LL}

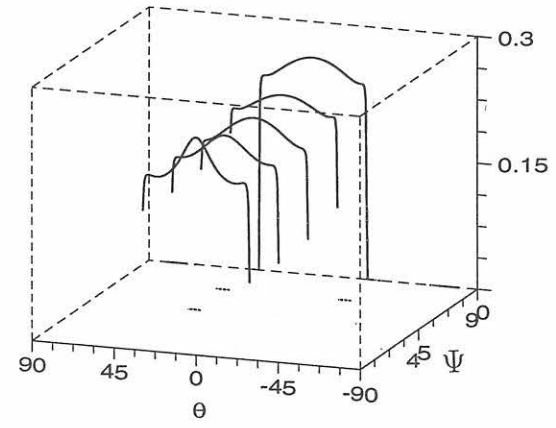

f) z-axis: t_{qLL}

Figure E.10: *Reflection and transmission energy coefficients of the three waves at the rigid interface between perspex and the transverse isotropic medium as a function of the incidence angle* Θ *and the layback angle* Ψ *in the transverse isotropic medium 2.* **Longitudinal (L)** *wave incidence. Medium 2: Columnar grain tilt angle* $\Phi = 0°$.

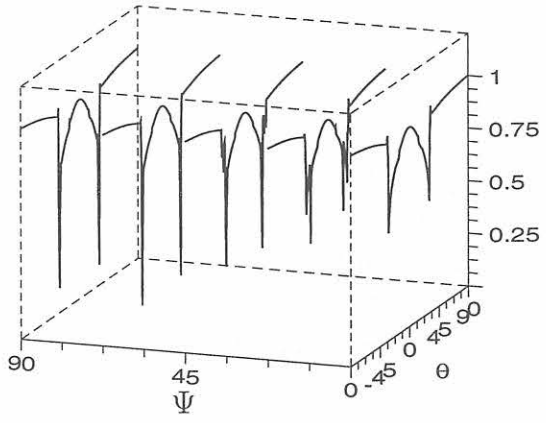

a) z-axis: r_{TvTv}

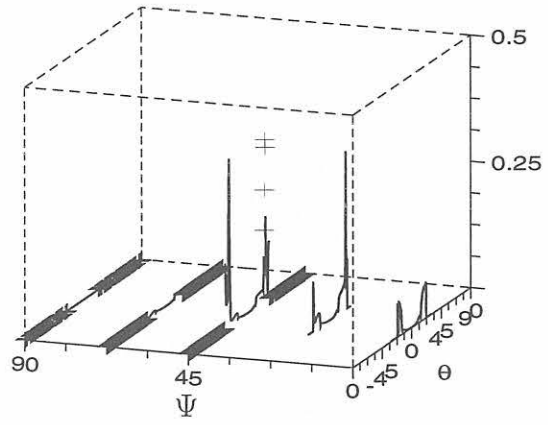

b) z-axis: t_{qT1Tv}

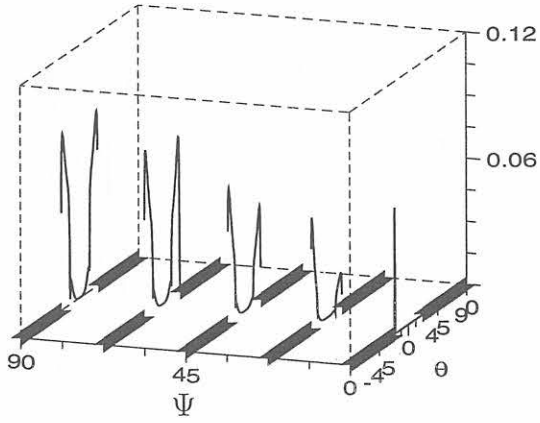

c) z-axis: t_{T2Tv}

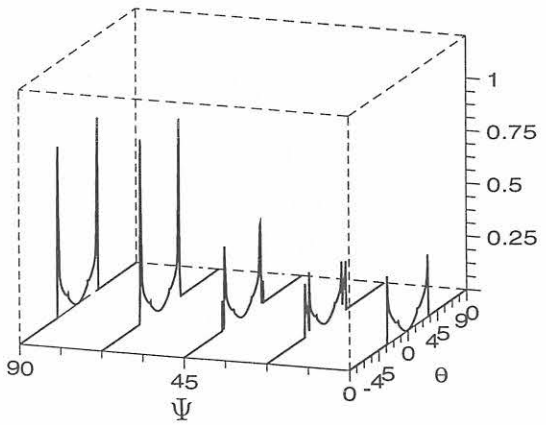

d) z-axis: r_{LTv}

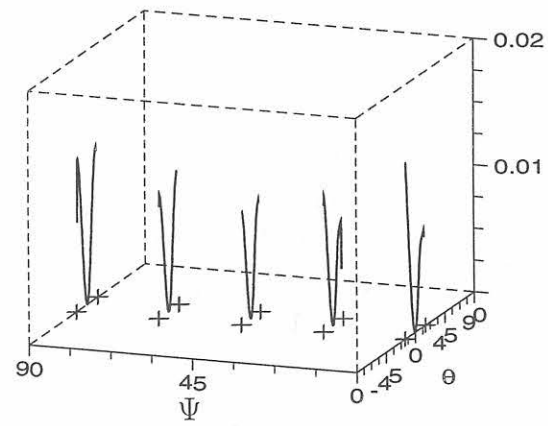

e) z-axis: t_{qLTv}

Figure E.11: *Reflection and transmission energy coefficients of the three waves at the glycerine coupling layer between perspex and the transverse isotropic medium as a function of the incidence angle* Θ *and the layback angle* Ψ *in the transverse isotropic medium 2.* **Vertically polarized transverse (Tv)** *wave incidence. Medium 2: Columnar grain tilt angle* $\Phi = 67,5°$. *Frequency* $f = 2$ *MHz, Layer thickness* $h = 50$ μm

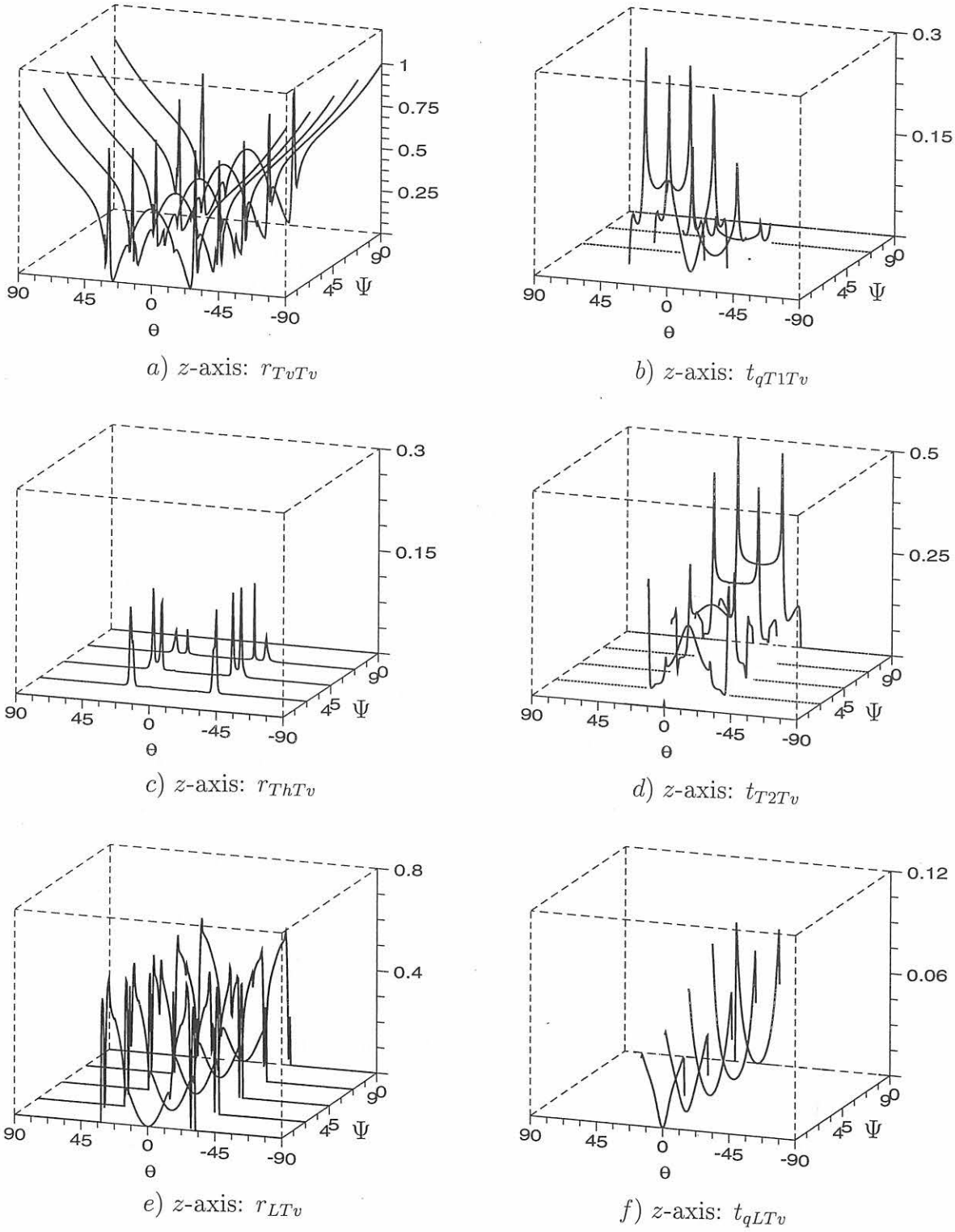

a) z-axis: r_{TvTv} *b*) z-axis: t_{qT1Tv}

c) z-axis: r_{ThTv} *d*) z-axis: t_{T2Tv}

e) z-axis: r_{LTv} *f*) z-axis: t_{qLTv}

Figure E.12: *Reflection and transmission energy coefficients of the three waves at the high viscosity 'Gel 3000' coupling layer between perspex and the transverse isotropic medium as a function of the incidence angle* Θ *and the layback angle* Ψ *in the transverse isotropic medium 2.* **Vertically polarized transverse (Tv)** *wave incidence. Medium 2: Columnar grain tilt angle* $\Phi = 0°$. *Frequency* $f = 2$ *MHz, Layer thickness* $h = 50$ μm

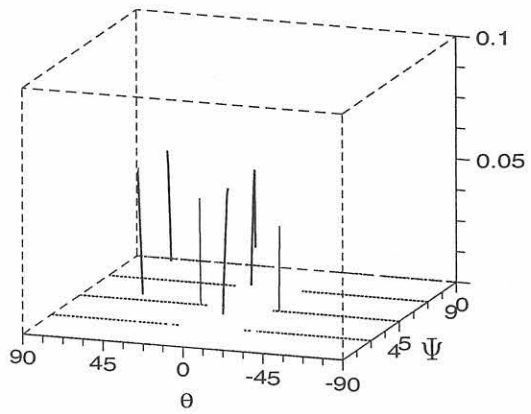

g) z-axis: $t_{qT1(2)Tv}$

Figure E.13: *Energy reflection and transmission coefficients of the second branch of the quasi transverse wave qT1(2) at the high viscosity 'Gel 3000' coupling layer between perspex and the transverse isotropic medium as a function of the incidence angle* Θ *and the layback angle* Ψ *in the transverse isotropic medium 2.* **Vertically polarized transverse (Tv)** *wave incidence. Medium 2: Columnar grain tilt angle* $\Phi = 0°$. *Frequency* $f = 2$ *MHz, Layer thickness* $h = 50$ μm

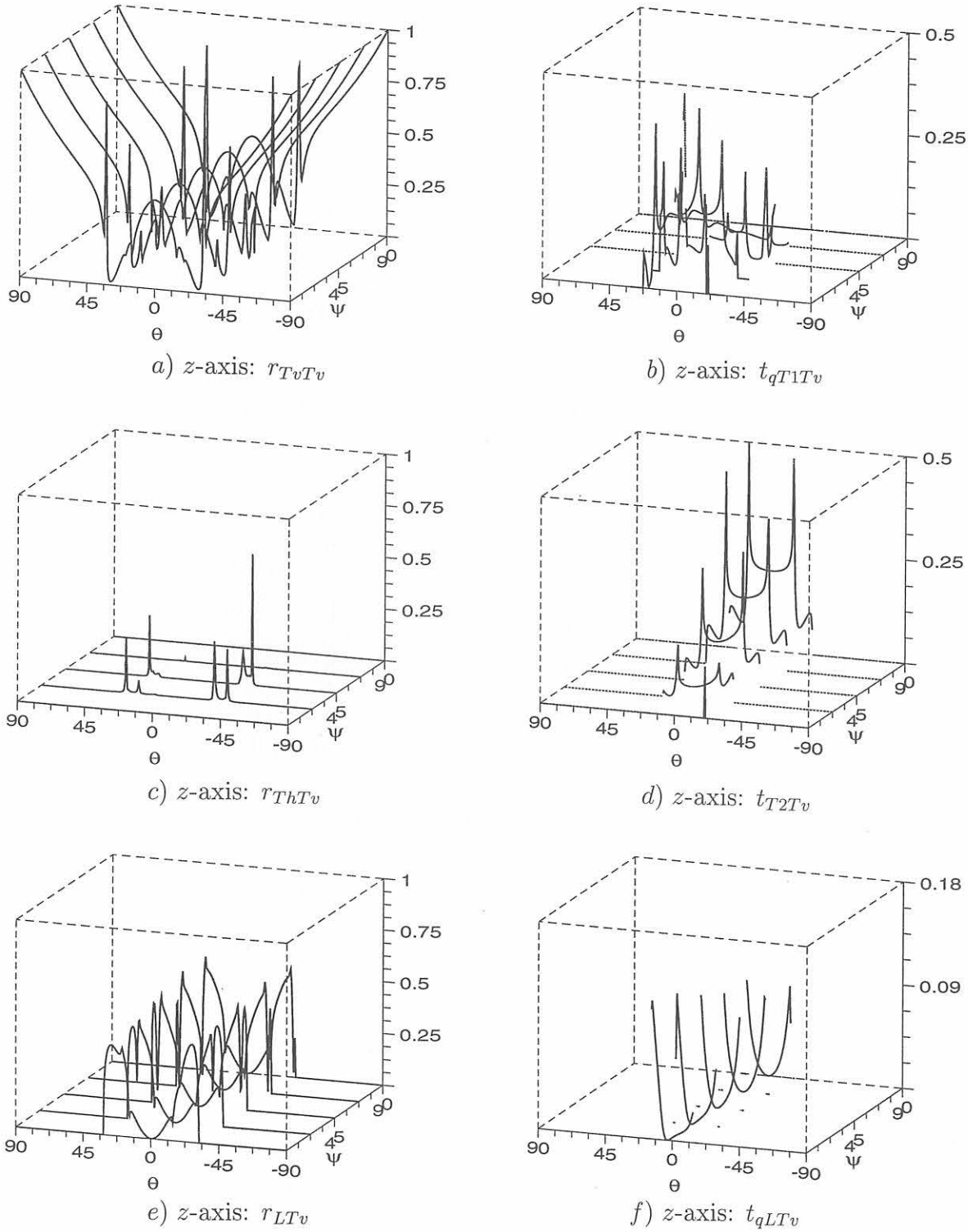

a) z-axis: r_{TvTv} *b*) z-axis: t_{qT1Tv}

c) z-axis: r_{ThTv} *d*) z-axis: t_{T2Tv}

e) z-axis: r_{LTv} *f*) z-axis: t_{qLTv}

Figure E.14: *Energy reflection and transmission coefficients of the three waves at the high viscosity 'Gel 3000' coupling layer between perspex and the transverse isotropic medium as a function of the incidence angle* Θ *and the layback angle* Ψ *in the transverse isotropic medium 2.* **Vertically polarized transverse (Tv)** *wave incidence. Medium 2: Columnar grain tilt angle* $\Phi = 67,5°$. *Frequency* $f = 2$ *MHz, Layer thickness* $h = 50$ μm

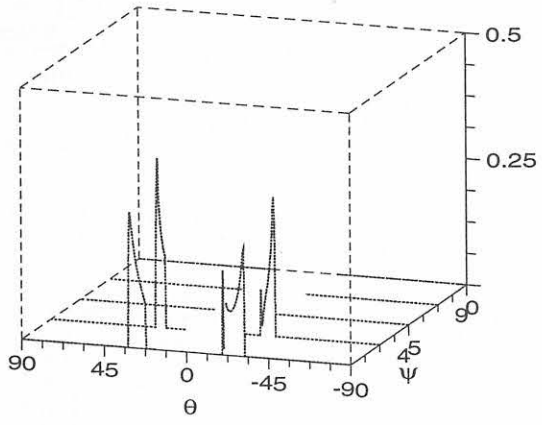

g) z-axis: $t_{qT1(2)Tv}$

Figure E.15: *Energy reflection and transmission coefficients of the second branch of the quasi transverse wave qT1(2) at the high viscosity 'Gel 3000' coupling layer between perspex and the transverse isotropic medium as a function of the incidence angle* Θ *and the layback angle* Ψ *in the transverse isotropic medium 2.* **Vertically polarized transverse (Tv)** *wave incidence. Medium 2: Columnar grain tilt angle* $\Phi = 67,5°$. *Frequency* $f = 2$ *MHz, Layer thickness* $h = 50$ μm

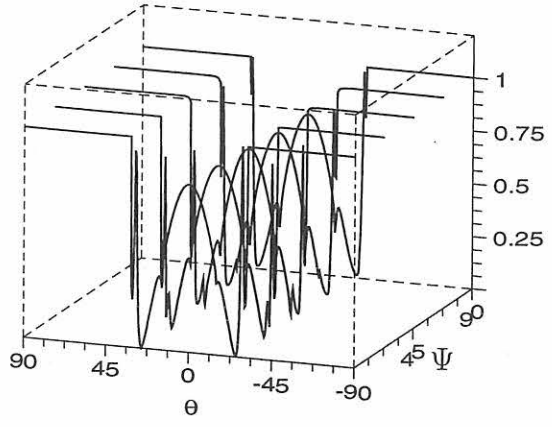

a) z-axis: r_{TvTv}

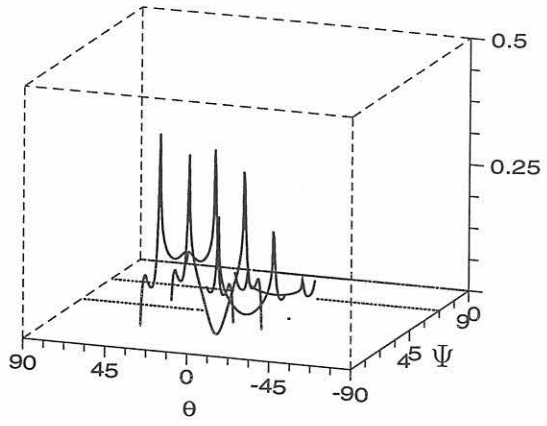

b) z-axis: t_{qT1Tv}

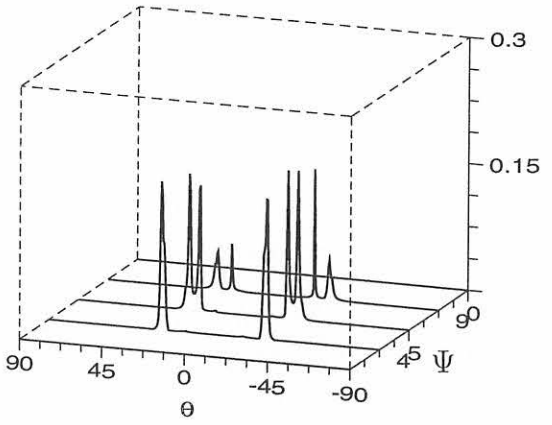

c) z-axis: r_{ThTv}

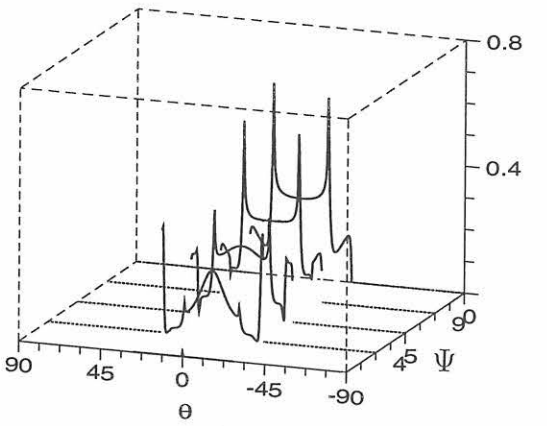

d) z-axis: t_{T2Tv}

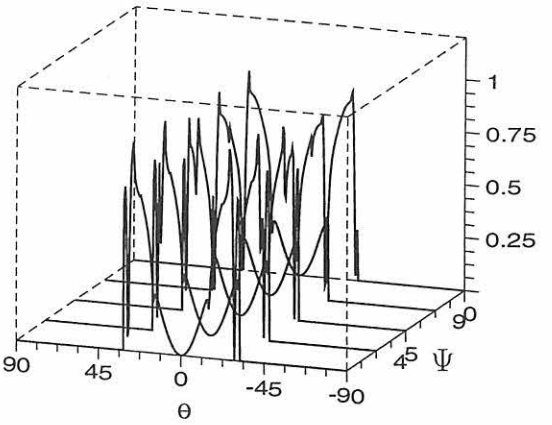

e) z-axis: r_{LTv}

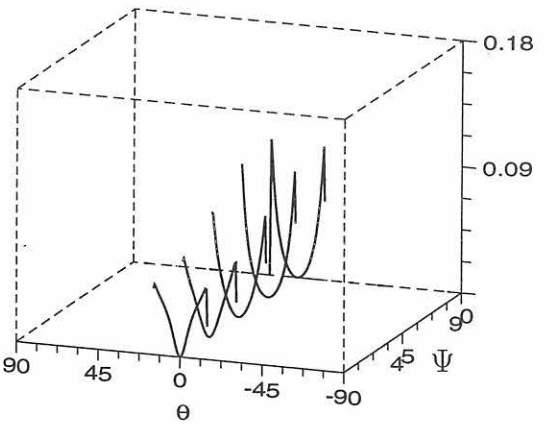

f) z-axis: t_{qLTv}

Figure E.16: *Reflection and transmission energy coefficients of the three waves at the rigid interface between perspex and the transverse isotropic medium as a function of the incidence angle* Θ *and the layback angle* Ψ *in the transverse isotropic medium 2.* **Vertically polarized transverse (Tv)** *wave incidence. Medium 2: Columnar grain tilt angle* $\Phi = 0°$.

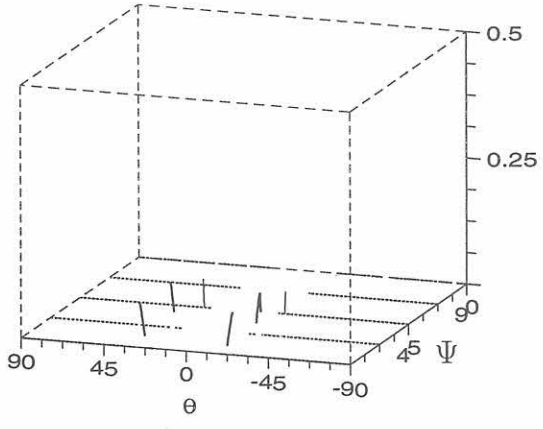

g) z-axis: $t_{qT1(2)Tv}$

Figure E.17: *Reflection and transmission energy coefficients of the second branch of the quasi transverse wave qT1(2) at the rigid interface between perspex and the transverse isotropic medium as a function of the incidence angle* Θ *and the layback angle* Ψ *in the transverse isotropic medium 2.* **Vertically polarized transverse (Tv)** *wave incidence. Medium 2: Columnar grain tilt angle* $\Phi = 0°$.

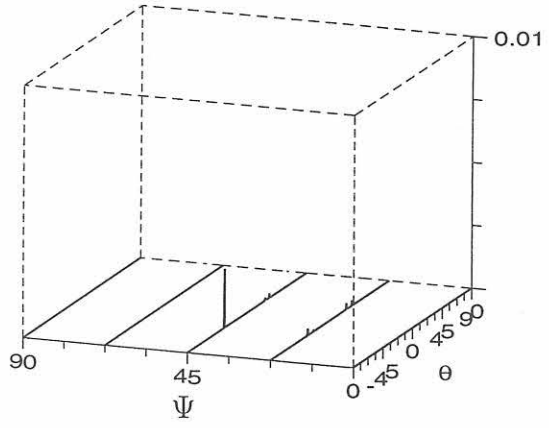

a) z-axis: r_{TvTh}

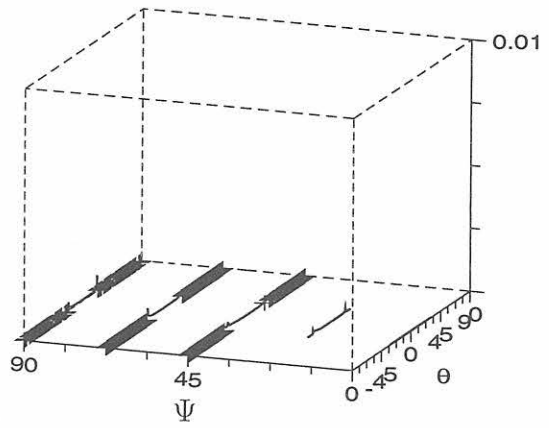

b) z-axis: t_{qT1Th}

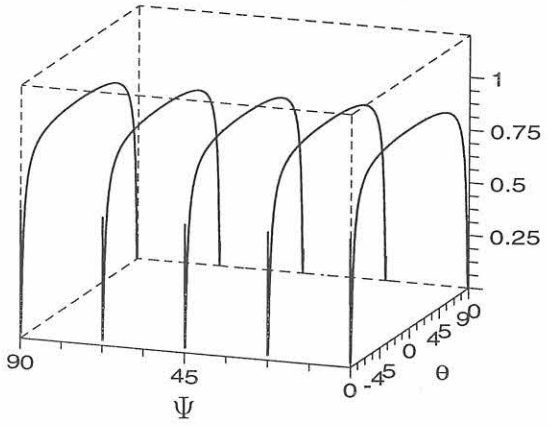

c) z-axis: r_{ThTh}

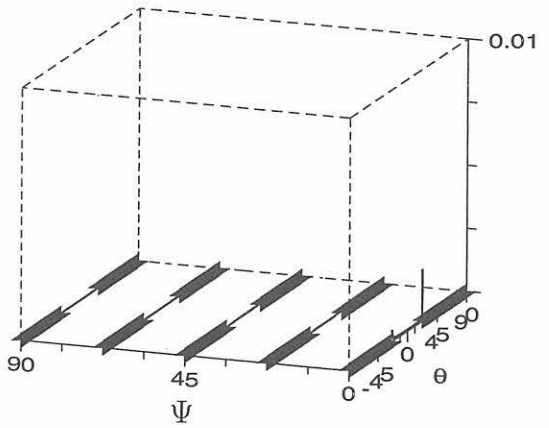

d) z-axis: t_{T2Th}

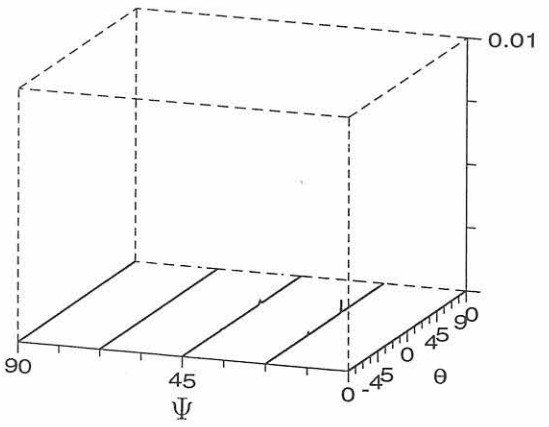

e) z-axis: r_{LTh}

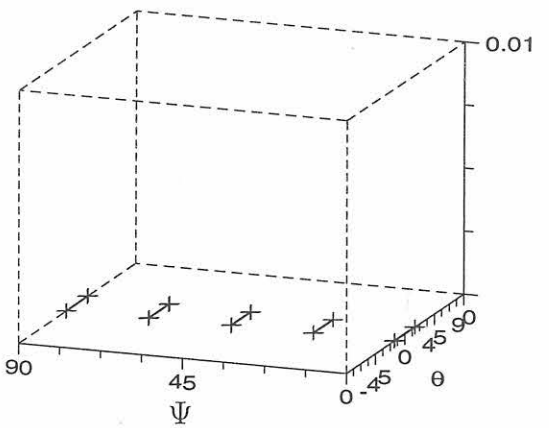

f) z-axis: t_{qLTh}

Figure E.18: *Reflection and transmission energy coefficients of the three waves at the glycerine coupling layer between perspex and the transverse isotropic medium as a function of the incidence angle* Θ *and the layback angle* Ψ *in the transverse isotropic medium 2.* **Horizontally polarized transverse (Th)** *wave incidence. Medium 2: Columnar grain tilt angle* $\Phi = 675°$. *Frequency* $f = 2$ *MHz, Layer thickness* $h = 50$ μm

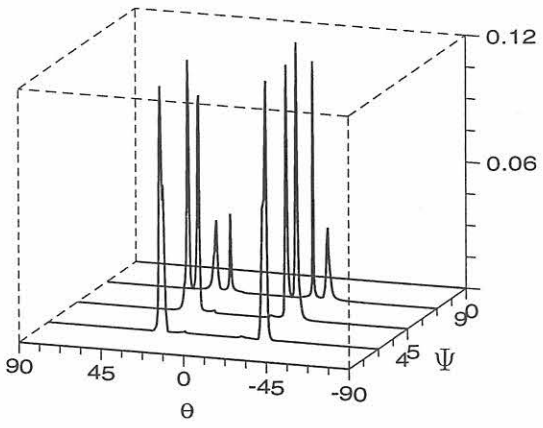

a) z-axis: r_{TvTh}

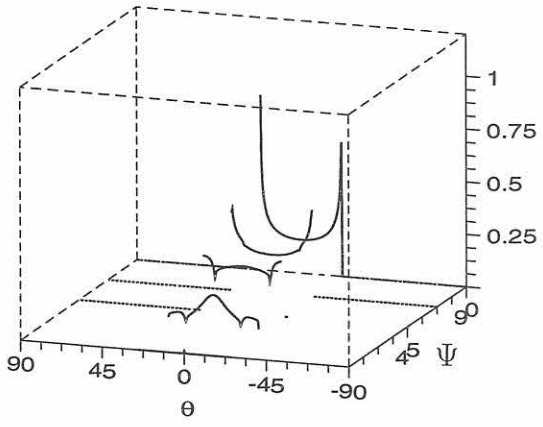

b) z-axis: t_{qT1Th}

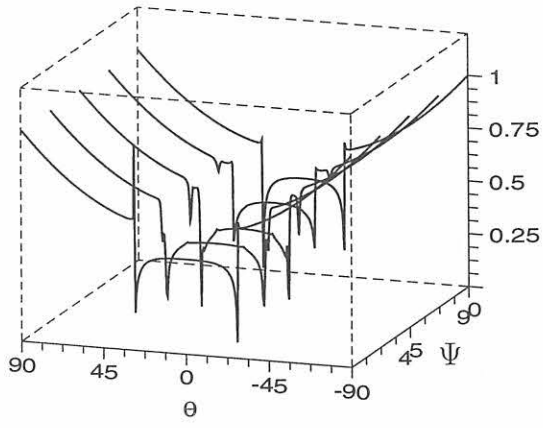

c) z-axis: r_{ThTh}

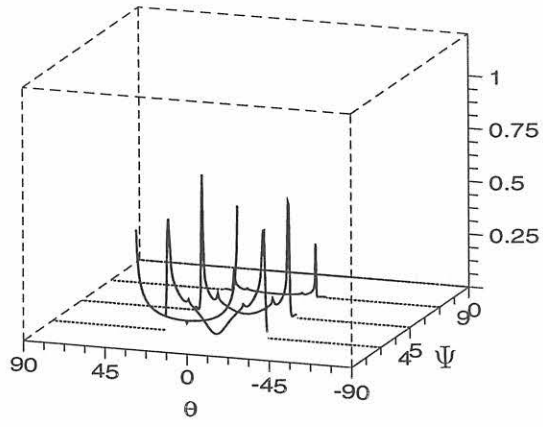

d) z-axis: t_{T2Th}

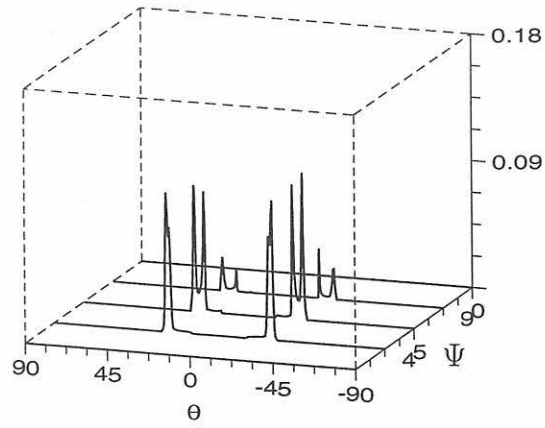

e) z-axis: r_{LTh}

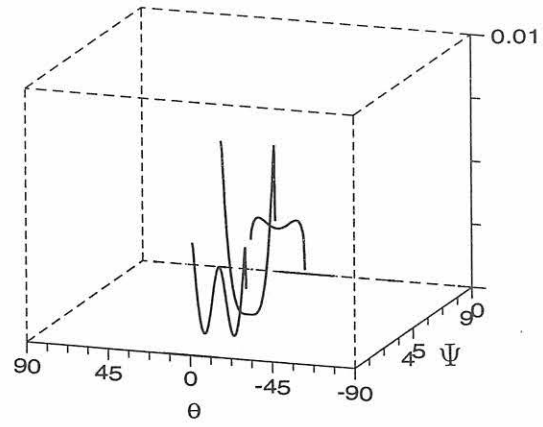

f) z-axis: t_{qLTh}

Figure E.19: *Reflection and transmission energy coefficients of the three waves at the high viscosity 'Gel 3000' coupling layer between perspex and the transverse isotropic medium as a function of the incidence angle* Θ *and the layback angle* Ψ *in the transverse isotropic medium 2.* **Horizontally polarized transverse (Th)** *wave incidence. Medium 2: Columnar grain tilt angle* $\Phi = 0°$*. Frequency* $f = 2$ *MHz, Layer thickness* $h = 50$ μm

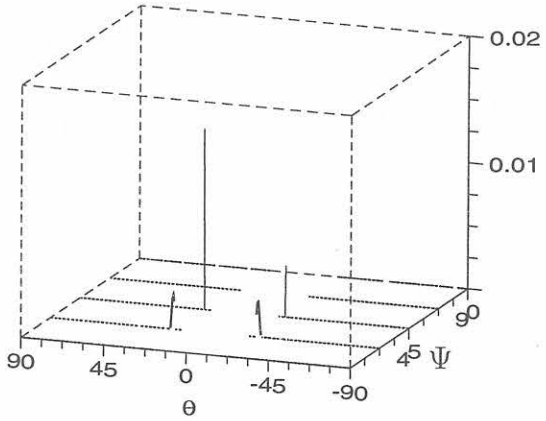

g) z-axis: $t_{qT1(2)Th}$

Figure E.20: *Energy reflection and transmission coefficients of the second branch of the quasi transverse wave qT1(2) at the high viscosity 'Gel 3000' coupling layer between perspex and the transverse isotropic medium as a function of the incidence angle* Θ *and the layback angle* Ψ *in the transverse isotropic medium 2.* **Horizontally polarized transverse (Th)** *wave incidence. Medium 2: Columnar grain tilt angle* $\Phi = 0°$. *Frequency f = 2 MHz, Layer thickness h = 50* μm

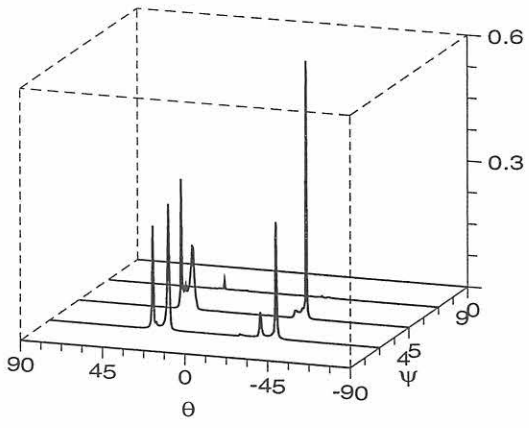

a) z-axis: r_{TvTh}

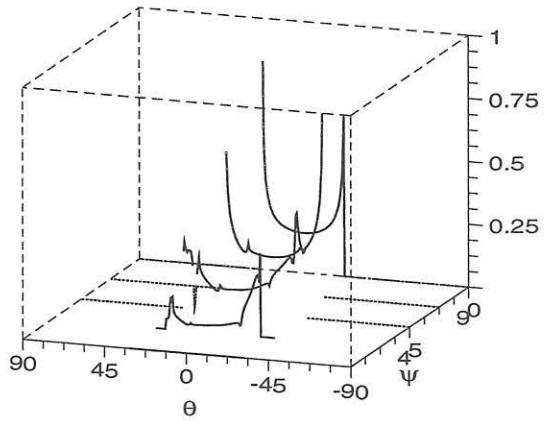

b) z-axis: t_{qT1Th}

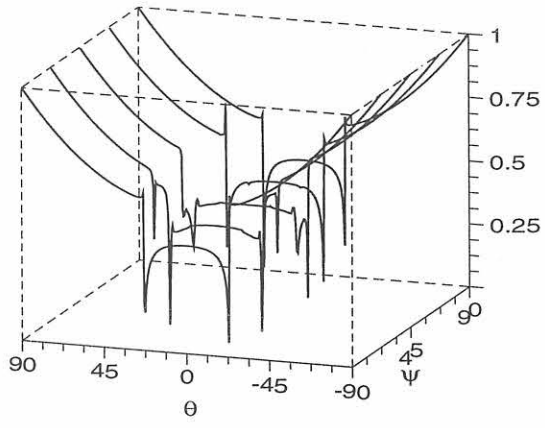

c) z-axis: r_{ThTh}

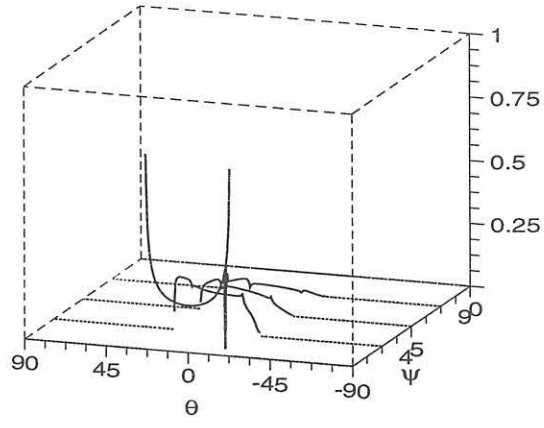

d) z-axis: t_{T2Th}

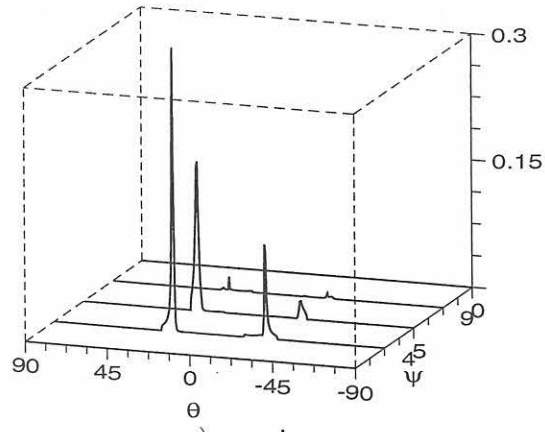

e) z-axis: r_{LTh}

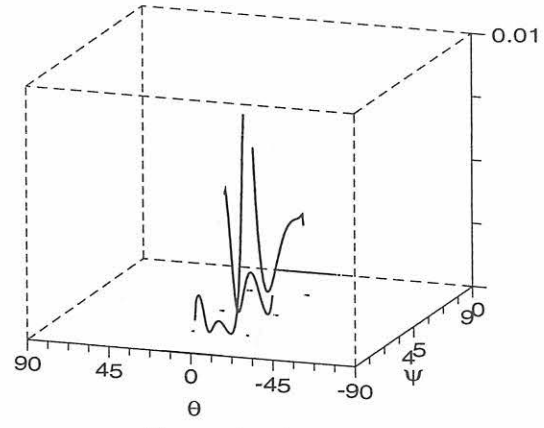

f) z-axis: t_{qLTh}

Figure E.21: *Energy reflection and transmission coefficients of the three waves at the high viscosity 'Gel 3000' coupling layer between perspex and the transverse isotropic medium as a function of the incidence angle* Θ *and the layback angle* Ψ *in the transverse isotropic medium 2.* **Horizontally polarized transverse (Th)** *wave incidence. Medium 2: Columnar grain tilt angle* $\Phi = 67,5°$. *Frequency* $f = 2$ *MHz, Layer thickness* $h = 50$ μm

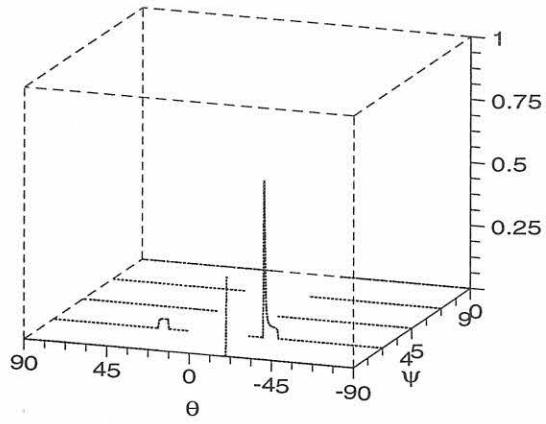

g) z-axis: $t_{qT1(2)Th}$

Figure E.22: *Energy reflection and transmission coefficients of the second branch of the quasi transverse wave qT1(2) at the high viscosity 'Gel 3000' coupling layer between perspex and the transverse isotropic medium as a function of the incidence angle* Θ *and the layback angle* Ψ *in the transverse isotropic medium 2.* **Horizontally polarized transverse (Th)** *wave incidence. Medium 2: Columnar grain tilt angle* $\Phi = 67,5°$. *Frequency* $f = 2$ *MHz, Layer thickness* $h = 50$ μm

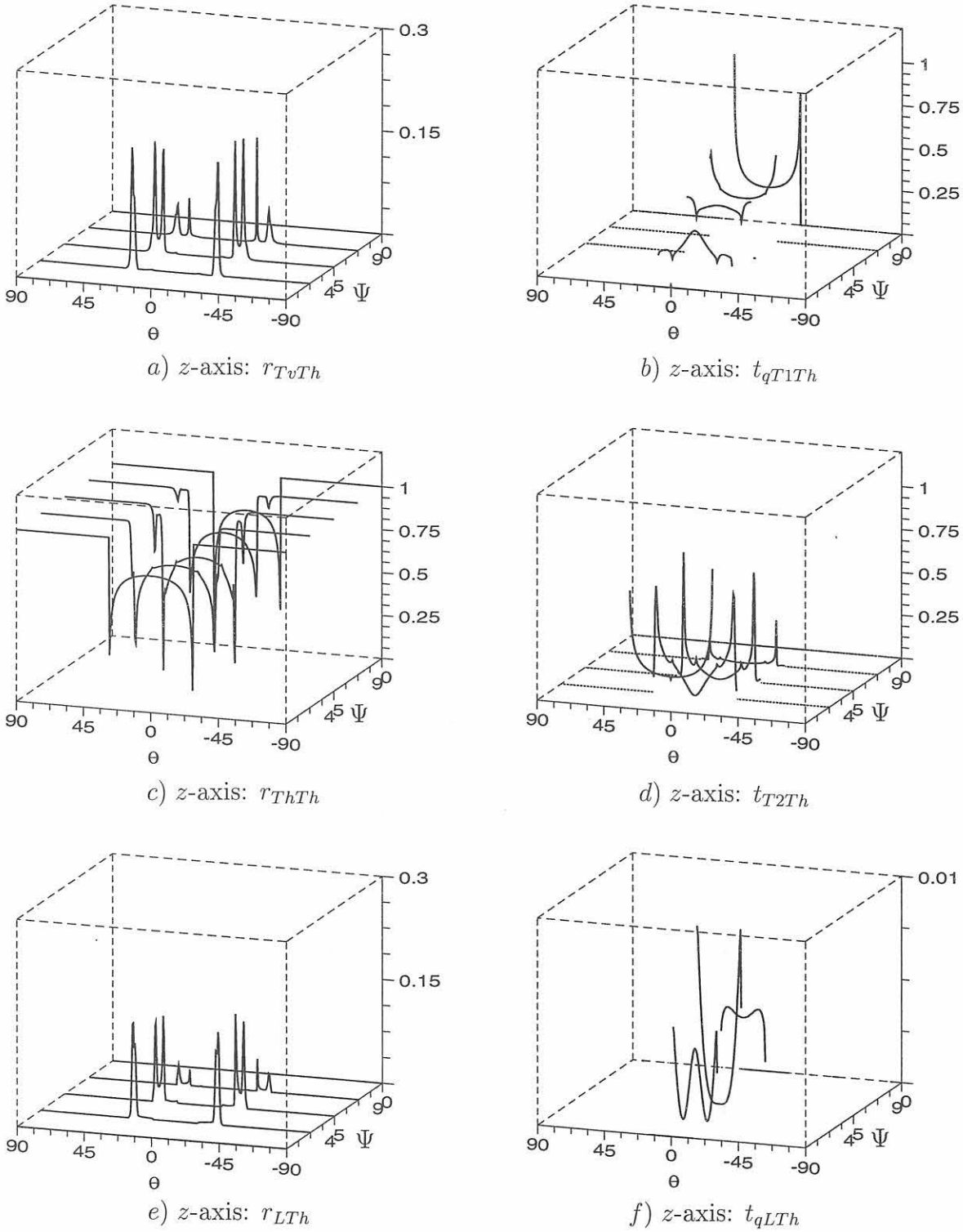

a) z-axis: r_{TvTh}

b) z-axis: t_{qT1Th}

c) z-axis: r_{ThTh}

d) z-axis: t_{T2Th}

e) z-axis: r_{LTh}

f) z-axis: t_{qLTh}

Figure E.23: *Reflection and transmission energy coefficients of the three waves at the rigid interface between perspex and the transverse isotropic medium as a function of the incidence angle* Θ *and the layback angle* Ψ *in the transverse isotropic medium 2.* **Horizontally polarized transverse (Th)** *wave incidence. Medium 2: Columnar grain tilt angle* $\Phi = 0°$.

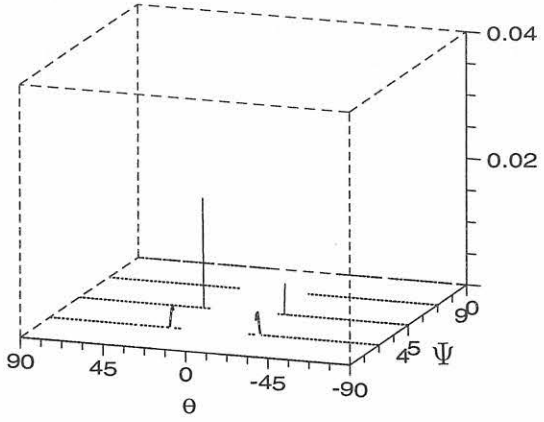

g) z-axis: $t_{qT1(2)Th}$

Figure E.24: *Reflection and transmission energy coefficients of the second branch of the quasi transverse wave qT1(2) at the rigid interface between perspex and the transverse isotropic medium as a function of the incidence angle* Θ *and the layback angle* Ψ *in the transverse isotropic medium 2.* **Horizontally polarized transverse (Th)** *wave incidence. Medium 2: Columnar grain tilt angle* $\Phi = 0°$.

Appendix F

Results of ray tracing in austenitic weld metal

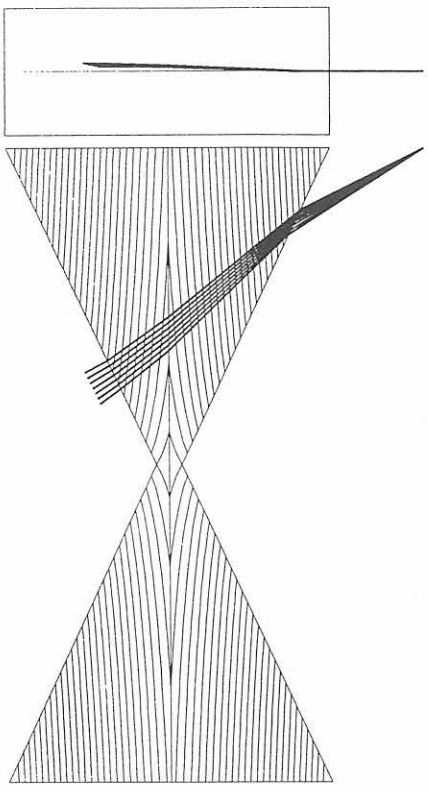

qL 60°

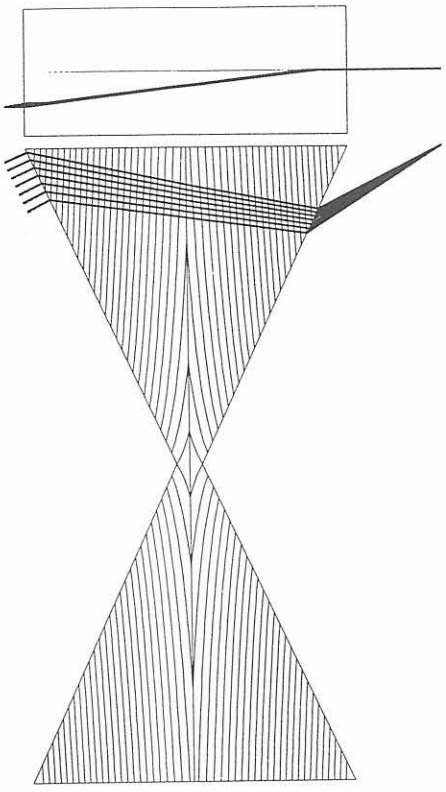

qT1 60°

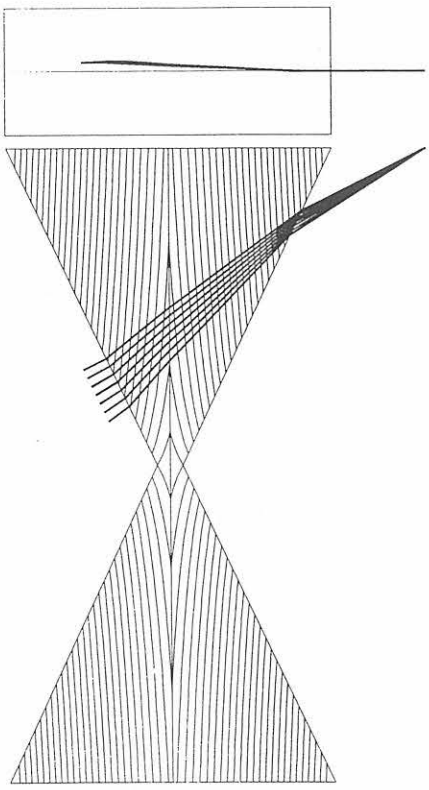

T2 60°

Figure F.1: *Beam path (group velocity direction) of quasi longitudinal (qL), quasi transverse (qT1), and pure transverse (T2) waves calculated three-dimensionally (side-view and top-view). Stiffness constant matrix of the austenitic weld metal s. page 49. Incidence angle = 60°. Weld thickness = 25 mm. Angle of bevel $\alpha' = 25°$. Gap between root faces $D = 1$ mm. $T' = 4.0$, $\eta = 0$, s. equation (3.1) [114, 116, 118, 126].*

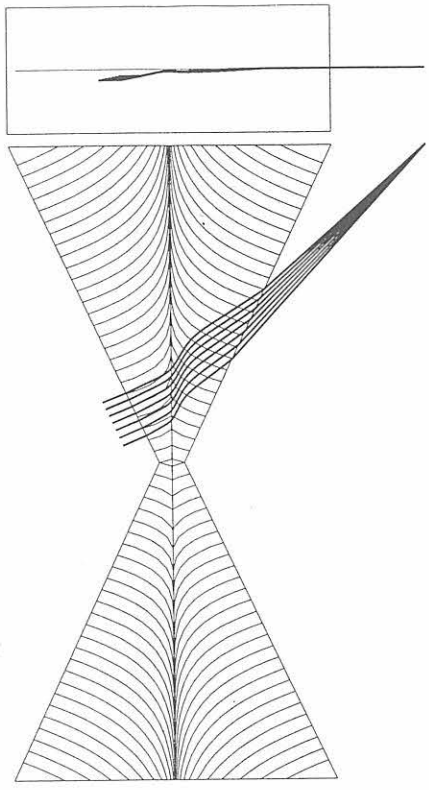

qL 45°

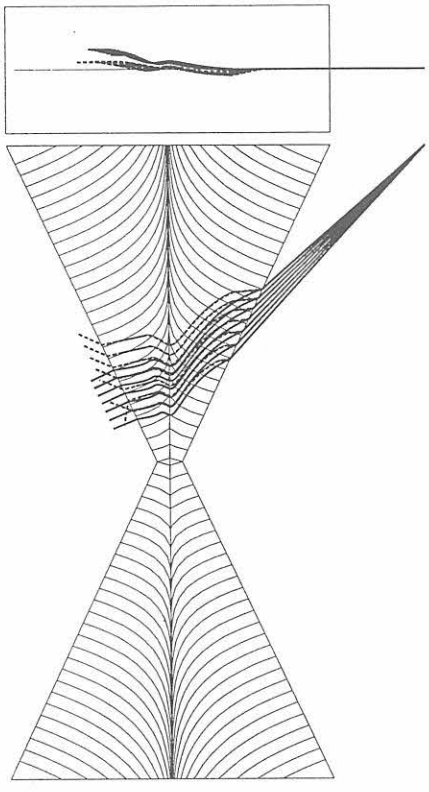

qT1 45°

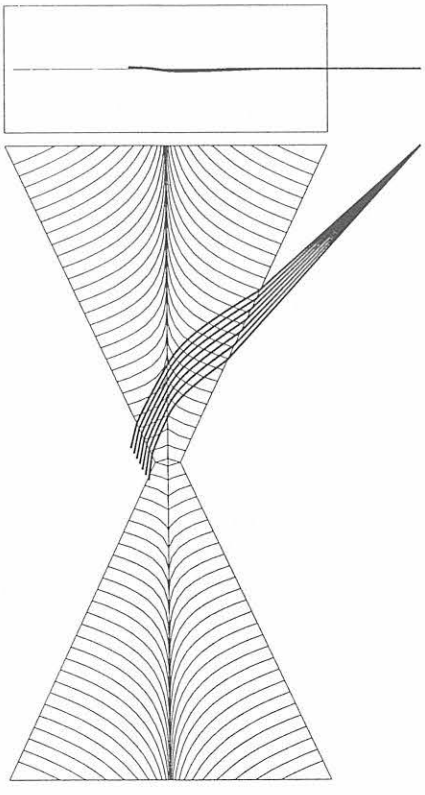

T2 45°

Figure F.2: *Beam path (group velocity direction) of quasi longitudinal (qL), quasi transverse (qT1), and pure transverse (T2) waves calculated three-dimensionally (side-view and top-view). Stiffness constant matrix of the austenitic weld metal s. page 49. Incidence angle = 45°. Weld thickness = 25 mm. Angle of bevel $\alpha' = 25°$. Gap between root faces $D = 1$ mm. $T' = 0.3$, $\eta = 0.85$, s. equation (3.1). [114, 116, 118, 126]*

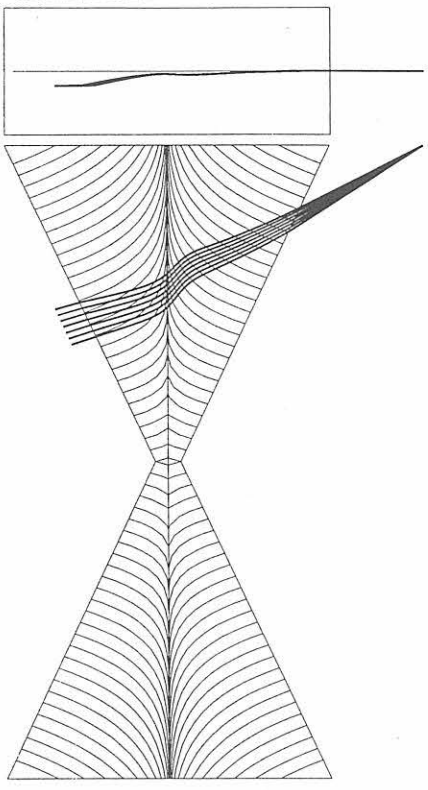

qL 60°

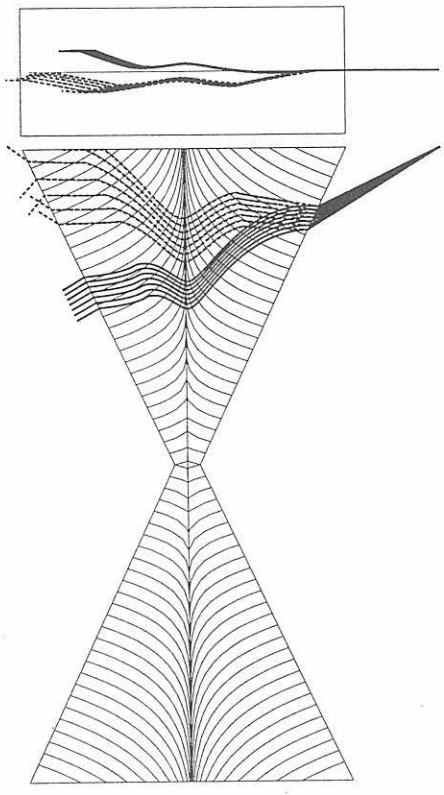

qT1 60°

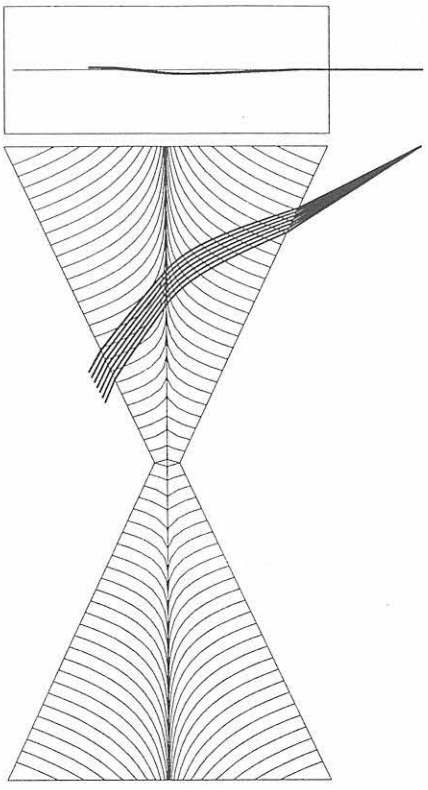

T2 60°

Figure F.3: *Beam path (group velocity direction) of quasi longitudinal (qL), quasi transverse (qT1), and pure transverse (T2) waves calculated three-dimensionally (side-view and top-view). Stiffness constant matrix of the austenitic weld metal s. page 49. Incidence angle = 60°. Weld thickness = 25 mm. Angle of bevel $\alpha' = 25°$. Gap between the root faces $D = 1$ mm. $T' = 0.3$, $\eta = 0.85$, s. equation (3.1). [114, 116, 118, 126]*

Appendix G

Definition of the terms in the stochastic wave equation

One point averages:

$$\epsilon \left\langle \Delta^{\xi}_{ijkl} \right\rangle = \frac{1}{2\pi} \int_0^{2\,\pi} C_{ijkl}(\Theta, \Phi, \Psi)\, d\phi - C^{\circ}_{ijkl} \tag{G.1}$$

Voigt's averages:

$$C^{\circ}_{ijkl} = \frac{1}{8\,\pi^2} \int_{\phi=0}^{2\,\pi} \int_{\theta=0}^{\pi} \int_{\psi=0}^{2\,\pi} f(\theta, \phi, \psi) \sin\theta \; d\theta \; d\phi \; d\psi \tag{G.2}$$

Two point averages:

$$\begin{aligned} \epsilon^2 \left(\left\langle \Delta^{\xi}_{ijmn} \Delta^{\xi}_{opkl} \right\rangle - \left\langle \Delta^{\xi}_{ijmn} \right\rangle \left\langle \Delta^{\xi}_{opkl} \right\rangle \right) = \\ \frac{1}{2\pi} \int_0^{2\pi} \left(C_{ijmn}(\Theta, \Phi, \Psi) - C^{\circ}_{ijmn} \right) \times \\ \left(C_{opkl}(\Theta, \Phi, \Psi) - C^{\circ}_{opkl} \right)\, d\phi - \\ \frac{1}{4\pi^2} \left(\int_0^{2\pi} \left(C_{ijmn}(\Theta, \Phi, \Psi) - C^{\circ}_{ijmn} \right)\, d\phi \times \right. \\ \left. \int_0^{2\pi} \left(C_{opkl}(\Theta, \Phi, \Psi) - C^{\circ}_{opkl} \right)\, d\phi \right) \end{aligned} \tag{G.3}$$

The isotropic Green's tensor (Lifshits & Parkhomovski 1950 [99], Mura 1987 [22]):

$$G_{ij}(r) = -\frac{1}{r} \left(\frac{x_i\, x_j}{r^2}\, g(r) + \delta_{ij}\, h(r) \right) \tag{G.4}$$

$$g(r) = \frac{1}{4\,\pi\,\rho\,\omega^2\,r^2} \left\{ 3\;(1 + \imath f) - f^2 \right\} \exp(-\imath f) \Big|_{k\,r}^{\kappa\,r}$$

$$h(r) = -\frac{1}{4\,\pi\,\rho\,\omega^2\,r^2} \left\{ (1 + \imath f) \exp(-\imath f) \Big|_{k\,r}^{\kappa\,r} - (\kappa\,r)^2\; \exp(-\imath\,\kappa\,r) \right.$$

where

$$F(f)|_{k\,r}^{\kappa\,r} = F(\kappa\,r) - F(k\,r)$$

Standard integrals arising in the evaluation of Green's integral:

$$\int_0^\infty \frac{\exp(-p\,r)\ \sin q\,r\ dr}{r} = \arctan\frac{q}{p}\ \ [p>0] \tag{G.5}$$

$$\int_0^\infty \exp(-p\,r)\ \sin q\,r\ dr = \frac{q^2}{p^2+q^2}\ \ [p>0] \tag{G.6}$$

$$\int_0^\infty \exp(-p\,r)\ \cos q\,r\ dr = \frac{p^2}{p^2+q^2}\ \ [p>0] \tag{G.7}$$

$$\int_0^\infty r\ \exp(-p\,r)\ \sin q\,r\ dr = \frac{2\,p\,q}{(p^2+q^2)^2}\ \ [p>0\ q>0] \tag{G.8}$$

$$\int_0^\infty r\ \exp(-p\,r)\ \cos q\,r\ dr = \frac{p^2-q^2}{(p^2+q^2)^2}\ \ [p>0\ q>0] \tag{G.9}$$

$$\int_0^\infty \frac{\exp(-p\,r)\,(\cos a\,r - \cos b\,r)\ dr}{r} = \frac{1}{2}\ \ln\frac{b^2+p^2}{a^2+p^2}\ \ [Re[p]>0] \tag{G.10}$$

Rotation matrix a:

a is the composite matrix resulting from rotating crystallographic axes with reference to a fixed laboratory coordinate axes system. The matrix is equivalent to

1. rotation around x axis by angle Θ
2. rotation around y axis by angle Ψ
3. rotation around z axis by angle Φ

$$\mathbf{a} = \begin{bmatrix} \cos\Phi\ \cos\Psi & \cos\Theta\ \sin\Phi + \cos\Phi\ \sin\Psi\ \sin\Theta & -\cos\Phi\ \cos\Theta\ \sin\Psi + \sin\Phi\ \sin\Theta \\ -\cos\Psi\ \sin\Phi & \cos\Phi\ \cos\Theta - \sin\Phi\ \sin\Psi\ \sin\Theta & \cos\Theta\ \sin\Phi\ \sin\Psi + \cos\Phi\ \sin\Theta \\ \sin\Psi & -\cos\Psi\ \sin\Theta & \cos\Psi\ \cos\Theta \end{bmatrix} \tag{G.11}$$

where angles Θ and Ψ describe the texture direction in three dimensional space.

Appendix H

Influence of scattering on phase velocity

The intrinsic loss mechanism by scattering is one of the causes which results in the attenuation of the ultrasound beam. It is assumed, that these losses are uniformly distributed throughout the volume of the solid. The plane wave ansatz as given by equation 2.1 is used. For sake of simplicity the wave propagating in the x direction is considered.

$$u = A \ \exp \ \imath \ (k \ x - \omega \ t) \tag{H.1}$$

where u = particle displacement
A = amplitude of the particle displacement
k = wave number
ω = circular frequency t = time
The ansatz that k is a complex quantity (describing attenuation) is considered:

$$k = k - \imath \ \alpha \tag{H.2}$$

where α = is the attenuation coefficient. Here both, k and α, are real quantities.
Referring to Chapter 2 the phase velocity V is defined as

$$V = \frac{\omega}{k} \tag{H.3}$$

or

$$\omega = V \ k \tag{H.4}$$

It is further assumed that the velocity V is complex:

$$V = V_0 + \imath \ V_1 \tag{H.5}$$

Again, V, V_0 and V_1 are real quantities. In the absence of any losses, the second terms in the equations (H.2),(H.5) vanish. Substituting equations (H.2),(H.5) in (H.4) yields

$$\omega = (k_0 \ V_0 + \alpha \ V_1) + \imath (k_0 \ V_1 - \alpha \ V_0) \tag{H.6}$$

The quantities α and k can be deduced from the above:

$$\alpha = (\omega - k_0 \ V_0)/V_1) \tag{H.7}$$

$$k_0 = (\alpha \ V_0)/V_1) \tag{H.8}$$

Substituting (H.8) in (H.7) yields:

$$\alpha = \frac{V_1\,\omega}{(V_0^2 + V_1^2)} \tag{H.9}$$

$$k_0 = \frac{V_0\,\omega}{(V_0^2 + V_1^2)} \tag{H.10}$$

Therefore phase velocity is:

$$V_p = \frac{(V_0^2 + V_1^2)}{V_0} \tag{H.11}$$

If $V_1 \ll V_0$ in the first approximation, the relation for phase velocity and attenuation coefficients can be derived.

$$V_p \approx V_0 \tag{H.12}$$

$$\alpha \approx \frac{V_1\,\omega}{V_0^2} \tag{H.13}$$

This simple analytical relation shows what is often observed in experiments, viz. the phase velocities and other associated properties in the attenuating medium are approximately the same as those in the non-attenuating medium, whereas attenuation depends on the phase velocity in the attenuating medium seen by the term V_1.

Appendix I

List of symbols

$\vec{a}_1$, $\vec{a}_2$, $\vec{a}_3$	Crystallographic basis vectors of the cubic lattice
$\mathbf{a}(\phi)$	Direction cosine matrix
A	Amplitude of the particle displacement velocity
A	Anisotropy factor
A'	Crack area fraction of the interface
α	Particle displacement direction
α'	Angle of bevel
α	Attenuation coefficient
C_{ijkl}	Elastic stiffness constants related to the crystallographic axes, i,j,k,l = X,Y,Z
C_{KL}	Stiffness constants in abbreviated notation
C_{IJ}	Stiffness constants in abbreviated notation
δ	Ultrasound penetration depth due to damping losses in a viscoelastic layer
δ_{ij}	Kronecker's delta symbol; i,j = x,y,z
δ_{scat}	Polarization deviation of the qL (qT1) wave, respectively, due to ultrasound scattering
Δ_{per}	Displacement at a perfect interface due to a static tensile force
Δ_{im}	Displacement in the presence of imperfections at an interface due to a static tensile force
D	Half width of the gap between root faces
$\overline{d}$	Average grain diameter (DIN 50601)
$\frac{\overline{d}}{h}$	Grain shape parameter: Average grain diameter to height ratio of the columnar grain
$\mathbf{E}$	Energy flux density vector
$\overline{\mathbf{E}}$	Time averaged energy flux density vector
E_{kin}	Kinetic energy
E_{pot}	Potential energy
E_{tot}	Total energy of the plane wave ($E_{kin} + E_{pot}$)
$\overline{E_{tot}}$	Time averaged total energy
ϵ	Step size during ray tracing
ε	Perturbation parameter in the Keller' approximation

η	Measure of the change of the grain orientation as a function of the distance x from the weld centre line
F_1	Vector sum of the traction forces exerted on the opposite sides of the imperfect interface
Γ_{ij}	Christoffel matrix
G'	Bulk modulus
h	Coupling layer thickness
$\mathbf{k}$	$\mathbf{k} = k \cdot \mathbf{n}$, k is the wave number
k	Wave number: $k = \frac{2\pi}{\lambda}$
$\frac{k}{\omega}$	Slowness (Inverse of the phase velocity V_p)
K_x, K_y, K_z	Slowness vector components used in the Snell's law
κ_1, κ_2	Transverse interfacial stiffnesses
κ_3	Extensional (longitudinal) interfacial stiffness
$l_x,\ l_y,\ l_z,\ l_{iK}, l_{Lj}$	Unit vector denoting the direction of the wave vector along x-, y-, and z-axes of the reference coordinate system
μ'	Shear viscosity coefficient of a viscous coupling medium
$\mathbf{n}$	Normal unit vector of a surface element
$\mathbf{n}^n$	Boundary normal vector
ν	Kinematic viscosity of a viscous fluid
ω	$\omega = 2\pi f$ (angular frequency)
ϕ	Incidence angle in the yz plane
ϕ'	Columnar grain angle measured with respect to the reference x-axis
Φ	Columnar grain tilt angle against the crystallographic XZ-plane
Ψ	Columnar grain layback angle against the crystallographic YZ-plane
qL	Quasi longitudinal (quasi compression) wave
$qT1$	Quasi transverse (quasi shear) wave
qT_V	quasi transverse (quasi shear) wave with polarization in the incidence plane (in-plane polarization)
$\mathbf{r}$	Space vector with x, y, z Cartesian coordinates
ρ	Density of the material
$\rho_I,\ \rho_i,\ \rho_j$	Densities of adjacent media
r, θ, ϕ	Polar coordinates
ϑ	Rotation angle for coordinate transformation
r_{1I}, r_{2I}, r_{3I}	Reflection coefficients (amplitude ratios of reflected waves to incident waves)
R_{iI}	Reflection energy coefficients
$\mathrm{r_{qLqL}},\ \mathrm{t_{qLqL}}$	The legend of this type has the following meaning:

- the first letter r (or t) denotes the energy reflection (or transmission) coefficient. (The energy coefficients are now denoted by lower-case letters. Confusion with amplitude ratios are not possible since these are only treated in sections 2.3.1 and 2.3.2.)

- The first term qL (or L, Tv, Th, qT1, T2) of the subscript denotes the type of wave for which the energy coefficient is calculated.
  qL: quasi longitudinal wave,
  qT1: quasi transverse wave,
  T2: pure transverse wave,
  L: pure longitudinal wave,
  Tv: vertically polarized transverse wave,
  Th: horizontally polarized transverse wave.
- The second term qL (or L, Tv, Th, qT1, T2) of the subscript denotes the type of the incident wave.

S_J	Strain tensor
$T2$	Pure transverse (pure shear) wave
T_H	Pure transverse (pure shear) wave with polarization perpendicular to the incidence plane (anti-plane)
θ	Incidence angle in the xz plane, the xy plane containing the boundary
Θ	Incidence angle between wave vector and z-direction of the laboratory system x, y, z
$\mathbf{T}, (T_{ij})$	Traction force tensor; $i, j = x, y, z$
$\mathbf{T}, \mathbf{T}'$	Traction force tensors across an interface
T_{ik}	Traction force components
$T_{zz1}, T_{yz1} \cdots T_{yz3}, T_{xz3}$	Traction force components for the reflected wave
$T'_{zz1}, T'_{yz1} \cdots T'_{yz3}, T'_{xz3}$	Traction force components for the transmitted wave
t_{1I}, t_{2I}, t_{3I}	Transmission coefficients (amplitude ratios of transmitted waves to incident waves)
T_{jI}	Energy transmission coefficients
T'	Measure of the slope of the columnar grain axis at the fusion faces
$\mathbf{u}$	Particle displacement of an incident wave
$\mathbf{u}'$	Particle displacement of a transmitted wave
$\mathbf{v}, v_j$	Eigenvector or particle displacement velocity (polarization) vector
$\mathbf{v}, \mathbf{v}'$	Particle displacement velocities across an interface
$\mathbf{v}^{conj}$	Complex conjugated eigenvector
$v_{x1}, v_{y1} \cdots v_{y3}, v_{z3}$	Particle displacement velocity components for the reflected wave
$v'_{x1}, v'_{y1} \cdots v'_{y3}, v'_{z3}$	Particle displacement velocity components for the transmitted wave
$V_p = \frac{\omega}{k}$	Phase velocity
$\mathbf{V}_g$	Group velocity
$\mathbf{V}_e$	Energy velocity
V_I	Phase velocity of the incident wave
$V_{g,z}$	Component of group velocity perpendicular to the interface
$V_{scat}^{ti,l,s}$	Phase velocity in the transverse isotropic medium (longitudinal, shear) in the presence of grain scattering

$V_{mono}^{ti,l,s}$	Phase velocity in the transverse isotropic mono-crystalline medium (longitudinal, shear)
w	Half beam width $\frac{f_0}{e}$ at the amplitude of a Gaussian amplitude profile $f(x)$
x, y, z	Laboratory (Cartesian) coordinate system
X, Y, Z	Crystallographic (Cartesian) coordinate system with Z being the columnar grain direction

Acknowledgements

This work has been the outcome of several years of research work that I have been doing during my employment as scientist at the Bundesanstalt für Materialforschung und -prüfung (BAM), Laboratory VIII.42: *Ultraschallprüfung von anisotropen Werkstoffen* headed by Dr.-Ing. E. Neumann. I gratefully acknowledge his help and support.

Dr.-Ing. E. Neumann has also been responsible for guiding me all along my Ph.D. work. Innumerable brain storming discussions that I have had with him has helped me develop deeper insight into the area of ultrasonic wave propagation in anisotropic materials. My sincere thanks to him for giving me an opportunity to be associated with him all these years and for all the encouragement and moral support he has extended to me.

I take this opportunity to express my sincere thanks to the management of the BAM especially to:

- Dir. u. Prof. Dr.-Ing. W. Paatsch, Head of the Department VIII: *Materials Protection; Non-Destructive Testing*
- Dir. u. Prof. Dr.-Ing. H. Wüstenberg, Head of the Division VIII.4: *Non-Destructive Testing; Acoustical and Electrical Methods*
- Dr. rer. nat. M. P. Hentschel, Head of the Laboratory VIII.32: *General X-Ray Topography*

for supporting me all these years.

During 1997 - 1998 under the purview of an European project funded by the Commission of the European Communities under the "Standards, Measurements and Testing"-Programme I worked for FORCE Institute, Denmark. I thank Mr. L. Jeppesen, Head of the Department for "Advanced NDE Services" and the Technical Director, Dr. W. D. Kristensen, for their support.

I have also been privileged to have

- Prof. W. Bergmann, Institut für Werkstofftechnik, Fachbereich 11, Technische Universität Berlin,
- Prof. Dr. H. Burkhardt, Dekan, Fachbereich 09, Angewandte Geophysik, Technische Universität Berlin, and
- Priv.-Doz. Dr. W. Dreyer, Abteilung für Kontinuumsmechanik, Weierstraß-Institut für Angewandte Analysis und Stochastik (WIAS), Berlin,

who have been my main advisors guiding me all along the work. Each of them has reviewed this work from their specialization point of view, which has enabled me to greatly improvise on the results presented here. My sincere thanks to them.

I have also had many opportunities to personally interact with Dr. Dreyer (WIAS). I have been immensely benefited by many discussions that I have had with him especially

concerning mathematical intricacies involved in the wave propagation. I gratefully acknowledge his readiness to help and for his patience in making me understand many aspects of mathematical analysis.
I have also electronically interacted with

- Prof. S. Ahmed, Parks College of Saint Louis University, Cahokia, Illinois, USA
- Dr. rer. nat. S. Hirsekorn, Fraunhofer-Institut für Zerstörungsfreie Prüfverfahren, Saarbrücken
- Prof. F. Margetan, Center for NDE at Iowa State Universiy, Ames, USA,
- Prof. P. B. Nagy, Department of Aerospace Engineering and Engineering mechanics University of Cincinnati, USA
- Dr. C. Pecorari, ABB Corporate Research, Sweden

I sincerely thank them for their assistance.
I thank my colleague Dr.-Ing. M. Weber, for his many suggestions and advice concerning this work.
I express my heartfelt thanks to my colleagues Dipl.-Ing. D. Gohlke, Ing. H. Mrasek for their enduring patience in preparing excellent quality diagrams which have been presented in this work.
My special thanks to Dipl.-Ing. K. Matthies for his constant encouragement and help he has extended to me throughout my career so far at the BAM.
I thank Dipl.-Ing. H. Ernst for allowing me to use his experimental results concerning scattering in polycrystalline materials.
Many thanks are due to my colleague Ing. W. Gieschler for his readiness to help in solving software/system administration problems.
My sincere thanks to Ing. B. Behrendt for helping me out with many secretarial jobs.
Finally I thank my family and many others who have directly and indirectly helped me.

ISSN 0938-5533
ISBN 3-89701-632-X